Statics and Dynamics of Drops on Solid Surfaces: Theory and Simulations

A Thesis
Submitted for the Degree of
Doctor of Philosophy

by

Sumesh P. Thampi

Engineering Mechanics Unit
Jawaharlal Nehru Centre for Advanced Scientific Research
(A Deemed University)
Bangalore – 560 064

APRIL 2012

Achu, Vava and My Parents

DECLARATION

I hereby declare that the matter embodied in the thesis entitled "**Statics and Dynamics of Drops on Solid Surfaces: Theory and Simulations**" is the result of investigations carried out by me at the Engineering Mechanics Unit, Jawaharlal Nehru Centre for Advanced Scientific Research, Bangalore, India under the supervision of **Prof. Rama Govindarajan** and that it has not been submitted elsewhere for the award of any degree or diploma.

In keeping with the general practice in reporting scientific observations, due acknowledgment has been made whenever the work described is based on the findings of other investigators.

Sumesh P. Thampi

CERTIFICATE

I hereby certify that the matter embodied in this thesis entitled "**Statics and Dynamics of Drops on Solid Surfaces: Theory and Simulations**" has been carried out by **Mr. Sumesh P. Thampi** at the Engineering Mechanics Unit, Jawaharlal Nehru Centre for Advanced Scientific Research, Bangalore, India under my supervision and that it has not been submitted elsewhere for the award of any degree or diploma.

Prof. Rama Govindarajan
(Research Supervisor)

Acknowledgements

It is my honor to acknowledge people who have directly or indirectly helped me in making this thesis a reality and I am unreservedly indebted to them.

First and foremost, my sincere gratitude is to my supervisor *Prof. Rama Govindarajan*. Several qualities which distinguished her from other supervisors have been crucial for my survival in JNC and realization of this thesis. Complete freedom to work on anything that I preferred, exceptionally brilliant questions and intelligent interpretations which turned out to be some of the chapters in this thesis, discussions and support in both personal and academic matters with no interference or indirect intimidation are just few to which any words cannot overstate my gratitude. Any of her decisions, steps and actions have always been to prepare me to face the competitive world and aimed at my better future. Let me thank her for everything.

I was fortunate to get introduced to *Ronojoy Adhikari* who created a feeling that I am closer to physicists and made me realize that noise is not just 'noise' in physics. His in-depth understanding of the subjects and abstraction of ideas have always been source of inspiration to me. I really appreciate the time that he has spent to teach me the basics, among his busy schedule, and the support and concern he has shown for my future endeavors. Fluctuating hydrodynamics got me in touch with *Ignacio Pagonabarraga* and the collaborations continued. His enthusiasm on scientific topics and interests and perseverance to go through the details are commendable. Patiently reading and replying to my long emails and any minute points and listening and responding to my long Skype conversations have indeed been great educative experiences. Without them both this thesis and my interests would have taken a different route.

Though not contributed directly to this thesis, my overall knowledge gain from *Ganesh Subramanian* is enormous. His intensive lectures, physical intuition on problems and ability to figure out mathematical mistakes from physics, physically motivated but mathematically rigorous and painstakingly algebraic problems and occasional pep talks have been intellectually satisfying and educationally rewarding. Incidental discussions with *Santosh Ansumali* and *K R Sreenivas* were joyful. So are the interactions with *Sauro Succi* which also taught me to look at numerical methods from a different perspective. Among others I should mention few names: *Rajaram Nityananda*, *Bruno Andreotti*, *Mahesh Panchagnula*, *Sanjeev Gupta*, *Sriram Ramaswamy* with whom I have had very little but fruitful and fundamentally sound discussions.

I would not have been able to venture out for my PhD without the silent support of *my parents*. This thesis would not have taken this form without the affectionate and emotional support of my beloved *Achu*. Though joined lately, my *vava* offers her innocent support unknowingly.

There are several friends who made my life in JNC memorable, scholastic, edifying, enjoyable and witty. Academic and non academic but serious discussions with *Harish*, combined studies, political and personal discussions with *Ponnu*, co-travels and lessons from *Anubhab*, clarifying

numerical methods and typical teasing conversations of *Gayathri*, educative sessions of *Ratul*, low Re discussions and jogging sessions with *Vivekanand*, thesis discussions with *Rakshith*, nostalgic and Malayalam discussions with *Navaneeth*, sharing the evil 'TA-ness' and random discussions with *Saikishan*, jogging sessions with *Prasanth*, Carnatic music sessions with *Aditya*, *Vineetha*, *Snehalatha*, lunch sessions with *Jose*, fun times with *Vishwanath*, bird watching discussions with *Vybhav*, *Amol*, *Shashank* and *Rohan*, 'intellectual' anecdotes of *Croor*, kinetic theory discussions with *Srikanth* and good times with *Rahul*, *Krithika*, *Vivek Prakash*, *Priyanka*, *Vinay*, *Rohith*, *Rajesh*, *Shahjahan*, *Mamta*, *Divya*, *Sunil*, *Shiwani*, *Mukund*, *Saurabh*, *Gaurav*, *Sarath*, *Reddy*, *Siddardh*, *Dhiraj*, *Ansari*, *Deepak*, *Rahul Karyappa*, *Tapan* are just few to mention and I earnestly thank all of you and my other EMU and JNC friends. My stay in the hostel with family was a pleasurable experience with the presence of *Pankaj* and *Anju*, *Kumar* and *Josena* and *Anubhab* and *Senjuti*. Summers in JNC were busier but redressing and thought provoking thanks to the summer students *Charudatt*, *Ashwin*, *Shikhar*, *Kunal*, *Astha* and *Vaishnavi*.

My IMSc visits would have been rather difficult experiences without the help of *Sameen*, whose company I enjoyed in academic and personal matters. I thank *Amit*, *Gayathri Jayaraman*, *Somdeb*, *Markus* and *Moradi* for their helps at various times. Support and inspiration from *Uday Agarwal* specially deserve mention without which I would not have probably thought about doing a PhD. Frequent or otherwise, calls from several of my friends like *Prince*, *Arun*, *Hooper*, *Amit*, *Prashant*, *JP* and *Venkat* helped me to unwind at various times.

I thank our administrative officer, *Jayachandra*, other *admin*, *library* and *complab* staff, *Vijayalakshmi*, *Harisha*, *Princy* for various helps from time to time. Let me acknowledge *DST*, *NBHM* and *APS* for providing sufficient funding to attend conferences. Finally let me thank JNCASR and DST for providing all the financial and infrastructural support to pursue my PhD here and I am sincerely grateful for that.

Abstract

Liquid drops supported on solid surfaces are commonly encountered in nature and in industries. While their aesthetically pleasing shapes and motion generate curiosity, the understanding of these shapes and their dynamics are a must in several applications. This classical problem in statics and dynamics poses several interesting but unresolved questions and we address some of them in this thesis.

Statics

We first carry out analytical and numerical studies on the shapes of two-dimensional and axisymmetric pendant drops hanging under gravity from a solid surface. We show that drop shapes with both pinned and equilibrium contact angles can be obtained naturally from a single boundary condition in the analytical energy optimization procedure. Our numerical procedure too yields optimum energy shapes which turn out to satisfy Young's equation, without the explicit imposition of a boundary condition at the plate. It is shown analytically that a static pendant two-dimensional drop can never be longer than 3.42 times the capillary length. A related finding is that a range of existing solutions for long two-dimensional drops correspond to unphysical drop shapes. Therefore two-dimensional drops of small volume display only one static solution. In contrast, it is known that axisymmetric drops can display multiple solutions for a given volume. We demonstrate numerically that there is no limit to the height of multiple-lobed Kelvin drops, but the total volume is finite, with the volume of successive lobes forming a convergent series. The stability of such drops is in question, though. Thus drops of small volume can some times attain large heights. A bifurcation is found within the one-parameter space of Laplacian shapes, with a range of longer drops displaying a minimum in energy in the investigated space. Axisymmetric Kelvin drops exhibit an infinite number of bifurcations.

Then we analyze, in two dimensions, the shapes that liquid drops will assume when resting statically on a solid surface inclined to the horizontal. Earlier experimental and numerical studies yield multiple solutions primarily because of inherent differences in surface characteristics. On a solid surface capable of sustaining any amount of hysteresis, we obtain the global, and hence unique, minimum energy shape as a function of equilibrium contact angle, drop volume and plate inclination. It is shown, in the energy minimization procedure, how the potential energy of this system is dependent on the basis chosen to measure it from, and two realistic bases, front-pinned and back-pinned, are chosen for consideration. This is at variance with previous numerical investigations where both ends of the contact line are pinned. It is found that the free end always assumes Young's equilibrium angle. Using this, simple equations which describe the angles and the maximum volume are then derived. The range of parameters where static drops

are possible is studied. We also introduce a detailed force balance for this problem and study the role of the wall in supporting the drop. We show that a portion of the wall reaction can oppose gravity while the other portion aids it. This determines the maximum drop volume that can be supported at a given plate inclination. This maximum volume is the least for a vertical wall, and is higher for all other wall inclinations. This study can be extended to three-dimensional drops in a straightforward manner, and even without this, lends itself to experimental verification of several of its predictions.

Dynamics

In order to study the dynamics of drops on solid surfaces, a numerical tool to simulate interfacial and wetting flows is necessary. A general algorithm for a hybrid numerical method for the solution of the model H fluctuating hydrodynamic equations for binary mixtures is developed. The momentum conservation equations with Landau-Lifshitz stresses are solved using the fluctuating lattice Boltzmann equation while the order parameter conservation equation with Langevin fluxes are solved using the stochastic method of lines. Two methods, based on finite difference and finite volume, are proposed for spatial discretisation of the order parameter equation. In earlier studies, discretization errors result in an effective break-down of the fluctuation dissipation theorem, especially at large wave numbers. We take special care to ensure that the fluctuation-dissipation theorem is maintained at the lattice level in both cases. The methods are benchmarked by comparing static and dynamic correlations and excellent agreement is found between analytical and numerical results. The Galilean invariance of the model is tested and found to be satisfactory. Thermally induced capillary fluctuations of the interface are captured accurately, indicating that the model can be used to study nonlinear fluctuations. (1) Different boundary conditions to simulate walls and desired wetting on the solid surface (2) an external force to introduce gravity and (3) a viscosity difference between the fluids by specifying relaxation time as a function of order parameter are also incorporated into the model. Several problems in multiphase fluid mechanics can now be investigated with this developed code as illustrated below.

First we study the motion of a two-dimensional droplet on an inclined surface under the action of gravity. We know that a solid sphere is likely to roll, while a rectangular box is likely to slide, on an inclined surface. In contrast, a liquid drop moving on an inclined surface can exhibit a variety of shapes and hence complex but interesting dynamics. The kinematics of drop motion is analyzed by decomposing the gradient of the velocity inside the drop into a shear and a residual flow. This decomposition helps in distinguishing sliding versus rolling motion of the drop. Our detailed study confirms intuition, in that rolling motion dominates as the droplet shape approaches a circle, and the viscosity contrast between the droplet and the ambient fluid becomes large. We show that for a general droplet shape, the amount of rotation follows a universal curve characterized by geometry in terms of isoperimetric quotient, and independent of Bond number, surface inclination and equilibrium contact angle, but determined by the slip length and viscosity contrast. Our results open the way towards a rational design of droplet-surface properties, both when rolling motion is desirable (as in self-cleaning hydrophobic droplets) or when it must be prevented (as in insecticide sprays on leaves).

Now we investigate the capillary spreading of drops on both hydrophilic and hydrophobic surfaces. On hydrophilic surfaces, we demonstrate that wetted radius of drops grows algebraically as is known as Tanner's law. Balancing the scaling estimates of viscous dissipation and capillary forces it is shown that there always exists two regimes of growth, (i) Tanner's law and then (ii) an exponential relaxation of both contact angle and contact radius, except in case of perfect wetting. This transition from algebraic to exponential regime is demonstrated analytically and numerically. On highly wetting surfaces our simulations show accelerated spreading rates after obeying Tanner's law for a small interval. These two observations also validate previous simulations reported in the literature establishing Tanner's law only for small durations of time and explains the reasons for finding different exponents in some of those cases. Though derived for small contact angles, the exponential relaxation is observed at the terminal stages of wetting on hydrophobic surfaces and in dewetting of drops. Effects of various parameters including thermal fluctuations on the spreading process are being studied.

List of Figures

List of Tables

Contents

Chapter 1

Introduction

The multitude of aesthetic shapes that liquid drops adopt in various situations has always been fascinating to human beings. After a rain or on cold mornings it is common to encounter drops sitting on window panes and plant leaves. These drops are held in a state of static equilibrium under the action of gravity and surface forces (de Gennes *et al.* 2004). Depending upon the solid-liquid properties, a variety of shapes may be formed. Beyond a certain volume or surface inclination these drops may move or fall down. While it is interesting to know this critical volume and inclination at which the drops start moving, one may also wonder about the dynamics inside the drop; how these drops wet or de-wet surfaces, whether these drops slide or roll down on a surface under gravity. In the case of solid objects, we know that a ball would roll down on an inclined plane and a rectangular box is likely to slide down. The shape, size and frictional characteristics determine the roll vs sliding motion in these rigid bodies. However, in the case of drops, neither the dynamics exhibited by the drops nor the important parameters affecting their motion are obvious. At the same time the shapes that both static and dynamic drops assume are complex but interesting. Some situations where the study of statics and dynamics of drops are important is illustrated in Fig. 1.1.

Besides the curiosity to understand the drop shapes and their dynamics, this knowledge is imperative in certain coating and paint industries (Dussan 1979; Yarin 2006). In most of these cases it is desirable to know the rate of spreading to ensure the uniformity of coating. In addition to the spreading rates, it is also important to know the maximum volume of a drop that can be held static on an inclined surface in certain spray applications, for example, pesticides and insecticides sprayed onto plant leaves. Any guidelines to tailor the liquid and surface properties to modify volume that can be held static, would also be useful. With the development of new materials such as smart textiles and super hydrophobic surfaces, it would be interesting to know the favorable conditions for the drops to move on surfaces, so that they can pick up the dirt, without sticking to the surface (Rothstein 2010). Another example is in dropwise-condensation heat exchangers where the vapor condenses on solid plates and the condensate drops are removed. It is necessary to know the maximum size of a drop that can be held on the surface and how easily it can be removed as both these factors affect the heat transfer efficiency (Daniel *et al.* 2001). With the latest developments in nano and microfluidics and miniaturization of devices, surface forces play at least an equally important role as body forces (Squires & Quake 2005; Rauscher & Dietrich 2008); some of these new applications are in biomedical industries and biomimetic designs (Koch & Barthlott 2009; Mitragotri & Lahann 2009; Castner & Ratner 2002) warranting a sound understanding of the basics of interfaces and their stability.

In this thesis, we intent to address several questions associated with statics and dynamics of drops. Though these are centuries old problems, we will see that there are many unattended

and unanswered questions in describing the mechanics of drops on surfaces. Some of the recent articles on the foundations of capillary science alert us to this situation (Marchand *et al.* 2011; Finn 2006; Lunati 2007; Finn 2008*a*,*b*; Shikhmurzaev 2008*b*; Finn *et al.* 2011; Blake & Shikhmurzaev 2002; Eggers & Evans 2004; Shikhmurzaev & Blake 2004).

The formulations by Young and Laplace (Pujado *et al.* 1972) to describe static menisci attracted physicists and mathematicians alike to solve such shapes. No general analytical solution has however been found. A pressure jump exists across any curved interface due to the surface tension and this has to be in balance with the bulk pressure existing in the fluid. For example, in the presence of gravity, the pressure jump across the curved interface has to be balanced by the hydrostatic pressure and such a balance always gives the description of the interface shape. When this interface meets a solid surface, a contact line is formed. At the contact line, the solid comes in contact with two fluids, generally a liquid and a gas as illustrated in Fig. 1.2. A force balance parallel to the solid plate then gives Young's equation,

$$\sigma_{sg} = \sigma_{sl} + \sigma \cos\theta_e \tag{1.1}$$

where σ_{sg}, σ_{sl}andσ are the tensions along solid - gas, solid - liquid and liquid - gas interfaces. This microscopic force balance fixes the equilibrium contact angle, θ_e between the fluids and the solid which also characterizes the wetting property of the fluids on the solid surface. When θ_e is small, it is termed as a hydrophilic surface while $\theta_e \to 180^\circ$ it is called a hydrophobic surface. It may be noted that the equilibrium contact angle, θ_e, defined by Eq. 1.1 can be achieved only on very smooth surfaces. Any heterogeneities, physical or chemical, present on the surface will cause the interface to exhibit a different contact angle, generally termed as an apparent contact angle. There may be a range of contact angles that a particular combination of liquids and solid exhibit due to the hysteresis of the solid surface. The maximum of which is when the static interface is formed from an advancing fluid and the minimum when it is formed from a receding fluid.

Though Young's equation has been accepted in the literature long ago, the validity of this equation in certain situations has been questioned in recent times, and controversies persist, with arguments for (Lunati 2007; Shikhmurzaev 2008*b*) and against (Finn 2006, 2008*a*,*b*; Finn *et al.* 2011) this equation. Our studies on static drops in chapters 2 and 3 which deal with energy minimization to determine the drop shapes never impose Young's equation as a boundary condition, but we always recover it for the minimum energy shapes. Sessile drops, i.e., drops sitting on a horizontal surface, have been studied extensively over the past few decades (Yonemoto & Kunugi 2009). So have pendant drops hanging from a support of fixed radius, or from an orifice. On the other hand, the body of work on pendant drops hanging from an infinite solid surface is smaller and we look at them in chapter 2. Considering an energy minimization problem without imposing any boundary conditions, as mentioned earlier, we derive a generalized boundary condition describing both pinned and unpinned drops. Both our analytical and numerical procedures yield minimum energy shapes with Young's equilibrium satisfied at the contact line. Several features about the height and stability of these drops are investigated. Interestingly, in contrast to sessile drops, some of these drops can exhibit multiple statically stable shapes for a given volume, we show that some them can be infinitely long. A similar

(a) Drops on glass surfaces, Picture source: http://wallpaperdreams.com/wallpapers/in_focus_rain_droplets_on_a_window_with_car_headlights_behind_at_dusk.1280x800.c42e77c2.jpg#rain%20drops%20on%20window, http://www.desktopedia.com/wallpaper/Rain-Drops-on-Glass

(b) Rain drops on plant leaves, Picture source: http://ian.umces.edu/imagelibrary/displayimage-761.html, http://14myrules.blogspot.in

(c) Dirt is removed on smart textiles without wetting, Picture source: http://www.geoffanderson.com/kat16-Fabrics/side301-Sympatex%C2%AE-technology.html

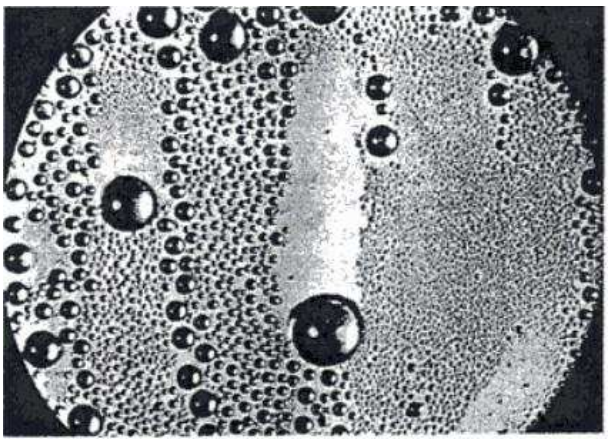

(d) Vapor condenses and form droplets and are removed to obtain high heat transfer efficiency in condensation heat exchangers. Chemically modified surfaces inducing Marangoni flows have been proposed as efficient mechanisms to remove these drops (Daniel *et al.* 2001), Picture source: Heat & Mass Transfer by Y. A. Cengel

Figure 1.1: Static and dynamic drops on solid surfaces are commonly seen in nature and industries.

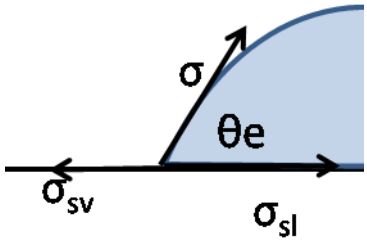

Figure 1.2: Horizontal force balance at the contact line gives Young's equation.

study is undertaken in chapter 3 about drops on inclined surfaces. Hysteresis, the very force in this case supporting the drop to remain static, is associated with uncertainties and hence, in the literature, drop shapes have been calculated by fixing either the contact angles or the contact area. Instead we use an energy minimization method assuming infinite hysteresis of the solid plate, and find that the unpinned end always obeys Young's equation. It should be pointed out that both microscopic force balance i.e., Young's equation at the contact line, and macroscopic force balance, i.e, a balance between the gravitational component and surface tension forces (as commonly used in literature) are force balances parallel to the solid surface. The force balance normal to the surface was never examined till recently (Marchand *et al.* 2011; Jerison *et al.* 2011; Thampi & Govindarajan 2011; Style & Dufresne 2012). We show the importance of reaction forces on the surface and at the contact line. The detailed force balance reveals that the solid reaction can be in different directions in different portions of the drop thus allowing only a maximum volume that can be held on a surface. A parametric study not only reveals the regions of possible solutions, it also gives directions to tailor the surfaces to hold larger volumes of static drops.

We then develop an algorithm to simulate the dynamics of drops in chapter 4. A very generic algorithm describing the dynamics of binary fluids is developed incorporating several features. Particularly important is the introduction of thermal fluctuations as they may form essential part of physics at mesoscopic length scales such as in fluctuations driven spreading of nano droplets on solid surfaces (Davidovitch *et al.* 2005), dewetting of thin films (Willis & Freund 2009) and break up of nano jets (Eggers 2002). The general algorithm that is developed is capable of studying various other phenomena such as dynamics of emulsions in complex fluids, nucleation and spinodal decomposition in binary fluids (Gompper *et al.* 1994; Gonnella *et al.* 1999) and so on. However, we do not pursue them in this thesis but we intend to do them in the future. Here, we study problems driven by capillary and gravitational forces on the macroscopic length scales as mentioned below. While it is relatively easy to analyze drop motion in different limits, say, under the lubrication approximation at small θ_e (Dussan & Chow 1983; Oron *et al.* 1997) or, at large θ_e, assuming the drops to be purely spherical (Quere 2005; Mahadevan & Pomeau 1999; Biance *et al.* 2004) it is very difficult to analyze the intermediate range of contact angles. This is because the governing equations do not lend themselves to any simplifying assumptions warranting the solution of full equations. As of now it is impossible to find any analytical solutions, numerical solutions also pose considerable challenges (Scardovelli & Zaleski 1998) since the interfacial flows involve tracking of interfaces and incorporation of mechanisms to escape the contact line singularity (Shikhmurzaev 2008*a*). Therefore our hybrid algorithm implementing

a lattice Boltzmann method to solve hydrodynamics and a diffuse interface model accounting the evolution of order parameter is a very promising method as illustrated in this thesis. The diffusion of the order parameter, here defining the concentration of drop and the outer fluid, across the interface at the contact line provides a mechanism for contact line movement and relieves the contact line singularity. A viscosity contrast between the fluids can also be achieved very easily by choosing the relaxation time in the lattice Boltzmann algorithm to be a function of the order parameter. We do not have any restriction on the size of the drop compared to relevant length scales such as capillary length in the problem. Also it is possible to simulate drops on surfaces with any contact angles ranging from 0° to 180°.

Having these advantages built into the algorithm, we analyze the motion of drops on inclined surfaces under the action of gravity in chapter 5. Most of the previous studies concentrate on calculating the velocity of a translating drop as a function of various parameters such as Bond number and equilibrium contact angle. We look at drop dynamics from a different perspective. We address the question of rolling vs sliding motion inside the drop in comparison with rigid body motion on an inclined surface. We borrow the concept of triple decomposition of velocity gradient tensor introduced in the context of turbulence to distinguish high vorticity regions from high shear regions and use it, for the first time, as a measure to characterize the rolling motion of a drop. The amount of rolling motion is found to be dependent only on certain parameters such as shape, viscosity difference between the fluids and slip length at the contact line. Not only are some intuitive predictions confirmed quantitatively, some surprising facts have also been found. For example, the relationship between the amount of rolling motion and a particular shape factor is a universal curve independent of capillary and gravitational forces. The shape factor is a measure of how far a given shape is from a circle. Drops of rather different shape but with same shape factor display the same amount of roll. Thus, this study is expected to provide guidelines to choose and design solid-fluid properties where rolling motion is desirable as in non-wetting textiles and smart materials and it is not desired as in coating and spray applications. A related problem that is of fundamental interest is the capillary spreading of a drop and we investigate this in chapter 6. We identify various regimes of spreading, establish them in simulations providing a comprehensive picture of spreading process. For highly wetting surfaces accelerating spreading rates are observed. For any finite equilibrium contact angle the terminal stage is an exponential relaxation of contact radius and contact angle. Before the occurrence of this regime an algebraic growth will be seen. The durations of each of these regimes depends upon the instantaneous and equilibrium contact angles. These observations are important, because, various studies in the literature examine specific regimes of the spreading process, sometimes reporting a variety of exponents in the algebraic growth regime or showing algebraic growth only for short durations of time. Our detailed investigation suggests the plausible explanations for these discrepancies as there may be interference from both accelerated spreading regimes and exponential spreading regimes. Also different methods such as molecular dynamics and dissipative particle dynamics are used in various situations. Using our hybrid algorithm we analyze the entire range of contact angles to show the validity of different regimes both in spreading and de-wetting cases along with some scaling estimates to verify the results.

Finally we conclude and provide a list of future studies in chapter 7.

Chapter 2

The possible equilibrium shapes of static pendant drops

The material in this chapter is reproduced in *J. Chem. Phys.*, 133(14):144707 (2010).

2.1 Abstract

Analytical and numerical studies are carried out on the shapes of two-dimensional and axisymmetric pendant drops hanging under gravity from a solid surface. Drop shapes with both pinned and equilibrium contact angles are obtained naturally from a single boundary condition in the analytical energy optimization procedure. The numerical procedure too yields optimum energy shapes satisfying Young's equation without the explicit imposition of a boundary condition at the plate.

It is shown analytically that a static pendant two-dimensional drop can never be longer than 3.42 times the capillary length. A related finding is that a range of existing solutions for long two-dimensional drops correspond to unphysical drop shapes. Therefore two-dimensional drops of small volume display only one static solution. In contrast, it is known that axisymmetric drops can display multiple solutions for a given volume. We demonstrate numerically that there is no limit to the height of multiple-lobed Kelvin drops, but the total volume is finite, with the volume of successive lobes forming a convergent series. The stability of such drops is in question, though. Drops of small volume can attain large heights.

A bifurcation is found within the one-parameter space of Laplacian shapes, with a range of longer drops displaying a minimum in energy in the investigated space. Axisymmetric Kelvin drops exhibit an infinite number of bifurcations.

2.2 Introduction

Often one encounters pendant drops hanging from an infinite solid surface. However the body of work on this geometry is far smaller than on drops hanging from a support of fixed radius, or from an orifice. In contrast to sessile drops that can be made as large as one would wish, a pendant drop larger than a certain volume cannot hang in a stationary fashion, as we will demonstrate. Interestingly, while sessile drops can be no taller than twice their capillary length, we will see that pendant drops can be infinitely tall, in theory. Thus an infinite number of shapes of pendant drops is possible for a given volume. A generalised boundary condition applicable in several situations is presented. Such shapes are obtained numerically without the explicit imposition of boundary conditions at the solid plate.

We begin by briefly discussing some of the earlier studies on this problem. Using calculus of variations, Gauss, in 1830, unified the results of Young and Laplace to obtain equations and boundary conditions describing drop shapes Finn (1999), while Plateau (1873) classified the solutions of the gravity-free Young-Laplace equation according to geometry. Bashforth & Adams (1883) obtained gravity-distorted drop shapes. Thomson (1886) (Kelvin) geometrically constructed menisci including the multiple-lobed pendant drops now known by his name. We go forward by almost a century to early numerical simulations, important among which are those of Padday (1971), for axisymmetric sessile and pendant drops and liquid bridges. Padday & Pitt (1973) calculated axisymmetric equilibrium shapes from the first variation of energy and graphically examined their stability through the second variations of energy. More formal calculations followed, from Pitts (1973, 1974), who derived the shape and stability of two-dimensional and axisymmetric pendant drops for various contact angles and showed that there is a maximum in the volume that can be sustained. He showed that drops are unstable in a regime where an increase in volume is associated with a decrease in height. Boucher & Evans (1975); Boucher *et al.* (1976) carried out a similar analysis on pendant and sessile drops, and emergent and captive bubbles. They explored the relationship between shape and contact-angle hysteresis. Many properties of the solutions, including for Kelvin drops, were elucidated by Concus & Finn (1979).

Meanwhile Majumdar & Michael (1976); Michael & Willaims (1976); Michael (1981) conducted a systematic analysis of the stability of two-dimensional drops hanging from a fixed support or fixed orifice, and axisymmetric drops hanging from a fixed tube, which are discussed in the last section. Wente (1980) carried out rigorous mathematical investigations whose conclusions include (i) that the drop height increases monotonically with volume throughout the range of stability, in agreement with Pitts (1974) (ii) that the area of contact of the drop with the solid surface attains a maximum before the volume does (iii) that the profile curve of a stable pendant drop never contains more than one inflection point.

Chesters (1977) attempted to calculate the shape of a pendant drop hanging from a tube as a first order perturbation to a circle. This approach was revisited by O'Brien (1991) with an alternate formulation. Through the introduction of different scaling and boundary layers, the shape of a pendant drop was calculated using matched asymptotic expansions. Later on O'Brien (2002) extended the theory to pendant drops with multiple necks (Kelvin's drops).

The recent approach of Snoeijer & Andreotti (2008) for sessile drops is particularly similar to the present, i.e., posing the problem with free end-points. By using a similar approach on pendant drops, we find that these can be much more interesting than sessile. In particular, they can have multiple minimum energy shapes at a given volume. Moreover, they have a different energy landscape, as we shall see. To the best of our knowledge, studies of pendant drops hanging from solid surfaces, which obtain shapes through an energy minimization procedure, all hold a fixed area of contact with the solid. Correct drop shapes are then obtained by additionally imposing Young's relation at the solid surface. In contrast, we fix only one parameter rather than two, and allow the second to come out of the solution. We could do this in many ways, e.g. by keeping the volume fixed and allowing the contact area to change, or by keeping the contact area fixed and allowing the volume to change. We choose the former since it is natural,

and many features such as multiple shapes are obtained directly rather than by an exhaustive search. Drop shapes obeying Young's relation emerge naturally in our procedure.

2.3 Drop shapes of minimum and maximum energy

We study both two-dimensional and axisymmetric drops. The shape of a two-dimensional drop, i.e., an infinite cylinder whose cross-section is a drop, is possible to obtain analytically, whereas axisymmetric drops warrant numerical computations. Since the analytical solution is often instructive, we study two-dimensional drops as well. although one may not often encounter them in reality, except as remnants of inverted rivulets and in some small-scale situations.

Consider a liquid drop suspended downwards from a horizontal solid surface, subjected to gravity and surface forces. For a given drop volume, we begin by obtaining shapes for which the energy is at an optimum. The solid-liquid contact area is not pre-defined nor is the contact line pinned. As sketched in Fig. 2.1 the bottom tip of the drop is taken to be the origin of the coordinate system, with the vertical coordinate z increasing upwards. The shape of the liquid-gas interface is described by $x(z)$ or $r(z)$, where x for a two-dimensional drop is the horizontal distance of the liquid-gas interface from the z-axis, and r is the corresponding radial distance for an axisymmetric drop. Following Pitts (1973, 1974), we write

$$E_0 = \int_0^h \left[\sigma\sqrt{1+x_z^2} - \rho g x(h-z)\right] \mathrm{d}z + (\sigma_{sl} - \sigma_{sg})\lambda \tag{2.1}$$

where the total energy for a two-dimensional drop is $2E_0$ per unit span. The solid plate is taken to be the base for potential energy. The drop is characterized by its total height h and the solid-liquid interface half-length λ. The liquid density is ρ, while σ, σ_{sl} and σ_{sg} respectively are the tensions of the liquid-gas, liquid-solid and solid-gas interfaces. We nondimensionalise the above equation by the capillary length $L_c \equiv \sqrt{\sigma/\rho g}$ as the length scale and σL_c as the two-dimensional energy scale. The functional E_0 must be extremised subject to the constraint of constant volume V.

Here we note one point of departure from earlier work Pitts (1973); Boucher *et al.* (1976). Whereas those studies specified the liquid-gas interfacial contact length 2λ to be held constant during the minimization procedure, thus making the contact line pinned in effect, we do not (as we should not for our problem!) impose this additional constraint. In a typical problem of this class, with the end point held fixed, one would need to specify an additional boundary condition at this point. Thus, in order to completely specify the shape, earlier studies imposed the equilibrium angle θ_e at the surface, where θ_e is given by Young's equation

$$\sigma_{sl} - \sigma_{sg} + \sigma\cos\theta_e = 0. \tag{2.2}$$

On the other hand, with the end point allowed to move, no additional information needs to be supplied (Brunt 2004), so our approach holds appeal in that the class of solutions of extremum energy that we obtain automatically have Young's contact angle θ_e. Also some additional features of the solution space are revealed as we shall see below.

The functional E_0 must be extremised subject to the constraint of constant volume V, i.e.,

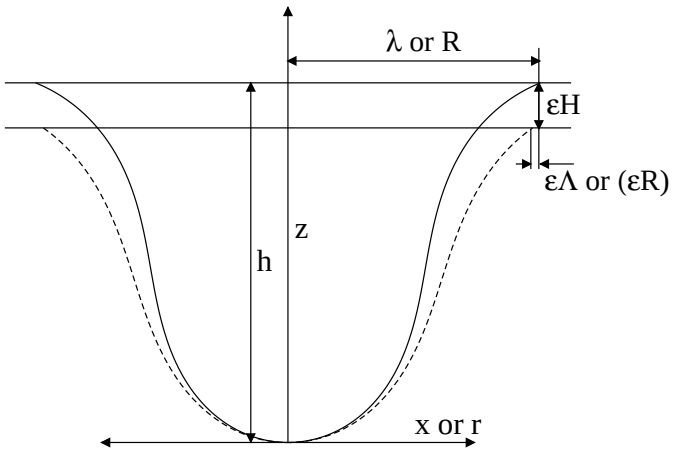

Figure 2.1: Definition of coordinate system (x, z) for two-dimensional and (r, z) for axisymmetric pendant drops. The perturbed shape is shown by the dashed line.

the first variation of

$$E_0 = \int_{z=0}^{z=h} G\,(z, x, x_z)\,\mathrm{d}z + \chi V \tag{2.3}$$

with respect to $x(z)$ must be zero. Here $V = \int_0^h x\mathrm{d}z$ is referred to as volume, as per convention. χ is the Lagrange multiplier, x_z denotes $\mathrm{d}x/\mathrm{d}z$, and

$$G \equiv \sqrt{1 + x_z^2} + \frac{\sigma_{sl} - \sigma_{sg}}{\sigma} x_z + xz - V - \chi x. \tag{2.4}$$

We consider a perturbed shape $\hat{x} = x + \epsilon\eta(z)$ where ϵ is a small parameter. We prescribe that the bottom tips of the perturbed and the original drops coincide, as seen in Fig. 2.1. Since the problem involves free end points, let the corresponding changes in the end points be $[\hat{\lambda} = \lambda + \epsilon\Lambda, \hat{h} = h + \epsilon H]$,. The extremization of a functional with variable end points is conducted in the standard manner prescribed, for example, by Brunt (2004). We give here the essential steps.

For the energy minimization functional defined as,

$$E_0(\hat{x}) - E_0(x) = \int_0^{h+\epsilon H} G(z, \hat{x}, \hat{x}_z)dz - \int_0^h G(z, x, x_z)dz$$

which may be written as

$$E_0(\hat{x}) - E_0(x) = I_1 + I_2 \tag{2.5}$$

$$I_1 = \int_0^h \left[G(z, \hat{x}, \hat{x}_z - G(z, x, x_z)\right] dz \tag{2.6}$$

$$I_2 = \int_h^{h+\epsilon H} G(z, \hat{x}, \hat{x}_z)dz. \tag{2.7}$$

The integrand of I_1 may be Taylor expanded as,

$$G(z,\hat{x},\hat{x}_z) - G(z,x,x_z) = \epsilon\left[\eta\frac{\partial G}{\partial x} + \eta_z\frac{\partial G}{\partial x_z}\right]\Bigg|_x + O(\epsilon^2), \tag{2.8}$$

to obtain

$$I_1 = \eta\frac{\partial G}{\partial x_z}\Bigg|_{z=0}^{z=h} + \int_0^h \eta\left[\frac{\partial G}{\partial x} - \frac{\mathrm{d}}{\mathrm{d}z}\left(\frac{\partial G}{\partial x_z}\right)\right]\mathrm{d}z. \tag{2.9}$$

A Taylor expansion at the end point (solid surface) at $\hat{\lambda} = \lambda + \epsilon\Lambda$ and since $\hat{\lambda} = (x+\epsilon\eta)|_{h+\epsilon H} = \lambda|_h + \epsilon H x_z|_h + \epsilon\eta(h) + O(\epsilon^2)$, we have

$$\eta(h) = \Lambda - H x_z(h) + O(\epsilon). \tag{2.10}$$

The second integral I_2 may be written as

$$I_2 = \int_h^{h+\epsilon H} G(z,\hat{x},\hat{x}_z)\mathrm{d}z = \epsilon H G(z,x,x_z)|_{z=h} + O(\epsilon^2). \tag{2.11}$$

Substituting for I_1 and I_2 from equations 2.9 - 2.11 in to Eq. 2.5 and after a few mathematical manipulations, we get,

$$\begin{aligned} E_0(\hat{x}) - E_0(x) = \epsilon\Bigg\{ &\int_0^h \eta\left[\frac{\partial G}{\partial x} - \frac{\mathrm{d}}{\mathrm{d}z}\left(\frac{\partial G}{\partial x_z}\right)\right]\mathrm{d}z \\ &+ \left[\Lambda\frac{\partial G}{\partial x_z} + H\left(G - x_z\frac{\partial G}{\partial x_z}\right)\right]\Bigg|_{z=h}\Bigg\}. \end{aligned} \tag{2.12}$$

For the functional E_0 to be stationary at $x(z)$, terms of $O(\epsilon)$ should add to zero in the above expression. The perturbation $\eta(z)$ can be chosen arbitrarily, which demands that the integrand be zero. This gives the Euler-Lagrange Eq. 2.13.

$$z - \frac{1}{r_0} = \frac{\mathrm{d}}{\mathrm{d}z}\left(\frac{x_z}{\sqrt{1+x_z^2}}\right). \tag{2.13}$$

A hydrostatic force balance indicates that $\chi = 1/r_0$ where r_0 is the radius of curvature at the origin, assigning a physical meaning to the Lagrange's multiplier. Defining $\cot\theta_s \equiv x_z$, the slope x_z at the solid surface, Eq. 2.13 can be written as

$$z = \left(\frac{1}{r_0} - \cos\theta_s\frac{\mathrm{d}\theta}{\mathrm{d}x}\right). \tag{2.14}$$

The Euler-Lagrange equations offer a static drop shape for every r_0, so we reduce the solution space to a one dimensional space in the Lagrange multiplier, all of which ensure force balance everywhere (Snoeijer & Andreotti 2008). Shapes of minimum or maximum energy among static shapes may then be picked from these. This property is exploited in the next section (2.4.1) to adopt a numerical approach. This approach is more elegant than looking for minimum-energy shapes by making arbitrary perturbations which may not satisfy force balance, such as that of Pitts (1973), where the curvature at the bottom was not disturbed. Pitts's procedure would result in a minimum energy for any trial shape, but a class of correct shapes was obtained by

imposing Young's contact angle at the surface. However, while the present analytical procedure yields correct extremum energy shapes, we resolve the issue of whether the energy of such shapes is at a maximum or a minimum numerically. Care must be exercised in interpreting these results in terms of stability, as discussed later.

To satisfy Eq. 2.12, in addition to the force balance, we must have

$$\left[\left(\frac{\epsilon\Lambda}{\epsilon H} - x_z\right)\frac{\partial G}{\partial x_z} + G\right]\Bigg|_{z=h} = 0. \tag{2.15}$$

assuming $\epsilon H \neq 0$. Noting that the volume may be expressed as (Pitts 1973),

$$V = h\lambda - \frac{\lambda}{r_0} + \sin\theta_s, \tag{2.16}$$

we get from (2.15)

$$\frac{\epsilon\Lambda}{\epsilon H}\left(\cos\theta_s + \frac{\sigma_{sl} - \sigma_{sg}}{\sigma}\right) = 0. \tag{2.17}$$

The above general boundary condition (Eq. 2.17) offers two possibilities corresponding to actual static drop shapes. (i) If we set the quantity within the brackets to zero, we see that θ_s is equal to the equilibrium contact angle θ_e, to the automatic satisfaction of Young's equation (Eq. 2.2) of local surface tension balance. We refer to these as Y-solutions. (ii) If the contact line is pinned due to surface roughness or chemical heterogeneities, then by definition $\epsilon\Lambda = 0$ illustrating that drops sitting on non-ideal surfaces need not satisfy Young's equation at the contact line. The explanation usually offered for static drops not satisfying Young's equation is that of contact-angle hysteresis (de Gennes *et al.* 2004). Wall roughness is particularly simple to imagine as a cause for hysteresis: the fluid at the triple-contact line adjusts its location very slightly to choose a point on the surface where the microscopic angle is θ_e, while maintaining the macroscopic angle at a different θ_s. Moreover, since the curvature at any height z is uniquely determined by r_0 the perturbed solution cannot cross the original one, i.e., $\eta(z)$ cannot change sign in a given shape. This implies that to attain a volume V the perturbed drop must be taller if the perturbation in r_0 is negative, and shorter if otherwise, so H cannot be zero.

These conclusions are easily extended to axisymmetric pendant drops. The energy functional of an axisymmetric drop with height h and liquid-solid contact radius R, defined in a coordinate system (r, z) (Fig. 2.1), when perturbed to a nearby function $\hat{r} = r + \epsilon\eta$ with the end point moving to $[\hat{R} = R + \epsilon\Omega, \hat{h} = h + \epsilon H]$,

For axisymmetric pendant drops, the energy functional (Fig. 2.1), will have the same form as in (2.3) but with

$$G \equiv 2\pi r\left[\sqrt{1 + r_z^2} + \frac{\sigma_{sl} - \sigma_{sg}}{\sigma} r_z\right] + \pi r^2\left[z - \frac{1}{r_0}\right] - V. \tag{2.18}$$

The appropriate value of the Lagrange multiplier has been used. In this case volume may be determined as

$$V = \pi R^2 h - \pi R\left[\frac{R}{r_0} - 2\sin\theta_s\right]. \tag{2.19}$$

As before, we obtain the Euler-Lagrange equation describing the shape of drop as

$$z - \frac{1}{r_0} = \left[\frac{r_{zz}}{(1 + r_z^2)^{3/2}} - \frac{1}{r\,(1 + r_z^2)^{1/2}} \right], \tag{2.20}$$

and the end-point condition

$$\frac{\epsilon\Omega}{\epsilon H} \left(\cos\theta_s + \frac{\sigma_{sl} - \sigma_{sg}}{\sigma} \right) = 0, \tag{2.21}$$

Again we obtain Y and pinned solutions by setting different terms in Eq. 2.21 to zero.

We have not yet resolved whether the solutions obtained correspond to maxima or minima in energy. We do this numerically, as discussed in the next section, where other features too come to light.

2.4 Results and Discussion

2.4.1 Two dimensional drops

Equation (2.13) may be integrated (Krasovitski & Marmur 2005) to give

$$\frac{\mathrm{d}z}{\mathrm{d}x} = \left[\frac{1}{(1 - (z/r_0) + 0.5z^2)^2} - 1 \right]^{1/2}. \tag{2.22}$$

The shape for each r_0 is obtained by numerically integrating Eq. 2.22 by a fourth order Runge-Kutta method, and placing the solid surface at the height h where the volume V is attained. Here the entire space of shapes has been reduced to a one-parameter space in r_0 since we know that any two dimensional or axisymmetric shape outside this family cannot satisfy force balance which is a necessary condition for an energy minimum. The liquid-gas and liquid-solid interfacial areas, and the center of mass of the shape were determined, and used to calculate the surface energy and potential energy respectively. The total energy is then obtained as a function of the shape factor r_0^2, and a line search is employed to obtain the minimum energy solutions along r_0 for each given volume. These solutions are shown in Fig. 2.2 in a height-volume space. Note that the shape of a drop is independent of interfacial tensions, but its energy depends on their combination, appearing through θ_e. As in the analytical calculations, the boundary conditions were never enforced, but they emerged naturally during the minimization procedure.

In Fig. 2.2 curves I to V show present extremum energy solutions whose contact angle θ_s turns out to be equal to θ_e, and which therefore belong to the Y branch. These lines agree very well with those obtained by Pitts (1973) by imposing Young's contact angle at the solid surface, except that Pitts obtained two solutions for every volume while the present solutions terminate at the curve $AFGH$. Any point below this curve corresponds to unphysical shapes which cross themselves, so we find that at low volumes only one solution exists. Note that for contact angles close to 90° the unphysical solutions (dashed lines) extend over a significant region. The curve AF corresponds to limiting shapes where the drop crosses itself at the solid surface, i.e., the contact area λ is zero, whereas drops on the curve FGH attain a zero width at some $z \neq h$. We thus conclude that all possible physical two-dimensional drop shapes are contained within the closed region $AFGHD0A$.

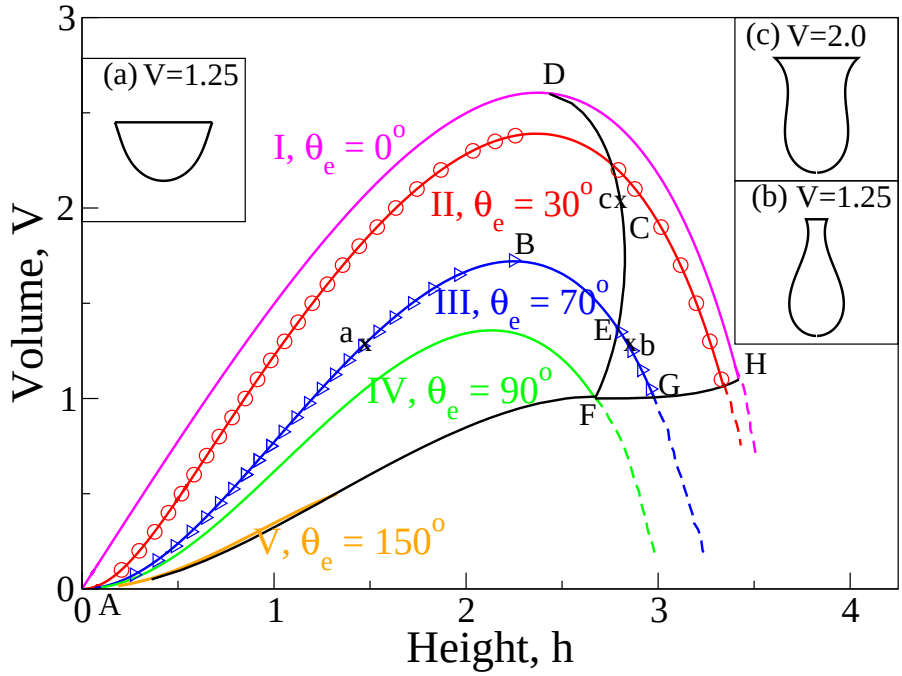

Figure 2.2: Volume of extremum energy shapes as a function of height for 2D drops. Curves I to V correspond to Y solutions of different contact angles. Points below $AFGH$, including the dashed lines of Pitts (1973) have unphysical drop shapes. Drop shapes shown in the insets correspond to the heights indicated by 'a', 'c' and 'b', all with a volume $V = 1.75$. The shape 'c' sits on the dot-dashed curve FD discussed in section 2.4.4.

2.4.2 Axisymmetric Pendant Drops

Following Boucher & Evans (1975), Eq. 2.20 is converted into three coupled first-order equations with θ, r and z as parameters dependent on s, the arc length from the origin:

$$\frac{d\theta}{ds} = \frac{1}{r_0} - z - \frac{\sin\theta}{r}, \tag{2.23}$$

where $\mathrm{d}r/\mathrm{d}s = \cos\theta$ and $\mathrm{d}z/\mathrm{d}s = \sin\theta$. This approach avoids zero and infinite slopes in the computation.

The same numerical procedure as for two-dimensional drops was adopted here too. Similar conclusions are arrived, with the important difference that many shapes are possible for a given volume. In fact in some range of volumes, one can have an infinite number of possible shapes displaying minimum energy. This is because the azimuthal curvature is now finite, ensuring that the drop never intersects itself. The $V - h$ profile of the shortest few of these drops are shown in Fig. 2.3. The first Y limb and a part of the second at low θ_e were already obtained by Pitts (1974), but again by pinning R and imposing θ_e.

Unlike in the two-dimensional case, at higher θ_e, one may have closed curves in the height-volume space, two examples are seen in Fig. 2.3. A very large number of such closed curves is possible (not shown). These are remarkable, because they represent another basic difference between possible shapes for two-dimensional and axisymmetric drops: axisymmetric drops of small volume can be very long. The second curvature also provides the facility for the longitudinal curvature to be non-monotonic, so many-lobed, or Kelvin, drops are possible. Of course

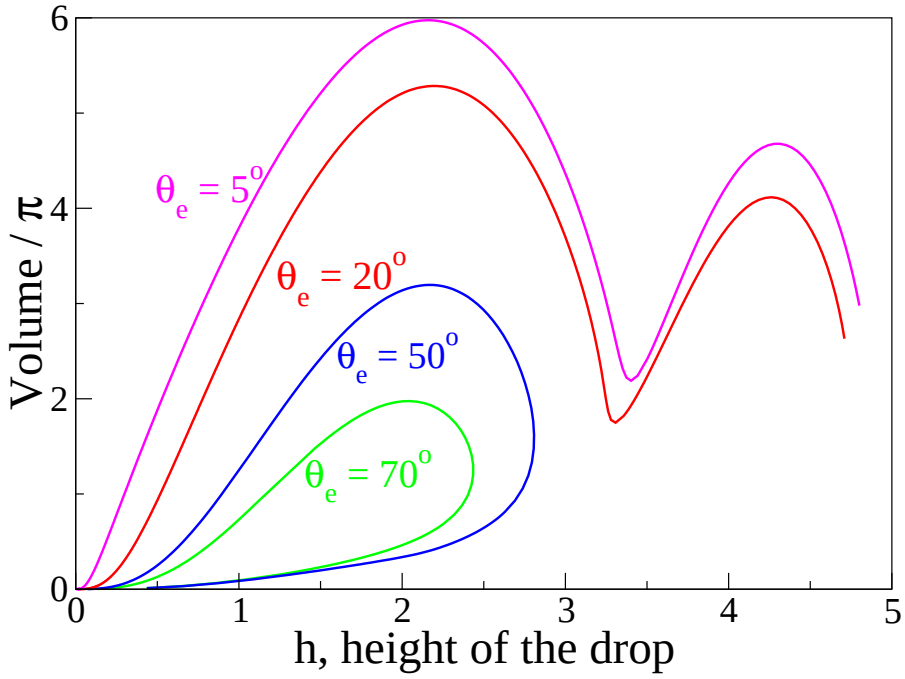

Figure 2.3: Volume versus height for extremum energy axisymmetric pendant drops of the Y class obtained during the numerical minimization of energy along with other solutions. Note that the condition $\theta_s = \theta_e$ was not explicitly imposed.

these shapes may or may not be stable.

2.4.3 Height of pendant drops

We show analytically that two-dimensional drops can never be taller than 3.42 times the capillary length. We then show numerically that the height of an axisymmetric drop has no limit, but its volume is always finite.

For two dimensional drops, Eq. 2.22 can be written as

$$z = \frac{1}{r_0} + \left[\frac{1}{r_0^2} - 4\sin^2\left(\frac{\theta_s}{2}\right)\right]^{1/2} \tag{2.24}$$

so the maximum height $h_{max} = 2/r_0$ occurs when $\theta_s = 0$. On examining Eq. 2.22 by putting the numerator and denominator to zero separately to obtain the locations of zero and infinite slopes for z_x, one can deduce that (Fig. 2.4), (i) when $0 \leq r_0 \leq 0.5$, moving upwards in z, θ will go through $\pi/2$ followed by a zero, without a neck, (see $r_0^2 = 0.24$ in figure (2.4)) (ii) when $0.5 \leq r_0 \leq \sqrt{0.5}$ between two points where $\theta = \pi/2$, a saddle point will exist. These are followed by $\theta = 0$, so a neck is seen, (see $r_0^2 = 0.36$ in figure (2.4)) (iii) when $\sqrt{0.5} \leq r_0$, the drop reaches zero slope with out going through any infinite slope. (see $r_0^2 = 0.55$ in figure (2.4)) For all cases, z_x has zeros at $z = 0$ and $z = 2/r_0^2$. In case of (i), z_x has additional zeros at $z = (1 \pm \sqrt{1 - 4r_0^2})/r_0$, and no drop can be taller than the lesser of these, which restricts the drop to $h \leq 2$. Hence arbitrarily small r_0 does not suggest arbitrarily tall drops. Also, self-crossing drops are not real solutions and should be excluded from consideration, which has often been overlooked (Pitts 1973; Michael 1981). In cases (ii) and (iii) a zero would occur at

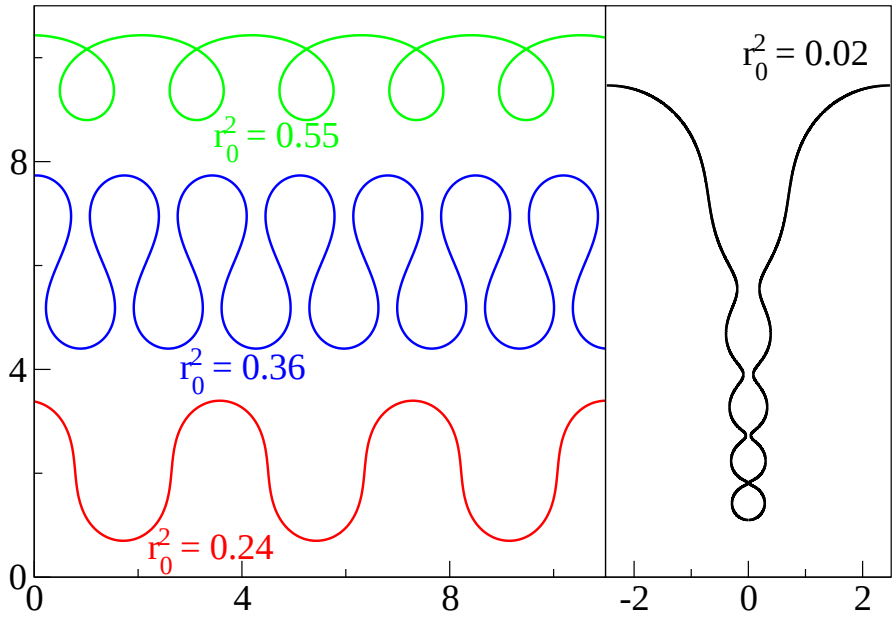

Figure 2.4: Solutions of Eq. 2.13 for various values of r_0 for two-dimensional drops. Once an r_0 is fixed the only possible shapes for any volume, are dictated by the curves on the left. Thus, to obtain a shape for a given volume, one merely draws a horizontal cut on the curve to enclose the desired volume. Shown on the right is a typical Kelvin drop, solution of (2.20).

$z \leq 8$, but the self-crossing condition occurs at a lower height, as seen below. Equation 2.13 may be integrated (Pitts 1973) to give

$$x = \mp \frac{1}{r_0} \left[(2r_0^2 - 1)u + E\left(u \left| 4r_0^2 \right.\right) \right], \tag{2.25}$$

where $u = F\left(\frac{\theta}{2} \left| 4r_0^2 \right.\right)$ and F & E denote respectively, elliptic integrals of the first and second kind. The tallest drop is one which barely grazes itself, i.e., achieves $x = 0$ with $\theta = \pi/2$ at $x = 0$. Equation (2.25) can be solved to yield $r_0^2 = 0.3419$ for such a drop, so $h_{max} = 2/r_0 = 3.420$ is the maximum height possible for a two-dimensional drop. This value matches very well with the numerical height at point H in Fig. 2.2. The calculations were repeated for various θ_s using Mathematica to generate the curve FGH in Fig. 2.2.

A typical shape of a Kelvin drop in also shown in Fig. 2.4, and possible solutions up to some height for Kelvin drops of $\theta_e = 30°$ are shown in Fig. 2.5. A larger h corresponds to a smaller r_0, enabling the drop to sustain larger hydrostatic pressures. At every neck, $\theta = 90°$, so at the j^{th} neck, Eq. 2.20 yields

$$r_{nj}(1 - r_0 z_{nj}) = r_0. \tag{2.26}$$

Here the suffix 'n' denotes the neck. This shows that each bulge is uniquely determined by r_0 and j, i.e., there is no similarity solution relating consecutive bulges. O'Brien (2002) calculated the first few bulges through asymptotic matching.

While it is evident that the volume tends to converge at about 2.5π, Fig. 2.5 does not make it clear whether the height is converging as well. Figure 2.6 shows the variation of h_h and h_l (heights at the highs and lows in volume respectively) with the index j of the Y cycle. Both grow as $j^{1/2}$, so there is no limit on the height of an axisymmetric drop, although the ratios of

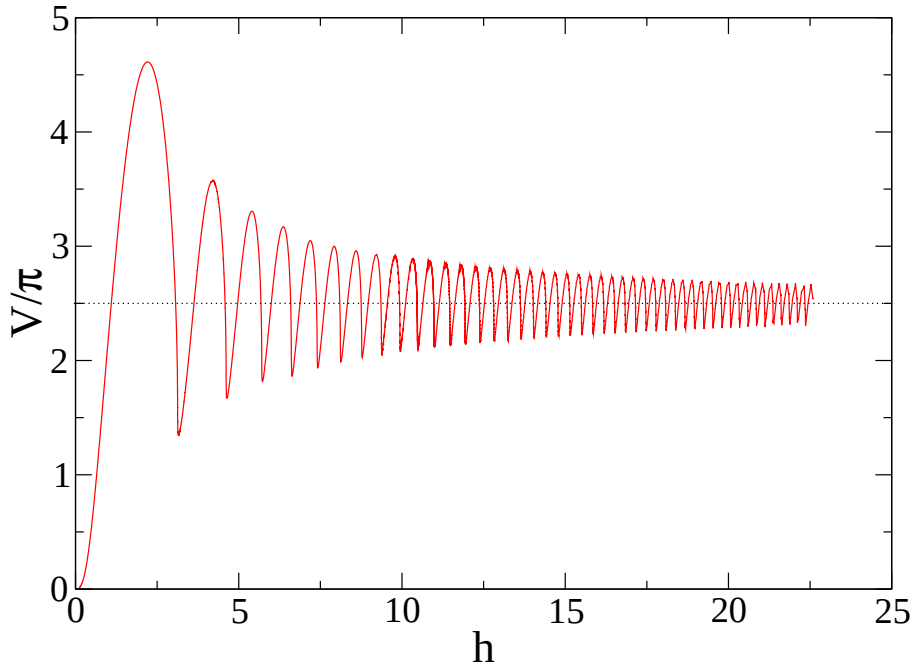

Figure 2.5: Kelvin's drop solutions for $\theta_e = 30°$ illustrating the existence of multiple configurations for certain volumes.

consecutive heights $h_{h(j+1)}/h_{hj}$ and $h_{l(j+1)}/h_{lj}$ tend towards unity. On comparing drops with j bulges and one with $j+1$, we see that the contribution to the height of each consecutive bulge is $j^{-1/2}$. The radius of each consecutive bulge also goes down roughly on this scale, so the volume of each additional lobe is $\sim j^{-3/2}$. The total volume of the drop is thus given by a convergent series, ensuring that it is finite.

2.4.4 Stability and minimum contact area shapes

As detailed in the introduction, the stability analysis of two-dimensional drops has been carried out by various authors Pitts (1974); Majumdar & Michael (1976). The region to the left of the volume maxima in Fig. 2.2 is found to correspond to energy minima, whereas it is believed that the region to the right of the volume maxima consists of shapes unstable to two-dimensional perturbations. The line joining the maxima in the $V - h$ plane, shown in Fig. 2.7 by DBJ, is thus a locus of bifurcation points separating stable and unstable solutions. This however, as we show below, is not the only bifurcation possible.

Before that, a word of caution about the present procedure is in order. Our analytical procedure ensures that the possible shapes we have obtained are all of optimum energy. About the stability of these optimum energy shapes, however, we can only obtain a partial answer from our numerical procedure. This is because, for a given θ_e, we restrict our investigations to a one-dimensional space of all possible Laplacian shapes. When we obtain a maximum in the energy we can be sure that the shape is unstable. However a minimum in energy does not ensure stability, since there is a possibility of non-Laplacian shapes of lower energy, i.e., the shape could be dynamically unstable. Secondly, the drops may be unstable to non-symmetric perturbations. Majumdar & Michael (1976) showed that two-dimensional drops hanging from a fixed support

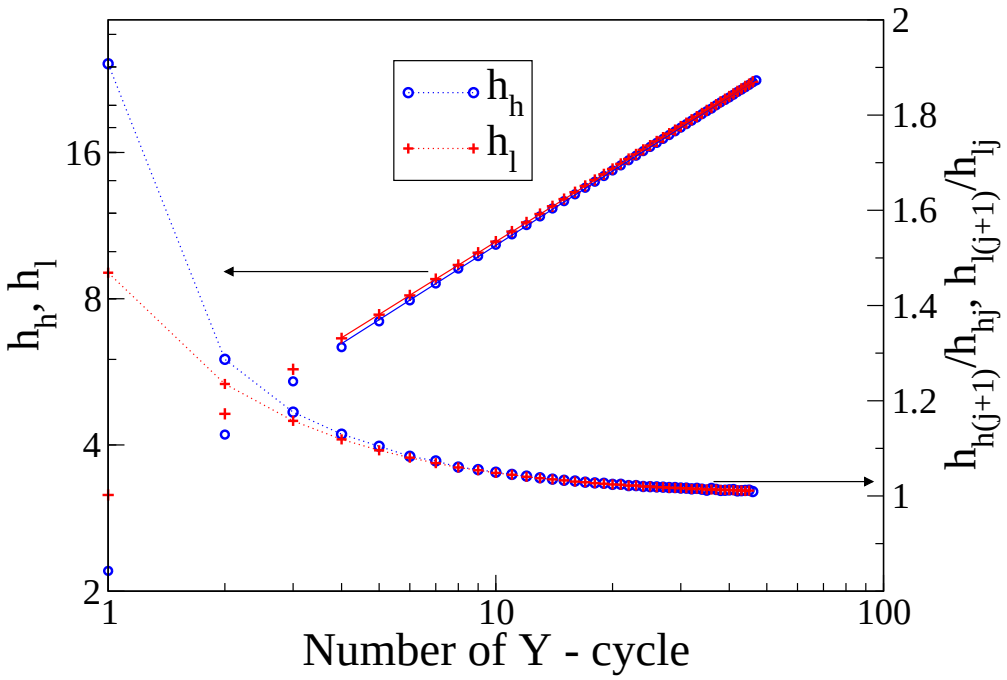

Figure 2.6: Heights of Kelvin drops corresponding to highs and lows in volume as a function of the index of the Y cycle. Symbols correspond to drop shapes, while the solid lines are best fits $h_h = 3.2j^{0.508}$ and $h_l = 3.3j^{0.497}$ The ratio of successive heights on the secondary y-axis is seen to asymptotically approach unity.

could be unstable to three-dimensional perturbations. Such a study needs to be conducted for drops hanging from an infinite solid plate.

Two-dimensional Shapes: Although Pitts mentioned that some range of longer drops appeared stable, he felt that the result was false due to the very restrictive assumptions he made about the nature of the perturbations. Without his assumptions we obtain a regime of energy minima among long drops. Consider curve III, for example, in Fig. 2.7. A computation of the energies shows that the left limb AB consists of energy minima, in accordance with accepted wisdom. However, only a portion of BEG, namely BE, contains energy maxima, whereas the leg EG consists again of energy minima. At any other contact angle as well, the picture is similar, with unstable static shapes to the right of the maximum volume solution, up to the curve $FECD$, to the right of which we again obtain energy minima. The curve $FECD$ thus describes another locus of bifurcation points. This curve also corresponds to shapes with a minimum in contact area (MCA) subtended at the solid surface. In other words, if we consider all shapes along a horizontal line in the Fig. 2.7, i.e. all shapes of a given volume, the shape with the smallest λ will occur at the intersection of the horizontal line with the curve $FECD$. This can be seen visually in the drop shapes for $V = 1.75$ shown in Fig. 2.2. We may thus summarise by dividing the energy landscape into four sections for a given Young contact angle (i) the region to the left of the maximum in the $V - h$ plot, i.e. height increases with increasing volume, corresponds to minimum energy shapes. (ii) shapes in the region lying between the maximum in the $V - h$ plane and the MCA shape on $FECD$, i.e., the shaded region in Fig. 2.7 correspond to energy maxima. Here the height decreases with increasing volume, and so does the contact area at the solid surface. (iii) the region contained within $FECDHGF$ again consists

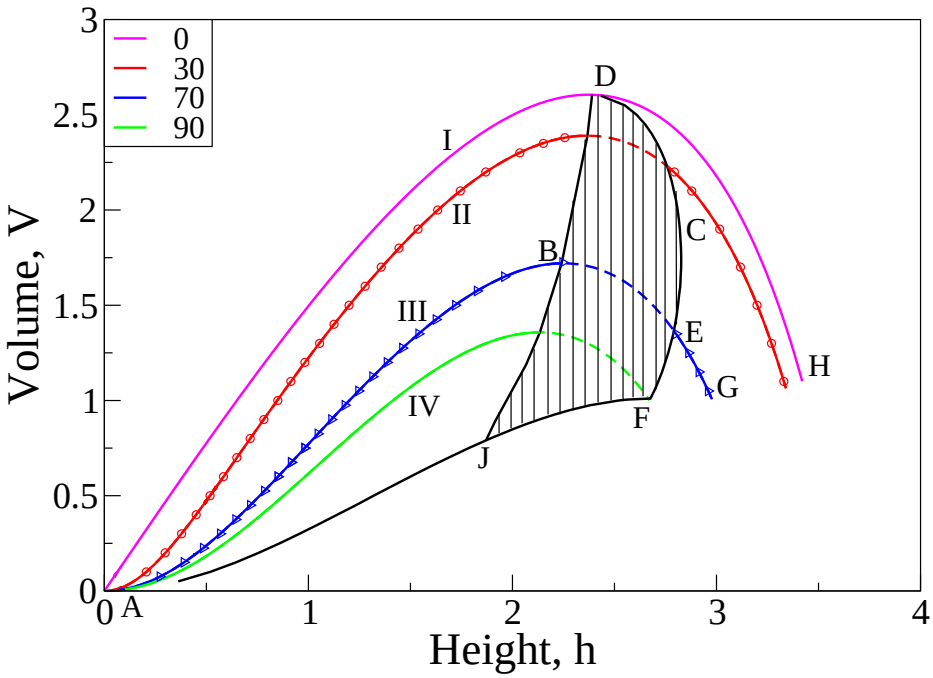

Figure 2.7: Possible energy minimum solutions for a two-dimensional drop, the curves labels are the same as in Fig. 2.2. The shaded area between the maxima in volume and the MCA is excluded since it consists of energy maxima. Energy minimum solutions for $\theta_e = 30$ and 70 degrees are indicated by symbols.

of energy minimum shapes. In this region, the height decreases with increasing volume, but the contact area with the solid increases. The stability of these shapes to dynamics perturbations needs to be investigated. (iv) the region below $AFGH$ consists of unphysical shapes.

Axisymmetric Shapes: Typical shapes for axisymmetric drops are illustrated in Fig. 2.8. The repeating pattern of limbs (figures 2.3 and 2.5) suggests the existence of more than one set of bifurcations. In fact each pair of limbs is associated with a minimum contact area locus, which also bifurcates the neighborhood as before, this is confirmed in Fig. 2.9. Since we find regions of static stability at all Y indices, it is intriguing why we do not see Kelvin's drops in nature. Apart from dynamic instability, since the energy wells are progressively shallower for increasing index, nonlinearities can become important. Thus the presence of extraneous forces, even if small, could play spoilsport, especially at the extremely narrow neck regions. Three-dimensional drops offer an additional possibility of non-axisymmetric shapes arising from the extra degree of freedom to choose two different radii of curvature at the origin. However we, following the literature (Padday & Pitt 1973; Pitts 1974), make the hypothesis that the symmetry of the problem should be reflected in the solutions as well and that non-axisymmetric shapes are less likely minimum energy candidates. Detailed studies on stability to non-axisymmetric perturbations are perhaps warranted now to prove this point. Such studies have so far been restricted to pinned/ fixed contact area pendant drops (Michael 1981). For example, Michael & Willaims (1976) showed that ahead of the maximum in volume, axisymmetric drops hanging from a tube are stable to axisymmetric and non-axisymmetric perturbations below a contact radius of 3.219. We expect that drops hanging from an infinite solid plate, being able to take up the most favorable contact area, are likely to be more stable to non-axisymmetric perturbations.

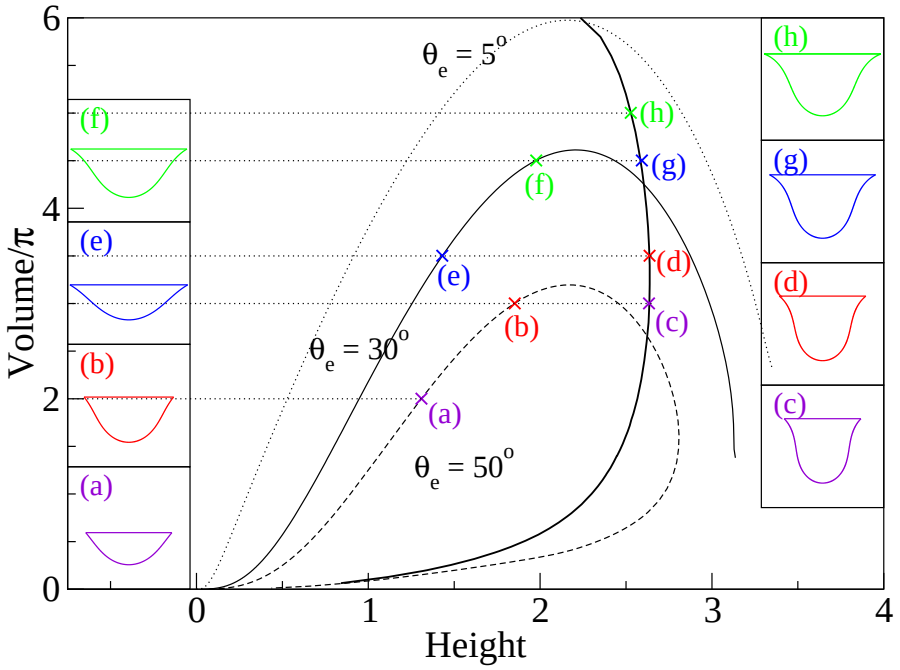

Figure 2.8: Typical shapes of axisymmetric drops. (a) $V = 2\pi, \theta_e = 50°$, (b) $V = 3\pi, \theta_e = 50°$, (e) $V = 3.5\pi, \theta_e = 30°$ and (f) $V = 4.5\pi$. Shapes subtending a minimum in contact area are shown in (c) $V = 3\pi, \theta_e = 45.2°$, (d) $V = 3.5\pi, \theta_e = 39.1°$, (g) $V = 4.5\pi, \theta_e = 26.8°$ and (h) $V = 5\pi, \theta_e = 20.7°$.

A word of caution: We notice that Eq. 2.17 can also be satisfied if $\epsilon\Lambda = 0$, i.e., if we restrict ourselves to a special class of perturbations which contain no terms of $O(\epsilon)$ in λ, i.e., when λ is at an extremum. Since one can always create a perturbation that contains terms of this order, the minimum energy shapes thus obtained would be spurious. In fact the entire MCA curve $FECD$ would correspond to spurious energy extremum shapes for **any** surface tension, because by definition MCA has a minimum area and no terms of $O(\epsilon)$ exists in λ.

An example of such a case is shown in 2.10 where one observes an exchange of stabilities for $\theta_e = 70°$. The horizontal solid line at $V = 1.1$, below the transcritical bifurcation point E, intersects the energy-extremum solutions at y_1, m_1 and y_2. Note that y_1 and y_2 are Y solutions, while m_1 is MCA solution. The energy variation along this line is shown by curve I, where it is evident that the Y solutions are of minimum energy, while the MCA solution is at a maximum. Above E, the roles are switched, as demonstrated by curve II, which gives the energy along $V = 1.55$. The Y shape y_3 is at a minimum, but the Y shape y_4 now displays an energy maximum. The MCA shape m_2 is now a minimum energy. The contact area measured by λ is shown in the inset to display a minimum at m_2. Since h varies monotonically with r_0, this minimum is equivalent to satisfaction of the condition $\epsilon\Lambda = 0$. However, as mentioned earler, this minimum energy MCA solutions are not statically stable solutions.

A final word on pinned solutions. Equation (2.1) is of the form $\int I dz + a \times b = 0$, where the integrand I and the product, given by Eq. 2.17, have to each vanish. Looking for a pinned solution with a particular λ will give us only the condition on I, leading to a contact angle usually different from θ_e. Several authors (Boucher & Evans 1975; Pitts 1973) have in effect

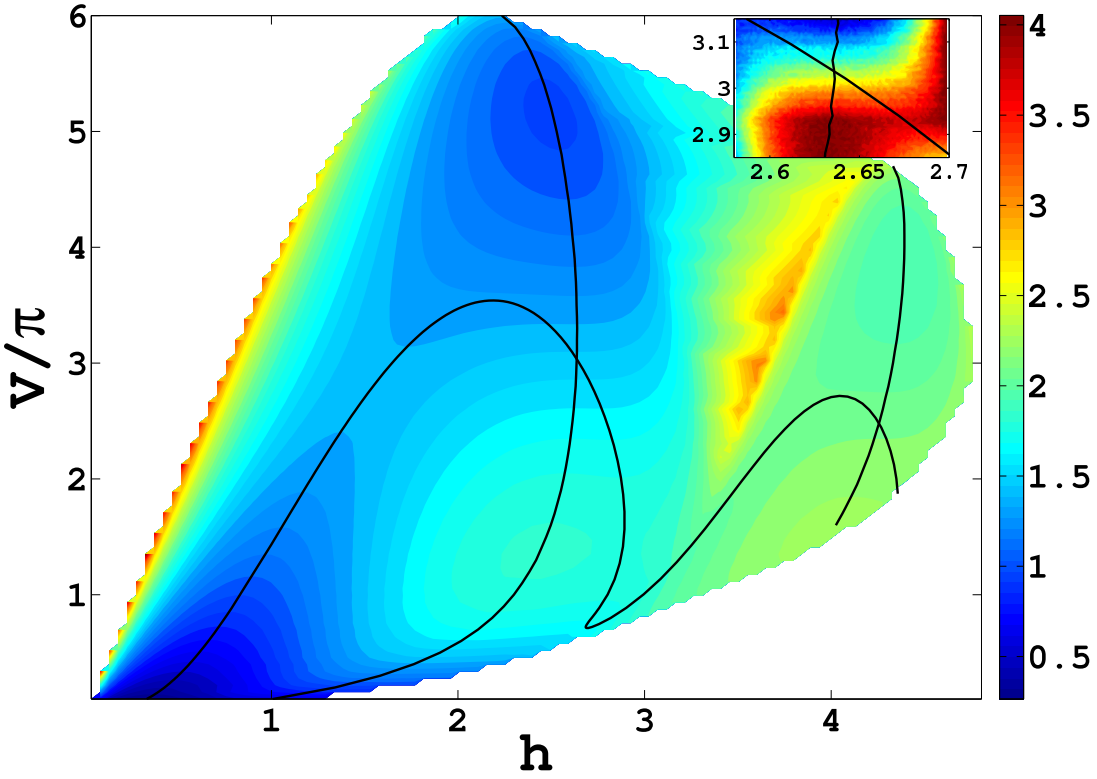

Figure 2.9: Energy landscape in height-volume space for $\theta_e = 45°$. Deep red corresponds to hills (energy maxima) and deep blue to valleys (minima). The neighborhood of the bifurcation point is enlarged in the inset showing an exchange of stabilities. For ease of visualization the energy in the inset is normalized between 0 and 1 for each volume.

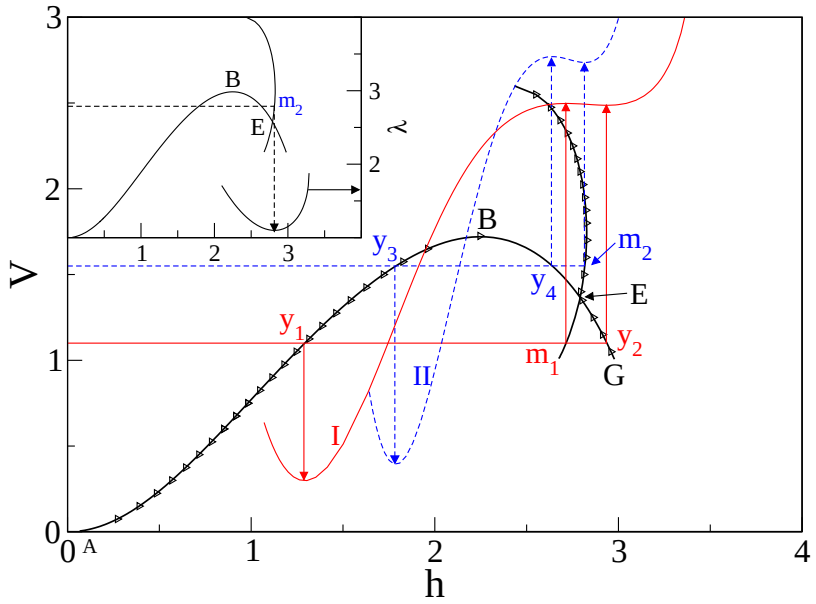

Figure 2.10: Exchange of stabilities at the transcritical bifurcation point E for $\theta_e = 70°$ giving rise to spurious minimum energy solutions or MCA solutions. Curves I and II show the total energy as a function of drop height for $V = 1.1$ and 1.55 respectively. The scales are different for the two curves. The MCA solution is at energy maximum in curve I, while the Y solutions are at minimum energy. On curve II, the MCA shape is at minimum energy while the second Y solution becomes unstable. The inset shows that the contact area λ is at a minimum for the MCA solution.

arrived at these shapes, and by imposing $b = 0$ by hand, obtained the Y solutions. However we do not have any externally imposed conditions and recover all these solutions. Also, pinned solutions are the result of macroscopic energy minimization where the only relevant length scale is the capillary length. At smaller length scales, intermolecular interactions manifest themselves in various ways at the contact line and a generalised Young's equation may be adopted (Swain & Lipowsky 1998; Wolansky & Marmur 1999).

2.5 Summary

A general energy minimisation procedure is adopted for studying static shapes of two dimensional and axisymmetric pendant drops supported by a solid wall. From this drops with both (i) pinned contact lines and (ii) equilibrium contact angle solutions emerge naturally as the only possible optimum energy solutions. Though sessile drops have been analyzed for variable contact area (Snoeijer & Andreotti 2008), the present approach is the only one to our knowledge which is valid for pendant drops hanging from a surface on which they can choose the minimum-energy. Not only do the possible solutions appear spontaneously and reveal various features of the solution space, the approach can be extended towards analytical solutions for patterned surfaces.

A range of solutions of long drops obtained by earlier workers is shown to consist of unphysical shapes, so at small volumes a two-dimensional drop has a unique static shape. This is confirmed analytically by showing that the maximum height achievable by a static two-dimensional drop is $3.42L_c$. It is obtained numerically that axisymmetric drops on the other hand, can be infinitely long, but their volume must remain finite. While a two-dimensional drop can have at most two static solutions of a given volume, an axisymmetric drop can adopt infinitely many shapes. A range of longer two-dimensional drops is found to be of minimum energy in a one dimensional space of Lagrange multipliers, and stable to two-dimensional perturbations. In this range, for a given contact angle, drop height decreases with increasing volume, while the contact area with the solid surface increases. There is thus an additional bifurcation curve between unstable and stable solutions, corresponding to minimum contact area shapes. In axisymmetric drops, over a small range of volume, repeated sets of left and right Y limbs are possible, with repeating regions of minimum and maximum energy separated by bifurcation curves.

Chapter 3

Minimum Energy Shapes of One-side Pinned Static Drops on Inclined Surfaces

The material in this chapter is reproduced in *Phys. Rev. E*, 84, 046304 (2011).

3.1 Abstract

The shape that a liquid drop will assume when resting statically on a solid surface inclined to the horizontal is studied here in two dimensions. Earlier experimental and numerical studies yield multiple solutions primarily because of inherent differences in surface characteristics. On a solid surface capable of sustaining any amount of hysteresis, we obtain the global, and hence unique, minimum energy shape as a function of equilibrium contact angle, drop volume and plate inclination. It is shown, in the energy minimization procedure, how the potential energy of this system is dependent on the basis chosen to measure it from, and two realistic bases, front-pinned and back-pinned, are chosen for consideration. This is at variance with previous numerical investigations where both ends of the contact line are pinned. It is found that the free end always assumes Young's equilibrium angle. Using this, simple equations which describe the angles and the maximum volume are then derived. The range of parameters where static drops are possible is presented.

We introduce a detailed force balance for this problem and study the role of the wall in supporting the drop. We show that a portion of the wall reaction can oppose gravity while the other portion aids it. This determines the maximum drop volume that can be supported at a given plate inclination. This maximum volume is the least for a vertical wall, and is higher for all other wall inclinations. This study can be extended to three-dimensional drops in a straightforward manner, and even without this, lends itself to experimental verification of several of its predictions.

3.2 Introduction

Understanding how liquid drops remain static on inclined surfaces, despite the action of gravity, is a classical problem. It is not too straightforward to predict the shape attained by such a drop, since a given volume can assume an infinite number of static shapes. Depending on the minute details of the solid surface on which the drop is supported, the contact line adjusts itself so that,

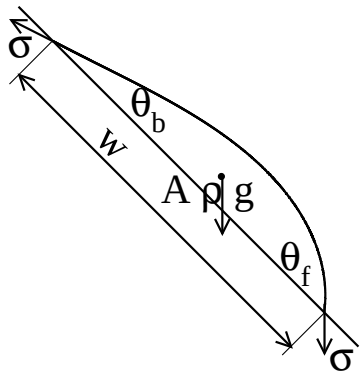

Figure 3.1: A static drop on an inclined surface. The weight of the drop is supported by the difference in surface tension forces at the front and rear of the drop.

microscopically, Young's equation

$$\sigma \cos\theta_e + \sigma_{sl} = \sigma_{sg} \tag{3.1}$$

is satisfied, thus balancing surface tension forces at the contact line. Here σ, σ_{sl} and σ_{sg} are the liquid-gas, solid-liquid and solid-gas interfacial tensions respectively, and θ_e is the equilibrium contact angle. This microscopic force balance is unaffected by external body forces. However, the observed macroscopic, or apparent, contact angle is often different from θ_e at both the front (θ_f) and the rear (θ_b) of the drop (Fig. 3.1). The possibility that the microscopic contact angle may be different from the macroscopic is called contact angle hysteresis. A drop on an inhomogeneous solid surface is capable of exhibiting contact angle hysteresis. This phenomenon has been well known experimentally for a very long time and there are many theoretical studies as well (for example see Joanny & de Gennes (1984)). For a drop on an inclined surface the difference in the apparent contact angles results in a net surface force which balances the gravitational force (Macdougall & Ockrent 1942; Frenkel 1948):

$$V\rho g \sin\alpha = k\lambda\sigma(\cos\theta_b - \cos\theta_f), \tag{3.2}$$

where V, ρ, g, and α are the volume, density of the fluid, acceleration due to gravity and the plate inclination with respect to the horizontal respectively. λ is some characteristic width of the drop. This equation is exact in two-dimensions with $k = 1$. However in three dimensional drops the value of k is not unique because of the complex shape that a drop may adopt on an inclined surface. Variations in the force related to contact area shape and size, and drop shape, are clubbed together into the factor k in these non-axisymmetric drops (Kawasaki 1960; ElSherbini & Jacobi 2004*b*). Detailed geometry investigations have been done both experimentally (Bikerman 1950; ElSherbini & Jacobi 2004*b*) and numerically (Larkin 1965; Brown *et al.* 1980).

Solids that can support any amount of hysteresis are referred to here as infinitely hysteretic surfaces. Here the small scale roughness or chemical heterogeneities make it possible for a contact line to shift imperceptibly, in order to microscopically satisfy Young's angle. We distinguish this general property of the surface from that displayed by special locations on the surface where forward motion is prevented, i.e., the contact line is pinned. These are associated with a sharp

heterogeneity providing a resistive force too large to be overcome by thermal fluctuations.

In all the numerical investigations we have come across, the shape of the drop is obtained by making some restrictive assumption or other, as listed in table 3.1. The most common assumption is to pin the contact line so that the contact area assumes a prespecified shape such as a circle (e.g. in Brown *et al.* (1980)), or ellipse (e.g. in Lawal & Brown (1982)). Other restrictions include the assumption of small spherical region somewhere on the surface (Larkin 1965), or prescribing apparent contact angles (Jr & Son 1987). Such prescriptions are not unreasonable in certain practical situations, but in the general context these assumptions are not valid (Extrand & Kumagai 1995). This is especially true when α is close to the critical angle of inclination, α_{cr}, beyond which surface forces are not able to counter gravity to provide a static shape (Milinazzo & Shinbrot 1987).

Here, we describe a method to determine the shape, which is based on minimizing the total energy of the drop, and which is not assisted by any assumptions related to the contact area or shape. There have been earlier studies where the static shape is determined by an energy minimization procedure, but these studies too make some restrictive assumptions. For example in Rotenberg *et al.* (1984), for small contact angles, the boundary condition is prescribed as an asymptotic static limit of a relation between the dynamic contact angle and contact line velocity, which itself is determined from experiments. The results are thus sensitive to the nature of the solid surface used in the experiments. Where there exist a multitude of meta-stable solutions, the experiment would lead to only a subset among them. A similar approach has been used in Dussan & Chow (1983); Dussan (1985) that is not limited to small contact angles and these analytical calculations have been verified experimentally by Briscoe & Galvin (1991) for the maximum volume supported at different plate inclinations. Here, the shape of the contact line is fixed based on certain experimental observations of Bikerman (1950) of parallel sided sliding drops, and this was prescribed, and a knowledge of the characteristics of solid surface is used to fix the advancing and receding contact angles (θ_a and θ_r). These however need not be the same as the front (θ_f) and back (θ_b) angles it would adopt in its minimum energy configuration (Krasovitski & Marmur 2005). In other words, a drop on a given surface may display a particular pair of advancing and receding contact angles in the limit of zero velocity. This however, need not be the same as the front and back angles it would adopt in its minimum energy configuration. In general there exist a multitude of meta-stable solutions depending upon the solid characteristics and a given experiment would lead to only a subset among them. We describe here a method to determine the shape, based on minimizing the total energy of the static drop, which does not require experimental input.

With the development of new experimental and computational techniques, this problem continues to draw the attention of researchers. An energy minimization procedure for non-axisymmetric drops based on the principle of virtual displacement has been developed in Iliev (1995, 1997) and a particle based simulation method in Das & Das (2009). While the former introduces resistive forces to obtain static shapes, the latter obtains them without explicit use of contact angle hysteresis. The idea of considering the resisting force of the solid surface as a gradient of a potential was introduced in Finn & Shinbrot (1988), however this was not pursued further, since this potential does not have a simple functional form. A detailed numerical study

of the drop geometry leading to an analysis of Eq. 3.2 is still lacking in the literature. Meanwhile there has been some progress in experimental investigations of various aspects relating shape and surface properties (ElSherbini & Jacobi 2004*b*; Extrand & Kumagai 1995; Quere *et al.* 1998; ElSherbini & Jacobi 2006; Yadav *et al.* 2008). In summary, though some issues have been addressed theoretically (Roura & Fort 2001; ElSherbini & Jacobi 2004*a*) to explain some aspects of experimental observations, further studies in theory and numerical simulations are obviously required for a better understanding. A representative but not exhaustive list of work done in this direction is listed in table 3.1.

Reference	**Relevant work**	**Assumptions/ remarks**
Macdougall & Ockrent (1942)	Use Eq. 3.2 to obtain surface tension from experimental data, show θ_a and θ_r as characteristics of specific solid/liquid considered	Eq.3.2 gives the product $k\sigma$, where k is unknown a priori
Frenkel (1948)	Energy minimization to determine the shapes, derives Eq. 3.2 from virtual displacements	Analyzes linearized equations, assumes that $\theta_f + \theta_b = 2\theta_e$
Bikerman (1950)	Experimental observation of parallel sides of sliding drop, systematically studies the effect of solid surface roughness	Roughness is not related to k or θ_f and θ_b
Kawasaki (1960)	Experimental verification of Eq. 3.2	No estimation of k
Larkin (1965)	Numerical solutions are obtained and tabulated for the shapes after performing some coordinate transformations and application of finite difference technique.	Neglects the elliptic nature of the problem, prescribes a fix radius of curvature at a given point to start the integration
Brown *et al.* (1980)	Finite element method to calculate drop shapes, several characteristics related to geometry and critical angle of inclination are discussed	Assume a circular contact area
Lawal & Brown (1982)	Stability analysis and extension of previous calculations to non-axisymmetric shapes are performed	Prescribes contact line shape, e.g. an ellipse
Dussan & Chow (1983); Dussan (1985)	Starting with Navier-Stokes equation, analyze statics as a limit of dynamics and obtained expressions for critical volume and drop velocity	Assume parallel sided drops and velocity-dependent front and rear contact angles measured from experiments

Rotenberg *et al.* (1984)	Shape is calculated for a sliding drop numerically, with the development of new model for boundary conditions	Assume shape is governed by Laplace's equation despite dynamics
Milinazzo & Shinbrot (1987)	Numerical studies show that wetted area is not constant and is a function of Bond number	Specify the wetted area beforehand
Jr & Son (1987)	Analyze and study 2D drops on vertical surfaces using variational methods and calculate the critical volume	Specify the contact length and front contact angle
Finn & Shinbrot (1988)	Introduces the idea of considering the resisting force of the solid surface as a gradient of a potential, obtained a maximum Bond number	Since this potential does not have a simple functional form, this is not further pursued
Briscoe & Galvin (1991)	Experiments to verify Dussan's equation and find agreements for $\alpha < 90^\circ$	Modifications required when $\alpha > 90^\circ$
Extrand & Kumagai (1995)	Experimental investigation to relate drop shape to contact angle hysteresis	A definitive conclusion on the shape or on the value of k is not arrived at
Iliev (1995, 1997)	Method of virtual displacement is used to carry out extensive computations, counter action to the rolling flow is modeled with a resistive force	No contact angle hysteresis permitted, model hypothesizes a form for resistive force
Quere *et al.* (1998)	Derives the conditions for sticking drops, a simple model was proposed and compared with experiments	Small drops under spherical cap approximation and small hysteresis
Roura & Fort (2001)	Energy based arguments to predict the critical angle of inclination and comparisons with experiments	Only for hydrophilic surfaces
ElSherbini & Jacobi (2004*b*,*a*, 2006)	Experimental investigation of geometric parameters to describe the shape and material properties, shapes are approximated by two circles at every azimuthal angle	A geometric model to fit experimentally observed shapes
Krasovitski & Marmur (2005)	Prove experimentally that the advancing and receding angles do not always equal the front and back angles respectively	
Yadav *et al.* (2008)	Experiments that show that retentive forces as a function of volume are different from those predicted by Eq. 3.2	

Das & Das (2009)	Smoothed particle hydrodynamics simulations done with smooth surfaces to obtain static drops	Role of hysteresis is not clear

Table 3.1: A selective summary of the literature on static drops on inclined surfaces. The assumptions made in the theoretical and numerical work are highlighted. In the present work these assumptions are not made, since the objective is to find static drop shapes of minimum possible energy. Inherent in our approach is the assumption that the solid can lend itself to any amount of hysteresis.

There are several situations in which one may ask what is the maximum volume of a drop that can be supported on a solid surface inclined at a certain angle to the horizontal. Put another way, what is the maximum plate inclination at which a drop of a given volume will stay statically on a surface? This question is relevant in various situations, e.g. when insecticides or pesticides are sprayed on plant leaves, in spray and paint industries or in applications using drop wise condensation heat exchangers. General answers to these questions require a large set of experimental investigations. Our objective here is to make predictions using simple analysis, assuming that the surface is infinitely hysteretic.

Our approach, based on a procedure of minimization of total energy to determine the shape of a static drop, is described in section 3.3. This fundamental approach has been used in several studies (Frenkel 1948; Rotenberg *et al.* 1984; Jr & Son 1987; Iliev 1995, 1997). The procedure contains one ambiguity, namely, what is the correct base with respect to which the potential energy should be defined. This question has not been addressed explicitly to our knowledge, but different studies get around it by choosing a base and making computations with respect to it. For example, Frenkel (1948) uses the center of drop as the base (besides using linearized equations and $\theta_f + \theta_b = 2\theta_e$), Rotenberg *et al.* (1984); Jr & Son (1987) fix the contact line while Iliev (1997) introduces an artificial resistive force in the procedure for virtual displacements with arbitrary parameters. Each of these choices will give rise to different answers for the minimum-energy shape, and we discuss what would be a good measure under a given situation. Note that the choice of potential energy basis corresponds to a pinning of the drop at a particular point. We deal with one side pinned situations and hence obtain a more general set of solutions than available in the literature. In fact a drop pinned on one of its sides and free to choose a minimum energy shape by moving its other end is not uncommon in experiments. The partial pinning of the contact line is a result of variations in solid surface inhomogenities. Experimental investigations in Berejnov & Thorne (2007) showed some front pinned and some rear pinned drops on inclined surfaces. Rear pinned drops are generally observed in rain drops on windowpanes; Roura & Fort (2001) investigated this problem experimentally and discussed the partial pinning of the contact line on various surfaces with different affinities. Moreover the phenomenon of hysteresis should be necessarily represented in a correct way to model these drops. But this phenomenon itself is associated with uncertainty and hence a consistent approach is required. This too has not been discussed to our knowledge and is therefore taken up in section 3.4. Since our approach does not make use of θ_a and θ_r, macroscopic behavior of drops on inclined surfaces such as the the variation of front and rear angles with respect to plate inclination, maximum volume that can

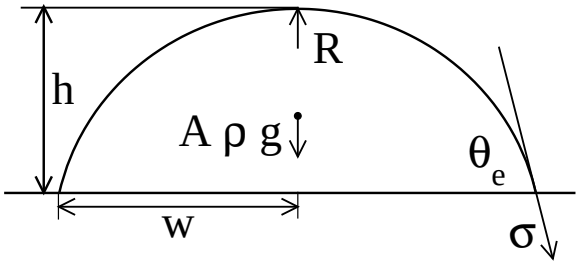

Figure 3.2: A sessile drop.

be supported on a solid surface at a given inclination etc. may be addressed consistently.

For simplicity and clarity we analyze two dimensional drops here, but the method described is general and can be extended to three dimensional non-axisymmetric drops. The conclusions of section 3.5 remain valid qualitatively there too. The shapes obtained here may be used as the starting point to study drop dynamics, and to perform stability analyses. Finally, in section 3.6, we discuss the future directions and conclude.

3.3 Energy minimization

We begin by constructing the force balance on a two dimensional drop under the action of gravity. We treat the drop as being made up of a liquid (l), in a fluid medium referred to as a gas (g), and supported by a solid surface (s). Since we deal with two dimensional drops, the term 'volume' stands for the cross-sectional area with a unit width in the third (spanwise) direction. The term 'contact area' similarly implies the length of corresponding surfaces times a unit spanwise width.

The hydrostatic pressure variation inside a drop is balanced by a suitable curvature adopted by the flexible liquid-gas interface. For force balance along the vertical (Z) direction therefore, we must have

$$\frac{\sigma}{R} + z\rho g = \sigma \left[\frac{d^2z/dx^2}{\left[1 + (dz/dx)^2\right]^{3/2}} \right] \tag{3.3}$$

where x is the horizontal coordinate at which z is the vertical location of the interface. The term in the square bracket on the right hand side is the inverse of the radius of curvature at z, whereas R is the radius of curvature at $z = 0$ (tip of the drop). It is easy to first analyze the two limits, viz., zero plate inclination for a sessile drop and a 180° plate inclination for a pendant drop.

Consider a sessile drop, illustrated in Fig. 3.2, of height h, contact area $2w$ with the solid, and liquid-gas interfacial tension σ, subjected to gravity g. At the contact line, a horizontal force balance yields nothing but Young's equation (3.1) with the equilibrium contact angle θ_e. The weight of the drop, and the vertical component $2\sigma \sin\theta_e$ of the forces due to surface tension are balanced by the reaction from the rigid solid surface (de Gennes *et al.* 2004). The reaction to the pressure forces is distributed along the contact area, while that to the tension along the interface is a point force at the triple contact point. Thus, an overall vertical force balance for

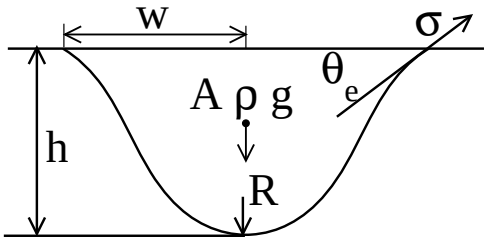

Figure 3.3: A pendant drop.

a sessile drop (Fig. 3.2) may be written (Briscoe & Galvin 1991) as

$$V\rho g = 2w\left(\frac{\sigma}{R} + \rho g h\right) - 2\sigma\sin\theta_e. \tag{3.4}$$

This expression may also be obtained from the integration of Eq. 3.3 (Pitts 1973). Note that surface tension manifests itself both as a point load and a distributed load.

On inverting the plate, we have a pendant drop as shown in Fig. 3.3, and an overall vertical force balance may be written as

$$V\rho g = -2w\left(\frac{\sigma}{R} - \rho g h\right) + 2\sigma\sin\theta_e \tag{3.5}$$

The reversal of the direction of the surface forces results in the shape of pendant drops being different from sessile ones. For a sessile drop, the solid surface can support any weight, but for pendant drops a part of the distributed reaction force acts in the direction of gravity, and the remainder must support both this and the weight of the drop. Thus drops of volume larger than a particular maximum cannot be 'hung' from a solid surface. A detailed discussion specific to pendant drop shapes and their stability can be found in Chapter 2. We now construct a force balance of a drop sitting on an inclined surface.

The force balance parallel to the solid surface is straightforward. However, the balance in the direction normal to the surface needs some care. A discussion of the normal force balance is not available in the literature to our knowledge, except Tadmor *et al.* (2008); Jerison *et al.* (2011), which discuss the normal reaction force at the contact line alone. Such a discussion is therefore included below. In fact, even for horizontal surfaces, the role of the surface reaction is an important issue drawing recent attention (see e.g. Finn (2006); Jerison *et al.* (2011)).

Consider a small element of volume dV shown in Fig. 3.4 of the drop discussed in Fig. 3.1. The forces acting on this element are (i) gravitational force $dV\rho g$ acting downward, (ii) surface tension forces σ acting at the corners of the liquid-gas interface along the interface (iii) pressure forces Px acting on the upper and lower surfaces of the element and (iv) the reaction force $F_N dw$ from the solid surface. Subscripts 1 and 2 denote the lower and upper faces of this element respectively. A horizontal force balance of this differential element is given by

$$\left[\frac{\sigma}{R} - \rho g z\right] dw\sin\alpha = \sigma(\cos\theta_1 - \cos\theta_2) \tag{3.6}$$

where R is the radius of curvature at a point on the interface from where the height z is measured.

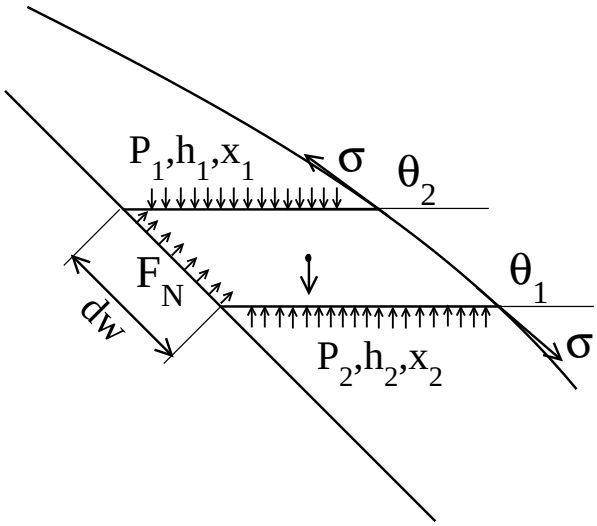

Figure 3.4: Forces acting on an elemental volume of drop resting on an inclined surface. The gravitational force is shown acting at the center of gravity of the element, pressure and normal reaction are shown as distributed forces acting over a length while the liquid-gas interfacial tension acts as point force at the two corners.

A vertical force balance is written as

$$\left[\left(\frac{\sigma}{R}-\rho g z_1\right)x_1-\left(\frac{\sigma}{R}-\rho g z_2\right)x_2\right]+\sigma\left[\sin\theta_2-\sin\theta_1\right]+\left[\frac{\sigma}{R}-\rho g z\right]dw\cos\alpha=dV\rho g. \quad (3.7)$$

It may be seen that, unlike in sessile and pendant drops, the variation of reaction force along the solid surface is not intuitively obvious. For example, the nontrivial geometry (say, $x_1 \neq x_2$) gives rise to several contributions. Integrating the horizontal and vertical force balances on such elements for the entire drop volume, and resolving the total force in a direction parallel to the plate, Eq. 3.2 may be recovered. Correspondingly the total force balance in a direction normal to the plate is

$$V\rho g\cos\alpha+\sigma(\sin\theta_f+\sin\theta_b)=\frac{1}{\sin\alpha}\left[\frac{\sigma}{R}(h_r-h_a)-\frac{\rho g}{2}(h_r^2-h_a^2)\right] \quad (3.8)$$

where h_r and h_a denote the height to the locations of rear and front contact points from where R is defined. This expression reduces to Eq. 3.4 and Eq. 3.5 respectively when plate inclination goes to 0° and 180° degree.

Just as Eqs. 3.4 and 3.5 are instrumental in distinguishing a sessile drop from a pendant one, the above Eq.3.8 has important consequences at the two extremes for drops on inclined surfaces, namely $\alpha \to 0°$ and $\alpha \to 180°$.

To understand the relative distribution of these forces, we plot them in Fig. 3.5. We consider a typical shape as shown in Fig. 3.5a. The force contributions along the vertical and horizontal directions are shown in the Fig. 3.5b and 3.5c respectively. In fact the reaction force changes direction at a particular height. Thus the bottom part of the drop is supported by the solid while the top is not. It is obvious that the solid wall should provide the necessary local moment reaction as well, since the lines of action of the various forces do not coincide. Therefore the drop cannot be thought of as *pivoted* at a single point on the plate, unlike a solid object hanging

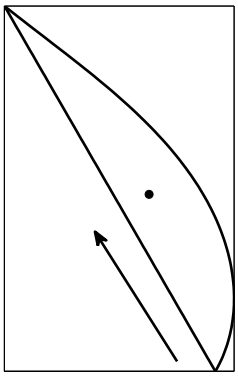

(a) Drop shape

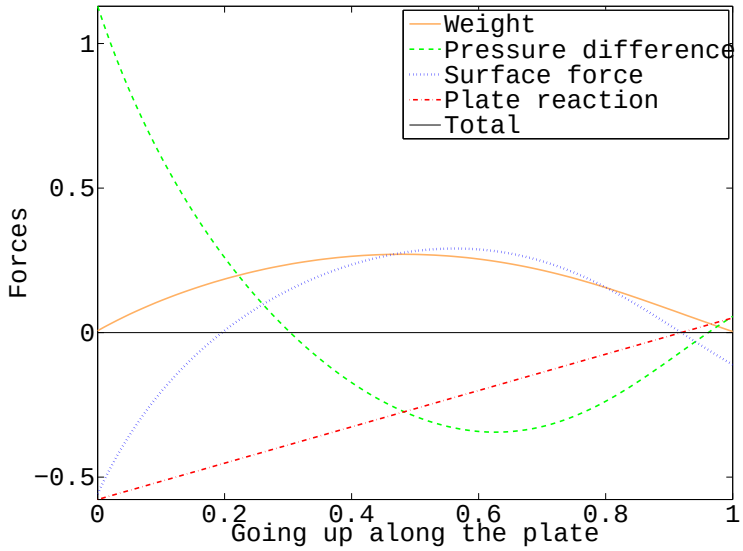

(b) Vertical force balance

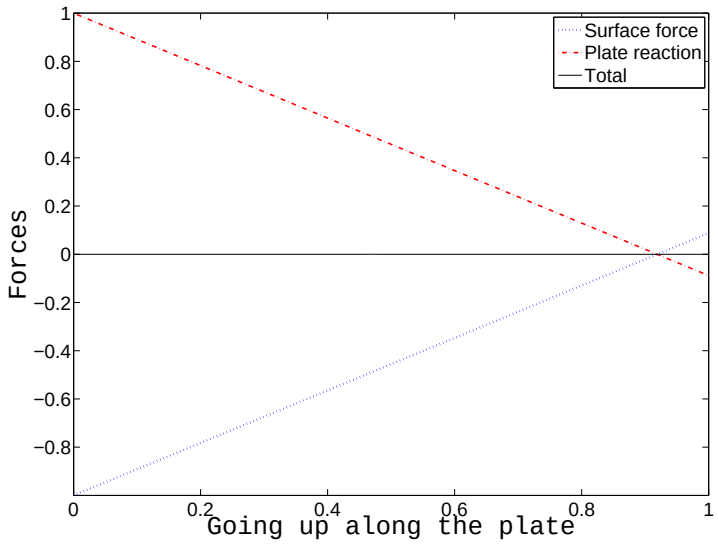

(c) Horizontal force balance

Figure 3.5: Distribution of forces acting on the drop along the plate, resolved into vertical (b) and horizontal (c) components for the shape shown in (a). $z = 0$ on the abscissa corresponds to the front end of the drop. Forces are normalized on the ordinate. In (a) and in subsequent figures, the center of mass is shown by a point.

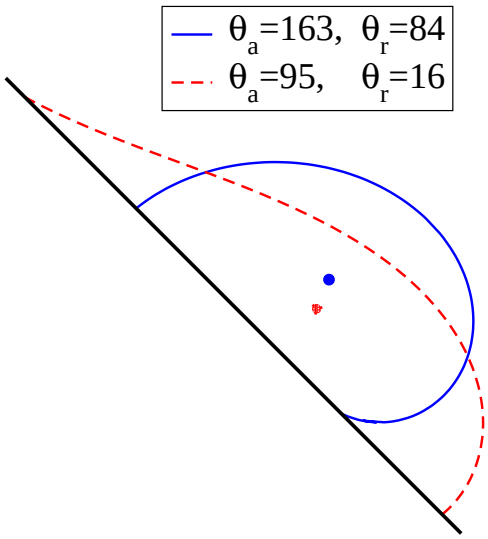

Figure 3.6: Illustrating two different shapes for the same volume and plate inclination, corresponding to two different values of R. Both shapes are possible to achieve in experiments by choosing solid surfaces of appropriate characteristics.

from a point.

3.4 Numerical method of determining the shape

The procedure used is an extension to inclined surfaces of that described in Chapter 2 for pendant drops. Beginning with a specified value of R, Eq. 3.3 is integrated to determine a possible equilibrium shape of the meniscus. Note that this equation is independent of the positioning of the solid plate. Using this freedom, the solid plate at a specified inclination is used to cut this curve when the volume of the closed shape corresponds to the desired volume V. For this fixed volume, the result corresponds to a unique force-balanced shape for the specified bottom-most radius of curvature R. Fig. 3.6 illustrates shapes so obtained, of a given volume on a particular plate inclination for two different values of R. In principle, an infinite number of such shapes can exist in nature for a given volume.

Given an infinitely hysteretic solid, the shape that will actually be displayed will be the minimum energy one for the given combination of solid surface and fluid. Our objective is to find that unique shape at which the drop attains the least energy it possibly can, on all possible surfaces of a given surface tension. The total surface energy (E_s) may be calculated as

$$E_s = \sigma L_{lg} + (\sigma_{sl} - \sigma_{sg}) L_{sl} \tag{3.9}$$

where L_{lg} and L_{sl} are the liquid-gas and solid-liquid interfacial lengths. The quantity that needs care in defining is the total potential energy (E_p), which may be written as

$$E_p = V \rho g (h_{cg} - h_{ref}) \tag{3.10}$$

where h_{cg} is the height of the center of gravity of the drop. There is an arbitrariness in choosing the reference height h_{ref}, and evidently the results depend crucially on this choice. For example

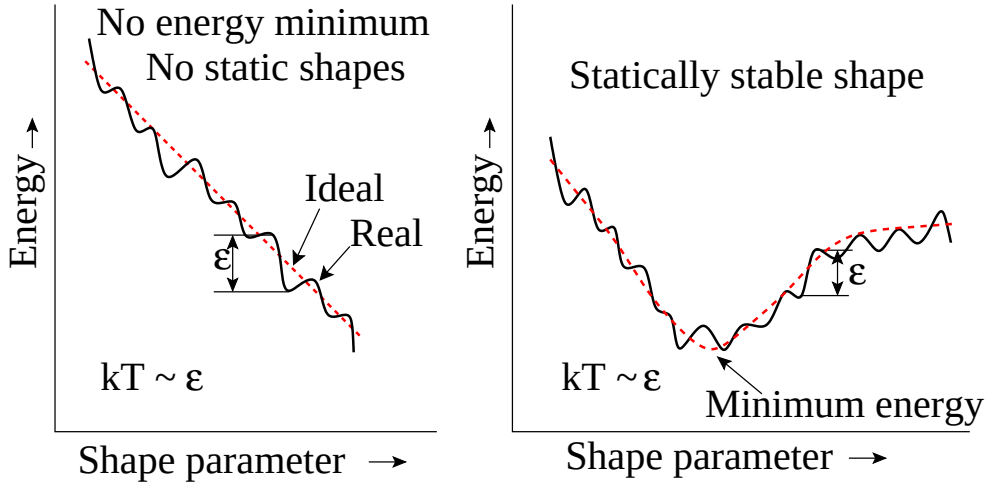

Figure 3.7: Example schematics of energy landscapes. The total energy for an ideal (dashed lines) and real (solid lines) solid surface is shown as a function of some continuous variation in drop shape characteristics. Local heterogeneities produce local minima of depth $O(\varepsilon)$, and kT is the thermal energy available to the system. Our procedure essentially looks for a global energy minimum of the type illustrated in the right schematic. The location of pinning provides an additional strong restraining force which is too strong for thermal fluctuations to overcome. In a landscape of the form shown on the left, our procedure will not yield a static shape.

one may take h_{ref} as the point on the plate vertically below the center of gravity. The rear or front contact line locations, and also the mid-point on the contact length present other natural choices. The physical basis for a particular choice is open to question. This problem of determining the right base for the calculation of potential energy is not very common in mechanics. It is usual that the choice of basis only changes the potential energy by a constant value in all cases, which does not matter in any comparisons. Here we have a peculiar situation in which a deformable body with free end points is allowed to slide on an inclined surface. In theory the drop as a whole may be translated to lower and lower positions on the solid surface and its total energy would keep decreasing. In the case of a solid object hanging from a wall, there would be a well-defined pivot point of suspension from the wall. There is no such unique point for a liquid drop as we have discussed. The reason the drop attains an equilibrium position in reality is because of pinning of some kind at one or more contact locations. The most reasonable choices for h_{ref} are thus either the advancing or the receding fronts of the drop, and we study both. We also do cross comparisons between these choices. As discussed in section 3.2, the more restrictive situation where both ends are pinned is well studied in the literature. That case however involves an arbitrary choice of contact line length. In reality when a drop slides on an inclined surface, its movement is restricted typically by the pinning of just one of its ends.

Not all boundary conditions are known a priori in this free boundary value problem, and are to be determined along with the full solution. Such a procedure is straightforward for droplets on a horizontal surface, where Young's equation arises naturally from the energy minimization process. One may apply a similar procedure for drops on inclined surfaces. In this case, the energy minimization procedure not only arrives at Eq. 3.2 as the boundary condition, but picks a unique combination of θ_f and θ_b. It is thus more powerful than earlier procedures, which needed to provide an additional prescription, e.g. of contact angle or contact area. More important, we

have the global minimum energy shape rather than innumerable metastable solutions. A drop on an inclined surface would remain in motion until it encounters a pinning location. At the pinning location, the surface provides a restraining force, which is far stronger than the thermal fluctuations can overcome. This strong force could come from a sharp chemical heterogeneity, for example. It is reasonable to assume that such pinning is likely to occur at one end of the drop (Berejnov & Thorne 2007; Roura & Fort 2001), and that both ends are unlikely to be pinned simultaneously. A choice of pinning location fixes the basis for potential energy calculations. At the free end, thermal fluctuations allow the contact line to relocate itself at small scales to minimize energy. We emphasize again our assumption that the solid surface is capable of exhibiting the full range of front and back contact angles, and that enough thermal energy is available to the drop to take up the most stable shape at the free end. This concept is pictorially represented in Fig. 3.7. The left portion of the figure shows a case where there is no minimum energy static shape, so the drop will continue to move downwards on the incline. This would happen when the drop is larger than the maximum permissible static volume, for example. On the right we have a possible energy minimum shape. We also need an appropriately placed pinning location, as discussed. This pinning on one side gives a general set of solutions unlike the solutions obtained in the literature with the entire contact area pinned.

The total energy may be written as the sum of potential and surface energies, $E_t = E_p + E_s$. Substituting Eq. 3.9 and 3.10 and nondimensionalising length scales by capillary length $L_c = \sqrt{\sigma/(\rho g)}$ and energy by σL_c we have the expression for total energy $E_t = B(h_{cg} - h_{ref}) + L_{lg} - \cos\theta_e L_{sl}$. Here, $B = V\rho g/\sigma$ is the Bond number describing the relative importance of two competing forces. We note that other forces which may become relevant in a given situation may be incorporated into the present procedure. It should be mentioned that energy contributions from small unevennesses in the surface are neglected in these calculations, as are other molecular forces.

3.5 Results and Discussion

3.5.1 Shape variations

The change in the minimum-energy shape of a drop of a given volume, when the solid surface is tilted in stages from $\alpha = 0°$ to $\alpha = 180°$, is illustrated in Fig. 3.8. It is seen that the shapes corresponding to front-pinned and rear-pinned drops can be dramatically different, highlighting the important role of solid surface heterogeneities. There is no such ambiguity of course for sessile or pendant drops. There is a continuous variation in the contact angle as a function of the tilt angle, with a reversal in behavior at the vertical position of the plate. This is illustrated in Fig. 3.9.

Fig. 3.9a shows the variation in front and rear contact angle as a function of tilt for a non-dimensional volume of $V = 0.5$. The plots are done for three different equilibrium contact angles $\theta_e = 30°, 90°$ and $150°$. It is seen that the variation in θ_f and θ_b is not symmetric, and depends on which side of the drop is pinned. First consider the case of $\theta_e = 90°$. For a drop pinned at its front, θ_f increases with tilt for $\alpha < 90°$, while the rear adjusts itself to attain $\theta_b = \theta_e$. The opposite happens when the receding side is pinned, in which case the advancing front takes up

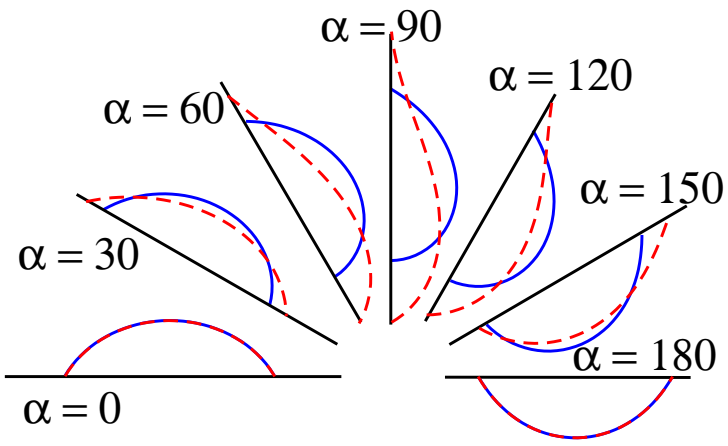

Figure 3.8: Illustration of change of global minimum energy shape as a function of plate inclination. Here $\theta_e = 60°$ and $V = 0.5$. Continuous and dashed lines are for shapes obtained by pinning the front and rear of the drop respectively. It may be noticed that the free end always reaches the equilibrium contact angle.

the most favored contact angle, i.e., θ_e, while the rear angle is forced to reduce. The maximum difference in the two contact angles is seen at the vertical position of the plate, with a monotonic and symmetric variation on either side, to θ_e at the sessile and pendant limits.

For $\theta_e = 30°$, when the front is pinned, the variation is similar to what is observed in the case of $\theta_e = 90°$. But when the back is pinned, there is a sharp decrease in the contact angle, reaching a value of $0°$ at an $\alpha = 15.5°$, with no solutions beyond, up to $\alpha = 164.5°$. Conversely for $\theta_e = 150°$, when the back is pinned, solutions exist for all inclinations, while there is a large range of α where no solution exists when the advancing front is pinned. There is thus a cross-symmetry in the solutions of $\theta_e = \beta°$ and $\theta_e = (180 - \beta)°$, seen for a range of β.

The important observation is that the contact angle at the free end remains at the equilibrium value except for a class of solutions discussed later. For a front-pinned drop then, $\theta_b = \theta_e$ and $\theta_f > \theta_b$, while $\theta_f = \theta_e$ and $\theta_b < \theta_f$ for a drop pinned on receding side. A use of this information reduces an unknown in Eq. 3.2, making it solvable. The angle at the pinned end can then be described by

$$\cos\theta_{f/b} = \cos\theta_e \mp V \sin\alpha. \tag{3.11}$$

Solutions of this equation are plotted as lines in Fig. 3.9 and are identical to the numerical solutions over most of the range. In experiment, depending on the surface properties, the free end may exhibit an angle lying between θ_r and θ_a, but different from θ_e. Nevertheless, this angle will remain constant for the given surface irrespective of the inclination and volume. This feature of minimum energy shapes has been seen, but not commented upon, in experiments (Macdougall & Ockrent 1942).

The discussion above was for a case when a drop is pinned at one of its ends. Consider now a drop which is effectively pinned elsewhere, or has a more complicated distribution of pinning. Many experimental observations show a simultaneous variation in the front and rear angles (ElSherbini & Jacobi 2006), which is characteristic of such pinning. In our simulations, with the drop pinned elsewhere we observed such a variation of θ_f and θ_b. We also found that for this situation we obtained equal deviations in front and back angles from the Young angle,

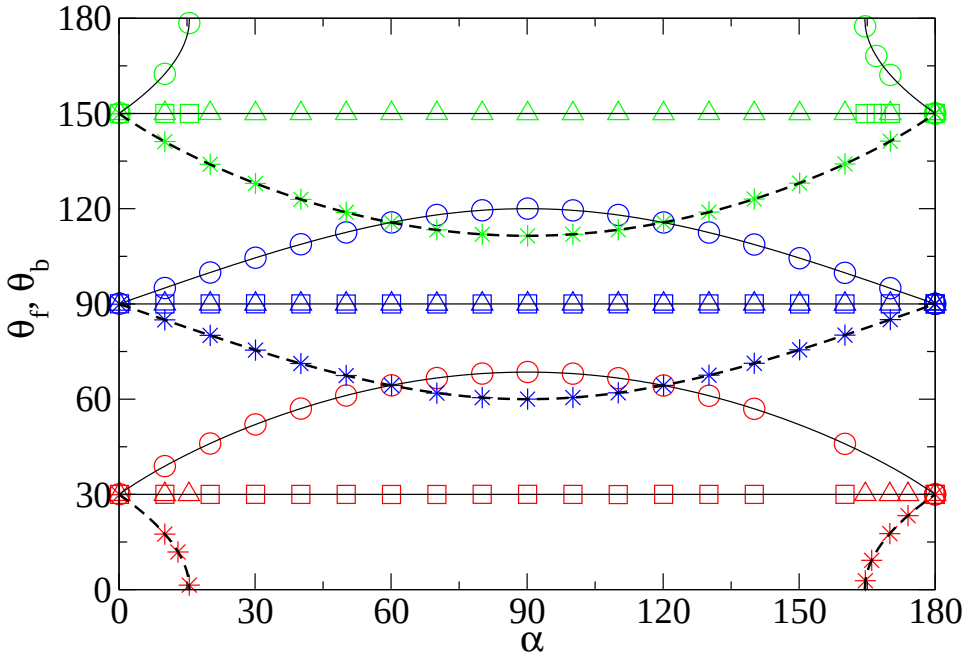

(a) for $V = 0.50$

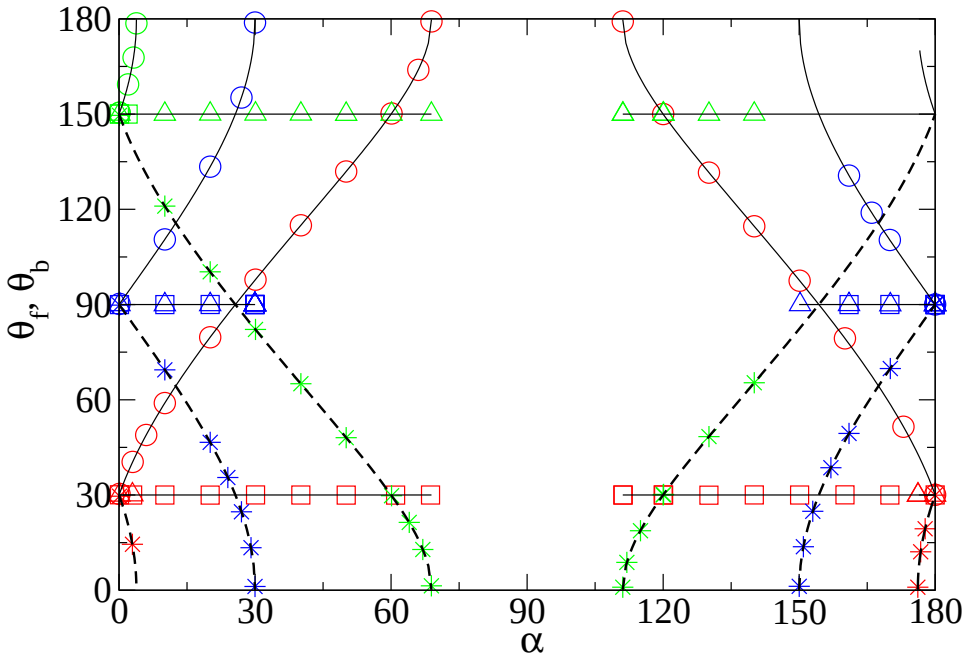

(b) for $V = 2.0$

Figure 3.9: Continued in next page.

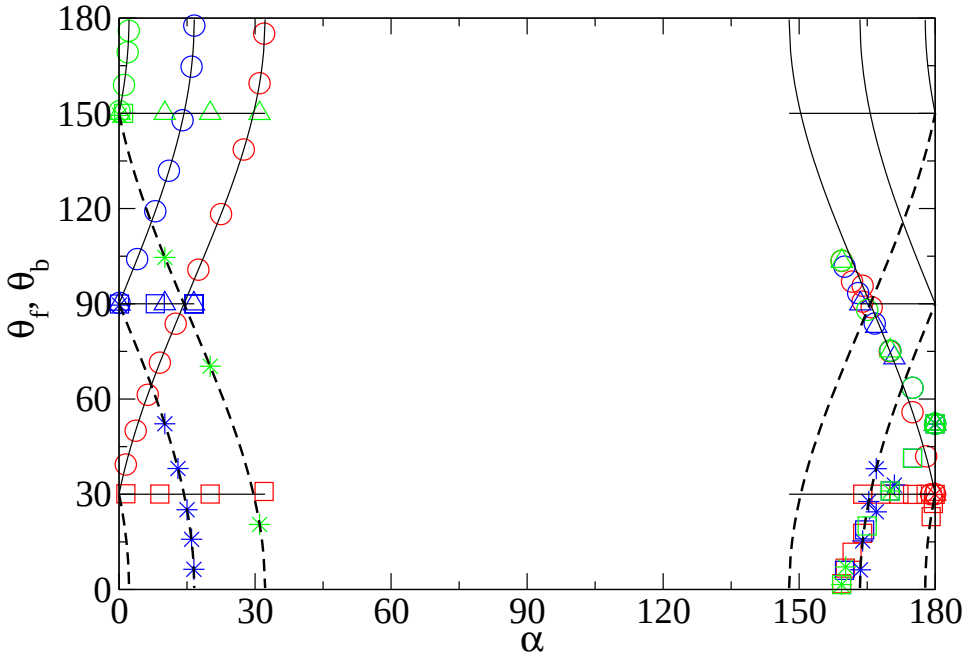

(c) for $V = 3.50$

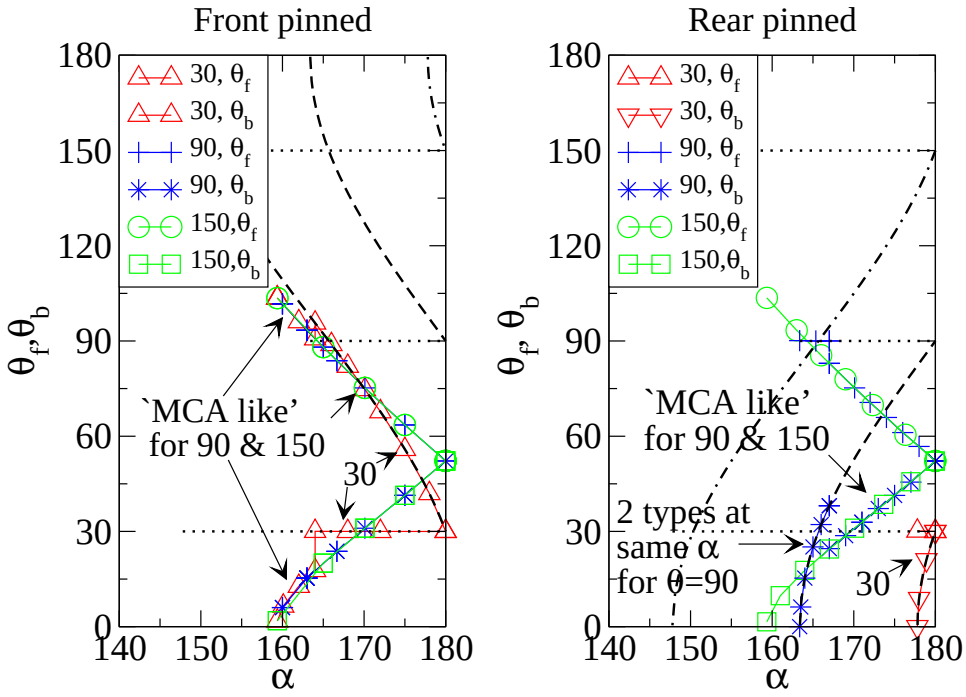

(d) for $V = 3.50$, expanded near $\alpha \to 180°$

Figure 3.9: Front and rear contact angles of minimum energy shapes are shown as functions plate tilt angle in (a), (b)& (c) for different volumes of the drop. Three different equilibrium contact angles, $\theta_e = 30°, 90°$ and $150°$ are considered for each volume. Always $\theta_f > \theta_r$. The computational results are shown with symbols. Solid lines and dashed lines are the theoretical predictions of Eq.3.11 for front-pinned and back pinned drop shapes respectively. When the front is pinned, the front and back contact angles are represented by $\circ$ and $\square$ respectively. In the case of back pinned, they are respectively represented by $\diamondsuit$ and $*$. For a range of inclinations, solutions may not exist, and this is accentuated at larger volumes as in figures (b) and (c). In (d), a portion of fig 3.9c is expanded, to show the existence of different types of solution when $\alpha \to 180°$ for both front pinned and rear pinned cases. The symbols for this plot are defined in the legend.

i.e., $\theta_f = \theta_e + \epsilon$ and $\theta_b = \theta_e - \epsilon$. For small ϵ, the force balance parallel to the plate (Eq. 3.2) then provides

$$V\frac{\sin\alpha}{\sin\theta_e} = \epsilon. \tag{3.12}$$

With an increase in the volume, as illustrated in Fig. 3.9b for $V = 2.0$ and Fig. 3.9c for $V = 3.5$, there is a wider range of tilt angles at which no solution is possible. The symmetry about $\alpha = 90°$ is seen here too. Eq. 3.11 predicts drop shapes over a larger range than that in which numerical shapes are found, especially for higher Young angle and higher α. This is because certain shapes have intersecting menisci and cannot be considered as physical solutions. This was pointed out in Chapter 2 for pendant drops. Since Eq. 3.11 does not care about this intersection of menisci, it predicts solutions in this range.

There is a crowding of solutions near $\theta_e = 30°$ in Fig. 3.9c when α is close to 180°. This region is expanded in Fig. 3.9d for both front pinned and rear pinned drops. This crowding is related to a subtle point described in detail in Chapter 2. For a pendant drop, there exists a maximum volume beyond which solutions respecting Young's contact angle do not exist (Pitts 1973). However, certain solutions, with contact angle smaller than θ_e, may be found beyond this maximum volume, upto $V \approx 5.2$, which is the maximum volume for a fully wetting pendant drop. These solutions are characterized by a local minimum in contact area (MCA). This is seen in Fig. 3.9c with larger volumes exhibiting small contact angles when $\alpha = 180°$. They remain as spurious solutions on a perfect solid where the horizontal force balance (equation 3.1) is violated and is not in a real energy minimum. However, on a surface which supports hysteresis or by some other mechanism through which the contact line can be pinned at this minimum contact area, this remains as a valid solution. Remnants of these solutions may be found for surfaces inclined at α close to 180° too, and we call them 'MCA like' solutions. It may be noted that maximum volume of pendant drop of θ_e that can be supported on a solid surface is ≈ 1.5 and here we are dealing with a larger volume. Therefore the only solution can be an MCA solution which will have a smaller contact angle than θ_e. Unlike the shapes so far discussed where either the front or rear angles have equilibrium contact angles depending on the pinning location, these 'MCA like' solutions do not exhibit equilibrium angles at either end. Therefore Eq. 3.11 cannot predict the details of these shapes, which explains the deviations observed in Fig. 3.9d. Instead, solutions for all equilibrium angles, e.g. $\theta_e = 90°$ and $\theta_e = 150°$, lie on a 'universal' curve characteristic of MCA-like solutions (Chapter 2) for a given inclination. This is what is seen in figure 3.9b and smoothly joins with solutions at other inclinations. These shapes will need further investigation for a full understanding, as discussed in Chapter 2, and we do not pursue that here.

3.5.2 Maximum volume

The previous observations lead to Fig. 3.10 where the maximum volume that can be supported by a plate is plotted against the plate inclination. Again a prediction for maximum volume may be made from Eq. 3.11, rewritten as

$$V_{max} = \frac{\cos\theta_e \mp \cos\theta_{f/b}}{\sin\alpha}. \tag{3.13}$$

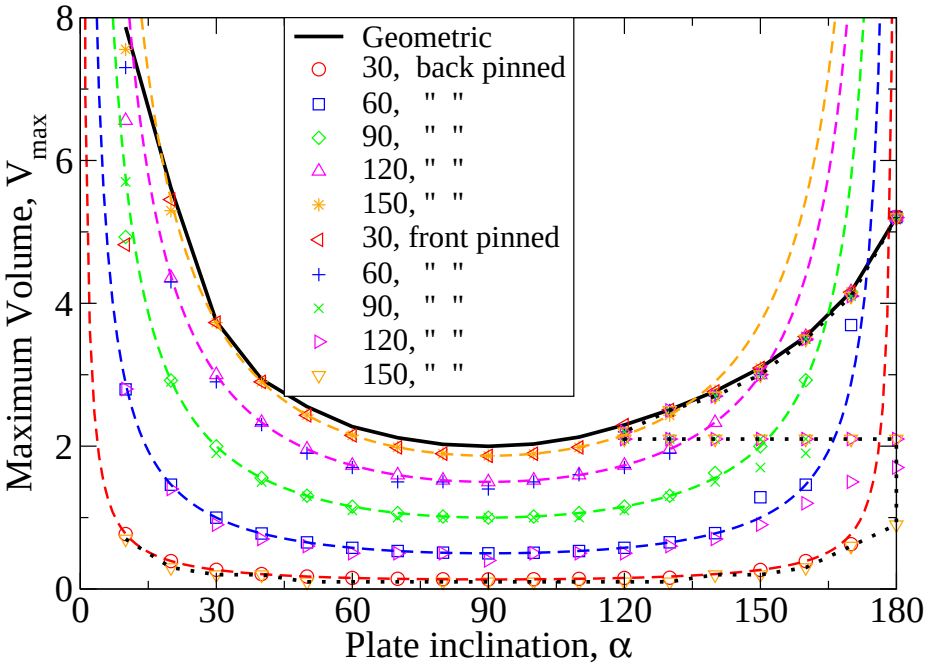

Figure 3.10: Maximum volume of a two dimensional drop that can be sustained on an inclined plate, as a function of inclination. There is a geometrical constraint shown by the dark continuous line. Different dashed lines are predictions of Eq. 3.13 and symbols are obtained from the numerical calculations for various equilibrium contact angles. A similarity between θ_e of front-pinned and $180^\circ - \theta_e$ and back-pinned is evident.

where $\theta_f = 180^\circ$ for a front pinned drop and $\theta_b = 0^\circ$ for a rear pinned drop. This is shown as a dashed line in the same figure. Note that by substituting Eq. 3.2 into the expression of Dussan (1985) for maximum volume (Eq. 5.3 in that paper) results in this critical volume becoming independent of plate inclination, and dependent only on θ_a. Eq. 3.13 would thus provide a more reliable estimate for inclined geometries. In fact, a special form of Eq. 3.13 for hydrophilic surfaces when the receding side forms a thin film, but for three dimensional drops, has been reported in Roura & Fort (2001) and experimentally verified. This particular case corresponds to a drop pinned at the back, with $\theta_b \sim 0^\circ$ and hence Eq. 3.13 conforms to Eq. 6 of Roura & Fort (2001). Secondly we recall that the maximum volume at a given inclination for a particular θ_e when advancing front is pinned coincides with solution for $180^\circ - \theta_e$ when receding side is pinned and vice-versa. This may be seen to be a consequence of Eq. 3.13.

Fig. 3.11 presents Fig. 3.10 slightly differently. Here $V_{max} \sin\alpha$ is plotted against α. Since V_{max} corresponds to extremum value of one of the contact angles, Eq. 3.11 is essentially a linear equation. As discussed earlier, since the force balance parallel to the plate is not the governing equation when $\alpha \to 180$ in determining V_{max}, this linearity is no longer valid and one may see the sudden drop in the value of $V_{max} \sin\alpha$.

There is another, geometrical, measure of maximum volume. This corresponds to a static drop shape but need not be a minimum energy shape, and is obtained merely by fixing the front angle to 180° and/or the rear angle to 0°. (It may not be possible always to satisfy both due to geometrical reasons.) This is shown by a continuous line. This geometrically achievable maximum need not in general correspond to a minimum in energy, so the true maximum would

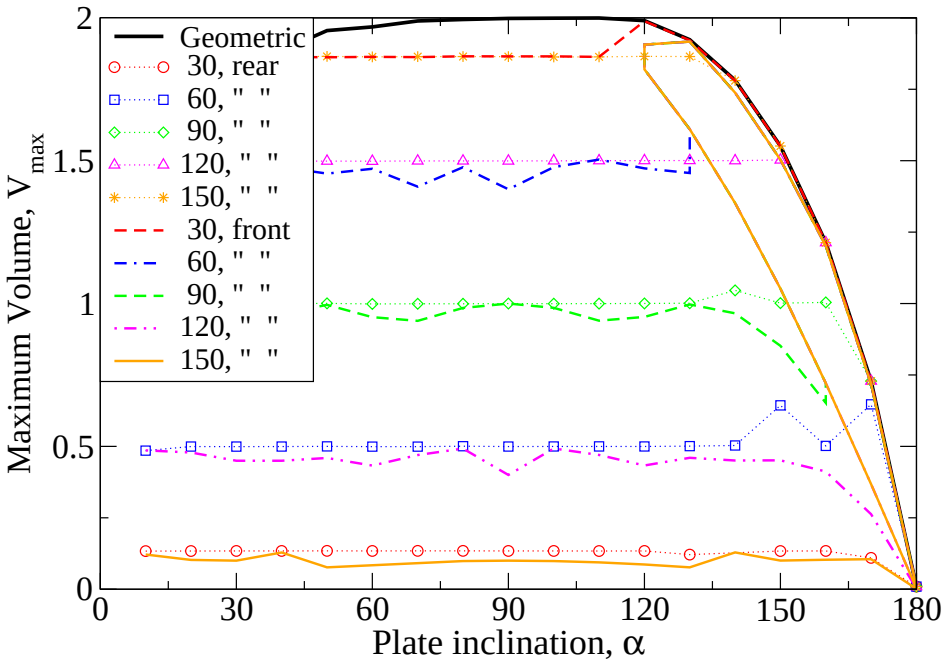

Figure 3.11: Maximum volume of a two dimensional drop of figure 3.10 plotted as $V \sin\alpha$ in the ordinate. Note that the force balance. Eq. 3.2 restraints the maximum value of $V \sin\alpha \leq 2$.

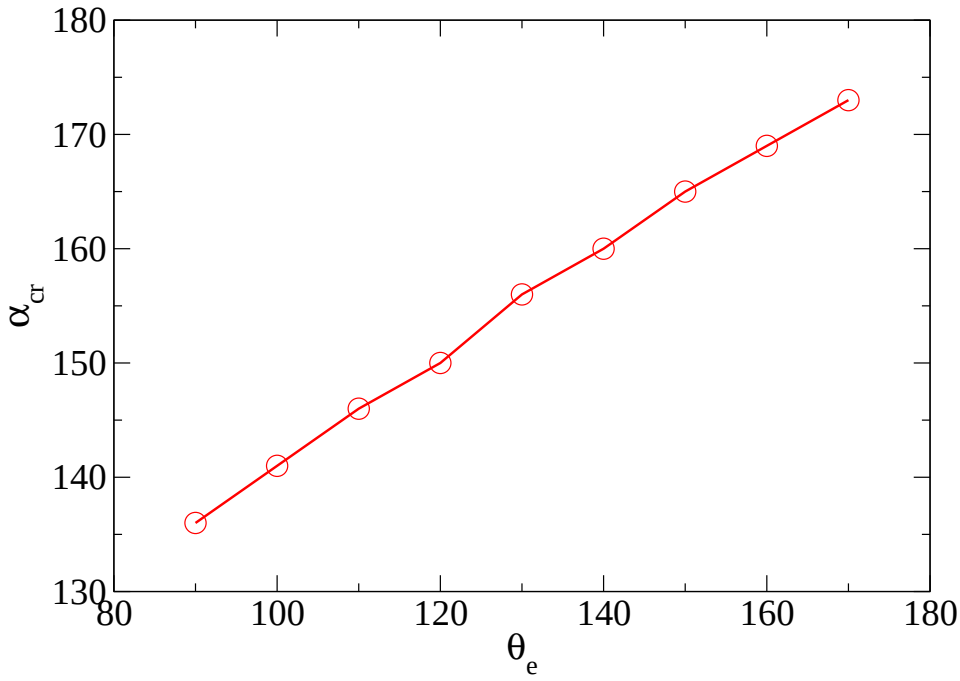

Figure 3.12: Critical inclination, beyond Eq. 3.13 is no longer the decisive condition, as a function of equilibrium contact angle when front end is pinned.

often be smaller, as seen. Since volume goes to infinity for sessile drops it was difficult to get accurate answers numerically for small plate inclinations.

There are some features to be noticed. Unlike the contact angles, the maximum volume is not symmetric with respect to the vertical position of the plate. The behavior seen is in qualitative agreement with experimental observations of Briscoe & Galvin (1991) and theoretical predications of Dussan & Chow (1983); Dussan (1985) for three dimensional non-axisymmetric drops. The asymmetry is to be expected because, as discussed, the plate cannot support an infinite volume in the pendant configuration but it can in the sessile one, since the plate reaction is finite in the pendant case. At some critical value α_{cr} of the inclination, the normal reaction becomes the limiting factor for maximum volume that can be supported, and Eq. 3.13 is no longer the decisive equation. In other words, Eq. 3.8 is the determining condition when $\alpha \to 180°$. This equation is not completely predictive unlike the force balance parallel to the plate due to several unknowns and the interface shape has to be solved to use this equation. This transition of dominant force balance is important in practical cases because it is not possible to achieve a static shape beyond this critical volume by adjusting fluid or solid properties. The critical inclination of transition, beyond which Eq. 3.13 is not the decisive condition, is found to vary linearly with equilibrium contact angle as shown in Fig. 3.12.

At higher θ_e, there is a range of α for which no numerical solution is possible, as seen in Fig. 3.10. As mentioned earlier, self-crossing menisci are not allowed. This leaves a gap in the solution space for higher α in Fig. 3.13. In Fig. 3.14, the origin of the gap is related to the existence of MCA solutions. It may be noted that for pendant drops, when $\theta_e > 90°$ there exists a gap between the maximum possible volume and MCA solutions (Fig. 2.2). Again, the presence of this gap continues in case of small tilts from $\alpha = 180°$ separating the normal solutions with 'MCA like' solutions. Due to these two reasons, solution space near $\alpha \to 180°$ is not completely predictable for V_{max} from analytical solutions. These two situations do not arise in axisymmetric pendant drops and hence no gap may be expected in three dimensional drops on inclined surfaces.

Fig. 3.13 and 3.14 respectively show the solution space in the $V - \alpha$ plane for $\theta_e = 90°$ and $\theta_e = 150°$ obtained from the numerical simulations. The gaps where self-crossing shapes are the only possibility are again revealed.

Similar to Eq. 3.13, the expression for maximum volume for a three dimensional drop may be written down as

$$V_{max} = k\lambda \frac{\cos\theta_e \mp \cos\theta_{f/b}}{\sin\alpha}. \tag{3.14}$$

where $\theta_f = 180°$ for a front pinned drop and $\theta_b = 0°$ for rear pinned drop.

In brief, a solid-philic drop has maximum volume when it is front pinned and a solid-phobic drop has maximum volume when it is back pinned. Our observations tell us how to manipulate solid and fluid properties to support a large volume on a solid surface. For example, by making $\theta_a - \theta_e$ larger one may be able to pin the drop at the front more easily to hold a large volume without falling off. In contrast it may be desirable to keep $\theta_e - \theta_r$ large to hold a solid-phobic drop on an inclined plate.

Lastly ,we look at the phase plots of volume vs height. These plots generally contain some information about the stability of these drops. One may find phase plots for the shape in terms

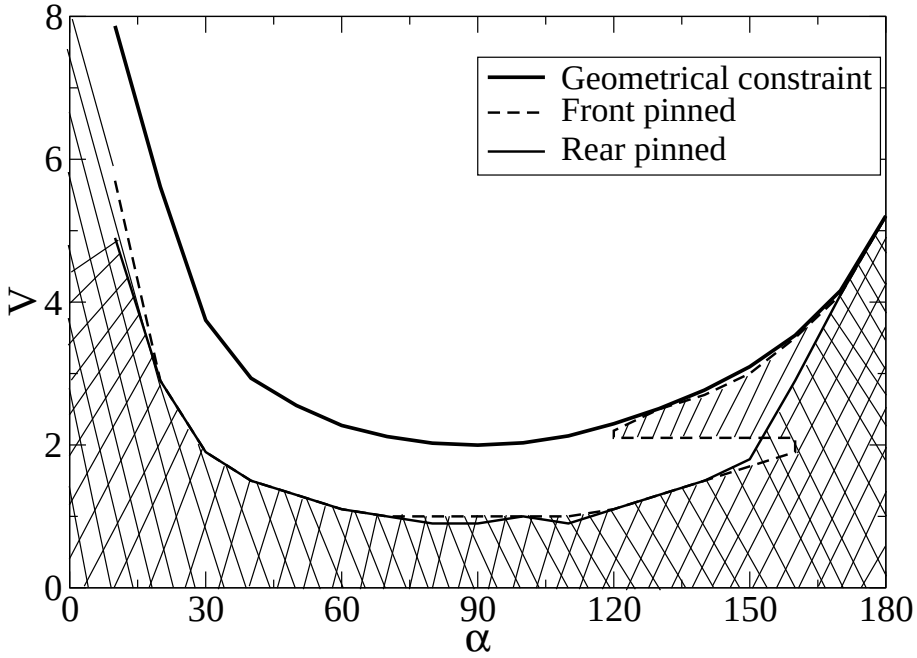

Figure 3.13: Solution space for $\theta_e = 90°$ plotted as volume vs plate inclination. Front pinned drops show a discontinuity in the solution space for a given inclination. The gap consists of unphysical, i.e. self-crossing, shapes.

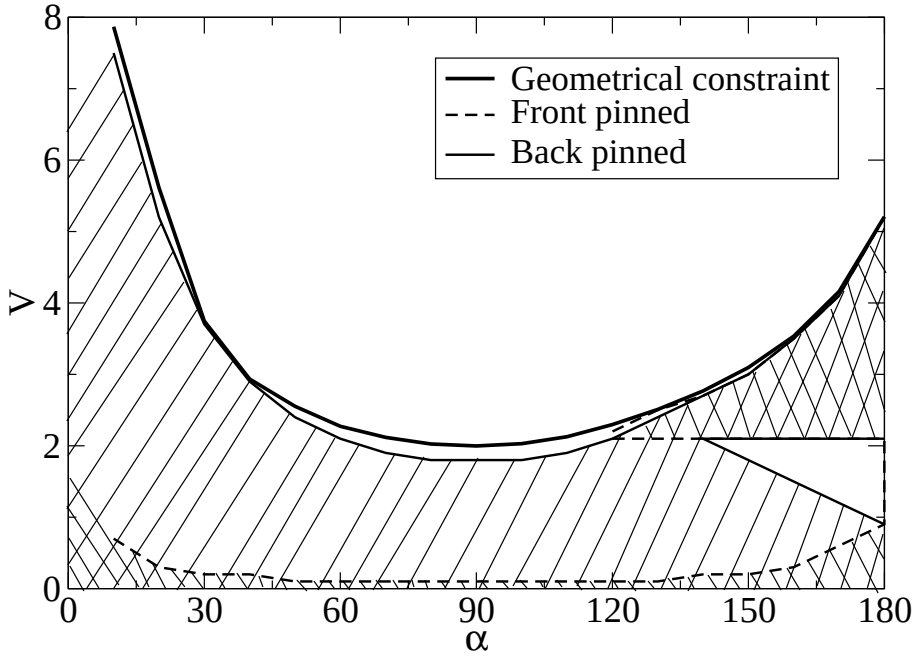

Figure 3.14: Solution space for $\theta_e = 150°$.

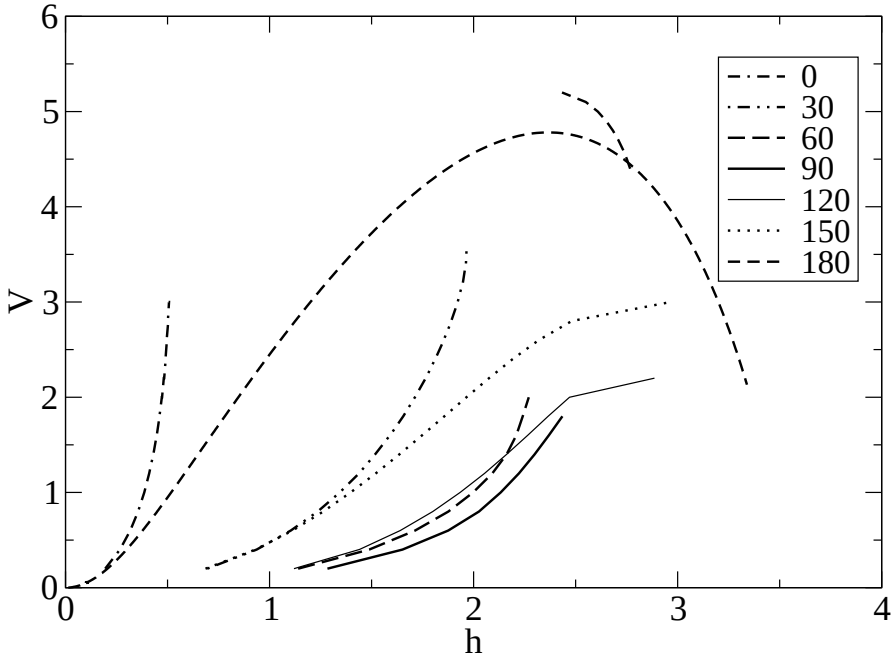

(a) for $\theta_e = 30°$

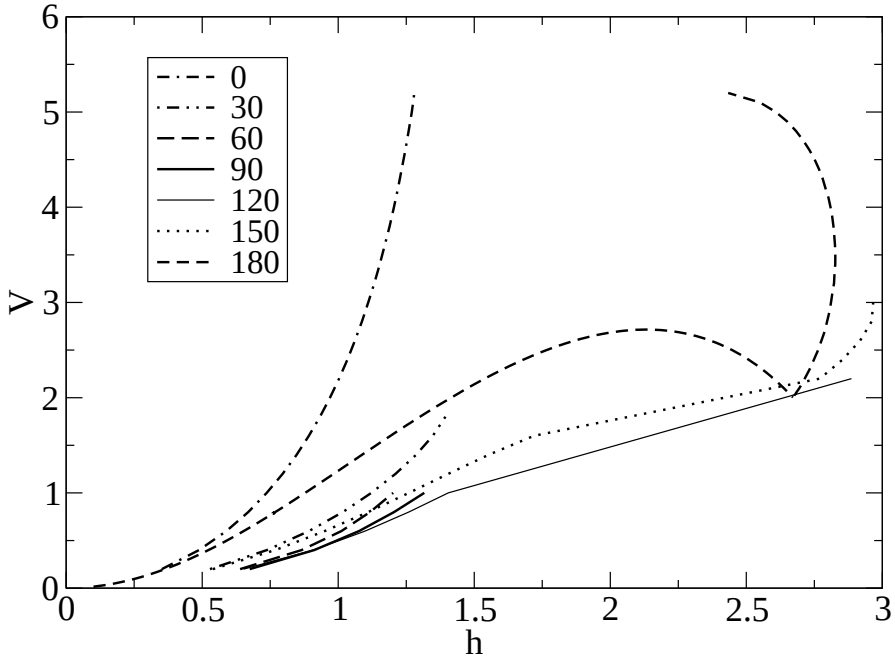

(b) for $\theta_e = 90°$

Figure 3.15: Volume vs height plots for various inclinations for an equilibrium contact angle of 30° and 90°.

of volume and height in the literature for sessile and pendant drops (Michael 1981). We tried to follow the same procedure for drops on inclined surfaces also. However, a clear definition of height for these drops could not be given unlike sessile and pendant drops. We defined the height of the drop to be the longest vertical line that can be drawn in the closed curve formed by the meniscus and the plate. The volume is plotted against this height in figures 3.15 for two different equilibrium contact angles and for a series of inclinations separately for advancing and receding sides pinned. Also plots of MCA curves are given for the completeness of the diagram. Curves for sessile and pendant drop may be found in literature; but the other curves are new.

It may also be seen that irrespective of the equilibrium contact angle, a given volume is tallest at a 90° inclination of the plate when volume is small (thick continuous line). As mentioned earlier, some of the larger volume solutions may belong to MCA class of solutions. Also, for pendant drops, part of the curve where volume reduces with height have been proved to be unstable (Pitts 1973) while our earlier numerical analysis restricted to Laplacian shapes (Chapter 2) disagree to it to some extent. Just as for sessile and pendant drops these curves may form the basis of stability analysis for drops on inclined surfaces, which is lacking at present.

3.6 Summary and Outlook

Static two-dimensional drops on inclined surfaces are studied using a one-dimensional energy minimization procedure, which determines the unique, global energy minimum shapes for a given volume and plate inclination. The contact line length and contact angles of this static drop shape emerge out of the solution procedure and are not fixed a priori unlike in earlier studies.

The solution depends on the basis chosen for potential energy. This is discussed, and pinning at the front end and the back end of the drop are chosen as two most realistic measures for freely sitting drops on inclined surfaces. The free end of the drop then attains Young's contact angle, while the angle at the pinned end adjusts itself to minimize the total energy. For any other choice of basis for potential energy calculation, both front and rear angles change simultaneously in equal magnitudes but in opposite sense. The angles subtended at the two ends for minimum energy are thus unrelated to the zero-velocity limit of the advancing and receding contact angles on a surface. The range of parameters over which solutions are possible are delineated.

A detailed force balance is carried out for the first time to our knowledge. It emerges that the reaction force of the solid surface can be of opposite signs over different portions of the contact area, the plate can thus aid and oppose gravity over different portions. This determines the maximum volume that the plate can support at a given inclination. It is seen that this maximum volume is the least when the plate is held vertical. Below a critical inclination α_{cr} for a given θ_e, the maximum volume varies symmetrically with respect to plate inclination about the vertical, and may be described by Eq. 3.13. Inclinations α larger than this angle, however can support only a smaller drop volume than inclinations of $180° - \alpha$.

This study may now be extended in several directions, the obvious one being to three dimensional non-axisymmetric drops. Many of these observations may be verified through experiments on a surface which permits large hysteresis. Another interesting experimental possibility is to obtain both the distributed load and the point forces on the surface, for example by using a

soft material with measurable deformation, and compare against the force balance study here. Apart from this, these minimum energy two dimensional shapes may be subjected to stability analyses. Though there exist a large literature on the stability of sessile and pendant drops, such studies on inclined drops are fewer.

Chapter 4

Lattice Boltzmann - Langevin simulations of binary mixtures

The material in this chapter is reproduced in *Phys. Rev. E*, 84, 046709 (2011).

4.1 Abstract

We report a hybrid numerical method for the solution of the model H fluctuating hydrodynamic equations for binary mixtures. The momentum conservation equations with Landau-Lifshitz stresses are solved using the fluctuating lattice Boltzmann equation while the order parameter conservation equation with Langevin fluxes are solved using the stochastic method of lines. Two methods, based on finite difference and finite volume, are proposed for spatial discretisation of the order parameter equation. Special care is taken to ensure that the fluctuation-dissipation theorem is maintained at the lattice level in both cases. The methods are benchmarked by comparing static and dynamic correlations and excellent agreement is found between analytical and numerical results. The Galilean invariance of the model is tested and found to be satisfactory. Thermally induced capillary fluctuations of the interface are captured accurately, indicating that the model can be used to study nonlinear fluctuations.

4.2 Introduction

Thermal fluctuations are an essential part of the physics at mesoscopic length scales in fluid mechanical problems. For instance, thermal fluctuations produce Brownian motion in colloidal suspensions, conformational fluctuations of polymers and membranes, capillary waves at fluctuating interfaces, and critical opalescence in binary mixtures. A consistent mesoscopic description of such phenomena follows from the equations of fluctuating hydrodynamics. The first instance of such a description was the fluctuating Navier-Stokes equations of Landau and Lifshitz (Landau & Lifshitz 1959). Similar equations were then introduced to study the dynamics of order parameter fluctuations in critical phenomena, as reviewed by Halperin and Hohenberg (Hohenberg & Halperin 1977). The coupled fluctuating equations of motion for the momentum and order parameter are known as model H in their classification.

The model H equations describe the fluctuating hydrodynamics of a conserved order parameter ψ and the conserved momentum density $\mathbf{g} = \rho\mathbf{u}$, where ρ and $\mathbf{u}$ are the total density and the local fluid velocity. To ensure conservation of local densities, fluctuations are incorporated as random stresses in the momentum equation (Landau & Lifshitz 1959) and as random fluxes in the order parameter equation (Zarate & Sengers 2006). At equilibrium, these random fluxes are

constrained by fluctuation-dissipation theorems, which relate their variances to the kinetic coefficients in the equations of motion. The fluctuation-dissipation theorem (FDT) ensures that the dynamical equations give rise to a Gibbs distribution for the fluctuating variables, as required by equilibrium statistical mechanics. Thus, together with the conservation laws, the FDT is an important constraint in the model H equations.

The model H consists of non-linear stochastic partial differential equations which admit no analytical solutions, requiring, therefore, numerical methods of solution. Numerical methods which proceed by discretising the equations of motion on a lattice must ensure, at least, that the conservation laws and the FDTs are obeyed. This requires care as naive discretisations often violate the FDT, leaving degrees of freedom incompletely equilibrated, and therefore, without a Gibbs distribution (Ladd 1994; Petschek & Metiu 1983; Rogers *et al.* 1988).

Here, we solve the model H equations by combining the fluctuating lattice Boltzmann equation (FLBE) (Adhikari *et al.* 2005; Dunweg *et al.* 2007) with a stochastic method of lines (SMOL) (Liskovets 1965; Bhattacharjee *et al.* 2008) using both finite difference and finite volume discretisations (Capuani *et al.* 2004). The formulation ensures conservation of local densities to machine precision, and a correct balance between fluctuation and dissipation for all the degrees of freedom on the lattice (Adhikari 1995). We expect our method to be widely applicable to problems in binary mixtures and other physical systems where model H is applicable, when thermal fluctuations form an essential part of the physics (Davidovitch *et al.* 2005; Willis & Freund 2009; Eggers 2002; Gonnella *et al.* 1999). Hybrid methods have been developed in the literature in different contexts, for example in case of dynamics of binary complex fluids (Xu *et al.* 2005; Orlandini *et al.* 2005), but without considering thermal fluctuations. We deal with fluctuating hydrodynamics of binary fluids in detail here. Alternative schemes based on finite volume methods have also been used to simulate the fluctuating hydrodynamics of single component fluids (Donev *et al.* 2010) and reaction-diffusion systems (Atzberger 2010). However, the methodology outlined here carries the advantages of the lattice Boltzmann method (Aidun & Clausen 2010) and can be generalized to other problems in fluctuating complex fluids, for instance, to the dynamics of microemulsions (Gompper *et al.* 1994) and liquid crystals.

The rest of the chapter is organized as follows. In the following section we provide a detailed description of model H. We review the current understanding of solving of these equations in section 4.4. In section 4.5 - 4.6 we present the numerical method followed by the validation results in section 4.7. We compare our method with previous approaches and end with a summary of our work in section 4.8.

4.3 Fluctuating hydrodynamics of a binary fluid mixture

We consider a coarse grained model for an isothermal binary fluid system, consisting of species I and II with local densities n_I and n_{II}. The mixture as a whole has density $\rho = n_I + n_{II}$. The order parameter ψ, which quantifies the local composition, is taken as the normalized density difference,

$$\psi = \frac{n_I - n_{II}}{n_I + n_{II}}. \tag{4.1}$$

4.3.1 Landau-Ginzburg theory

The equilibrium thermodynamics of the fluid is described by the Landau free-energy functional (Chaikin & Lubensky 1995; Rowlinson & Widom 1982)

$$F(\psi) = \int \left(f(\psi) + \frac{K}{2}\left|\nabla\psi\right|^2\right) d\mathbf{r}. \tag{4.2}$$

Here, ψ is allowed to vary beyond the limits of ± 1 that follow from its definition. This "softening" of the order parameter has no consequence in the thermodynamic limit (Wilson & Kogut 1974). The first term represents the local free energy density of the bulk fluid, and is approximated as

$$f(\psi) = \frac{A}{2}\psi^2 + \frac{B}{4}\psi^4 \tag{4.3}$$

with $A < 0$ and $B > 0$. The second term of Eq. 4.2 involving the square gradient gives a free energy cost to any variation in the order parameter, and is related to the interfacial tension between the two fluid phases (Kendon *et al.* 2001). Minimization of Eq. 4.3 with respect to the order parameter gives two uniform solutions $\psi = \pm\sqrt{A/B}$, corresponding to two equilibrium fluid phases. These two phases can coexist through a fluid interface. For a planar interface, the profile joining the two bulk phases reads

$$\psi(z) = \sqrt{\frac{A}{B}}\tanh\frac{z}{l} \tag{4.4}$$

where z is the co-ordinate normal to the interface while

$$l = \sqrt{\frac{2K}{A}}. \tag{4.5}$$

determines the interfacial thickness. The excess energy associated to this profile with respect to the bulk energy provides the interfacial tension

$$\gamma = \frac{2}{3}\sqrt{\frac{2KA^3}{B^2}} \tag{4.6}$$

The corresponding chemical potential is given by the variational derivative of the free energy with respect to the order parameter $\mu = \delta F/\delta\psi = A\psi + B\psi^3 - K\nabla^2\psi$. The three parameters A, B, and K control the interfacial thickness and interfacial energy of the mixture and after suitable non-dimensionalisations, allow for comparisons with real fluids. The additional stress due to the presence of order parameter gradients follows from the relation $\psi\nabla\mu = \nabla\cdot\boldsymbol{\sigma}^{\psi}$ (Anderson *et al.* 1998), which is solved by

$$\sigma^{\psi}_{\alpha\beta} = K\left(\nabla_\alpha\psi\right)\left(\nabla_\beta\psi\right) + \delta_{\alpha\beta}\left[\psi\frac{\partial f}{\partial\psi} - f - K\psi\nabla^2\psi - \frac{K}{2}\left|\nabla\psi\right|^2\right]. \tag{4.7}$$

This additional stress includes the Laplace and Marangoni stresses due to a fluid-fluid interface. The form of this stress tensor can be motivated on the basis of an electrostatic analogy or derived directly from Poisson brackets (Dzyaloshinskii & Volovick 1980).

4.3.2 Model H

Model H of Halperin and Hohenberg (Hohenberg & Halperin 1977) describes the coupled dynamics of a conserved scalar order parameter ψ and the conserved momentum density $\mathbf{g}$. The order parameter is described by a fluctuating Cahn-Hilliard equation, known as model B, which includes advection by fluid flow, relaxation due to chemical potential gradients, and spontaneous thermal fluctuations,

$$\partial_t \psi + \nabla\cdot(\mathbf{u}\psi) = \nabla\cdot(M\nabla\mu) + \nabla\cdot\hat{\boldsymbol{\xi}}. \tag{4.8}$$

The mobility M is the constant of proportionality in the linear phenomenological law relating the thermodynamic flux of ψ to the thermodynamic force $\nabla\mu$. We consider M to be a constant, though such an assumption is not necessary. Thermal fluctuations associated with ψ are introduced through the random flux $\hat{\boldsymbol{\xi}}$.

The order parameter dynamics is coupled to a fluctuating Navier-Stokes equation (Landau & Lifshitz 1959) with additional stress densities arising from the order parameter. For a compressible fluid, the dynamics is governed by

$$\partial_t \mathbf{g} + \nabla\cdot(\mathbf{ug}) = -\nabla p + \eta\nabla^2\mathbf{u} + \left[\frac{d-2}{d}\eta + \eta_b\right]\nabla(\nabla\cdot\mathbf{u}) + \psi\nabla\mu + \nabla\cdot\hat{\boldsymbol{\sigma}} \tag{4.9}$$

together with the continuity equation for the density. In the above, p stands for the isotropic contribution of the pressure, $\hat{\boldsymbol{\sigma}}$ is the random stress introduced by Landau and Lifshitz, $\psi\nabla\mu$ is the order parameter stress η and η_b are the shear and bulk viscosities respectively and d is the dimensionality of the system. Qualitatively, these equations describe the coupled dynamics of order parameter and flow : inhomogeneities in the order parameter generate chemical potential gradients, which in turn produce stresses in the fluid. These stresses are relaxed by fluid flow, which in turn advects the order parameter to produce inhomogeneities.

The random flux is a zero-mean Gaussian white noise whose variance is fixed by the FDT to be

$$\left\langle \hat{\xi}_\alpha(\mathbf{r},t)\hat{\xi}_\beta(\mathbf{r}',t')\right\rangle = 2kTM\delta_{\alpha\beta}\delta(\mathbf{r}-\mathbf{r}')\delta(t-t') \tag{4.10}$$

for an isothermal fluid at temperature T, where k stands for the Boltzmann constant. Similarly, the random stress is a zero-mean Gaussian white noise whose variance is fixed by the FDT to be

$$\left\langle \hat{\sigma}_{\alpha\beta}(\mathbf{r},t)\hat{\sigma}_{\gamma\delta}(\mathbf{r}',t')\right\rangle = 2kT\eta_{\alpha\beta\gamma\delta}\delta(\mathbf{r}-\mathbf{r}')\delta(t-t'). \tag{4.11}$$

where $\eta_{\alpha\beta\gamma\delta}$ is the tensor of viscosities formed out of the isotropic tensor $\delta_{\alpha\beta}$ and the shear viscosity, η, and bulk viscosity,η_b:

$$\eta_{\alpha\beta\gamma\delta} = \eta\left(\delta_{\alpha\gamma}\delta_{\beta\delta} + \delta_{\alpha\delta}\delta_{\beta\gamma}\right) + \left(\eta_b - \frac{2}{d}\eta\right)\delta_{\alpha\beta}\delta_{\gamma\delta} \tag{4.12}$$

For simplicity we assume the same viscosity for the two fluid phases.

In the next section we briefly review previous algorithms to numerically solve these coupled equations and point out why they lead to an incomplete equilibriation of both the order parameter and momentum degrees of freedom. This drawback imposes severe restrictions in the applicability of these algorithms to situations where a complete equilibriation is required, a gap

which our work attempts to fill.

4.4 Discretisation and FDT violation

There are ample instances in the literature where a naive discretisation of both the momentum (Ladd 1994) and order parameter (Petschek & Metiu 1983; Rogers *et al.* 1988; Ibanes *et al.* 2000) equations have led to FDT violations on the lattice. An important question, then, is how best FDTs, derived in the continuum with respect to appropriate conservation laws, can be implemented in discrete space and time. In this section, we present a very brief survey of previous numerical schemes, to clarify when naive discretisations lead to FDT violations.

In order to gain insight into the inconsistencies associated with the order parameter discretisation, let us consider a low-order discrete representations of the divergence of a vector $\hat{\boldsymbol{\xi}}$ and the Laplacian of a scalar ψ,

$$\left[\nabla\cdot\hat{\boldsymbol{\xi}}\right](\mathbf{r}) = \sum_i \omega_i \mathbf{c}_i\cdot\hat{\boldsymbol{\xi}}(\mathbf{r}+\mathbf{c}_i) \tag{4.13}$$

$$\left[\nabla^2\psi\right](\mathbf{r}) = \sum_i \widehat{\omega}_i\psi(\mathbf{r}+\mathbf{c}_i). \tag{4.14}$$

Here, ω_i and $\widehat{\omega}_i$ are weight factors which depend on the stencil, i refers to the number of neighboring grid points considered, $\{\mathbf{c}_i\}$ corresponds to a lattice vector and hence $\mathbf{r}+\mathbf{c}_i$ represents the points of the chosen stencil. In a Fourier representation, they become

$$\left[\nabla\cdot\hat{\boldsymbol{\xi}}\right](\mathbf{q}) = \sum_i \omega_i\mathbf{c}_i e^{i\mathbf{q}\cdot\mathbf{c}_i}\cdot\widetilde{\boldsymbol{\xi}}(\mathbf{q}) = \Gamma(\mathbf{q})\cdot\widetilde{\boldsymbol{\xi}}(\mathbf{q}) \tag{4.15}$$

$$\left[\nabla^2\psi\right](\mathbf{q}) = \sum_i \widehat{\omega}_i e^{i\mathbf{q}\cdot\mathbf{c}_i}\widetilde{\psi}(\mathbf{q}) = L(\mathbf{q})\widetilde{\boldsymbol{\psi}}(\mathbf{q}). \tag{4.16}$$

where $\Gamma(\mathbf{q})$ and $L(\mathbf{q})$ are the Fourier representations of the divergence and Laplacian operators, respectively. It is easy to see that $\Gamma(\mathbf{q})\to i\mathbf{q}$ and $L(\mathbf{q})\to -q^2$ as $\mathbf{q}\to 0$ for any admissible choice of stencil. In that limit, we recover the lattice analogue of the familiar relation between the gradient and Laplacian operators, so that $L(\mathbf{q}) = \Gamma(\mathbf{q})\cdot\Gamma(\mathbf{q})$. At high wavenumbers, however, this relation is no longer true. Indeed, it is violated by all standard node based nearest neighbour stencils (Abramowitz & Stegun 1965), unless a corresponding non-standard, non-negative definite Laplacian is chosen. Alternative formulations can be found in Donev *et al.* (2010).

To see how this affects discretisations of the fluctuating Cahn-Hilliard equation, we linearize Eq. 4.8 about a state of zero flow, for completely local and harmonic free energy ($B=0, K=0$ in Eq. 4.2), with a mobility that is independent of the order parameter. Discretising and Fourier transforming, we obtain

$$\partial_t\widetilde{\psi}(\mathbf{q}) = ML(\mathbf{q})A\widetilde{\psi}(\mathbf{q}) + \Gamma(\mathbf{q})\cdot\widetilde{\xi}(\mathbf{q}). \tag{4.17}$$

It is evident from Eq. 4.17 that fluctuations in the order parameter equation will satisfy the FDT of Eq. 4.10 on the lattice *if and only if* $L(\mathbf{q}) = \Gamma(\mathbf{q})\cdot\Gamma(\mathbf{q})$. Equivalently, the discrete operators should satisfy $\nabla^2 = \nabla.\nabla$ in real space. Since this is not true for the standard choices

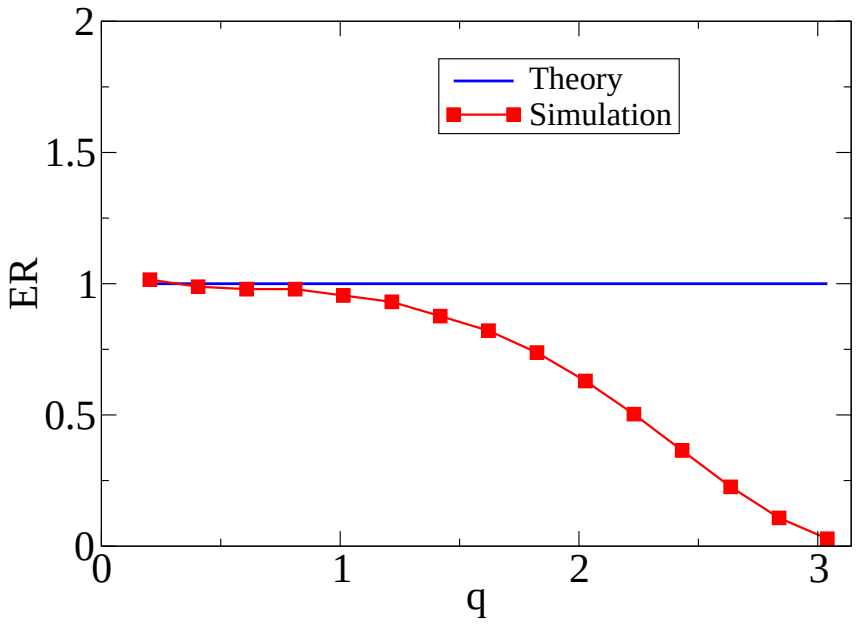

Figure 4.1: Equilibrium ratio (ER) according to Eq. 4.18 as a function of wave vector magnitude q along the diagonal $x = y = z$ from using a conventional method (Petschek & Metiu 1983) based on finite difference discretisation for both the divergence and Laplacian operators. Simulation results show significant differences with theoretical predictions at large wavenumbers.

of the previous operators (Abramowitz & Stegun 1965), resulting discretisations violate FDT.

To verify the above analysis, we perform simulations using the method proposed by Petschek & Metiu (1983) and used, for example, in Rogers *et al.* (1988) and Ibanes *et al.* (2000). Their method is essentially the one outlined above, with specific choices of the gradient and Laplacian. Simulations are carried out on a $32 \times 32 \times 32$ domain with a cubic grid and unit spacing, $\Delta x = 1$ and unit time step $\Delta t = 1$ using a stochastic Runge-Kutta algorithm (Wilkie 2004). We compare the theoretical value of the Fourier mode amplitudes of order parameter as given by the Gibbs distribution

$$\langle |\widetilde{\psi}(\mathbf{q})|^2 \rangle = \frac{kT}{A} \tag{4.18}$$

with our simulation data. We define the equilibrium ratio ER as the ratio of simulated values to the theoretical value. If all Fourier modes are in equilibrium, the ER will be unity as dictated by Eq. 4.18. The results obtained are displayed in Fig. 4.1. As can be seen, the difference from the expected theoretical value of ER = 1 is quite significant : the match is restricted to only small wave numbers and clearly shows the breakdown of FDT at high wavenumbers. Having identified the spatial discretisation as the main source of error in FDT violation on the lattice, we will analyze in the next section how to circumvent it for a scalar order parameter. Its generalization to vector and tensor order parameters is straightforward.

Fluctuations have also been included in lattice Boltzmann equation (LBE) to recover fluctuating Navier-Stokes equations. Ladd (1994) proposed a modification of the LBE with the addition of fluctuating stresses. A Langevin interpretation of the Boltzmann equation then yields the equations of fluctuating hydrodynamics (Landau & Lifshitz 1959). However, as was pointed out in Adhikari *et al.* (2005), Ladd's method ensures thermalisation only in the small wave number limit. This was resolved by relating thermal fluctuations to all sources of dissipa-

tion associated with the collision operator in the lattice Boltzmann equation, leading to thermal equilibrium for all modes, including the ghost modes (Succi 2001). This was confirmed subsequently in Dunweg *et al.* (2007). The fluctuating lattice Boltzmann equation (FLBE) (Adhikari *et al.* 2005; Dunweg *et al.* 2007) provides a consistent lattice discretisation for the Navier-Stokes equations and is the approach we shall use in this work.

The FLBE approach has recently been generalized to hydrodynamic fluctuations of non-ideal gases (Gross *et al.* 2010, 2011), but only a few studies have addressed thermal fluctuations in binary mixtures in the context of LBE. Noise driven spinodal decomposition was studied in Gonnella *et al.* (1999) by combining Ladd's fluctuating LBE with a fluctuating kinetic equation for the order parameter. However, this method does not respect FDT for either the momentum or the order parameter. Extending this to binary fluids maintaining FDT is considerably more difficult and so we prefer the alternative hybrid method described below.

4.5 Fluctuating Navier-Stokes solver

We use the FLBE method for solving the fluctuating Navier-Stokes equations. The FLBE introduced in Adhikari *et al.* (2005) needs to be modified to include force densities, which in the hybrid method, are the divergences of order parameter stresses. Since the combination of noise and external force densities (Nash *et al.* 2008) modifies the moment relations between the distribution functions and the hydrodynamic variables, we discuss now the main new features of FLBE.

In a standard $DdQn$ LBE model where the velocity space is discretized into n components in d dimensional space, the discrete form of the fluctuating Boltzmann equation reads (Gross *et al.* 2011)

$$\partial_t f_i + \mathbf{c}_i \cdot \nabla f_i + [\mathbf{F} \cdot \nabla_{\mathbf{c}} f]_i = -\sum_j L_{ij}(f_j - f_j^0) + \zeta_i \tag{4.19}$$

where $\mathbf{F}(\mathbf{x}, t)$ is an effective force density, $\zeta_i(\mathbf{x}, t)$ stands for the fluctuations in the populations, and L_{ij} is the discrete form of the collision integral and is related to the fluid viscosity. The moments of the single particle distribution function f_i, defined at lattice node $\mathbf{x}$ with velocity $\mathbf{c}_i$ at time t, give the fluid mass, momentum and stress densities:

$$\rho = \sum_{i=0}^{n} f_i, \quad \rho\mathbf{v} = \sum_{i=0}^{n} f_i \mathbf{c}_i, \quad S_{\alpha\beta} = \sum_{i=0}^{n} f_i Q_{i\alpha\beta} \tag{4.20}$$

where $Q_{i\alpha\beta} = c_{i\alpha}c_{i\beta} - c_s^2\delta_{\alpha\beta}$. The collision operator L_{ij} controls the relaxation of f_j to equilibrium, f_j^0.

A multi-scale expansion, or a moment closure method, shows that the above equation has Eq. 4.9 as its hydrodynamic limit (Succi 2001). Since FLBE is a hyperbolic equation with local non-linearities, it is considerably easier to solve than Eq. 4.9, which has a parabolic-hyperbolic character with advective non-linearities. The methodology of the FLBE has been explained in detail in Dunweg *et al.* (2007), while the method by which force densities are added is given in detail in Nash *et al.* (2008). Here we outline the integration scheme we use when force densities and fluctuating forces are combined in the FLBE.

We can rearrange equation, Eq. 4.19 to obtain

$$\partial_t f_i + \mathbf{c}_i.\nabla f_i = R_i(\mathbf{x},t) \tag{4.21}$$

where $R_i(\mathbf{x},t) = -\sum_j L_{ij}(f_j - f_j^0) + \Phi_i$ represents the effects of collision, forcing and thermal fluctuations. $\Phi_i \equiv \zeta_i - \mathbf{F}\cdot\nabla_c f$ accounts for the fluctuating and external forces acting on the distribution function. We can take advantage of the hyperbolic character of the FLBE and use the method of characteristics to evolve Eq. 4.19 over a finite time step. Therefore over a time interval Δt

$$f_i(\mathbf{x}+\mathbf{c}_i\Delta t, t+\Delta t) - f_i(\mathbf{x},t) = \int_0^{\Delta t} ds R_i(\mathbf{x}+\mathbf{c}_i s, t+s) \tag{4.22}$$

The integral above may be approximated to second order accuracy using the trapezium rule and the resulting terms transposed to give a set of implicit equations for the f_i :

$$f_i(\mathbf{x}+\mathbf{c}_i\Delta t, t+\Delta t) - \frac{\Delta t}{2}R_i(\mathbf{x}+\mathbf{c}_i\Delta t, t+\Delta t) = f_i(\mathbf{x},t) - \frac{\Delta t}{2}R_i(\mathbf{x},t) + \Delta t R_i(\mathbf{x},t). \tag{4.23}$$

When accounting for the effect of forces and fluctuations in the evolution of f_i, it is convenient to introduce the auxiliary distribution function

$$\bar{f}_i(\mathbf{x},t) = f_i(\mathbf{x},t) - \frac{\Delta t}{2}R_i(\mathbf{x},t) \tag{4.24}$$

in terms of $R_i(\mathbf{x},t) = -\sum_j L_{ij}(f_j - f_j^0) + \Phi_i$, which represents the effects of collision, forcing and thermal fluctuations. For a single-time relaxation operator, $L_{ij} = \delta_{ij}/\tau$, the hydrodynamic variables are related to the auxiliary distributions as

$$\rho = \sum_{i=0}^{n} \bar{f}_i \tag{4.25}$$

$$\rho v_\alpha = \sum_{i=0}^{n} \bar{f}_i c_{i\alpha} + \rho F_\alpha \frac{\Delta t}{2} \tag{4.26}$$

$$S_{\alpha\beta} = \sum_{i=0}^{n} \bar{f}_i Q_{i\alpha\beta} + \frac{\Delta t/2}{\tau + \Delta t/2}\left(-\sum_{i=0}^{n} \bar{f}_i Q_{i\alpha\beta} + \rho v_\alpha v_\beta + \tau(v_\alpha F_\beta + F_\alpha v_\beta) + \tau\sum_{i=0}^{n}\zeta_i Q_{i\alpha\beta}\right). \tag{4.27}$$

where the equilibrium distribution, f_i^0, can be reconstructed from ρ and $\rho\mathbf{v}$. In Eq. (4.27) $\sum_{i=0}^{n}\zeta_i Q_{i\alpha\beta}$ is the fluctuating contribution to the stress.

In terms of the auxiliary distribution function, Eq. 4.24, the evolution equation reduces to

$$\bar{f}_i(\mathbf{x}+\mathbf{c}_i\Delta t, t+\Delta t) = \bar{f}_i(\mathbf{x},t) + R_i(\mathbf{x},t)\Delta t. \tag{4.28}$$

indicating that we can understand LBE evolution through a simple relaxational step in which the distributions $\bar{f}_i$ are relaxed to their postcollisional values $\bar{f}_i(\mathbf{x},t^*)$,

$$\bar{f}_i(\mathbf{x},t^*) = \bar{f}_i(\mathbf{x},t) + R_i(\mathbf{x},t)\Delta t, \tag{4.29}$$

followed by a propagation step in which the postcollisional distributions are propagated along a Lagrangian trajectory without further change,

$$\bar{f}_i(\mathbf{x} + \mathbf{c}_i\Delta t, t + \Delta t) = \bar{f}_i(\mathbf{x}, t^*). \tag{4.30}$$

Thus the computational part of the method is most naturally framed in terms of the auxiliary distributions $\bar{f}_i$ instead of the physical distribution functions f_i themselves. To obtain the postcollisional $\bar{f}_i$ without having to refer to the f_i, the latter must be eliminated from Eq. 4.28. Inverting the equations defining the $\bar{f}_i$ in Eq. 4.24, we obtain

$$R_i = \left(1 + \frac{\Delta t}{2}L\right)^{-1}_{ij} [-L_{jk}(\bar{f}_k - f^0_k) + \Phi_j(\mathbf{x}, t)]. \tag{4.31}$$

Combining this with Eq. 4.28 we obtain a numerical scheme for the discrete Boltzmann equation with a general collision operator in terms of the $\bar{f}_i$:

$$\bar{f}_i(\mathbf{x} + \mathbf{c}_i\Delta t, t + \Delta t) = \bar{f}_i(\mathbf{x}, t) + \left(1 + \frac{\Delta t}{2}L\right)^{-1}_{ij} [-L_{jk}(\bar{f}_k - f^0_k) + \Phi_j(\mathbf{x}, t)]\Delta t. \tag{4.32}$$

For a single time relaxation operator, where $L_{ij} = \delta_{ij}/\tau$, this takes on a particularly simple form,

$$\bar{f}_i(\mathbf{x} + \mathbf{c}_i\Delta t, t + \Delta t) = \bar{f}_i(\mathbf{x}, t) + \frac{\Delta t}{\tau + \Delta t/2}[-(\bar{f}_i - \bar{f}^0_i) + \tau\Phi_i(\mathbf{x}, t)], \tag{4.33}$$

For a nondiagonal collision operator, the collision term is best evaluated in the moment basis. For example, using a collision operator in which the ghost modes are projected out (Succi 2001) and the stress modes relax at a rate of τ^{-1}, the post collisional $\bar{f}_i$ are given by

$$\bar{f}_i(\mathbf{x}, t^*) = w_i\left(\rho + \frac{A_\alpha c_{i\alpha}}{c_s^2} + \frac{B_{\alpha\beta}Q_{i\alpha\beta}}{2c_s^4}\right) \tag{4.34}$$

where the normalized weights w_i ensure the isotropy, and A_α, the momentum component of the postcollisional auxiliary distributions, is

$$A_\alpha = \sum_{i=0}^{n} \bar{f}_i c_{i\alpha} + \rho F_\alpha \Delta t \tag{4.35}$$

while $B_{\alpha\beta}$, the stress component, reads

$$B_{\alpha\beta} = \sum_{i=0}^{n} \bar{f}_i Q_{i\alpha\beta} + \frac{\Delta t}{\tau + \Delta t/2}\left(-\sum_{i=0}^{n} \bar{f}_i Q_{i\alpha\beta} + \rho v_\alpha v_\beta + \tau(v_\alpha F_\beta + F_\alpha v_\beta) + \tau\sum_{i=0}^{n} \zeta_i Q_{i\alpha\beta}\right). \tag{4.36}$$

The mass and momentum densities are obtained as $\rho = \sum_{i=0}^{n} \bar{f}_i$ and $\rho v_\alpha = \sum_{i=0}^{n} \bar{f}_i c_{i\alpha} + \rho F_\alpha \frac{\Delta t}{2}$, respectively. The equilibria can be reconstructed from ρ and $\rho\mathbf{v}$.

The effective force density is the divergence of the order parameter stress

$$\mathbf{F} = \nabla \cdot \boldsymbol{\sigma}^\psi = \psi\nabla\mu \tag{4.37}$$

which can be verified using Eq. 4.7. To compute this force density we use a symmetrized, second order accurate nearest-neighbor central difference stencil for the gradient

$$\nabla\mu(x,y,z) = \frac{1}{2}\left[\mu(x+1,y,z) - \mu(x-1,y,z)\right]\hat{x} + \frac{1}{2}\left[\mu(x,y+1,z) - \mu(x,y-1,z)\right]\hat{y} + \frac{1}{2}\left[\mu(x,y,z+1) - \mu(x,y,z-1)\right]\hat{z} \tag{4.38}$$

and Shinozaki & Oono (1993) discretisation of the Laplacian (Eq. A.3) to calculate $\nabla^2\psi$ in the chemical potential.

4.6 Fluctuating Cahn-Hilliard solver

We use a stochastic method of lines (SMOL) discretisation (Bhattacharjee *et al.* 2008) to solve the fluctuating Cahn-Hilliard equation for the order parameter. Since it does not contain a pressure term which acts as a Lagrange multiplier in the incompressible Navier-Stokes equations, there is no particular benefit in using a kinetic algorithm with its large number of degrees of freedom in solving for a single scalar variable. Here, we adopt a semi-discretisation strategy (Liskovets 1965; Bhattacharjee *et al.* 2008), discretising the spatial variables to obtain a set of coupled stochastic ordinary differential equations. The spatial discretisations we propose ensure that the conservation law is respected to machine precision and that the fluctuation and dissipation are in balance for all wave vectors. We propose a finite-difference and finite-volume discretisations, discussing their relative merits below. The temporal integration of the resulting stochastic differential equations is done using a Runge-Kutta algorithm proposed recently by Wilkie (2004). This is a straightforward generalization of the deterministic Runge-Kutta algorithm where the noise is held constant through the integration step. The methodology may be improved using implicit schemes to increase the accuracy.

4.6.1 Finite difference method

To proceed towards a discretisation of the fluctuating Cahn-Hilliard equation which preserves FDT, we write the order parameter evolution equation in Fourier space

$$\partial_t\widetilde{\psi}(\mathbf{q}) = ML(\mathbf{q})\widetilde{\mu}(\mathbf{q}) + \Gamma(\mathbf{q})\cdot\widetilde{\xi}(\mathbf{q}) \tag{4.39}$$

assuming a constant mobility. Defining the divergence of the noise in Fourier space as $\widetilde{\eta}(\mathbf{q}) = \Gamma(\mathbf{q})\cdot\widetilde{\xi}(\mathbf{q})$, we see that it must satisfy

$$\left\langle\hat{\eta}(\mathbf{q},t)\hat{\eta}(\mathbf{q}',t')\right\rangle = -2kTML(\mathbf{q})\delta(\mathbf{q}+\mathbf{q}')\delta(t-t'). \tag{4.40}$$

Instead of constructing a divergence operator $\Gamma(\mathbf{q})$ which satisfies $\Gamma(\mathbf{q})\cdot\Gamma(\mathbf{q}) = L(\mathbf{q})$ we directly use the above relationship to construct the noise in Fourier space. This is then inverse-transformed to real space to provide a noise which has correlations compatible with the discretisation of the Laplacian and the same Laplacian stencil is used to calculate $\nabla^2\mu$ and $\nabla^2\psi$. The generation of noise in Fourier space has been used earlier in spectral methods (Atzberger *et al.*

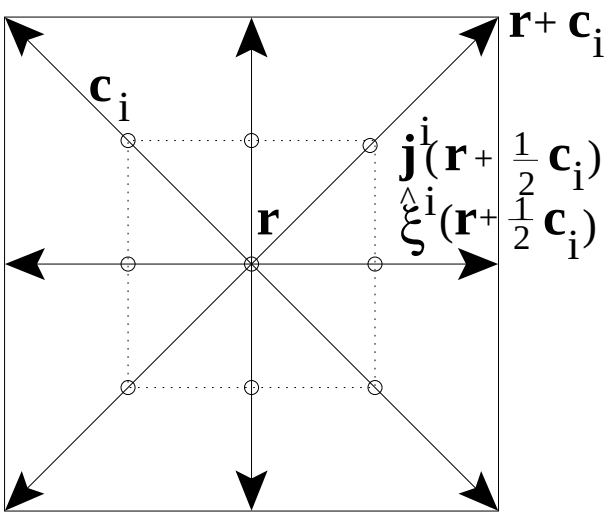

Figure 4.2: Illustration of the stencil used for the numerical tests in the finite volume method for a two dimensional case. This stencil corresponds to the D2Q9 lattice Boltzmann model. Physical quantities ,e.g. $\psi, \mu, \nabla\mu$, and $\mathbf{u}$, are defined at node $\mathbf{r}$ which has its neighbors at $\mathbf{r}+\mathbf{c}_i$. All fluxes $\mathbf{j^i}, \boldsymbol{\xi}^i$ (diffusive, convective and random) are defined at the mid point of the links $(\mathbf{r}+\frac{1}{2}\mathbf{c}_i)$ connecting $\mathbf{r}$ and $\mathbf{r}+\mathbf{c}_i$. (See Eq. 4.42 - 4.45)

2007) to respect FDT in discrete space.

It is important to ensure as isotropic a discretisation of the Laplacian as possible, to avoid artifacts like spurious pinning of interfaces by the lattice. We have compared in Appendix A four standard finite-difference stencils reported in the literature, see Fig. A.2 in Appendix A where expressions for their Fourier transforms $L(\mathbf{q})$ are also provided. The Laplacian of Shinozaki & Oono (1993) is the most isotropic one and we use it for our discretisation. The advective flux, $\nabla\cdot(\mathbf{u}\psi)$, is discretized using a second order accurate, conservative, central difference scheme

$$[\nabla\cdot(\mathbf{u}\psi)](x,y,z) = \frac{1}{2}\left\{[u_x\psi](x+1,y,z) - [u_x\psi](x-1,y,z)\right\} + \frac{1}{2}\left\{[u_y\psi](x,y+1,z) - [u_y\psi](x,y-1,z)\right\} + \frac{1}{2}\left\{[u_z\psi](x,y,z+1) - [u_z\psi](x,y,z-1)\right\}. \tag{4.41}$$

4.6.2 Finite volume method

It is possible to formulate an alternative discretisation for the fluctuating Cahn-Hilliard equation, based on a finite-volume formulation. Such an approach, using fluxes defined on lattice links, has been proposed to study the electrokinetic equations in the absence of fluctuations in Rotenberg *et al.* (2008, 2010). Alternative finite volume schemes may also be found in the context of reaction-diffusion systems (Atzberger 2010). Specifically, we choose a *DdQn* cubic lattice and a set of link vectors $\{\mathbf{c}_i\}$ as done usually with lattice Boltzmann models. Thus, for any node $\mathbf{r}$, the set of points $\mathbf{r}+\mathbf{c}_i$ are also lattice nodes. The divergence at a node $\mathbf{r}$ is then written as a sum of fluxes $\mathbf{j}^i$ defined on the midpoint $\mathbf{r}+\frac{1}{2}\mathbf{c}_i$ of the link connecting the node to its neighbour $\mathbf{r}+\mathbf{c}_i$. This is schematically represented in Fig. 4.2 for *D2Q9*. Then, Eq. 4.8 can be discretised as

$$\partial_t\psi = \sum_i w_i\mathbf{c}_i\cdot\mathbf{j}^i + \sum_i w_i\mathbf{c}_i\cdot\hat{\boldsymbol{\xi}}^i \tag{4.42}$$

where w_i are a normalised set of weights that ensure isotropy and $\mathbf{j}^i$ and $\hat{\boldsymbol{\xi}}^i$ are the deterministic and random contributions to the order parameter flux, respectively. This ensures the conservation of the order parameter to machine accuracy.

The choice of expressions which relate the fluxes to the densities at the nodes must now be dictated by the requirement that the FDT holds for all wavevectors. We use a symmetric average of node values to compute the mid-point fluxes (Capuani *et al.* 2004),

$$\mathbf{j}^i = M\frac{1}{2}\left[\nabla\mu(\mathbf{r}) + \nabla\mu(\mathbf{r}+\mathbf{c}_i)\right] - \frac{1}{2}\left[(\mathbf{u}\psi)(\mathbf{r}) + (\mathbf{u}\psi)(\mathbf{r}+\mathbf{c}_i)\right] \tag{4.43}$$

$$\hat{\boldsymbol{\xi}}^i = \frac{1}{2}\left[\hat{\boldsymbol{\xi}}(\mathbf{r}) + \hat{\boldsymbol{\xi}}(\mathbf{r}+\mathbf{c}_i)\right]. \tag{4.44}$$

Here, $c_s^2\delta_{\alpha\beta} = \sum_i c_{i\alpha}c_{i\beta}$. To be consistent with this choice, the gradient of the chemical potential must be computed using

$$\nabla\mu(\mathbf{r}) = \frac{1}{c_s^2}\sum_i w_i\mathbf{c}_i\mu(\mathbf{r}+\mathbf{c}_i). \tag{4.45}$$

It is only with the combined choice of the divergence, symmetric averaging, and the gradient that the fluctuating Cahn-Hilliard equation takes the form

$$\partial_t\psi(\mathbf{q}) + \boldsymbol{\Gamma}(\mathbf{q})\cdot(\mathbf{u}\psi)(\mathbf{q}) = \boldsymbol{\Gamma}(\mathbf{q})\cdot[M\boldsymbol{\Gamma}(\mathbf{q})\mu(\mathbf{q})) + \boldsymbol{\xi}(\mathbf{q})] \tag{4.46}$$

where $\boldsymbol{\Gamma}(\mathbf{q}) \equiv \sum_i w_i\mathbf{c}_i\exp(i\mathbf{q}\cdot\mathbf{c}_i)$ is the representation of the ∇ operator on the lattice. Our choice of discretisation ensures that the same operator $\boldsymbol{\Gamma}(\mathbf{q})$ appears in both the gradient and the divergence in the diffusive term in the Cahn-Hilliard equation. As a result, $\nabla\cdot\nabla = \nabla^2$ is preserved at all wavevectors, and not only when $\mathbf{q}\to 0$ as happens with standard discretisations. The resulting Laplacian $[L(\mathbf{q})]_{FV} = \boldsymbol{\Gamma}(\mathbf{q})\cdot\boldsymbol{\Gamma}(\mathbf{q})$ is less isotropic than the Shinozaki-Oono Laplacian as shown in Fig. A.2e in Appendix A. Therefore, we use the Shinozaki-Oono Laplacian to calculate $\nabla^2\psi$ in the chemical potential.

Compared to the finite-difference method of the previous section, the finite-volume method is not restricted to periodic geometries, and thus allows for simulations with wall or shear boundary conditions, though a careful implementation is necessary in these cases. The computational overhead is significantly reduced since the expensive Fourier construction of the noise is no longer required.

4.7 Results and Validation

The order parameter induces a force on the fluid, accelerating it while the fluid, in turn, advects the order parameter. Although this requires, in principle, an algorithm which updates self-consistently both fields, we have to do it sequentially at every time step due to the coupling of two different methods, resulting in a hybrid scheme for the model H equations. However, we have not found any event where the proposed algorithm of alternate marching in time of FLBE and SMOL leads to spurious cross correlations between momentum and order parameter fluctuations.

A number of tests have been carried out to validate the algorithm including static and dynamic correlations for the order parameter and standard tests for hydrodynamics. We have

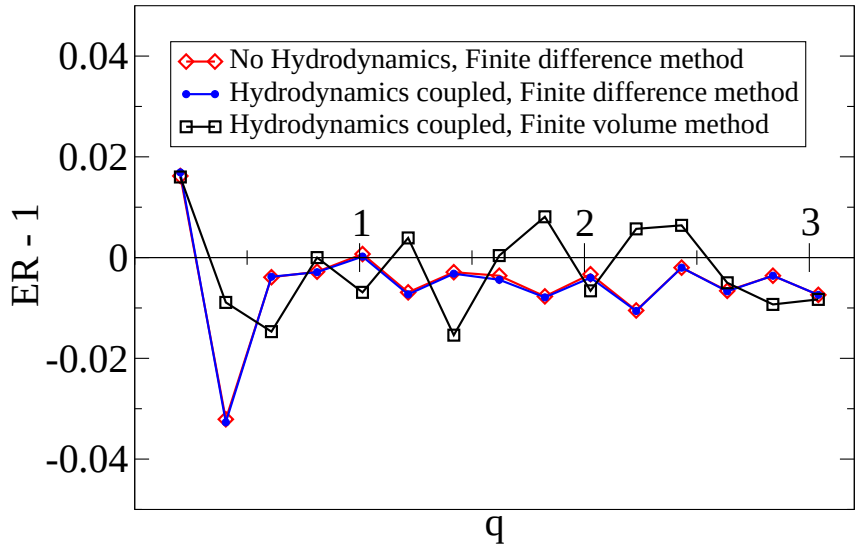

Figure 4.3: Error in the equilibrium ratio as a function of wave vector magnitude, q, along the diagonal $x = y = z$ considering (1) diffusion alone and (2) coupled hydrodynamics with (i) finite difference and (ii) finite volume method for the quadratic free energy functional (see Eq. 4.18). Simulations have been done on a $32 \times 32 \times 32$ lattice with equilibrium initial conditions and parameters used are $A = 0.625$, $B = 0$, $K = 0.0$ and $M = 0.095$. Ensemble averaging is done over 10^4 time steps and over 25 realizations.

always used a D3Q15 model for FLBE with lattice units $\Delta x = \Delta t = 1$ which leads to a speed of sound $c_s = \sqrt{1/3}$. To ensure that compressibility is negligible, we work in parameter regimes where the Mach number is small, $Ma = u/c_s \ll 1$. Except when otherwise stated, all simulations have been performed on a $32 \times 32 \times 32$ lattice which is initialized with a uniform random distribution, and statistics are collected once the system has equilibrated. The relaxation parameter, $\tau = 1.1$ and the temperature $kT = 1/3000$ are used (Adhikari *et al.* 2005) in FLBE unless otherwise specified. Note that this temperature is chosen to stick to low Mach number limit in the lattice Boltzmann algorithm and will produce a net variance in thermal momentum of $\Delta V \rho kT$ (Landau & Lifshitz 1959) in a volume ΔV in a quiescent fluid. Periodic boundary conditions are used in all directions in all the simulations.

4.7.1 Order parameter fluctuations

We analyze initially a miscible mixture without surface tension, characterized by $B = K = 0$. Since in this case the free energy functional, Eq. 4.2 , is parabolic, the equilibrium order parameter distribution follows the Gibbs distribution with Gaussian order parameter fluctuations of amplitude given in Eq. 4.18.

Fig. 4.3 displays the error in the equilibrium ratio (ER) between the measured static correlation functions of the order parameter and the theoretical prediction, Eq. 4.18 independent of the wave vector magnitude, as a function of the magnitude of the wave vector, for $q_x = q_y = q_z$, both without and with hydrodynamic coupling. In the latter situation we have also compared the performance of the finite difference method (section 4.6.1) and the finite volume method (section 4.6.2). In all cases we obtain an excellent agreement for the entire wave vector spectrum, as opposed to the spurious deviations observed in Fig. 4.1 for a standard discretisation of

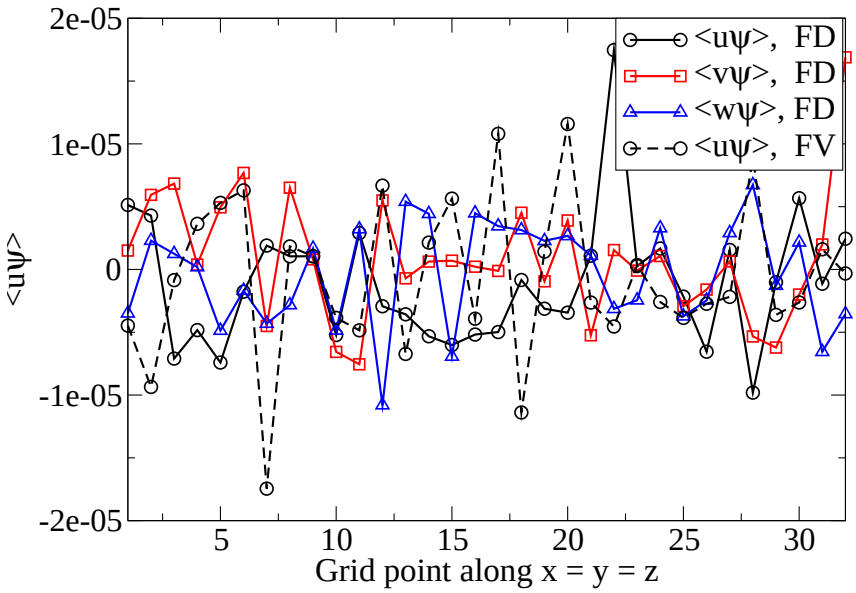

Figure 4.4: Velocity-order parameter correlation for all three components of the velocity in Cartesian coordinates along the diagonal $x = y = z$ of the domain considering coupled hydrodynamics and using the finite difference scheme for the quadratic free energy functional (see Eq. 4.18) and for the same set of parameters as in Fig. 4.3. Ensemble averaging is done over 10^4 time steps and over 25 realizations. No cross correlations are present between fields of different tensorial nature. The results obtained using finite volume method are shown only for one velocity component for clarity.

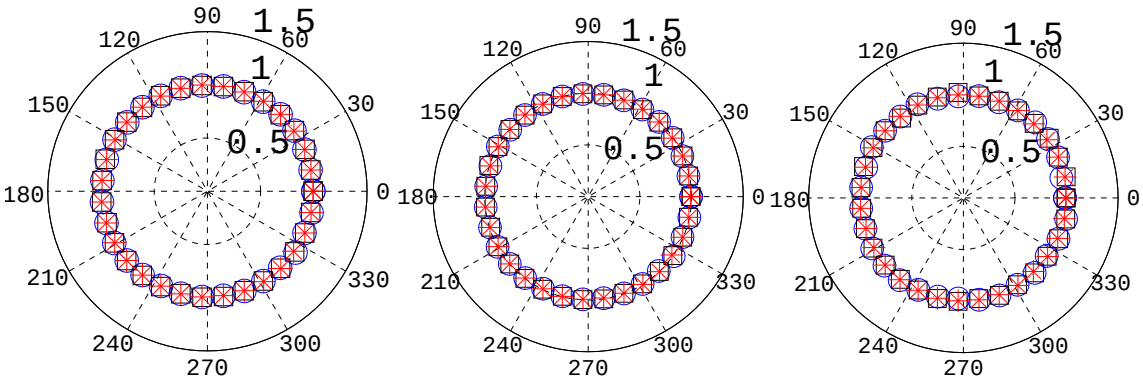

(a) (b) (c)

Figure 4.5: Polar plots where the radius indicates the ER as a function of azimuthal angle on lattice points of a fixed modulus (16 lattice units from the center), i.e. along a $(\cos\theta, \sin\theta, z =$ constant) for (a) diffusion alone, finite difference method and (b) hydrodynamics coupled with finite difference method, (c) hydrodynamics coupled with finite volume method. Three different symbols o, □, $*$ correspond to $z = N/8, 2N/8$ and $3N/8$ planes respectively. Data obtained from the same simulations used in Fig. 4.3.

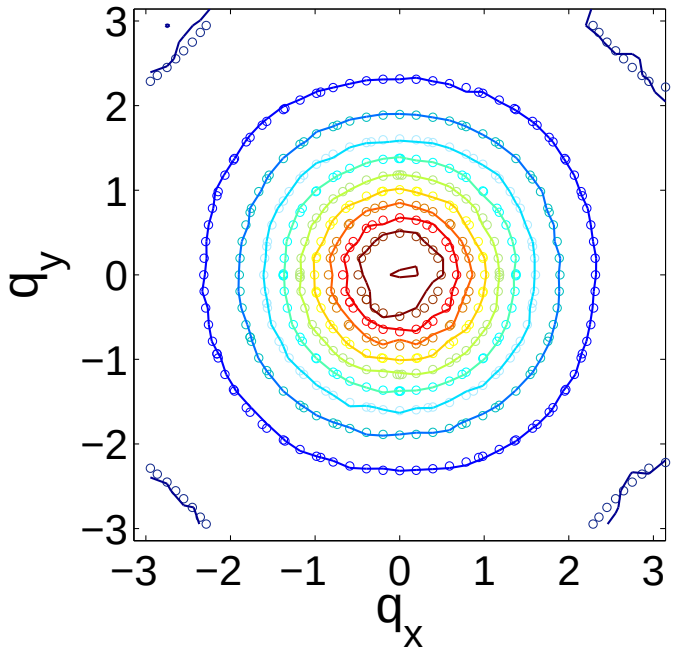

Figure 4.6: Constant $\langle|\widetilde{\psi}(q)|^2\rangle$ values obtained at equilibrium, from a simulation considering diffusion alone (without any coupling to hydrodynamics) for the free energy functional described by Eq. 4.2 with $B = 0$. Simulations obtained using the finite difference method. Results are shown in a wave number plane of (q_x, q_y). Analytical expression from Eq. 4.47 are superposed onto it using symbols for comparison. Simulations are performed on a $32 \times 32 \times 32$ lattice with equilibrium initial conditions, $A = 0.025$, $K = 0.01$ and $M = 0.1$. Ensemble averaging is done over 10^5 time steps and over 25 realizations.

Eq. 4.8. In Fig. 4.4 the velocity-order parameter correlations are plotted using both the finite difference and finite volume method to show that no spurious scalar-tensor correlations develop in the proposed numerical scheme.

In order to check the homogeneity and isotropy of the fluctuations, polar plots are shown in Fig. 4.5. In these plots, the radius represents the ER as a function of the azimuthal angle in a given z plane in lattice space. Different symbols correspond to three different z planes. ER remains essentially unity in all cases, indicating that FDT is satisfied in all directions in the lattice.

The equilibrium structure factor of a miscible binary mixture, $B = 0$, (above the critical temperature) which experiences an energy cost to order parameter gradients is

$$\langle|\widetilde{\psi}(\mathbf{q})|^2\rangle = \frac{kT}{A + K\mathbf{q}^2}. \tag{4.47}$$

On a lattice, the discrete representation of the Laplacian must be accounted for, and the static spectrum reads accordingly, $\langle|\widetilde{\psi}(\mathbf{q})|^2\rangle = kT/(A - KL(q))$.

Since we have used the Shinozaki - Oono form for the Laplacian, Eq. A.3, to calculate $\nabla^2\psi$ in our simulations, $-\mathbf{q}^2$ of Eq. 4.47 is replaced by the Fourier transform of appropriate Laplacian $L(\mathbf{q})$, i.e, Eq. A.8.

Fig. 4.6 displays the simulated $\langle|\widetilde{\psi}(\mathbf{q})|^2\rangle$ at equilibrium on a wavenumber plane of constant

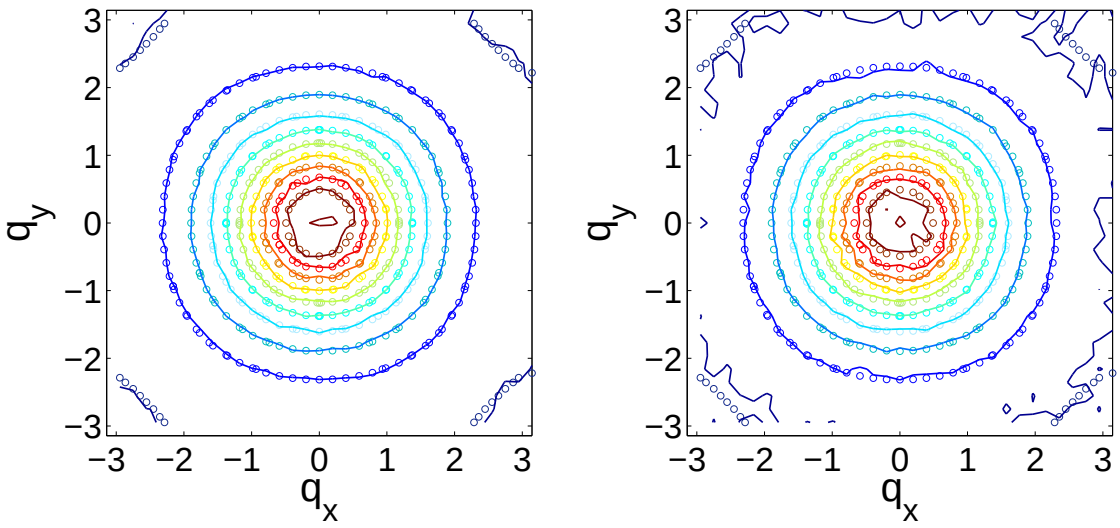

(a) (b)

Figure 4.7: Constant values of $\langle|\widetilde{\psi}(q)|^2\rangle$ from the simulations when the dynamics of the order parameter is coupled to the fluid dynamics for the same parameters and lattice size used in Fig. 4.6. Results for both the finite difference method (a) and the finite volume method (b) are shown at a constant q_z plane and expected values from Eq. 4.47 are superposed as symbols.

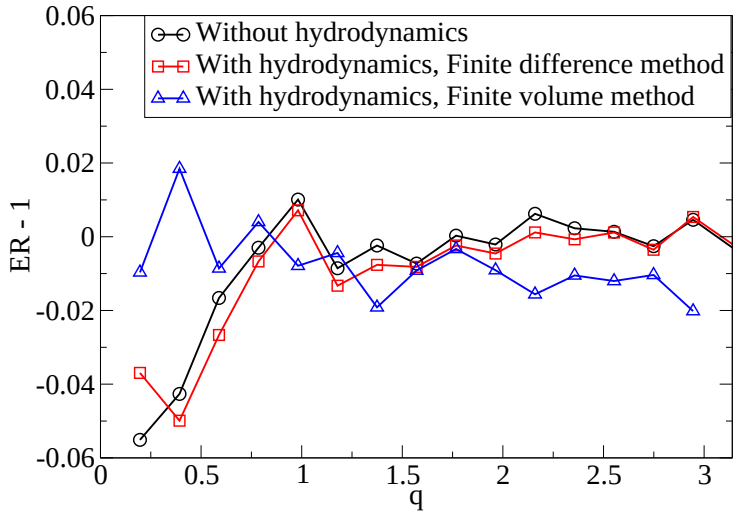

Figure 4.8: Error in the equilibrium ratio as a function of wave vector magnitude, q, along the diagonal $q_x = q_y = q_z$ considering (1) diffusion alone and (2) coupled hydrodynamics with (i) finite difference and (ii) finite volume method for the free energy functional described by Eq. 4.2 with $B = 0$ for the same set of parameters in Fig. 4.6 and Fig. 4.7.

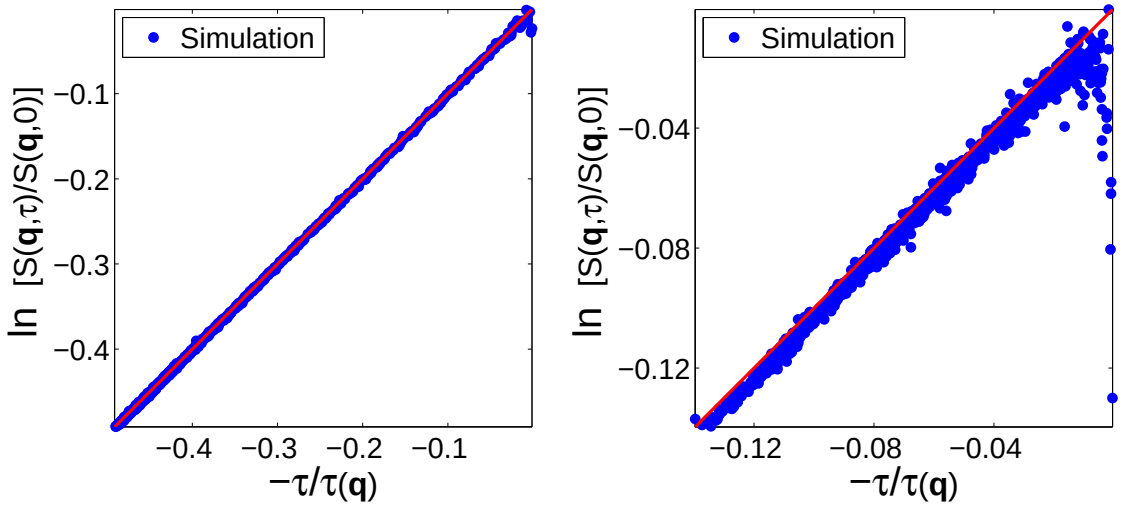

(a) (b)

Figure 4.9: Verification of the dynamic correlation function, Eq. 4.48, of the order parameter Fourier components. Finite difference scheme (a) and finite volume scheme (b) have been used to carry out simulations on a $32 \times 32 \times 32$ lattice with $A = 0.065$, $B = 0$, $K = 0.04$ and $M = 0.095$ with an initial equilibrium distribution. Ensemble averaging is done over 10^5 time steps and 20 realizations.

q_z in the absence of hydrodynamic coupling while Fig. 4.7 shows results for the full dynamics using the two complementary spatial discretisation approaches. The analytical prediction is superimposed showing the high degree of accuracy and isotropy obtained in all situations. Only at large wave vectors the results obtained using the finite difference method compare better with theory than those obtained from finite volume method. We attribute this accuracy loss to the different structure of the lattice Laplacian in both approaches, although the errors are consistent with the statistical uncertainty associated to the sampling performed. To show that there is no systematic errors hidden in Fig. 4.6 and Fig. 4.7, a one dimensional plot of the error in the equilibrium ratio is plotted against q, along the diagonal $q_x = q_y = q_z$ in the wave vector space in Fig. 4.8.

We have also analyzed the equilibrium dynamic structure factor of this miscible mixture, $S(\mathbf{q}, \tau) \equiv \langle \widetilde{\psi}(\mathbf{q}, t)\widetilde{\psi}(\mathbf{q}, t + \tau)\rangle$, for which we have an analytic expression. Taking into account the lattice structure, it reads

$$S(\mathbf{q}, \tau) = \frac{kT}{A - KL(q)} e^{-M\mathbf{q}^2(A - KL(q))\tau}. \tag{4.48}$$

Fig. 4.9 displays $\ln [S(\mathbf{q}, \tau)/S(\mathbf{q}, 0)]$ as a function of the scaled time $\tau/\tau(\mathbf{q})$, where we introduce the characteristic decay time for each mode, $\tau(\mathbf{q}) = [M(-L(\mathbf{q}))(A - KL(\mathbf{q}))]^{-1}$. The simulation results recover the expected slope with a high degree of accuracy over all the times covered for each mode for the two discretisation schemes of the fluctuating Cahn-Hilliard equation.

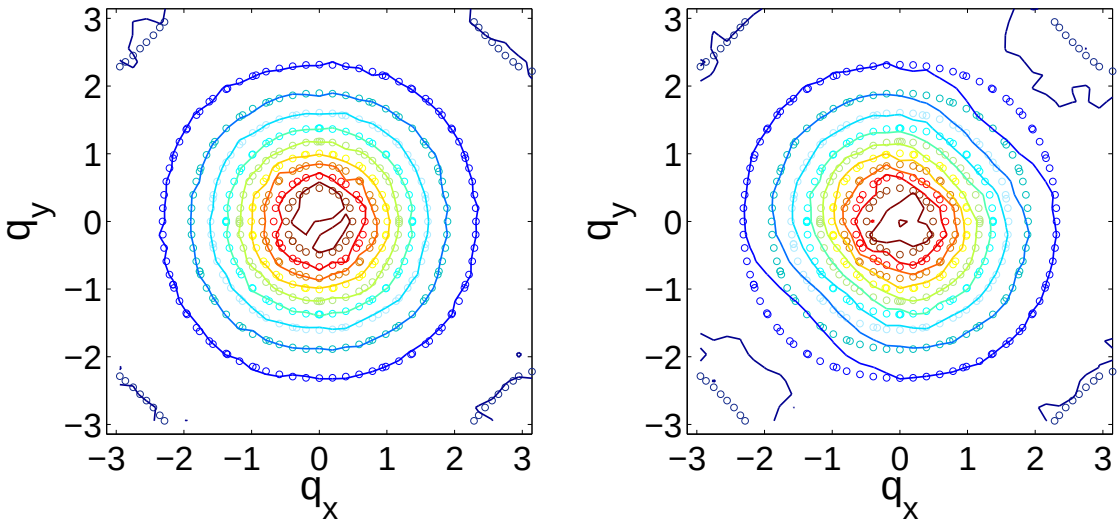

(a) (b)

Figure 4.10: Galilean invariance of the scheme is tested by applying a uniform velocity field along a diagonal direction. Constant values of $\langle|\widetilde{\psi}(\mathbf{q})|^2\rangle$ from the simulations are plotted along with theoretical predictions as symbols using the same parameters as in Fig. 4.7. (a) At small flow velocities, $Ma = 0.08$, correct equilibrium is maintained in the simulations. (b) However at large flow velocities, $Ma = 0.57$, an anisotropic distribution of the order parameter fluctuations develops.

4.7.2 Galilean invariance

The coupling of the order parameter dynamics to the fluid motion must respect Galilean invariance. In order to test if the proposed algorithm recovers this basic symmetry, we have imposed a constant velocity along one of the system's diagonal, $x = y$. Fig. 4.10 displays the order parameter static structure factor, $S(\mathbf{q}) = \langle|\widetilde{\psi}(\mathbf{q})|^2\rangle$, for a miscible mixture with an energy cost gradient, subject to a uniform flow with different magnitudes. Due to Galilean invariance, $S(\mathbf{q})$ must not be affected by the fluid motion and must coincide with the equilibrium curves in Fig. 4.6 .

At small flow rates (small Ma), Fig. 4.10.a, we do not see any deviation from the equilibrium predictions, as expected. However, increasing the velocity for $Ma > \frac{1}{2}$, Fig. 4.10.b shows the development of an anisotropic structure factor, which we attribute to the numerical dissipation associated with advection terms in the order parameter conservation equations. Although in principle, the proposed LB algorithm does not ensure Galilean invariance at high Ma (a situation which can be improved with complementary LB implementations (Prasianakis *et al.* 2009)), the main source for inaccuracies comes from numerical dissipation in the order parameter dynamics. This is because the balance between fluctuation and dissipation is calculated assuming no diffusive error in the advection scheme. Numerically less dissipative schemes such as operator splitting may be resorted to avoid these limitations (LeVeque 2002). Alternatively, schemes accounting for the dissipation associated with advection may be implemented as done e.g. in Donev *et al.* (2010). However, in our simulations we have considered only RK algorithms, which recover the correct behavior for small Ma flows. Due to the coupling between two evolving

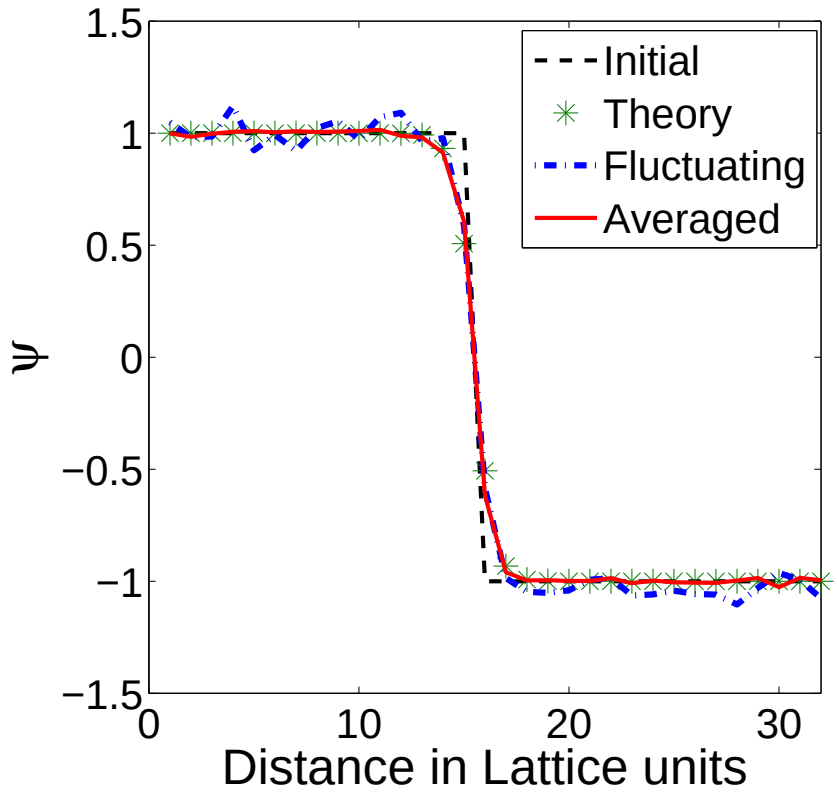

Figure 4.11: Mean equilibrium profile of the order parameter for two fluid phases coexisting through a planar interface. The dashed line is the initial set sharp profile on a 64 x 64 lattice of interface in order parameter with left-right symmetry (only left half is shown in the plot). Symbols show the theoretical predictions, (Eq. 4.4), the continuous line is an instantaneous profile from simulations while the thick line corresponds to the ensemble averaged profile. The continuous line illustrates the magnitude of fluctuations around the mean shape. Ensemble averaging is done after attaining equilibrium(10^5 time steps) over 4×10^5 time steps and 7 realizations. Parameters used in the simulation are $-A = B = 0.025$, $K = 0.01$ and $M = 0.1$.

fields, there is no need to improve the accuracy of FLBE or SMOL separately beyond the lesser accurate among these. Also, it may be noted that this being a hybrid scheme changing dt or dx may have different implications in each of these schemes.

4.7.3 Fluctuating interfaces

All the tests described above have used a harmonic free energy functional. Below, we present a test of the model including the quartic anharmonicity in the free energy. At two phase coexistence, with $A < 0$ and $B > 0$, the order parameter variation across the diffuse interface separating the two phases is the well-known hyperbolic tangent of Eq. 4.4. In Fig. 4.11 we show the order parameter profile across the interface, averaged over time and initial conditions. We have verified that the mean profile follows Eq. 4.4 with a characteristic width predicted by Eq. 4.5.

Fluctuations about the mean profile are in general complicated. However, long-wavelength harmonic fluctuations are well-described by capillary wave theory as explained in Rowlinson & Widom (1982); Grant & Desai (1983). The energy of an interface with instantaneous height,

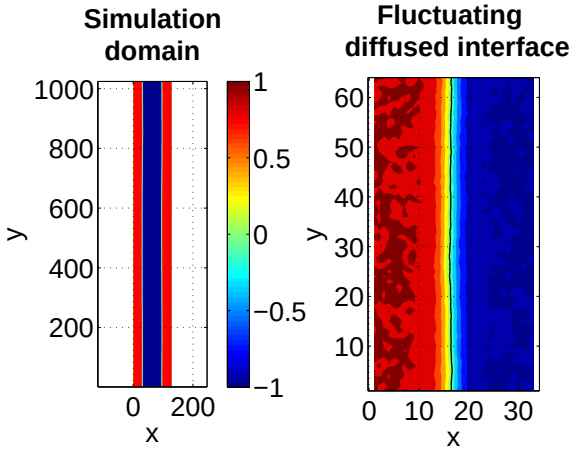

Figure 4.12: Instantaneous order parameter field used for capturing the capillary spectrum. Here two fluid phases coexist through two planar fluctuating interfaces. The full domain used for simulation is shown on the left side and the fluctuating diffused interface is on the right side. The continuous line is for $\psi = 0$.

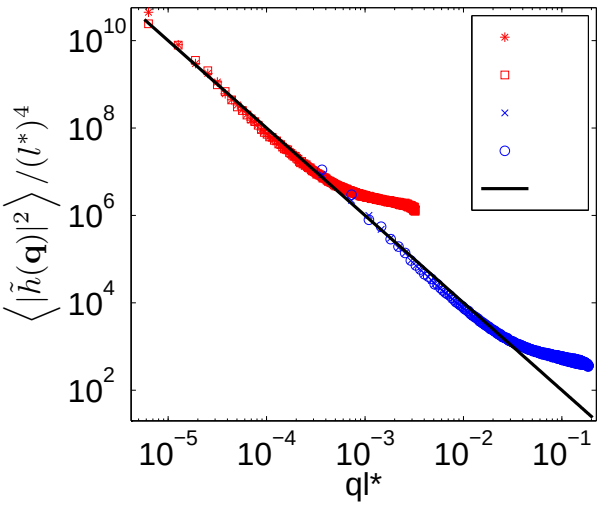

Figure 4.13: Logarithmic plot of the interfacial height fluctuation spectrum as a function of the wave vector magnitude. Symbols show the simulations results and continuous line correspond to the theoretical prediction (Eq. 4.51). The wave vector magnitude is scaled with the capillary length, l^*, and the magnitude of the height fluctuations has also been scaled with l^{-4} to highlight the universal nature of the capillary spectrum, which is recovered over several orders of magnitude. Four different symbols $*$, $\square$, $\times$, $\circ$ correspond to simulations with $kT = 10^{-7}$ using finite-difference method, $kT = 10^{-7}$ using finite-volume method, $kT = 1/3000$ using finite-difference method and $kT = 1/3000$ using finite-volume method respectively, on a 1024×128 lattice (See Fig. 4.12). Free energy and LB simulation parameters are $-A = B = 0.05, K = 0.2, M = 0.1$ and $\tau = 0.45$.

$h(x, y)$ is approximated as

$$\Delta F_s = \frac{1}{2}\gamma \int d^2\mathbf{x}(\nabla h)^2 \tag{4.49}$$

In Fourier space, this is

$$\Delta F_s = \frac{\gamma}{2}\sum_{\mathbf{q}} \mathbf{q}^2|\tilde{h}(\mathbf{q})|^2, \tag{4.50}$$

from which it follows that

$$\langle|\tilde{h}(\mathbf{q})|^2\rangle = \frac{kT}{\gamma\mathbf{q}^2}. \tag{4.51}$$

Since our simulations evolve the entire order parameter field, which has both short-wavelength bulk fluctuations and long-wavelength capillary fluctuations, it is necessary to tune parameters appropriately to capture the capillary fluctuations. This is ensured when the thermal capillary length $l^* = \sqrt{\frac{kT}{\gamma}}$, the interfacial width l, and the system size Λ obey $l^* \ll l \ll \Lambda$. The first inequality ensures that the energy scale of the thermal fluctuations excites capillary modes and not bulk order parameter modes, while the second ensures that the long-wavelength capillary regime is accessible in the simulation. The capillary length condition is equivalently $\gamma l^2/kT >> 1$.

We have carried out simulations on a system of size 128×1024 where interfaces of linear dimension of 1024 are symmetrically placed about the center of the domain at a gap of 64 lattice units (see Fig. 4.12) at two different temperatures. Results from these simulations are shown in Fig. 4.13 using both finite difference and finite volume methods. In diffuse interface models, alternative definitions of the interface and its location are possible (Blokhuis 2009). We have used a simple linear interpolation to determine the location of the interface as the zero of the order parameter. The cross over time for roughening transition and the longest relaxation time (Flekkoy & Rothman 1995, 1996) may be estimated as $\sim 10^4$ and $\sim 10^3$ time steps. Therefore, simulation data was collected only after 10^5 times steps, to ensure stationarity of the fluctuations. The logarithmic plot of Fig. 4.13 shows that the algebraic theoretical prediction can be recovered over several orders of magnitude by scaling appropriately the wave vector and height spectrum magnitudes and changing the system parameters. Exploiting the underlying scaling structure of the interface height fluctuations, we can combine several numerical simulations with appropriate fluid parameters to reconstruct the whole universal curve, a strategy already exploited in the kinetics of phase-separating fluid mixtures (Pagonabarraga *et al.* 2002). Since the quartic anharmonicity is essential in maintaining the interface and its fluctuations, this provides a non-linear test of the equilibriation in our numerical scheme.

4.8 Conclusions and outlook

A hybrid method for the numerical solution of the model H equations has been developed and validated. A fluctuating lattice Boltzmann algorithm is used for hydrodynamics while a stochastic method of lines is proposed for order parameter conservation equation. Spatial discretisation in the latter case may be done using finite difference or a finite volume schemes both of which ensure correct FDT at the lattice level. FLBE takes care of fluctuations in momentum at the lattice level. The momentum and order parameter equations are coupled

through stress and advection terms. The accuracy of the algorithm is demonstrated through various hydrodynamic and order parameter fluctuation tests. The capillary spectrum of height fluctuations is reproduced accurately.

There are several situations where simulations of fluctuating hydrodynamics of binary fluid system is necessary. For example, our method can be used to study phenomena such as critical fluctuations in symmetric binary mixtures and nucleation in asymmetric binary mixtures. In the light of discussions in section 4.4, the role of noise in the spinodal decomposition of a binary system remains unclear (Gonnella *et al.* 1999). This method may be successfully employed in studying the noise driven growth in different regimes of the decomposition process. Similarly interface fluctuations play an important role in several meso scale phenomena such as fluctuations driven spreading of nano droplets on solid surfaces (Davidovitch *et al.* 2005), dewetting of thin films (Willis & Freund 2009) and break up of nano jets (Eggers 2002). Traditionally, molecular dynamics simulations have been used to study these problems. We expect our mesoscale algorithm to be an effective complement to MD simulations which are currently limited to short time scales.

Chapter 5

Do liquid drops roll or slide on inclined surfaces?

The material in this chapter is reproduced in arXiv:1111.3789v1 [cond-mat.soft].

5.1 Abstract

A solid sphere is likely to roll, while a rectangular box is likely to slide, on an inclined surface. In contrast, a liquid drop moving on an inclined surface can exhibit a variety of shapes and hence complex but interesting dynamics. Combining lattice Boltzmann method for hydrodynamics with a diffuse interface model, a hybrid numerical scheme is used to study the dynamics of binary fluids on an inclined plate under the action of gravity. Using a triple decomposition of the velocity gradient tensor inside a drop, the vorticity associated with the rolling motion is distinguished from that of shearing motion. The average angular velocity based on this residual vorticity becomes significant when the external fluid viscosity is reduced and the shape of the drop approaches a circle. For a given slip length and viscosity ratio with the external fluid, irrespective of the equilibrium contact angle, plate inclination or Bond number, a universal curve is observed for the amount of rotation as a function of the drop shape characterized by the isoperimetric quotient. Results from a large number of simulations over a wide range of parameters are shown to lie on this curve. The rolling motion is also found to be strongly dependent on the slip length at the contact line.

5.2 Introduction

On an inclined surface, a solid sphere rolls down while a rectangular object is more likely to slide down under the action of gravity. The choice of sliding versus rolling motion is determined by the shape and weight of the body and the frictional forces at the supporting surface. On the other hand, a liquid drop attains a variety of shapes depending on gravitational, capillary forces and solid surface characteristics; a moving drop has to contend in addition with viscous and inertial stresses (de Gennes *et al.* 2004). Moreover, the reaction forces and moments provided by the supporting surface are distributed and depend strongly on the shape, see e.g. Chapters 2 - 3. These differences between a solid and a liquid make the study of the latter complex, but pose an interesting question, viz. whether a liquid drop sitting on an inclined surface will roll, slide, or do both. We address this simple question here though the answer is not straightforward due to the spatially inhomogeneous flow field. A systematic analysis reveals the decisive parameters of drop dynamics. Rolling droplets play an important role in self-cleaning devices (Rothstein 2010) and it is desirable to know under what situations one can maximize the rolling motion

inside the drop. Therefore, understanding this kinematics is not just a curiosity but is expected to have relevance in several applications also.

The contribution of roll vs slip in the measured velocity profiles of accelerating drops on hydrophobic surfaces as a function of surface characteristics is investigated experimentally in Sakai *et al.* (2006); Suzuki *et al.* (2008). When the contact angle is small, the lubrication approximation of the Navier-Stokes equation is a good model to describe the dynamics (Oron *et al.* 1997) and has received much attention theoretically (Dussan & Chow 1983; Snoeijer *et al.* 2005) and experimentally (Grand *et al.* 2005). At the other limit, i.e in non-wetting drops, a complete rolling of the drop is observed (Richard & Quere 1999; Aussillous & Quéré 2004; Quere 2005) under certain situations and is in agreement with the scaling arguments of Mahadevan & Pomeau (1999). The intermediate contact angles are studied much less since they do not lend themselves to simplifying approximations and are harder to analyze. While analytical solutions are practically impossible, numerical solutions pose considerable challenges due to the multiple length scales present and the coupling between the evolving field and the interface shape (Scardovelli & Zaleski 1998). Alternative techniques such as molecular dynamics simulations (Servantie & Muller 2008) and lattice Boltzmann simulations (Moradi *et al.* 2011) have shown the rolling motion in cylindrical drops. However, such studies have concentrated on the total velocity of the droplet and its dependence on the driving force and the contact angle. A splitting of the velocity field into slip and roll was done recently by Mognetti *et al.* (2010) restricted for drop sizes smaller than capillary length. In their analysis the linear part of the velocity profile inside the drop was attributed to rotation which overestimates it as we will see.

Now a word about the contact line movement in this context. Though the exact mechanism is not understood (Bonn *et al.* 2009), this, by slipping or otherwise, is imperative for a moving drop unless the contact angle is exactly 180° allowing a rolling motion (Mahadevan & Pomeau 1999). A small amount of global rotation in the drop can manifest itself as tank-treading near the contact line (Dussan & Davis 1974). Most earlier studies have concentrated on the rolling motion near the contact line (Clarke 1995; Chen *et al.* 1996) while we look at the rolling motion in the bulk of the drop. The association between the two, if any, implies the nonlocal hydrodynamic effects of the contact line movement (Shikhmurzaev 2008*a*).

Here we numerically investigate the motion of cylindrical drops on inclined surfaces using a new algorithm - a hybrid method combining lattice Boltzmann and diffuse interface model for binary fluids. This model allows different viscosity for two fluids and a large range of contact angles on smooth surfaces. Unlike previous cases (Mognetti *et al.* 2010), we analyze the entire spectrum of shapes, irrespective of the capillary length, for a range of the relevant non-dimensional parameters. As we will see, the standard methods of fluid mechanics (Batchelor 1967) do not work. It is necessary to split the flow field into sliding, shear and rolling in the manner introduced by Kolar (2007) in a different context in order to distinguish local rotation from global rotation inside the drop. We show that, among other factors, the shape and hence the size is very important in determining the amount of rolling inside the drop. Non-intutively, it will be seen that the rolling behavior can be uniquely described by a shape parameter, independent of capillary and gravitational forces. For small Bond numbers, it is possible to predict this shape parameter from the static shapes. While standard scaling laws can be applied, both slip length

and the viscosity of the external fluid are seen to be very important in the overall motion.

5.3 Diffuse Interface Model and Hydrodynamics

We use a coupled system of equations describing the hydrodynamics of a conserved order parameter ψ, defined as a normalized density difference, and the conserved momentum density $\rho\mathbf{u}$, where ρ and $\mathbf{u}$ are the total density and the local fluid velocity, (See Chapter 4). The order parameter dynamics is described by a Cahn-Hilliard equation (CHE), which includes advection by fluid flow and relaxation due to chemical potential gradients. This is coupled to a Navier-Stokes equation (NSE) with additional stress densities arising from the order parameter. We use a hybrid algorithm by combining the lattice Boltzmann (LB) method for hydrodynamics and method of lines for the order parameter dynamics. Force densities such as the divergences of order parameter stresses and gravity are included in the modified LB method used here. We use a $D3Q15$ model and collision integral is a single relaxation time (τ) approximation. The viscosity is obtained as $\eta = \tau c_s^2$ where $c_s = 1/\sqrt{3}$ is the sound speed in LB units. The spatial discretization of the CHE is based on a finite-volume formulation and this set of equations is temporally integrated using a Runge-Kutta algorithm. All the details of simulation are described in Chapter 4.

Before analyzing the results some of the new features of the hybrid algorithm vis a vis (i) implementation of viscosity contrast for a binary fluid system in the above mentioned model, (ii) incorporating gravitational forces, (iii) implementation of wetting boundary conditions are to be discussed. We will also look at the characterization of rolling motion inside a drop.

5.3.1 Viscosity contrast in binary fluids

The differences in properties between the two fluids could be introduced at a molecular level, as done by Luo & Girimaji (2003); Asinari (2005). Our approach is macroscopic, and the simplest way to introduce a viscosity difference across the fluid interface is to prescribe the relaxation time as a function of the order parameter. The underlying assumption is that the molecular structure of two fluids is the same, and is analogous to the introduction of interfacial tension using Cahn-Hilliard theory. To test this, we first design a model problem, of the laminar pressure-driven flow of two fluids in a two-dimensional channel. Fluid I is of higher viscosity η_I, and occupies the lower portion of the channel, while fluid II of lower viscosity η_{II} occupies the upper portion.

In the literature we find two different expressions for the relationship between the concentration and the relaxation time.

(i) Effective relaxation time as a polynomial function of order parameter, the simplest being linear (He *et al.* 1999; Grunau *et al.* 1993),

$$\tau = 0.5[\tau_I(1-\psi)] + [\tau_{II}(1+\psi)]. \tag{5.1}$$

(ii) As Arrhenius suggested, prescribe an effective relaxation time as a product of relaxation

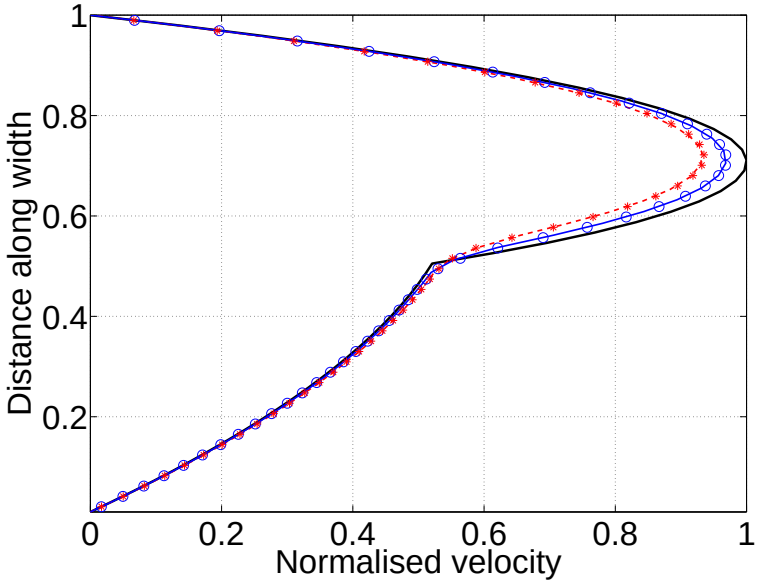

Figure 5.1: Comparison of 2D channel flow velocity profiles of an immiscible binary system and its approximations in the DI framework. The thick continuous line is the velocity profile of an immiscible binary fluid. In the simulations, the binary fluid was approximated as a viscosity stratified fluid flow according to Eq. 5.1 and 5.2, the results are shown by red stars and blue circles respectively. The corresponding analytical solutions for viscosity-stratified flow are shown by the red dashed and blue solid lines respectively. While LB perfectly reproduces the flow for a given viscosity stratification, the use of a thin viscosity stratified layer itself is a good approximation for an immiscible binary fluid system.

times, but raised to a power proportional to concentration (Langaas & Yeomans 2000)

$$\tau = \tau_I^{(\frac{1-\psi}{2})} \tau_{II}^{(\frac{1+\psi}{2})}. \tag{5.2}$$

We test both relationships by simulating the two-fluid flow described above, first defining the viscosity ratio simply by $\eta_r = \eta_I/\eta_{II} = \tau_I/\tau_{II}$. The velocity profile from simulations using the two expressions above are compared to the analytical solution for two immiscible fluids separated by a sharp interface in Fig. 5.1. When the viscosity contrast is small, both match well with the analytical solution. However, when the ratio is large ($\eta_r = 10$), Eq. 5.2 is closer to the immiscible result than Eq. 5.1. This is because the effective mixed layer where the viscosity varies between η_I and η_{II} is smaller by the former relationship. This is evidenced by the fact that a corresponding analytical solution for the laminar velocity profile for the parallel flow of two miscible fluids with a thin mixed region between them agrees in each case with the computed result. We have thus shown that this approach is a good one for incorporating viscosity contrasts in LB simulations. Note that no ad-hoc fixes are needed. We have used Eq. 5.2 in our calculations.

5.3.2 Gravity

The hybrid algorithm written using a single particle distribution function is modified to include gravitational effects as follows. Following Buick & Greated (2000), we may write the

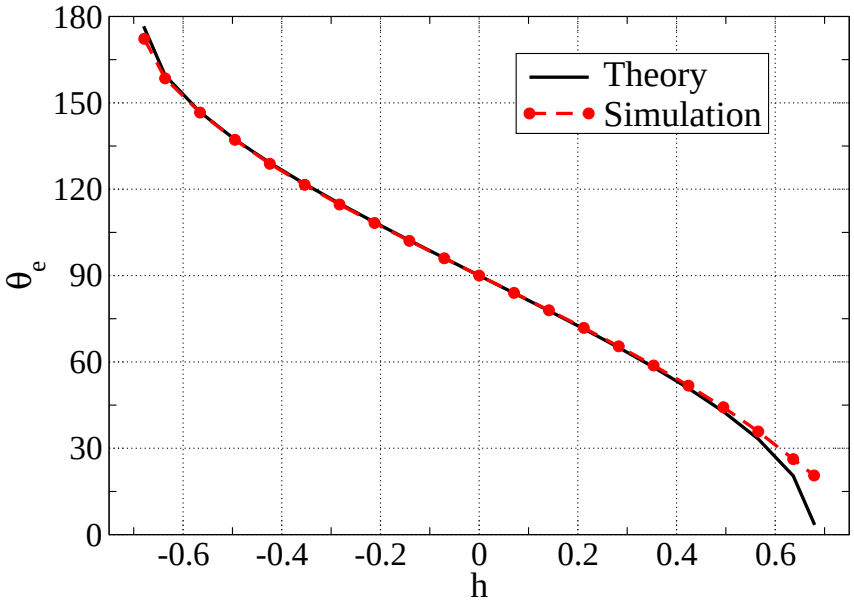

Figure 5.2: Verification of the implementation of wetting conditions, Eq. 5.6, on the walls by comparing the numerically obtained contact angle with Eq. 5.7. The agreement is good except at very large and small contact angles.

gravitational force acting on the fluids as,

$$\mathbf{G} = \frac{\rho}{2}[g_I(1-\psi) + g_{II}(1+\psi)]\mathbf{1_g}, \tag{5.3}$$

where $\mathbf{1_g}$ is the direction in which gravity is acting. Therefore, when $\psi = 1$, $\mathbf{G} = \rho g_{II}\mathbf{1_g}$ and when $\psi = -1$, $\mathbf{G} = \rho g_I \mathbf{1_g}$. At the interface when $\psi = 0$, $\mathbf{G} = \frac{\rho}{2}(g_I + g_{II})\mathbf{1_g}$. Thus g_I/g_{II} determines the density ratio between two fluids. In order to ensure that we are in the incompressible limit, we must have $|\mathbf{G}z| << \rho c_s^2$ where z is the vertical extent of the simulation domain, which means that thermodynamic pressure is large compared to the hydrostatic pressure difference.

In our simulations, wall boundary conditions are applied on two sides of the domain. Thus a computation of a single component fluid, with gravity prescribed along the flow direction, develops a channel flow between the walls. For droplet simulations, we implement the body force only on one fluid, which is equivalent to solving the NSE with the Boussinesq approximation as described below. For small density variations, i.e., $\Delta\rho \equiv g_I - g_{II} << g_I$, the Boussinesq approximation provides that we may neglect the density variation everywhere in the NSE except in the buoyancy term, $\mathbf{G}$ of Eq. 4.9. For simplicity we may further absorb the body force ρg_{II} into the pressure term by redefining pressure. Density in the interface region is prescribed as a linear function of the order parameter. Note that the validity of our simulations is thus limited to situations where the Boussinesq approximation holds.

5.3.3 Wetting Boundary Conditions

The algorithm implemented to get the correct contact angle on the wall is based on Desplat *et al.* (2001); Briant *et al.* (2002). The solid-fluid surface tensions are introduced by defining

the Landau free energy functional

$$F = F_{bulk}(\psi) + \int f(\psi_s) ds, \tag{5.4}$$

where ψ_s is the value of order parameter at the wall. Minimization of this energy functional near the wall gives a relation between energy gradient and the gradient of the order parameter

$$\frac{df_s}{d\psi_s} = k\nabla\psi \cdot \mathbf{n}, \tag{5.5}$$

where $\mathbf{n}$ is normal to the wall. The form $f_s = \frac{C}{2}\psi_s^2 + H\psi_s$ is known to be sufficient to produce various wetting behavior. By tuning the parameters C and H we can modify the properties of the surface. If $H = 0$ we have neutral wetting. Nonzero values of H therefore allows an asymmetry in the surface value of the order parameter and a contact angle different from 90°. Therefore we have,

$$\frac{df_s}{d\psi_s} = C\psi_s + H = K\nabla\psi \cdot \mathbf{n}. \tag{5.6}$$

It is found sufficient to retain only the linear term of the surface energy functional (Desplat *et al.* 2001; Briant *et al.* 2002), i.e., to set $C = 0$. We use a second order central difference formula to calculate the normal derivative of order parameter at the wall. Thus, $H = K\frac{\psi_1 - \psi_0}{\Delta x}$, where the subscripts 0 and 1 represents the 0^{th} and first node respectively, which may be used to obtain the order parameter ψ_0 at the boundary node. The wall is placed at the $\frac{1}{2}$ location, as is usual in the bounce back schemes used to represent wall in LB procedures (Succi 2001). Defining a parameter $h \equiv H\sqrt{\frac{2}{kB}}$, the contact angles may be calculated as

$$\cos\theta = \frac{1}{2}\left[(1+h)^{3/2} - (1-h)^{3/2}\right]. \tag{5.7}$$

In addition $\mu_0 = \mu_1$ is imposed to ensure no order parameter flux into the wall, up to second order accuracy. Also, advection terms have been carefully discretized to preserve mass conservation upto machine accuracy. The implementation of the wetting properties of the wall is verified by comparing the static equilibrium angle obtained from the simulation to that from Eq. 5.7 as shown in Fig. 5.2. Deviations are seen at very large and very small contact angles and this appears to be consistent with the literature (Desplat *et al.* 2001; Briant *et al.* 2002) (both used kinetic schemes for CHE). Both the grid size and the interfacial thickness were doubled separately to ensure that the deviations seen are not due to the contact line pinning. We restrict our simulations as far as possible to the wide range of intermediate contact angles where we are sure the simulations capture the relevant physics in this respect.

5.3.4 Measure of Rolling Motion

Before discussing the simulations and results, we take a typical simulated drop and discuss how the slide, shear and roll may be estimated. The droplet is illustrated in 5.3a. The rolling motion inside the drop is evident in the corresponding velocity field, plotted in the center of mass reference frame of the moving drop as illustrated in 5.3b. Our objective is to quantify this

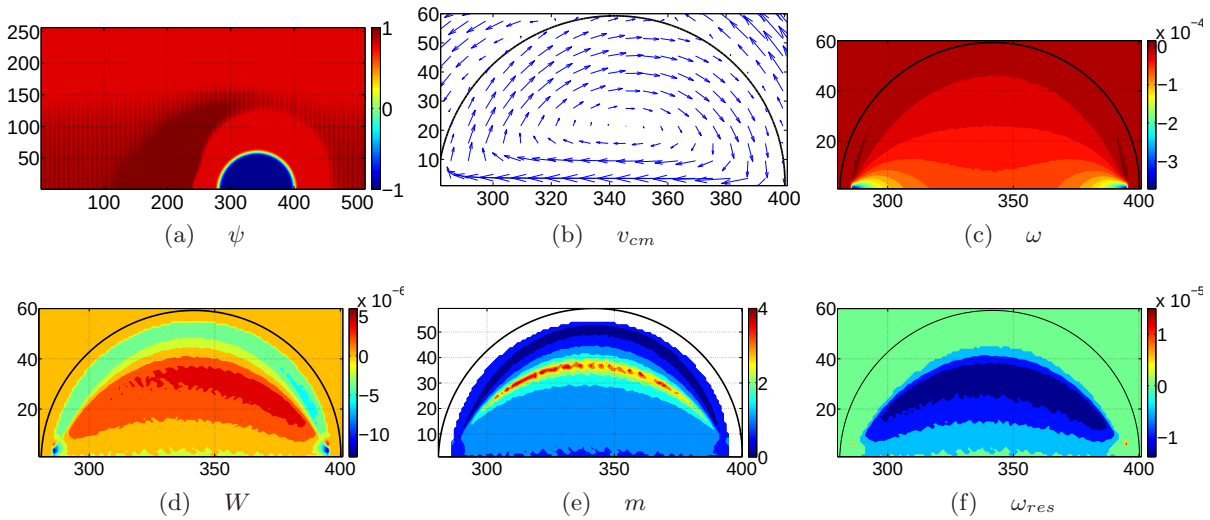

Figure 5.3: (a) ψ, order parameter field in the entire simulation box, two colors for the two different fluids with a thick interface. (b) v_{cm}, velocity field in the center of mass frame of the drop, the rolling motion of the drop may be observed. (c) ω, the vorticity field inside the drop, regions concentrated vorticity may be noticed near the contact line. (d) W, Weiss criterion to distinguish regions of high shear from vortical regions. (e) m, the kinematic vorticity number, again a measure of highly vortical regions, (f) ω_{res}, residual vorticity showing the regions associated with solid body rotation.

rotation. The first quantity to look at would be the vorticity field, shown in 5.3c. The velocity gradient tensor is usually split (Batchelor 1967) into a symmetric part $\mathbf{S}$ and an antisymmetric part $\mathbf{\Omega}$ as $\nabla\mathbf{u} = \mathbf{S} + \mathbf{\Omega}$. Here, $\mathbf{S}(x, y)$ for shear tensor is a measure of the deformation of a small fluid element located at (x, y), while the vorticity tensor $\mathbf{\Omega}(x, y)$ identifies the angular velocity of the fluid element, with (x, y) as the center of rotation. There are different measures available in the literature to identify regions of high vorticity relative to shear (J. Wu 2006), and most of them have been derived in the context of turbulence. A commonly used measure is $W = \frac{1}{2}(||\mathbf{\Omega}||^2 - ||\mathbf{S}||^2)$ of the Weiss criterion. This is illustrated in Fig 5.3d for the drop under consideration. Another measure is the kinematic vorticity number, defined as $m = ||\mathbf{\Omega}||/||\mathbf{S}||$ where $|||[.]||| = \text{trace}([.] \cdot [.]^T)^{1/2}$. This quantity is plotted in Fig 5.3e. Different criteria have been developed later on to define a vortex exactly and many of them reduce in two dimensions to the Weiss criterion (Jeong & Hussain 1995). However the main drawback of these measures is that they all estimate vorticity, which does not in general give a direct measure of rolling motion. This is because the vorticity $\boldsymbol{\omega} = \nabla \times \mathbf{u}$ is a local quantity which includes both solid body rotation and shearing motion of a fluid element, and thus cannot distinguish between them. The residual vorticity which we describe below is shown in 5.3f. Although all three measures broadly describe the region of high rotationality in a similar fashion, only the last is good for obtaining a quantitative estimate of solid body rotation.

To demonstrate that the residual vorticity is a useful way of describing the global rolling motion inside a drop, let us discuss a simple flow configuration, namely, a shear flow with $u = \dot{\gamma}y$ where x is the flow direction and y is the gradient direction. The velocity gradient tensor $\nabla\mathbf{u}$

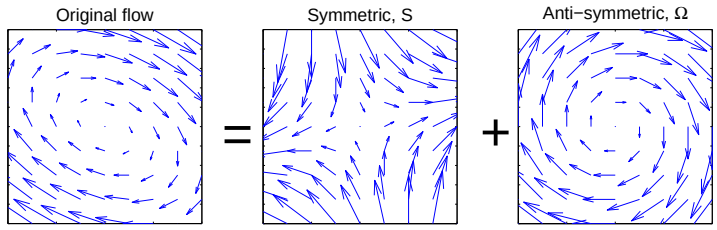

(a)

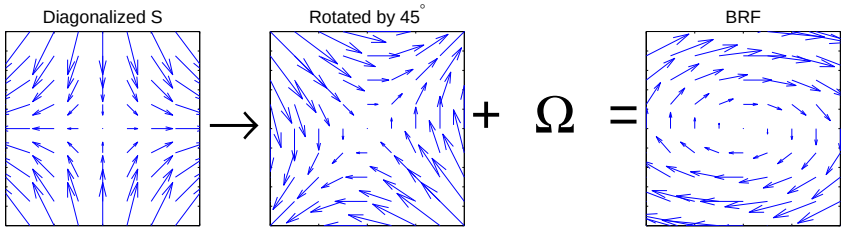

(b)

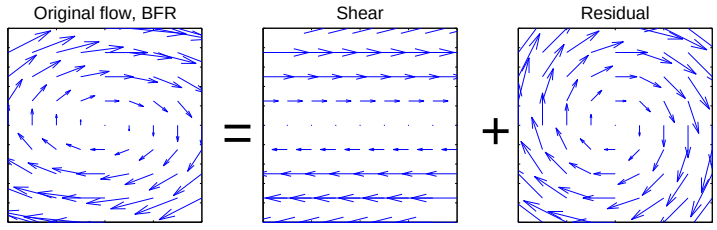

(c) Example I

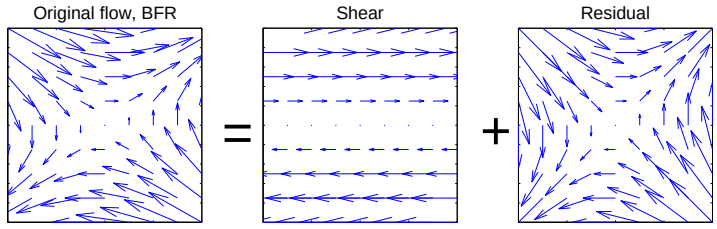

(d) Example II

Figure 5.4: (a) Standard velocity gradient decomposition into symmetric and antisymmetric parts for a flow with $u_x = 0.1$, $u_y = 0.3$, $v_x = -0.2$, $v_y = -0.1$ is shown here. (b) The strain rate tensor in the principal coordinate system is rotated by 45° and added to the antisymmetric tensor to generate the same flow in BFR. (c) The same flow is decomposed into a simple shear flow and residual flow, the residual being purely rotational flow. (d) A strain dominated flow, $u_x = 0.1$, $u_y = 0.2$, $v_x = 0.1$, $v_y = -0.1$ is decomposed into simple shear and residual flow, with residual consists of only straining flow.

splits into its symmetric and antisymmetric parts as follows:

$$\nabla \mathbf{u} = \begin{pmatrix} 0 & \dot{\gamma} \\ 0 & 0 \end{pmatrix} = \begin{pmatrix} 0 & \dot{\gamma}/2 \\ \dot{\gamma}/2 & 0 \end{pmatrix} + \begin{pmatrix} 0 & -\dot{\gamma}/2 \\ \dot{\gamma}/2 & 0 \end{pmatrix} = \mathbf{S} + \mathbf{\Omega}.$$

Although $\mathbf{\Omega}$ is non-zero, there is no rolling motion, which tells us that we need a modified vorticity to characterize rolling motion.

To demarcate a coherent vortex correctly from high shear regions, Kolar (2007) proposed a scheme to remove the 'shear' vorticity from the total vorticity. He proposed a triple decomposition of the relative motion of a fluid element, where the velocity gradient tensor is split into a straining part, a rigid body rotation and a simple shear flow part. For clarity, we illustrate these pictorially in Fig. 5.4. Given a velocity field in two dimensions, $\mathbf{u}$, the velocity gradient tensor is a 2×2 matrix

$$\begin{pmatrix} u_x & u_y \\ v_x & v_y \end{pmatrix} = \begin{pmatrix} u_x & \frac{u_y+v_x}{2} \\ \frac{u_y+v_x}{2} & v_y \end{pmatrix} + \begin{pmatrix} 0 & \frac{u_y-v_x}{2} \\ \frac{v_x-u_y}{2} & 0 \end{pmatrix}. \tag{5.8}$$

The symmetric part (Fig. 5.4a) can be diagonalized to $\begin{pmatrix} s/2 & 0 \\ 0 & -s/2 \end{pmatrix}$ where $s = \sqrt{4u_x^2 + (u_y + v_x)^2}$. This is the strain rate tensor in the principal coordinates, see Fig. 5.4b, which represents the total straining of the fluid element. The rotation tensor being antisymmetric will not change with a rotation of the coordinate system, and remains as $\begin{pmatrix} 0 & -\omega/2 \\ \omega/2 & 0 \end{pmatrix}$ where $\omega = v_x - u_y$, the vorticity. Therefore, in the principal axis coordinates, the velocity gradient tensor is, $\begin{pmatrix} s/2 & -\omega/2 \\ \omega/2 & -s/2 \end{pmatrix}$. We now rotate the coordinate system further by $\pi/4$ (Fig. 5.4b). This frame is called a basic frame of reference (BFR), and the velocity gradient tensor in this frame is

$$\begin{pmatrix} 0 & (s-\omega)/2 \\ (s+\omega)/2 & 0 \end{pmatrix} = \begin{pmatrix} 0 & s/2 \\ s/2 & 0 \end{pmatrix} + \begin{pmatrix} 0 & -\omega/2 \\ \omega/2 & 0 \end{pmatrix}.$$

In this reference frame, the contribution due to shear is maximized in a triple decomposition of $\nabla \mathbf{u}$. One may write (Kolar 2007)

$$\begin{aligned} \nabla u &= \nabla u_{shear} + \nabla u_{residual} \\ &= \mathbf{S}_{shear} + \mathbf{\Omega}_{shear} + \mathbf{S}_{residual} + \mathbf{\Omega}_{residual}. \end{aligned}$$

Only one of the residual terms $\mathbf{S}_{residual}$ or $\mathbf{\Omega}_{residual}$ will be non-zero. The residual matrices above are constructed as explained below. The residual vorticity and strain may be written respectively as

$$\begin{aligned} \omega_{res} &= 0 \quad \text{if} \quad |s| \geq |\omega| \\ &= \text{sgn}(\omega)\,[|\omega| - |s|] \quad \text{if} \quad |s| \leq |\omega|, \\ s_{res} &= \text{sgn}(s)\,[|s| - |\omega|] \quad \text{if} \quad |s| \geq |\omega| \\ &= 0 \quad \text{if} \quad |s| \leq |\omega|. \end{aligned}$$

An example flow which is vorticity dominated, where $|s| < |\omega|$ is illustrated in figure 5.4c. For

this case we may write

$$\nabla \mathbf{u}_{BFR} = \begin{pmatrix} 0 & s/2 \\ s/2 & 0 \end{pmatrix} + \begin{pmatrix} 0 & -sgn(\omega)|\frac{s}{2}| \\ sgn(\omega)|\frac{s}{2}| & 0 \end{pmatrix} + \begin{pmatrix} 0 & 0 \\ 0 & 0 \end{pmatrix} + \begin{pmatrix} 0 & -sgn(\omega)\frac{|\omega|-|s|}{2} \\ sgn(\omega)\frac{|\omega|-|s|}{2} & 0 \end{pmatrix},$$

where the first two matrices will combine to produce a simple shear flow. The residual straining, shown by the third matrix, is zero. The portion of the velocity gradient tensor contributing to solid body rotation is given by the fourth matrix as illustrated in Fig. 5.4c. On the other hand, for a flow which is strain dominated, i.e. $|s| > |\omega|$, an example of which is demonstrated in Fig. 5.4d, we write

$$\nabla \mathbf{u}_{BFR} = \begin{pmatrix} 0 & sgn(s)|\frac{\omega}{2}| \\ sgn(s)|\frac{\omega}{2}| & 0 \end{pmatrix} + \begin{pmatrix} 0 & \frac{-\omega}{2} \\ \frac{\omega}{2} & 0 \end{pmatrix} + \begin{pmatrix} 0 & sgn(s)\frac{|s|-|\omega|}{2} \\ sgn(s)\frac{|s|-|\omega|}{2} & 0 \end{pmatrix} + \begin{pmatrix} 0 & 0 \\ 0 & 0 \end{pmatrix}.$$

Again the first two matrices on the right hand side together produce a simple shear flow. The remainder is seen in the third matrix to be purely straining, as illustrated in Fig. 5.4d. We may now see that for the simple shear flow discussed above, $|s| = |\omega|$ and $\omega_{res} = 0$, while for a solid body rotation, $\omega = \omega_{res}$. If $|s| < |\omega|$, the flow is vorticity dominated, and the residual tensor will consist of only rotation, and vice versa. Therefore residual vorticity can characterize the rolling motion inside a drop.

This separation of the shear vorticity from residual vorticity is different from the shear and curvature vorticity used by the atmospheric science community. There the shear vorticity is defined as $-\frac{\partial u}{\partial n}$ where u is the local velocity along the streamline and $\mathbf{n}$ is normal to the stream line. The remainder is defined as the 'curvature vorticity', which is associated with the curvature of streamlines. Note that these values will not be Galilean invariant. This procedure, when applied to a solid body rotation, predicts equal values for both shear and curvature vorticity, though there is no shear component present in solid body rotation. Hence, we will not benefit here from this procedure. The residual vorticity that we use does not suffer from this drawback.

In contrast, in an irrotational vortex where $u_r = 0$ and $u_\theta = 1/r$ the residual vorticity is zero because vorticity associated with shear and rotation are equal and of opposite signs. However the curvature vorticity is non-zero showing the swirling motion of fluid elements. We may neglect such a contribution as we do not expect a point vortex like motion inside the drop. In other words, in the strict limit of Stokes flow, the velocity field inside a drop is constituted by growing harmonics alone. Therefore it is reasonable to consider that the residual vorticity gives the correct quantitative measure of rolling motion inside a drop. Note that neither residual vorticity nor curvature vorticity are complete measures of rolling motion. As a general rule, one may use residual vorticity in low Re flows and curvature vorticity in high Re flows.

By splitting the vorticity into two parts, one can identify the regions of shear. This could have also been identified by looking at the shear rate or viscous dissipation. However, such an

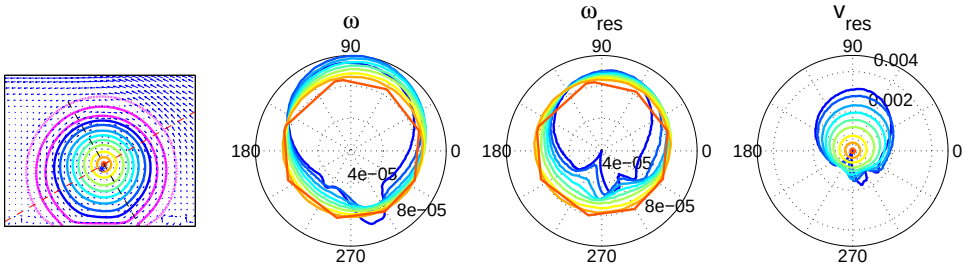

(a) $Bo = 0.038, \eta_r = 10, \theta_e = 152^\circ, Re = 11.8, Ca = 10^{-3}, \%R = 38.1$

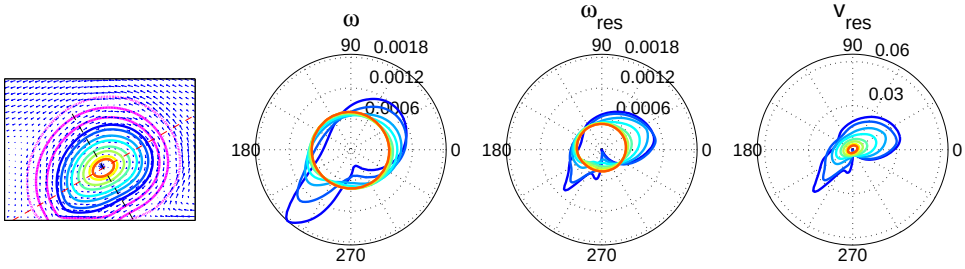

(b) $Bo = 0.38, \eta_r = 10, \theta_e = 152^\circ, Re = 124, Ca = 10^{-2}, \%R = 28.7$

Figure 5.5: Effect of gravity on the drop shape, streamline patterns, vorticity (ω), residual vorticity (ω_{res}) and residual angular velocity (v_{res}) are illustrated in a coordinate frame moving with the center of mass of the drop. ω, ω_{res} and v_{res} are shown using polar plots. The azimuthal angle, measured from a line parallel to the solid plate, corresponds to that of the streamline, and the radial location at a given polar angle indicates the magnitude of the respective quantities. In these polar plots, color of each curve matches with the corresponding streamline in the left-most figure. The magenta lines represent $\psi = 0.9, \psi = 0$ and $\psi = -0.9$, showing the thick interface. The drop is moving on a surface inclined to the horizontal, and the black dashed line indicates the direction of gravity. The red dashed line is normal to it.

approach will miss a very important factor to the motion which is solid body rotation which will not produce shear, but is important in determining the dynamics. Hence looking at the actual and residual vorticity plots gives an idea about overall motion, straining regions and rotating regions. As we will see that solid body rotation is indeed an important ingredient in the dynamics.

5.4 Results and discussion

Simulations have been performed in a box of dimensions $512 \times 256 \times 1$ LB units for a cylindrical drop. Wall boundary conditions are applied on two sides and periodic boundary conditions are applied on the other two sides. The simulation is initiated with a semicircular drop of radius $L = 60$ sitting on one wall, which is inclined at an angle α to the horizontal. In response to gravity and surface forces, the drop starts moving on the solid surface. We impose a smooth surface which thus does not display any hysteresis. The simulation is continued till the drop reaches a steady state velocity $\mathbf{V}$. Before compiling all the results into a unified framework, we first examine the effect of varying one physical quantity at a time. We define the Bond number as $Bo \equiv L^2|\mathbf{G}|/\sigma$, the Reynolds number as $Re \equiv LV\rho/\eta$ and the Capillary number as $Ca \equiv \eta V/\sigma$.

5.4.1 Drop shapes and rolling dynamics

We will first look at the effects of parameters contributing to capillary and gravitational forces that primarily affect the drop shapes.

Effect of gravity

The effect of increasing gravity on the steady state drop shape and streamline patterns, total and residual vorticity and angular velocity are illustrated in Fig. 5.5. A larger driving force means larger deformations, so the drop deviates further from its equilibrium shape at zero plate inclination. The streamlines are plotted in the center of mass frame. Fixing the center as the innermost streamline, vorticity and residual vorticity along different streamlines are plotted as functions of azimuthal angle, thus mapping the entire vorticity field inside the drop. The thick interface and the contact line region are excluded from quantitative consideration as there may be spurious velocities generated due to the LB-DI model (Pooley *et al.* 2008).

In Fig. 5.5a, the total vorticity is seen to lie within a small range almost everywhere in the drop, but as discussed above, we may not use this to determine whether there is a solid body rotation. In this case, the residual vorticity indicates that the bulk of the drop is indeed in solid body rotation. The total and residual vorticity values are comparable, showing that there is hardly any shear vorticity. However, in a region near the rear contact line, shear vorticity dominates. Thus the up-down symmetry is broken. Finally the angular velocity based on residual vorticity, $v_{res} = r\omega_{res}$ where r is taken as the radial distance from the center of the innermost streamline, is plotted as a function of azimuthal angle. A perfect solid body rotation, such as that of a solid wheel would have appeared as concentric circles in this plot. At small Bond number, the angular velocity plot has a similar structure, except for a slight loss of symmetry in that the outer streamlines move faster at the top and slower at the bottom.

In the case of large Bo, the drop is elongated normal to gravity, with a clear breakdown in left-right symmetry in its shape, as illustrated in Fig. 5.5b. Except for the very center of the drop there is no resemblance to solid body rotation or even to tank-treading. This is reflected in the the angular velocity plot as well. The residual vorticity is higher in the direction of elongation. Interestingly the residual vorticity is now higher near the rear of the drop, exactly where it was lower at low Bo. This is because at higher gravity the rear of the drop has a tendency to lift off the surface. A given fluid element accelerates and decelerates significantly as it moves on a streamline.

If a solid body is rolling on an inclined surface with an angular velocity of N, then the corresponding vorticity is $2N$. Therefore, we can find the average residual vorticity inside a drop and calculate a corresponding forward velocity of the drop corresponding to the roll as

$$V_{rolling} = \frac{\text{Average}(\omega_{res})}{2} \times \frac{\text{Height of the drop}}{2}. \tag{5.9}$$

Here we take the radius of the drop to be half of the maximum height. Then a quantity called percentage rotation, denoted by $\%R$, is calculated based on the total translational velocity V of the drop, as

$$\%R = V_{rolling}/V \times 100. \tag{5.10}$$

This is different from the roll versus slip velocity as defined in Mognetti *et al.* (2010), where the velocity profile at a single location is considered and the definition does not distinguish the shear vorticity from residual vorticity. In Fig. 5.5 one may see that increasing gravity increases the translational velocity by an order of magnitude, as seen in the increase in Reynolds number, but the associated deformation reduces the percentage rotation $\%R$ by 10%.

Therefore one may infer that an important property that determines the motion of a drop is its geometrical characteristics. Needless to say, the geometry is in turn determined by the volume, the contact angle, the gravitational force and the plate inclination, apart from the viscosity and density ratios and we will investigate some of these below.

The present study is thus valid over a wide range of parameters in contrast to Mahadevan & Pomeau (1999) wherein a spherical drop deformed by incremental gravity was studied. The crucial assumption in Mahadevan & Pomeau (1999) was that the deviation of the shape from a sphere is very small. Relevant length scales of the deformation as a response to gravity were thence derived. These scaling arguments break down when $\theta_e \neq 180°$ due to a finite contact area as we have in our simulations. Also, since we do not restrict our analysis to small Bo, the changes in the surface energy need not scale with that of gravitational potential energy and hence the scaling relations of Mahadevan & Pomeau (1999) will not be valid here.

Effect of contact angle

We now analyze the effect of contact angle alone as illustrated in Fig. 5.6 for drops of same volume. Here gravity is adjusted so that the drop attains the same terminal settling velocity and hence the same Reynolds number. We thus ensure that effects of inertia are nullified in this comparison. In Fig. 5.6, in contrast to the case of $\theta_e = 138°$, one may see that no contribution of rotation is present when $\theta_e = 42°$. Here the entire vorticity of the fluid elements can be attributed to that associated with shear, a typical case dealt under lubrication approximation (Dussan & Chow 1983). As the equilibrium contact angle increases, the percentage rotation increases with the maximum in the case of an almost circular drop. The effect of equilibrium contact angle is thus an intuitive result.

Effect of plate inclination

It is of interest to study how the rolling behavior changes as a function of the tilt angle of the plate. This is because the ratio of the components of gravity normal and tangential to the plate changes. The application of the normal component alone does not produce any movement of the drop, but both components contribute to deciding the shape, and hence the dynamics. The effect of plate inclination on the shape, streamlines and vorticities and their angular dependencies are illustrated in Fig. 5.7. This illustration is for an equilibrium contact angle of 90°. As the plate inclination increases the height of the drop increases, and it tends to lift off from the plate. In turn the percentage rotation increases, and is highest for a tilt angle of 176°. This is another indication that the drop shape is a very important parameter in determining the kinematics inside the drop. The presence of corners and deformed parts of the drop always increase the shear vorticity locally.

As the plate inclination changes, not only the ratio of normal to tangential forces changes, but also their magnitudes. In order to study the effect of this ratio alone, the normal force

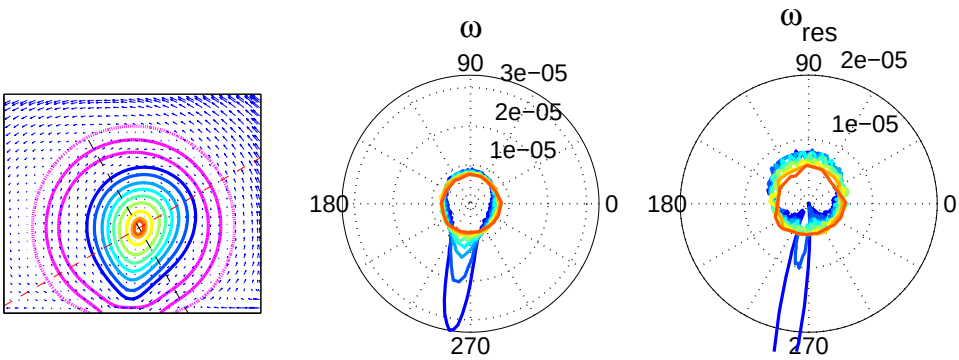

(a) $Bo = 0.027, \theta_e > 180^\circ (h = -0.7), \%R = 17.8, Re = 0.23, Ca = 0.002$

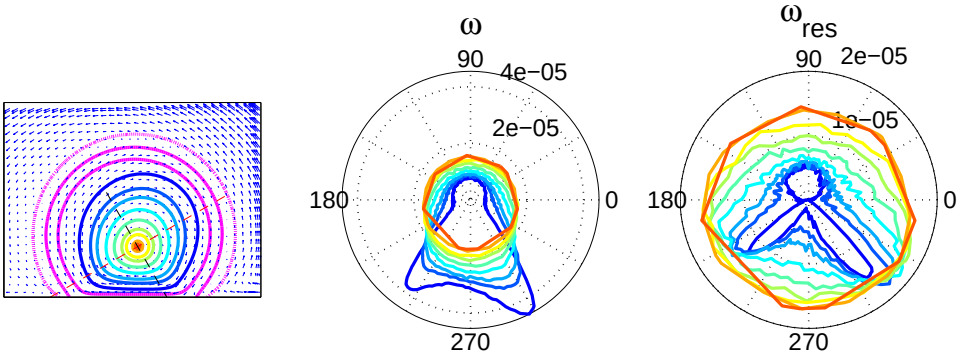

(b) $Bo = 0.028, \theta_e = 138^\circ, Re = 0.23, Ca = 0.002, \%R = 18.5$

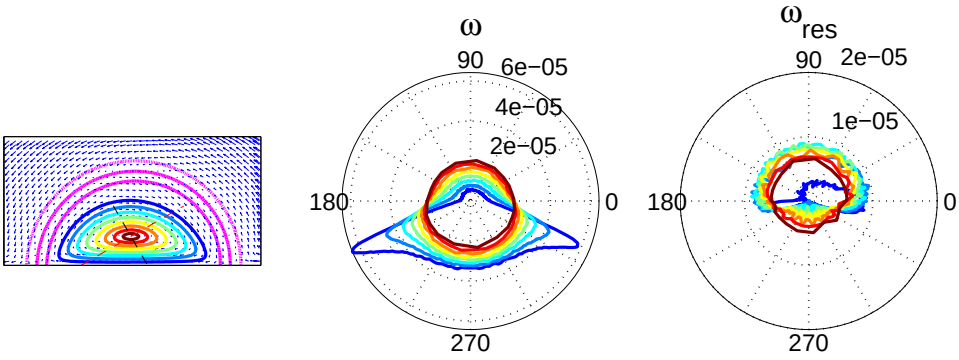

(c) $Bo = 0.038, \theta_e = 90^\circ, Re = 0.23, Ca = 0.002, \%R = 8.7$

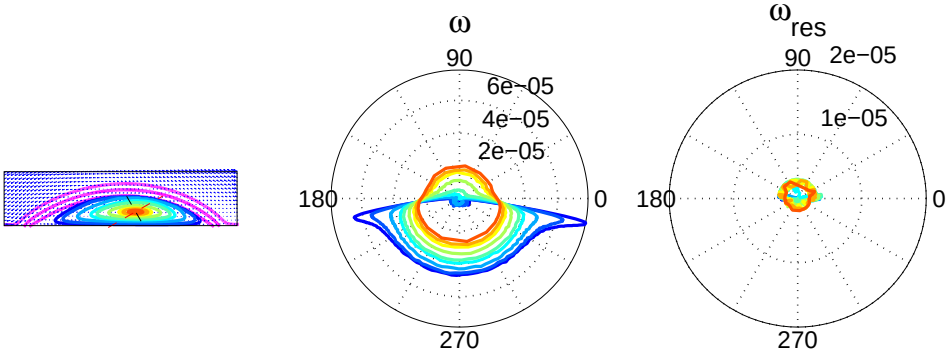

(d) $Bo = 0.068, \theta_e = 42^\circ, Re = 0.23, Ca = 0.002, \%R = 1.9$

Figure 5.6: Effect of contact angle and thence the geometry on the rolling behavior is illustrated. The $\%R$ is larger when the drop shape is closer to a circle. In these cases Re and Ca are kept constant by adjusting the Bo. η_r is kept as 10. A larger reduction in ω_{res} as compared to ω may be observed as θ_e decreases.

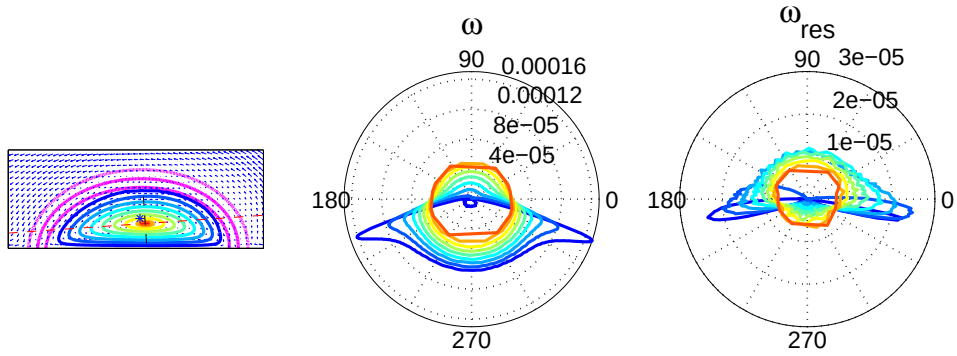

(a) $\alpha = 4, Bo = 0.1, Re = 0.57, Ca = 0.005, \%R = 5.73$

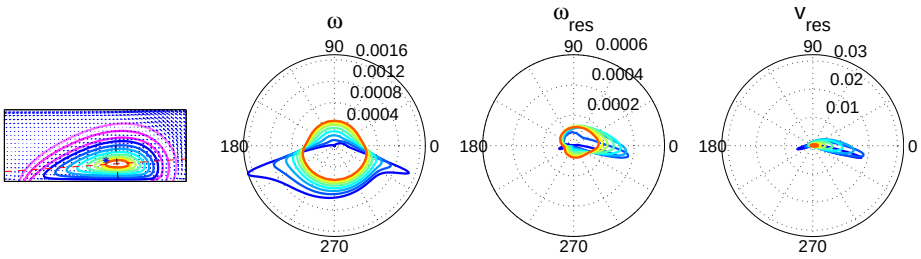

(b) $\alpha = 45 Bo = 1.0, Re = 5.8, Ca = 0.04, \%R = 6.55$

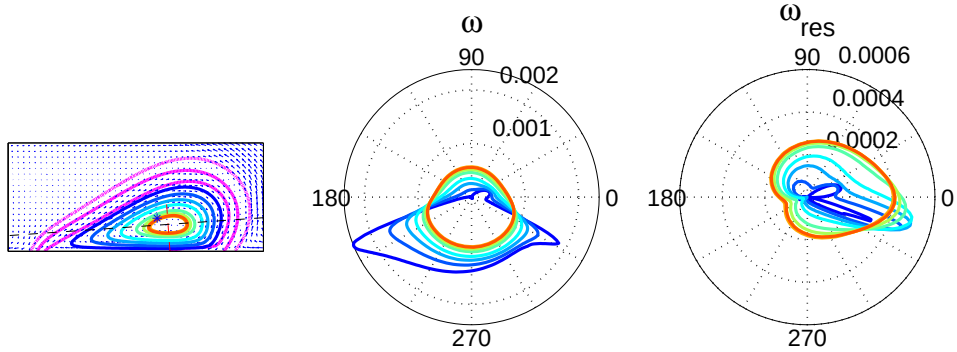

(c) $\alpha = 94, Bo = 1.5, Re = 8.1, Ca = 0.065, \%R = 7.3$

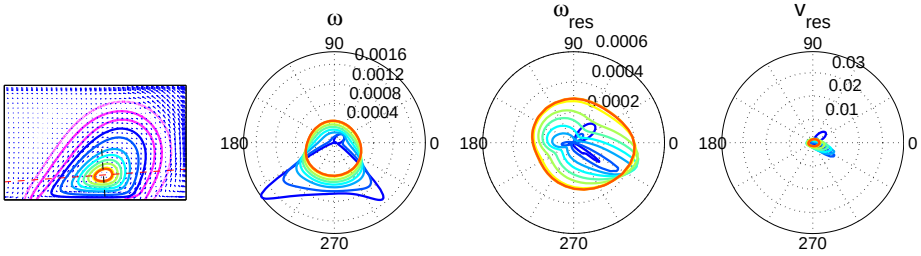

(d) $\alpha = 135, Bo = 1.0, Re = 6.5, Ca = 0.05, \%R = 10$

Figure 5.7: Figure continued in next page.

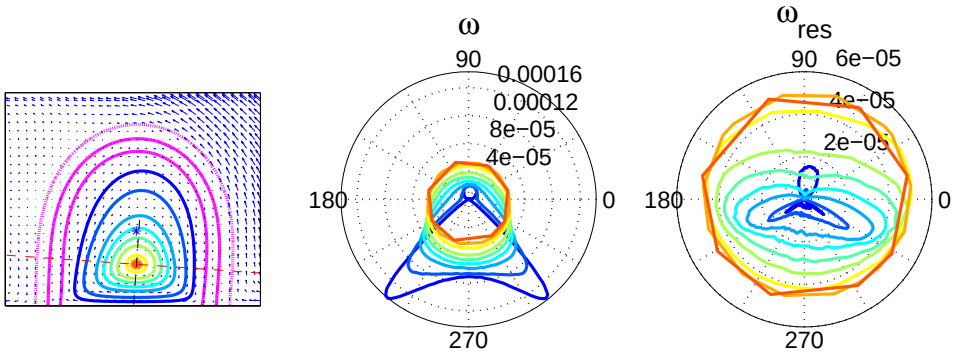

(e) $\alpha = 176, Bo = 0.1, Re = 0.67, Ca = 0.005, \%R = 10.7$

Figure 5.7: Effect of plate inclination on the shape and rotation behavior of drops is illustrated. Equilibrium contact angle is 90° and $\eta_r = 10$. A pendant drop is elongated to almost same size as the radius, producing more solid body rotation in the drop.

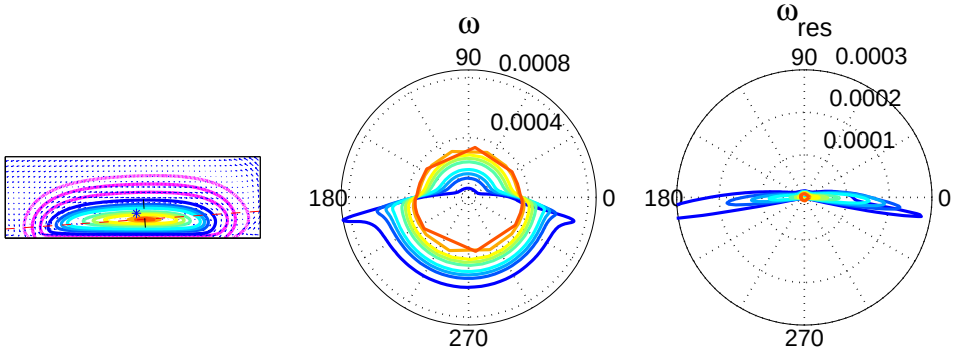

(a) $\alpha = 4, Bo = 0.53, Re = 3.3, Ca = 0.03, \%R = 5.3$

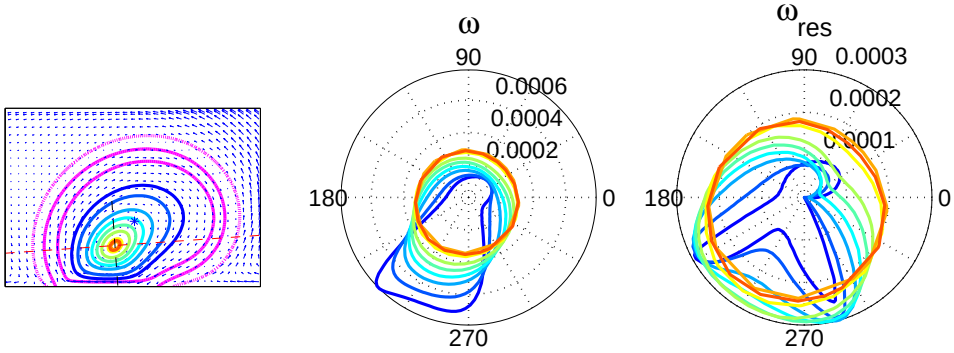

(b) $\alpha = 4, Bo = 0.53, Re = 4.2, Ca = 0.03, \%R = 14.5$, Normal component of gravity is $1/10^{th}$ of the above.

Figure 5.8: Effect of normal component of gravity on the shape and rolling behavior of drops. Equilibrium angle is 90° and $\eta_r = 10$. The tilt angle is chosen as 4°. To differentiate the effect of the tangential component of gravity, the normal component of gravity in (b) is artificially suppressed to $1/10^{th}$ of its value. However, the tangential component being maintained the same in both (a) and (b) yields a comparable settling velocity. The percentage rotation can clearly be very different even at the same settling velocity, due to the change in shape.

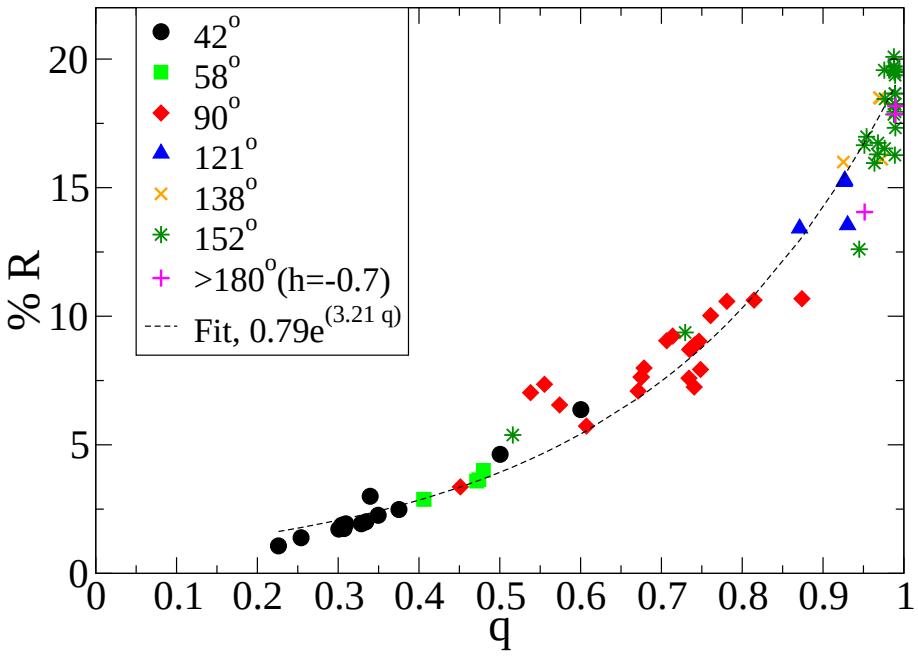

Figure 5.9: The variation of percentage rotation with the isoperimetric quotient is illustrated for different sets of simulations. Each color represents a fixed equilibrium contact angle. Within each set, plate inclinations vary from $\alpha = 4°$ to 176°. Also, Bo ranges from 5×10^{-3} to 1.5 by varying gravity and surface tension. The slip length and the viscosity ratio are kept fixed. An exponential curve fitted through all data points is also shown. Note that moving drops for a wide variation in physical properties fall on this curve.

component was artificially varied keeping the tangential force the same. This corresponds to a simultaneous variation in plate inclination and gravity to achieve the same settling velocity. The results are illustrated in Fig. 5.8. One can clearly see that as the normal component of gravity is reduced, the shape becomes more and more elongated in the direction normal to the plate and this increases the amount of rotation considerably. This is yet another indication that the shape of the drop plays a big role in the rolling behavior of the drop.

5.4.2 Isoperimetric quotient - A shape parameter

In all the previous cases, we see that the deviation from a circular shape plays an important role in determining the dynamics. One can then suitably define a shape parameter to describe the closeness of the shape to a circle, for example, the isoperimetric quotient

$$q = \frac{4\pi \times \text{Area}}{\text{Perimeter}^2}. \tag{5.11}$$

This ratio is unity for a circle and is less than this value for any other shape, since a circle has the least circumference for a given area.

A universal behavior

The percentage rotation in all the cases we have computed so far shows a direct dependence on the isoperimetric quotient, as shown in Fig. 5.9. As expected, the percentage rotation is higher for a shape which is closer to a circle. It is however of interest to note that irrespective of the

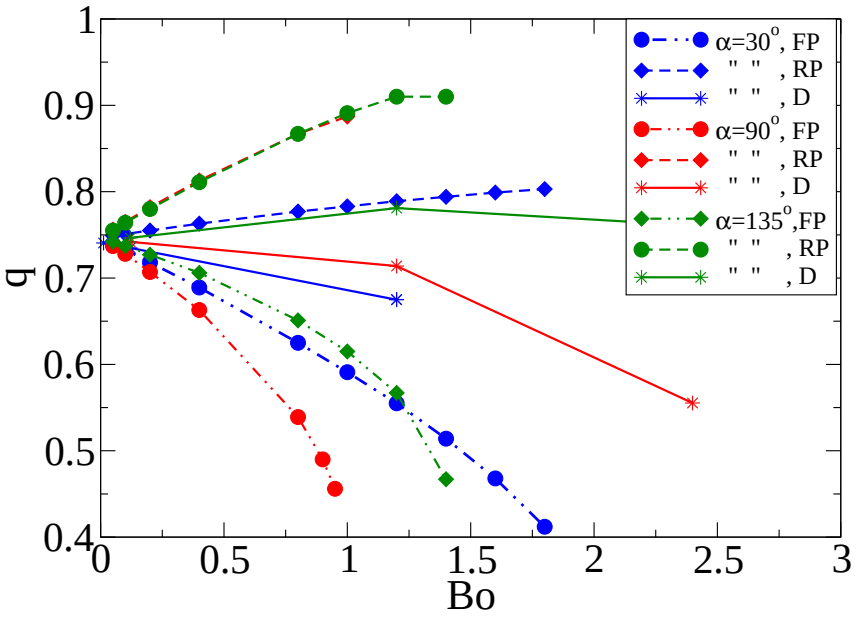

Figure 5.10: Isoperimetric quotient of static shapes is compared with that of dynamic drops for the same Bond numbers. The equilibrium contact angle is 90° and three different plate inclinations, $30°, 90°$ and 135°, are chosen for comparison. Here 'FP' stands for 'front pinned', 'RP' stands for 'rear pinned' and 'D' stands for dynamic cases. The shape parameter of a dynamic drop lies in between those corresponding to front pinned and back pinned static shapes (Chapter 3). This behavior breaks down at large Bond numbers where inertia is higher. In that case, the moving drop is closer to circular than either static shape.

parameters such as equilibrium contact angle, gravity and plate inclination which determines the shape and the deformation, the percentage of roll is a function *only* of this quantity. The collapse of data that we obtain here is a strong indication of this. Note that the data in this figure represents results from over 100 simulations, spanning a wide range of θ_e, α and Bo. However the viscosity, the mobility and the viscosity ratio are kept fixed in the simulations shown so far. As we will see below, percentage rotation curve gets shifted in response to changes in these parameters. Having these parameters same, any change in capillary or gravitational forces will change the shape of the drop and then the amount of rotation can be uniquely provided by Fig. 5.9. Though the dependence of the shape is intuitive, this uniqueness is not.

We have defined the outline of the drop as a contour of $\psi = -0.9$ which can be thought of as the inner limit of the interface. As mentioned earlier, since we use a combination of LB and DI models, there can be spurious interface velocities (Pooley *et al.* 2008) and hence the data outside this line is not considered. We have also tried to calculate this shape parameter from $\psi = 0$ which is theoretically the interface. However this shape fails to capture the deformations correctly for large contact angles.

Comparison with static shapes

It would be interesting to compare the isoperimetric quotient of static drops with that of dynamic cases and see whether any predictions can be made. As explained in Chapter 3 we obtain minimum energy static shapes of drops with either the front end or the rear end pinned. As illustrated in Fig. 5.10, the isoperimetric quotient of the dynamic drops resides between that of

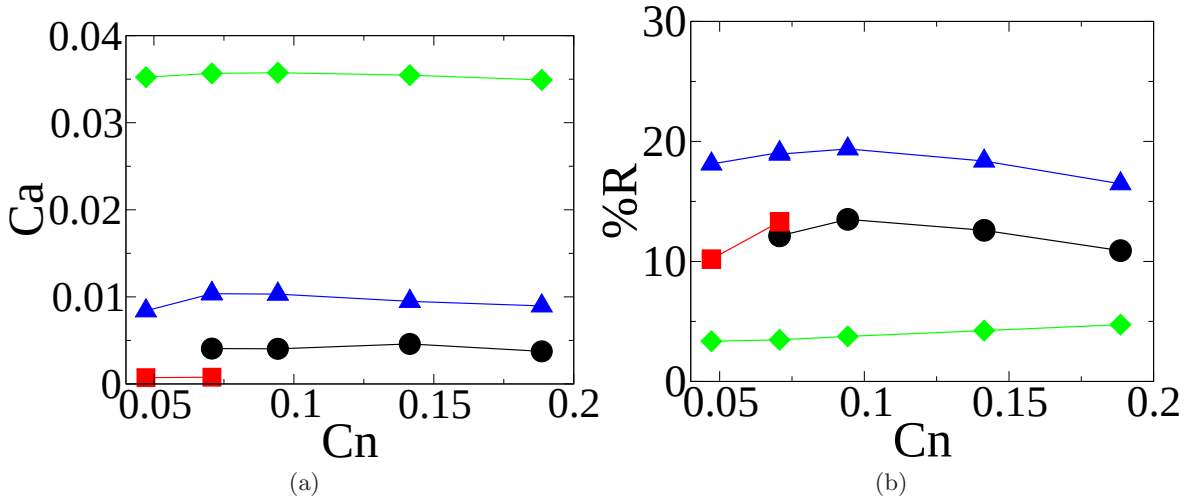

(a) (b)

Figure 5.11: A wide interface is an artifact of the DI method. However, here the Ca and $\%R$ are shown to be independent of Cn.In the above plots the symbols represent different sets of simulations; • for $Bo = 0.19$,$\theta_e = 138°$, $\eta_r = 1$, ■ for $Bo = 0.04$, $\theta_e = 138$, $\eta_r = 1$, ♦ for $Bo = 1.90$, $\theta_e = 90$, $\eta_r = 1$ and ▲ for $Bo = 0.19$, $\theta_e = 138$, $\eta_r = 10$.

front pinned and back pinned cases. This is interesting because one can make predictions about kinematics inside the drop by the analysis of static drops, but only for small Bond numbers. As Bo increases, such monotonic variations in the shape parameter is violated, necessitating the full calculations.

5.4.3 Effect of Cahn number

One of the main drawbacks of the DI models is that it imposes a finite thickness of the interface while for most macroscopic drops, the interface thickness would be negligible compared to any other length scale in the problem. In order to ensure that our results are independent of the assumed interfacial width, simulations with a range of interface thicknesses were conducted. As shown in Fig. 5.11, both the Capillary number and the percentage rotation remain insensitive to interfacial width, to within numerical errors. Here $Cn = \xi/L$, the ratio of interfacial thickness to the macroscopic length, is the Cahn number.

5.4.4 Effect of slip length

Apart from the solid body rotation, which gives a forward velocity to the entire drop, the contact line moves due to the slip provided by the diffusion of the order parameter (Jacqmin 2000). Balancing the advection and diffusion of order parameter across the interface provides a length scale for this diffusion as $\lambda = \sqrt{\eta M}$. We define a nondimensional slip length as $S = \lambda/L$. This slip length is the same as that used in the slip-induced movement of contact line in sharp interface models, and is not an artificial parameter (Yue *et al.* 2010). This slip length should not be dependent on the interfacial width. Hence we can use λ as a measure of slip at the contact line. This means that either mobility or viscosity can be independently or simultaneously varied to change the slip at the contact line. Slip length is here defined using the viscosity of the drop

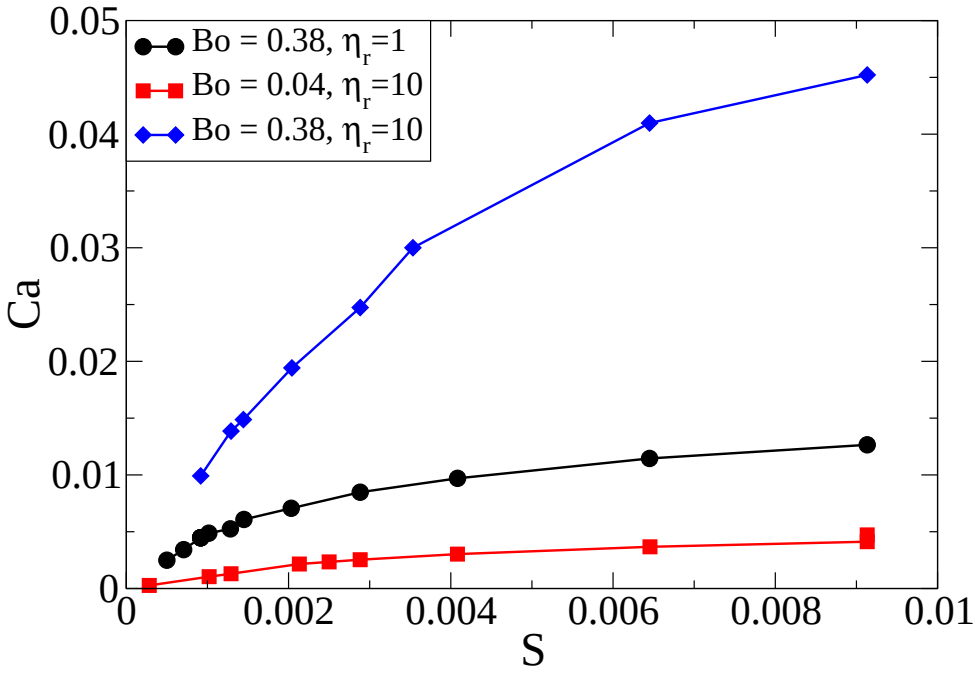

(a)

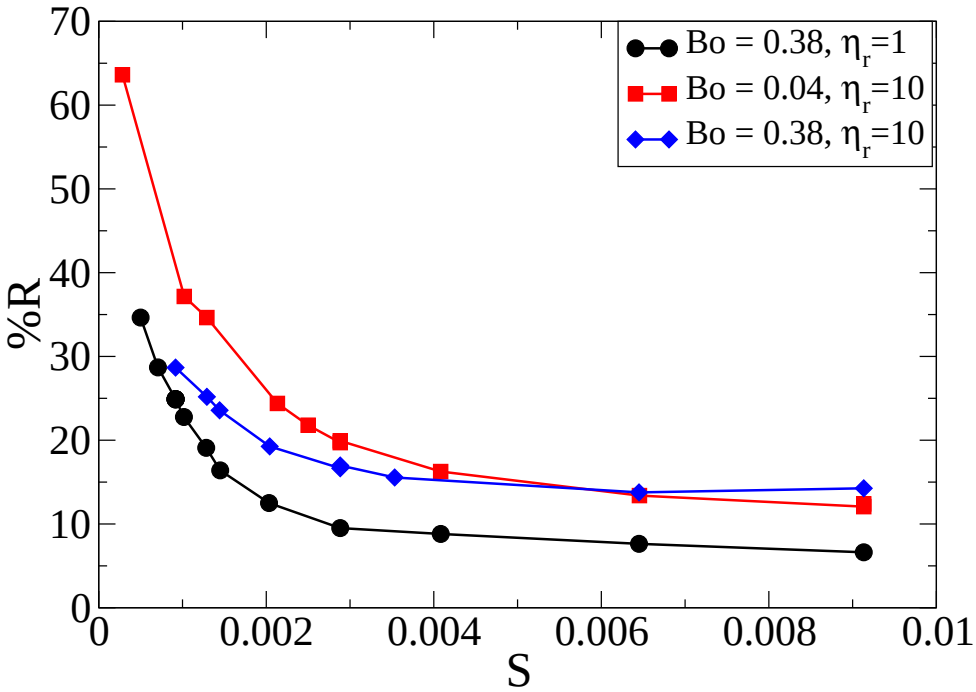

(b)

Figure 5.12: Ca and rolling behavior are plotted as a function of the nondimensional slip length, S. In order to obtain a range of S, the viscosity was independently varied by three orders of magnitude and mobility by one order of magnitude. The equilibrium contact angle is 152°. Larger slip length at the contact line results in larger translational velocity of the drop. Percentage rotation, %R, also strongly depends on the slip length.

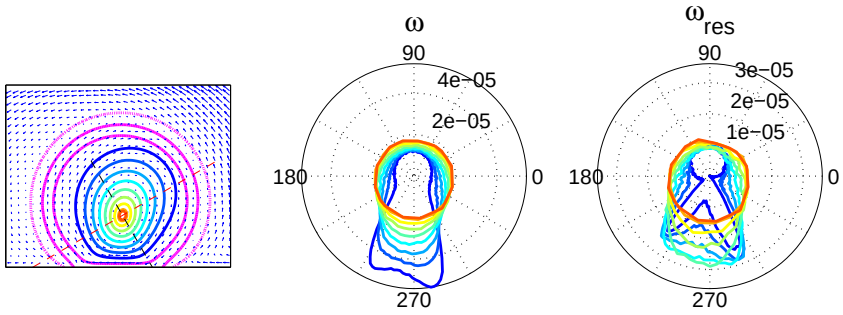

(a) $Bo = 0.04, M = 0.2, \eta = 0.15, Re = 0.3, Ca = 0.003, \%R = 19.7$

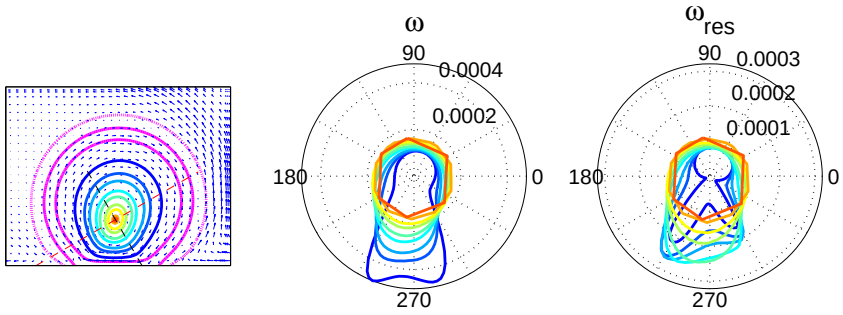

(b) $Bo = 0.03, M = 2, \eta = 0.015, Re = 25, Ca = 0.002, \%R = 19.9$

Figure 5.13: Though viscosity affects the overall dynamics, the contribution of rolling motion to the dynamics remains the same. Here $\alpha = 30°, \theta_e = 152°$ and $\eta_r = 10$. Since viscosity plays a direct roll in the slip of the contact line, mobility was simultaneously adjusted to obtain same slip length to isolate the effect of viscosity alone.

η_I. In principle, the external fluid plays a very important role and viscosity ratio η_r may be needed to define an effective viscosity. For example a geometric mean of η_I and η_{II} is used in Yue *et al.* (2010). However, we refrain from using this relation as it lacks a physical significance.

Both viscosity and mobility are independently varied by at least one order of magnitude in Fig. 5.12 to obtain a range of S. As the slip length increases, the Ca also increases as illustrated in Fig. 5.12a. Intuitively, a slipping drop on an inclined surface will roll less. This is verified in our simulations as shown in Fig. 5.12b wherein the importance of slip length in determining the amount of rotation inside the drop may be inferred. And this dependence appears to be exponential. Larger percentage rotations than those shown, which would correspond to smaller slip lengths could not be obtained reliably with the present numerical simulations.

In our simulations, the nondimensional slip length, S, varies from 10^{-3} to 10^{-2}. In the light of experimental evidence where slip length varies from nm to μm (Tretheway & Meinhart 2002) we expect that our observations remain valid for a range of drop sizes. For macroscopic drops smaller than the capillary length, this ratio is very small and hence a larger fraction of rolling motion may be expected than those seen here. It is worth mentioning however that slip lengths of $10 - 100$ of micron have been reported on patterned surfaces (Tsai *et al.* 2009) or when lubricating gas layers are present (Feuillebois *et al.* 2009) or on super-hydrophobic surfaces (Rothstein 2010). Since we concentrate on the bulk motion of fluid elements, we expect that our simulations are relevant in several practical applications independent of the particular mechanism responsible for the slip.

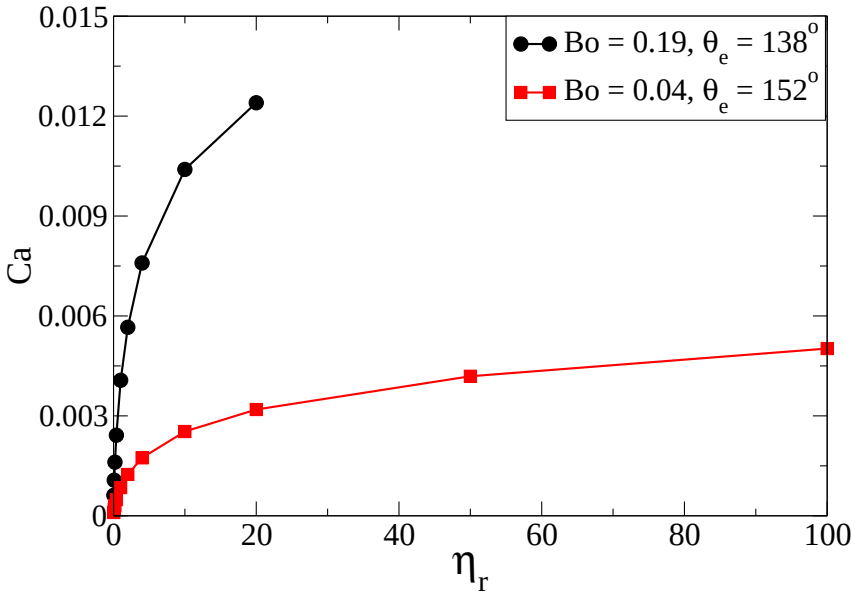

Figure 5.14: Effect of external fluid viscosity on Ca. As the viscosity ratio η_r increases, which corresponds to a reduction in the viscosity of the external fluid, the drop translates faster.

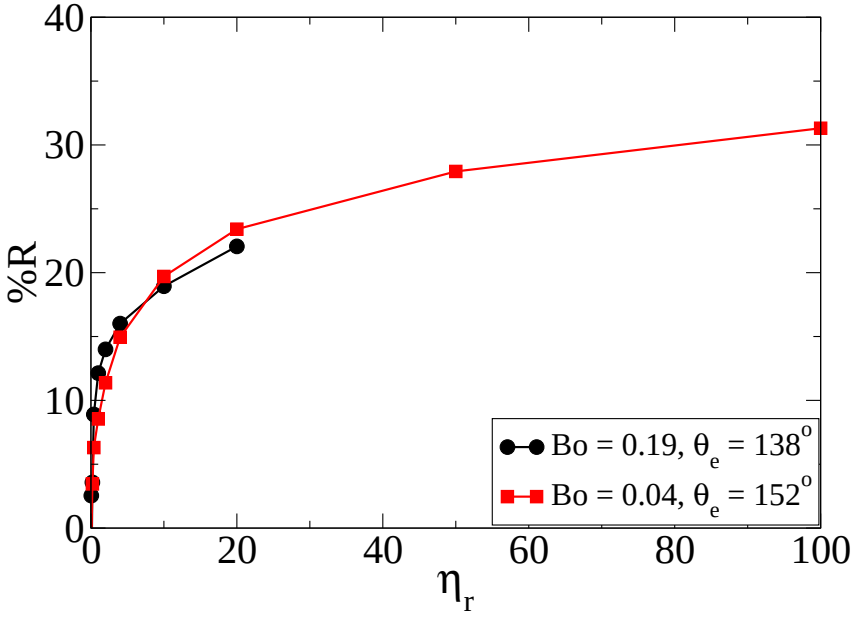

Figure 5.15: Effect of external fluid viscosity on rolling behavior of the drop. The percentage rotation exhibits a strong dependence on the viscosity ratio, η_r. As the external fluid viscosity comes down, rolling motion inside the drop increases. Low viscosity drops in a higher viscosity fluid are seen to almost slide on the wall rather than execute a rolling motion.

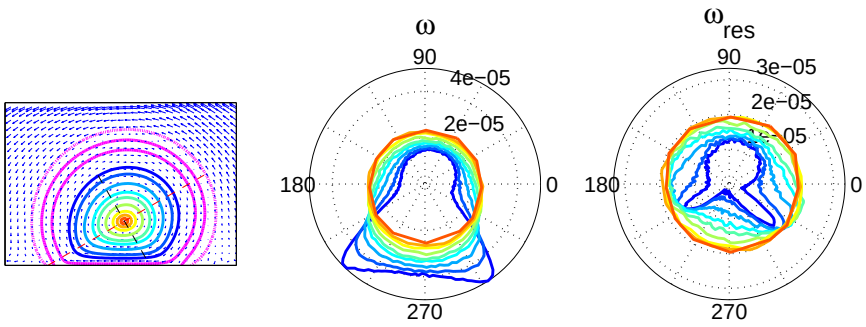

(a) $Bo = 0.19, \eta_r = 20, Re = 0.3, Ca = 0.01, \%R = 22.0$

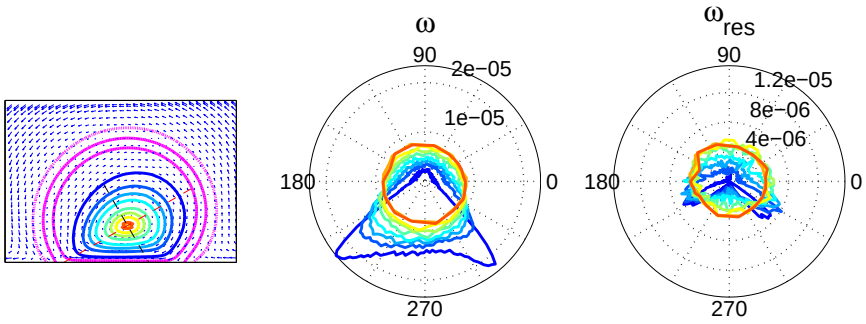

(b) $Bo = 0.19, \eta_r = 1, Re = 0.1, Ca = 0.004, \%R = 12.1$

Figure 5.16: Change in the velocity and vorticity fields when the external fluid viscosity is changed keeping the drop viscosity same. Here $\alpha = 30°$ and $\theta_e = 138°$. As the external viscosity increases, it start affecting the dynamics more as seen in Fig. 5.15.

5.4.5 Effect of viscosity

Here we can vary both η_I and η_{II} simultaneously or individually. Let us look at the case when $\eta_r = 1$ first. Viscosity enters the problem in two ways, via the Reynolds number, and via the slip at the contact line. The former effect is illustrated in Fig. 5.13. In order to effect changes in viscosity in the stress term alone, the slip length was maintained the same in the two cases shown in Fig. 5.13 by simultaneously changing the mobility by the appropriate factor. As a consequence of change in dissipation, the settling velocity is different. But the percentage contribution of rolling is the same in the two cases showing that the viscosity does not explicitly affect the rolling motion.

Now we investigate the role of the viscosity ratio between the drop and the external fluid, in Fig. 5.15. When the viscosity of the external fluid is reduced, the settling velocity and hence the Ca, as expected, increase. Also the percentage of rolling motion is larger. In line with this, one may expect significant amount of rolling in case of a water-air system where viscosity contrast is large. As the viscosity of the external fluid increases and goes beyond that of the drop, the entire dynamics shifts to the external fluid. The drops slides in that case. This too is consistent with intuition, since a 'bubble' will simply slide in a liquid rather than roll when moving on a surface. The changes in the vorticity and residual vorticity fields are illustrated in Fig. 5.16. One may observe that, despite the geometry remaining similar, the percentage rotation increases when the viscosity ratio increases. Therefore the universal curve obtained in Fig. 5.9 will be shifted appropriately by a change in the slip length and viscosity ratio.

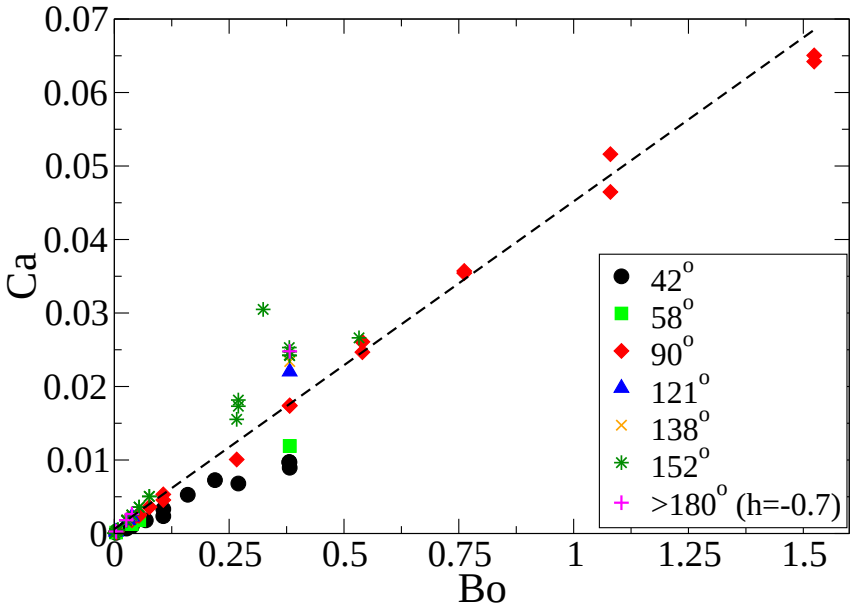

Figure 5.17: The linear relationship between Ca and Bo is illustrated for the data given in Fig 5.9. This data consists of different contact angles, plate inclinations, gravity and surface tension values.

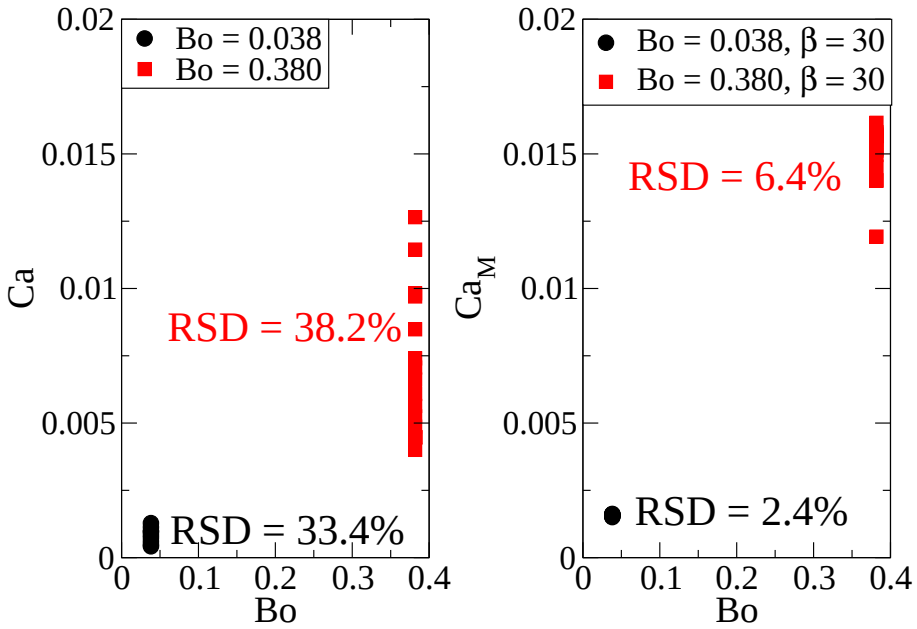

Figure 5.18: Both Capillary number, Ca and modified Capillary number, Ca_M are plotted against Bo. The relative standard deviation (RSD) is small for Ca_M justifying Eq. 5.15. Both viscosity and mobility are varied by at least one order of magnitude to produce a range of slip lengths in these simulations. Equilibrium contact angle is 152° and $Cn = 0.07$. Value of β is adjusted in Eq. 5.15 to obtain the least RSD, hence verifying the role of slip length. Since, $0.1 < Re < 70$ for these simulations, a wider distribution at large Bo may be related to the unaccounted inertial effects.

5.4.6 Scaling relations

Neglecting inertial terms in NSE, one may balance the gravitational driving forces to viscous dissipation to obtain (Kim *et al.* 2001; Grand *et al.* 2005),

$$Ca \sim Bo - \Delta_\theta, \tag{5.12}$$

where $\Delta_\theta = \cos\theta_r - \cos\theta_a$, which is small for most of our simulations. A plot of Ca vs Bo is shown in Fig. 5.17 which corresponds to the data described in Fig. 5.9. This scaling holds good for all our simulations. The small deviations seen are due to inertial effects not accounted for in Eq. 5.12, as well as by the intercept, as shown below. Having seen the effect of contact-line slip on the drop dynamics, we now make a connection between the slip velocity and the above scaling relation. For this we use the generalized Navier's boundary condition (Qian *et al.* 2003; Bonn *et al.* 2009),

$$\frac{u^{slip}}{\lambda} = [\partial_n u] + \frac{\mathcal{L}(\psi)}{\eta}\partial_x\psi \tag{5.13}$$

to make quantitative estimates of the sliding velocity. In the above equation n is a direction normal to the wall. The second term is called the uncompensated Young's stress and one may see that

$$\int_{int} dx[\mathcal{L}(\psi)\partial_x\psi] = \gamma(\cos\theta_d - \cos\theta_e), \tag{5.14}$$

where *int* means 'across the interface' and θ_d is the dynamic contact angle. We can calculate an order of magnitude estimate of Δ_θ from the above equation as $Ca\xi/\lambda$. Since the drop moves at a steady state, both the advancing and receding contact lines move with the same velocity as the center of mass of the drop. We assume that any variation in order parameter and hence the slip is felt over a region of interfacial thickness ξ while the associated slip length λ is the same slip length calculated in a DI model. Accounting for a possible pre-factor in the addition of scaling estimates in Eq. 5.12 we obtain,

$$Ca\left[1 + \frac{\xi}{\beta\lambda}\right] \sim Bo, \tag{5.15}$$

which explicitly includes the role of slip length at the contact line. This relationship is verified in Fig. 5.18, where the change in only the slip length affects the linear relationship between Ca and Bo. We define $Ca_M \equiv [1 + \xi/(\beta\lambda)]$. By choosing a suitable pre-factor β one may see that the second term in the above equation explains in part the distribution in Ca at a given Bo. In other words, the relative standard deviation, which is the ratio of standard deviation to the mean value expressed as a percentage comes down dramatically when Eq. 5.15 is used.

5.5 Conclusions

A hybrid simulation method implementing lattice Boltzmann algorithm with diffuse interface model is used to analyze the drop motion on inclined surfaces under gravity. Modification of the model to provide a viscosity contrast between the fluids, wetting boundary conditions and to introduce gravity are discussed. Following a triple decomposition of velocity gradient

tensor, shear vorticity is removed from the total vorticity. The balance known as residual vorticity is a good measure to characterize the global rolling motion inside the drop. It is shown that the drop shape can be described by a geometrical quantity, isoperimetric quotient, that is primarily responsible for determining the fraction of forward motion accruing from solid body rotation. For a given slip length and viscosity ratio with the external fluid, this dependence is universal, irrespective of the equilibrium contact angle, plate inclination and Bo. The external fluid certainly affects the drop motion with larger rolling motion observed when its viscosity is small compared to the drop viscosity. The importance of the slip mechanism of the contact line is discussed, not only in relation to the rolling motion inside the drop, but also in modifying the coefficient in the scaling relationship between Bo and Ca.

These findings answer the question of roll vs slip in a drop on an inclined surface. Though the analysis is done in two dimensions it can be easily extended to three dimensions and the observations are easily verifiable from the experiments. The method of characterization of rotation from residual vorticity may be applied to the velocity fields obtained through PIV measurements and correlated to a shape parameter defined in 3D. Similarly the effect of slip length can also be easily verified from experiments on patterned surfaces as the results in this work concentrate on the bulk motion of the drop. There is a lack of experimental investigations of binary fluids in presence of a wall as well. We hope that our results will motivate readers to perform experiments to deepen the insights into the drop dynamics on inclined surfaces.

Chapter 6

Capillary spreading of partially wetting drops

6.1 Abstract

Simulations have been performed to understand the capillary spreading behavior of drops on solid surfaces for a wide range of wetting conditions in the absence of gravity. On highly wetting surfaces accelerated regimes of spreading is observed. For drops with finite but small equilibrium contact angle, an evolution equation for the instantaneous contact angle is derived from scaling estimates and under the lubrication approximation. It is shown that there exist two different regimes of growth in two limits of this evolution equation (i) an algebraic regime commonly known as Tanner's law and (ii) an exponential regime where both the contact angle and contact radius relax exponentially to their equilibrium values. The duration where each of these regimes is displayed varies depending on the instantaneous and equilibrium contact angle. Simulations show consistency with these calculations. Though derived for small contact angles, the exponential relaxation is found to be valid for both wetting and de-wetting of drops of all equilibrium contact angles. The presence of various regimes probably explains the small duration of algebraic growth observed in various studies in literature and the discrepancy in the exponents observed in this regime.

6.2 Introduction

A liquid drop when brought in contact with a solid surface changes its shape in order to minimize its free energy. Therefore, on a wettable substrate the contact area of the drop increases until it reaches an equilibrium shape. In the absence of any external forces like gravity, this equilibrium shape is determined by capillary forces alone. The wettability of the substrate is solely characterized by the equilibrium contact angle (θ_e), which satisfies Young's law $\sigma \cos\theta_e + \sigma_{sl} = \sigma_{sg}$ balancing the surface tension forces at the contact line. Here σ, σ_{sl} and σ_{sg} denote the liquid-gas, solid-liquid and solid-gas interfacial tensions respectively. Any drop with a different contact angle (θ) will spread/recede on the surface to finally attain its equilibrium contact angle. The physics of this dynamic process has been a topic of interest to several communities (Bonn *et al.* 2009) e.g. in the conventional chemical industries such as paint and spray industries (Dussan 1979), nano and microfluidics industries (Squires & Quake 2005; Rauscher & Dietrich 2008) including bio-mimetic and biomedical applications (Koch & Barthlott 2009; Mitragotri & Lahann 2009; Castner & Ratner 2002).

As is the case with most studies on interfaces, drop spreading on hydrophilic surfaces can be analyzed using the lubrication approximation of the Navier Stokes equations (NSE) (Oron

et al. 1997). Under this long wavelength approximation, variations normal to the solid surface are neglected in comparison with those along the solid surface. The assumption of small contact angle of the drop justifies this approximation. As a consequence of this approximation, the contact radius of the spreading drop increases algebraically with time. This is called Tanner - Voinov - Hoffman law, often known simply as Tanner's law. This was suggested and observed by Tanner (1979) and later on verified by several investigators (de Gennes 1985; Bonn *et al.* 2009). It is easy to obtain Tanner's law from scaling estimates, in a balance between viscous dissipation and capillary driving force (de Gennes *et al.* 2004). A self-similar solution to the lubrication equation also provides the same (Leal 2007) through a rigorous approach. The asymptotic growth of contact radius is predicted by these calculations, with θ_e assumed to be very small and hence neglected. While an overwhelming literature deals with this regime (de Gennes 1985; Bonn *et al.* 2009), relatively few studies report the exponential relaxation of contact radius on partially wetting substrates (de Ruijter *et al.* 1999; Hocking & Davis 2002). In this chapter we study the transition between these two regimes. By analyzing a wide range of contact angles, different regimes of spreading are identified. Physical properties of the drop affecting the spreading process are also examined.

Several variations of these laws exist when other effects or mechanisms present in the spreading process are taken into account. For example, different mechanisms have been suggested to overcome the contact line singularity (de Gennes 1985) which has been a deterrent in studying spreading processes (Shikhmurzaev 2008*a*). Hocking (1994) showed that inclusion of intermolecular forces to relieve the contact line singularity does not change the scaling laws. But if the spreading process itself is driven by these forces it may give rise to new kinetic laws (Lopez *et al.* 1976) as may happen in the final stages of spreading. Models based on kinetic theory to describe the spreading process provide different scaling laws as reported by de Ruijter *et al.* (1999). However it is also shown how a combination of kinetic theory and hydrodynamics gives rise to several time scales in the problem (de Ruijter *et al.* 2000) and explains the change in exponents observed in experiments. Similarly presence of a precursor film also predicts different scaling laws (Chibbaro *et al.* 2008). Inertia can be important in some situations; Biance *et al.* (2004) studied the initial regime of spreading to predict a square root dependence of time for completely wetting drops while Bird *et al.* (2008) extended this study to partially wetting drops. Another variation was the finding of thermal fluctuations capable of altering these scaling laws (Davidovitch *et al.* 2005; Willis & Freund 2009). A list (but not exhaustive) of spreading laws predicted by various studies is presented in table 6.1.

Experimental and theoretical investigations on partially wetting drops are fewer than those on completely wetting drops. Using silicone oils, Tanner (1979) had verified his scaling laws on capillary spreading of drops. Kinetic laws formulated by incorporating gravity or intermolecular forces at various stages of spreading have also been experimentally verified as in Lopez *et al.* (1976). Since spreading drops are seen everywhere and is a simple geometry to experiment, many of these studies aim to analyze the contact line movement and study the flow near the contact line in detail (Starov *et al.* 1994). Generally correlations obtained from capillary - viscous balance on contact line movement is applicable for any geometry as shown in the spreading experiments of Chen (1988). Experiments of Hocking & Rivers (1982) using spreading of molten glass allowed

Driving force	Theory / Reference	$r(t) \sim$	2D	3D	Assumptions, Valid regime
Inertia	Biance *et al.* (2004)	$r(t) \sim$	$t^{1/2}$	$t^{1/2}$	Any θ, $t \to 0$
Capillarity	de Ruijter *et al.* (1999)	$r(t) \sim$		t	On starting with $\theta \approx \frac{\pi}{2}$, $t \to 0$
	Voinov-Hoffman-Tanner	$r(t) \sim$	$t^{1/7}$	$t^{1/10}$	$\theta, \theta_e \to 0$, $t \to \infty$, Lubrication approx.
	Molecular Kinetics, de Ruijter *et al.* (1999)	$r(t) \sim$		$t^{3/7}$	$\theta, \theta_e \to 0$, $t \to \infty$, Lubrication approx.
	Finite θ_e, de Ruijter *et al.* (1999)	$r_e - r(t) \sim$	e^{-t}	e^{-t}	θ, θ_e are finite, $t \to \infty$
Gravity	Huppert (1982)	$r(t) \sim$	$t^{1/5}$	$t^{1/8}$	$\theta, \theta_e \to 0$, $t \to \infty$, Lubrication approx.
Thermal	Davidovitch *et al.* (2005)	$r(t) \sim$	$t^{1/4}$	$t^{1/6}$	$\theta, \theta_e \to 0$, $t \to \infty$, Lubrication approx.

Table 6.1: Different regimes in spreading of a drop

them to compare their theory on moving contact lines. An exponential power law has been proposed by Lavi & Marmur (2004) based on the experimental observations of partially wetting drops. In the limit of complete wetting the proposed expression reduced to Tanner's law. In nanoscales, the spreading process can be very different on hydrophilic and hydrophobic surfaces (Heslot *et al.* 1990). Also experiments have been performed to verify some of the new theories of interface formation and contact line movement (Shikhmurzaev 1997). Some of the recent studies concentrate on the spreading of inertial drops, especially after impact onto a surface (Rioboo *et al.* 2002; Sikalo *et al.* 2005; Yarin 2006).

Most attempts to establish Tanner's law by simulations have been somewhat unsatisfactory. In a comparison between diffuse interface modeling and level set methods to study the drop spreading problem, Ding & Spelt (2007) showed the approach towards Tanner's law, but this held for less than a decade in time. In the Monte-Carlo simulation study of Milchev & Binder (2002) and in the molecular dynamics (MD) simulation study of He & Hadjiconstantinou (2003), this law is shown, again holding for a small duration. Therefore it is not clear whether these observations indeed represent the expected algebraic growth or represent a different kinetics. Such doubts obviously arise when results from some of the studies reported various exponents eg. in the MD simulations of Yaneva *et al.* (2003); Milchev *et al.* (2002) and lattice Boltzmann (LB) simulations of Iwahara *et al.* (2003). In many of these cases, the presence of a precursor film made it difficult to determine the location of edge of the drop; Wolf *et al.* (2009) who also used LB simulations, introduced a method to extract the expected exponent by choosing the edge of the drop from the knowledge of inflection point in the interface profile. Again behavior consistent with Tanner's law held for less than a decade. Simulations of Merabia & Pagonabarraga (2006) based on particle based models were an improvement, showing the validity of this regime for two

decades. All these simulations were aimed at studying the highly wetting limit. Two numerical studies of the partially wetting situations are discussed later. Here, we scan the entire range, viz highly wetting to highly non-wetting drops, over long times to identify various regimes of spreading in various cases.

Before this we discuss the few studies on the spreading of partially wetting drops. de Ruijter *et al.* (1999) showed that the driving force which is the gain in free energy due to the change in surface area balances various dissipation terms such as kinetic and viscous losses . They then obtained a general relationship to predict the growth of the contact radius of a partially wetting drop. When the dynamic contact angle approaches the equilibrium contact angle this equation predicts an exponential relaxation of the contact radius of the drop. An algebraic growth rate is predicted at intermediate times. These calculations have been justified based on experimental observations, but only for the algebraic regime where a switch-over from hydrodynamics to kinetics takes place. Here, we show that both algebraic and exponential regimes indeed exist in the spreading process of any partially wetting drops both in terms of contact radius and contact angle. The exponential regime disappears for completely wetting drops. Our analytical results are obtained by assuming a finite but small contact angle. This allows us to treat such partially wetting drops under the lubrication approximation. Thus we derive the conditions for the existence of each regime. The duration of each regime can be considerably different depending upon the value of θ_e. We then use a hybrid method combining lattice Boltzmann method for hydrodynamics and a diffuse interface model to simulate the spreading process in two dimensions. Note that no approximation on θ_e is made in our simulations. The analytical calculations are verified through these simulations over long times to observe different regimes of spreading. In fact the algebraic growth, followed by an exponential one, is observed for contact angles well beyond those that could reasonably be covered under the lubrication approximation. In our simulation technique the wetting properties of the solid surface can be easily adjusted to cover both positive and negative spreading parameters, with positive values corresponding to a "super-wetting" situation. Note that spreading parameter is defined as $S = \sigma_{sg} - (\sigma_{sl} + \sigma)$. Thus the entire spectrum viz, completely wetting to completely non-wetting surfaces, is analyzed. While growth rates faster than Tanner's law is observed for super-wetting surfaces, the exponential relaxation is found to be valid for spreading on even hydrophobic surfaces and dewetting of drops.

Spreading of drops with a finite contact angle have been studied using a similar method by Khatavkar *et al.* (2007). Though their data seems to suggest an exponential relaxation (visually) this has never been discussed qualitatively or quantitatively. A similar study by Ding & Spelt (2007)again focused on verifying only the algebraic spreading law and making comparisons with other simulation techniques.

6.3 Theory

6.3.1 Tanner's law

The lubrication approximation of the Navier Stokes equations, along with mass conservation yields

$$\frac{\partial \xi}{\partial t} = \frac{1}{3\eta}\nabla.(\xi^3 \nabla p) \tag{6.1}$$

where $\xi(\mathbf{x})$ represents the interface and $\mathbf{x}$ is the transverse plane, t the time, p the dynamic pressure and η the viscosity. In the case of curvature driven pressure difference, neglecting the nonlinear terms, one arrives at

$$\frac{\partial \xi}{\partial t} = \frac{1}{3\eta}\frac{\partial}{\partial x}\left(\xi^3 \frac{\partial^3 \xi}{\partial x^3}\right) \tag{6.2}$$

in one dimension. This expression admits self similar solutions (Leal 2007) of the form

$$\xi(x,t) = \frac{\Xi(x/t^{1/7})}{x}. \tag{6.3}$$

Then mass conservation implies an algebraic growth of the contact radius. A simple scaling between viscous and capillary forces also implies the same (de Gennes *et al.* 2004) as shown in the next section.

6.3.2 Evolution equation of drops: Different regimes

Retaining a finite but small value of θ_e provides the growth laws of contact radius in the final stages of partially wetting drops. The lubrication approximation is used in Hocking & Davis (2002) to analyze this regime. In de Ruijter *et al.* (1999), the analysis includes a combination of hydrodynamics and kinetic theory. Therefore we provide the essentials of the derivation to show that both contact angle and contact radius relax exponentially at the terminal stages of drop spreading. An algebraic growth regime may be observed at intermediate stages. In the capillary driven spreading of drops on horizontal surfaces, the drag force due to viscous dissipation will be balanced by the driving force. If θ is the dynamic contact angle, then $\sigma(\cos\theta_e - \cos\theta)$ is the driving force at the contact line. The drag force due to viscous dissipation in a wedge is given by a well known result (de Gennes *et al.* 2004):

$$F = \frac{3\eta l}{\theta} U \tag{6.4}$$

where $l = \log(R/a)$, a nondimensional parameter dependent upon the macroscopic length, R, and the cut off length a. The contact line velocity is denoted as U. Since the dissipation is concentrated near the contact line, Eq. 6.4 is sufficient to estimate the total dissipation and the dissipation in the rest of the drop may be considered. Hence the capillary - viscous balance provides

$$U = \frac{dR}{dt} = \frac{U^*}{3\eta l}\theta[\cos\theta_e - \cos\theta] \tag{6.5}$$

where $U^* = \sigma/\eta$, the characteristic capillary velocity. For complete wetting

$$U \approx \frac{U^*}{6l}\theta^3 \tag{6.6}$$

which represents the well known result of Tanner's law. Imposing the mass conservation for a wedge, $\theta \sim R^{-2}$, the above expression gives $R \sim t^{1/7}$. We are interested in calculating the variations of this when the drop has a finite equilibrium contact angle and it cannot spread forever. In this case, we use the entire shape of the drop rather than just the wedge while imposing mass conservation. Assuming quasi-steady state, the drop takes only circular shapes. The area of the drop is then given by

$$A = R^2\frac{\theta - \sin\theta\cos\theta}{\sin^2\theta} \tag{6.7}$$

providing a relation between contact angle θ and contact radius R as

$$R = \sqrt{A}\frac{\sin\theta}{(\theta - \sin\theta\cos\theta)^{1/2}} \tag{6.8}$$

and mass conservation implies

$$\frac{dR}{dt} = -\frac{d\theta}{dt}\sqrt{A}\frac{\sin\theta - \theta\cos\theta}{(\theta - \sin\theta\cos\theta)^{3/2}}. \tag{6.9}$$

Non dimensionalising the time, $\tau = t/(3l\sqrt{A}/U^*)$, we have

$$\frac{d\theta}{d\tau} = -\theta\frac{(\theta - \sin\theta\cos\theta)^{3/2}}{\sin\theta - \theta\cos\theta}[\cos\theta_e - \cos\theta], \tag{6.10}$$

which describes the evolution of the dynamic contact angle during the spreading process. This ordinary differential equation does not have an analytical solution, however it reduces in different limits as follows.

In the limit of complete wetting where $\theta \to 0$, we have

$$\frac{d\theta}{d\tau} \sim -\sqrt{\frac{2}{3}}\theta^{9/2} \tag{6.11}$$

which corresponds to Tanner's law. In the case of finite equilibrium contact angle, we can define $\delta = \theta - \theta_e$ and then to the leading order of δ, we get the following expression,

$$\frac{d\delta}{d\tau} \sim -\alpha\delta + O(\delta^2) \tag{6.12}$$

where

$$\alpha = \theta_e\sin\theta_e\frac{(\theta_e - \cos\theta_e\sin\theta_e)^{3/2}}{\sin\theta_e - \theta_e\cos\theta_e} \sim \sqrt{\frac{8}{3}}\theta_e^{7/2} + O(\theta_e^{9/2}) \tag{6.13}$$

which sets the relaxation of the dynamic contact angle to equilibrium contact angle. Hence,

$$\theta = \theta_e + Ce^{-\alpha\tau} \tag{6.14}$$

where C is the constant of integration. When $\tau \to \infty$, $\theta \to \theta_e$. Since this equation is valid only in the later stages of spreading process, only a matching procedure with a description of early or intermediate stages of dynamics is necessary to determine the constant C. Now, Eq. 6.8 when expanded to leading order in δ gives the evolution of contact radius

$$R_e - R = \frac{C\sqrt{A}\theta_e \sin\theta_e}{\alpha} e^{-\alpha\tau} \sim C\sqrt{\frac{3A}{8}}\theta_e^{-3/2} e^{-\alpha\tau} \tag{6.15}$$

where R_e is the contact radius when the drop is completely relaxed. Hence the contact radius also relaxes exponentially. This stage of spreading is termed as 'exponential' regime of spreading and is in the same form as derived by de Ruijter *et al.* (1999) and Hocking & Davis (2002).

6.3.3 Transition from Tanner's law to exponential regime

We will now show the connection between the two seemingly different regimes, exponential vs algebraic growth. In fact these are two completely separate regimes of spreading due to the different behavior of the trigonometric functions in Eq. 6.10 in two limits as described below. These trigonometric functions are associated with both the shape of the drop and the driving force. This analysis is simple in the limit of $\theta \to 0$ and considering the leading order terms. Hence Eq. 6.10 gives

$$\frac{d\theta}{d\tau} \sim \sqrt{\frac{8}{3}}\theta^{5/2}\left[\frac{\theta^2}{2} - \frac{\theta_e^2}{2}\right] = -\sqrt{\frac{2}{3}}(\theta_e + \delta)^{5/2}(2\delta\theta_e + \delta^2) \tag{6.16}$$

$$\text{When} \quad \delta << \theta_e, \quad \frac{d\delta}{d\tau} \sim -\sqrt{\frac{8}{3}}\theta_e^{7/2}\delta \quad \Rightarrow \quad \text{exponential regime} \tag{6.17}$$

$$\text{When} \quad \delta >> \theta_e, \quad \frac{d\theta}{d\tau} \sim -\sqrt{\frac{2}{3}}\theta^{9/2} \quad \Rightarrow \quad \text{Tanner's regime} \tag{6.18}$$

Therefore there are two limits. When $\theta >> \theta_e \Rightarrow \delta >> \theta_e$, the drop spreads according to Tanner's law. When $\theta - \theta_e \sim \theta_e$ spreading process slows down. Finally when $\theta - \theta_e << \theta_e$, the exponential regime is observed. In the case of a complete wetting drop where strictly $\theta_e = 0$, an 'exponential' regime is not observed. In short, Tanner's law followed by the exponential regime is observed in any spreading process of a drop with finite equilibrium contact angle, the durations vary from case to case depending upon the numerical values of θ and θ_e.

It is possible to get a general expression describing these regimes in rather restricted case of small angles where Eq. 6.5 reduces to

$$\frac{dR}{dt} = \frac{U^*}{3l}\frac{\theta}{2}[\theta^2 - \theta_e^2] \tag{6.19}$$

and the relation between R and θ (Eq. 6.8) reduces to $3A = 2R^2\theta$ to yield

$$\frac{R^6 dR}{R_e^4 - R^4} = \frac{27A^{7/2}}{16R_e^4} d\tau. \tag{6.20}$$

Then we obtain

$$\tanh^{-1}(\frac{R}{R_e}) - \tan^{-1}(\frac{R}{R_e}) - \frac{2}{3}\left(\frac{R}{R_e}\right)^3 = \frac{27A^{7/2}}{16R_e^4}\tau + \text{Constant} \tag{6.21}$$

This expression describes the evolution of the drop in all three regimes. When $R \to R_e$, the above expression predicts exponential regime:

$$R_e - R \sim R_e e^{-\sqrt{\frac{8}{3}}\theta_e^{7/2}\tau} \tag{6.22}$$

which corresponds to the small angle limit of Eq. 6.15. But if $\theta_e = 0$ or very small, we have $R_e \to \infty$ so that $R << R_e$ then Eq. 6.21 may be expanded in R/R_e to obtain,

$$\frac{2}{7}\left(\frac{R}{R_e}\right)^7 + \frac{2}{11}\left(\frac{R}{R_e}\right)^{11} + O\left(\frac{R}{R_e}\right)^{15} \sim \frac{27A^{7/2}}{8R_e^7}\tau + \text{Constant} \tag{6.23}$$

This recovers Tanner's law to the leading order. We can expect this to be applicable in all perfectly wetting situations. Note that the correction term is only at $O(R/Re)^{11}$ showing the robustness of this universal law. When the dynamic contact angle of the drop approaches the equilibrium contact angle, i.e, when $\delta \sim \theta_e$, contact radius $R \to R_e$, correction terms start making a difference and the drop spreads slowly. Finally when $\theta \to \theta_e$, exponential regime sets in.

6.4 Simulations - Diffuse interface model

The drop spreading process is simulated using a diffuse interface model (Kendon *et al.* 2001) . The hydrodynamics is described by the Navier Stokes equations (NSE) (Batchelor 1967; Landau & Lifshitz 1959),

$$\partial_t(\rho\mathbf{u}) + \nabla\cdot(\rho\mathbf{u}\mathbf{u}) = -\nabla p + \eta\nabla^2\mathbf{u} + \psi\nabla\mu. \tag{6.24}$$

along with the equation for mass conservation. An order parameter ψ is defined as the normalised difference in density distinguishes the two fluids. Its dynamics is governed by the Cahn - Hilliard equation (CHE) (Chaikin & Lubensky 1995).

$$\partial_t\psi + \nabla\cdot(\mathbf{u}\psi) = \nabla\cdot(M\nabla\mu) \tag{6.25}$$

Here the mobility M relates the order parameter flux and the chemical potential gradient driving the diffusion. While the order parameter is advected by the flow field in Eq. 6.25, the gradients in the order parameter give rise to forces driven by chemical potential, and extra stresses appear in the NSE (Anderson *et al.* 1998). The equilibrium thermodynamics of the order parameter is described by the Landau free energy functional (Chaikin & Lubensky 1995; Rowlinson & Widom 1982)

$$F(\psi) = \int\left(\frac{A}{2}\psi^2 + \frac{B}{4}\psi^4 + \frac{K}{2}\left|\nabla\psi\right|^2\right)d\mathbf{r}, \tag{6.26}$$

with $A < 0$, $B > 0$ and $\mathbf{r}$ stand for the spatial dimensions. Two uniform solutions $\psi = \pm\sqrt{A/B}$ coexists across a fluid interface for this free energy functional form. The interfacial

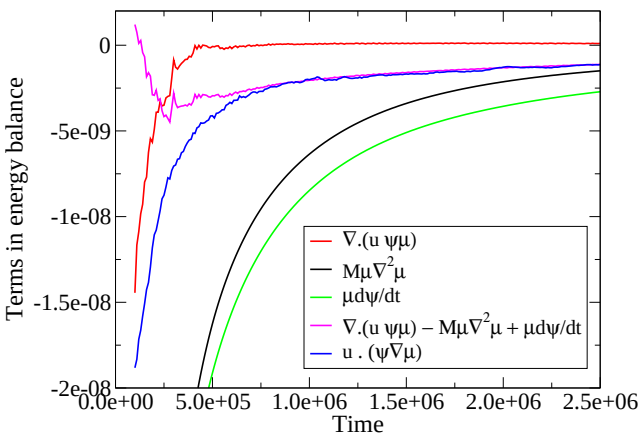

(a) Verification of the energy balance associated with CHE, Eq. 6.27

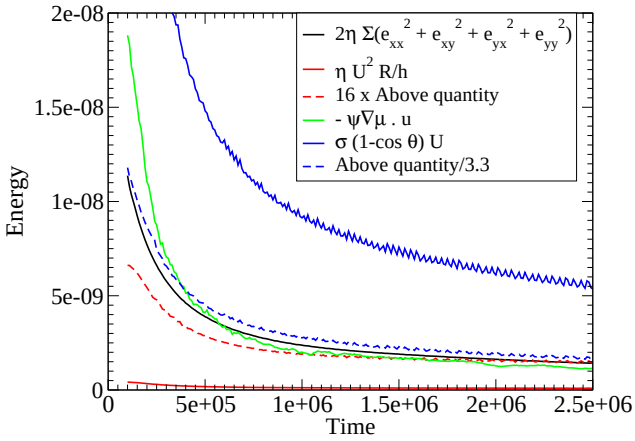

(b) Scaling estimates of driving and dissipating energies differ only by a numerical factor from the actual values

Figure 6.1: Verification of different energy calculations during the spreading process in the diffuse interface model.

thickness $\xi = \sqrt{2K/A}$ and the interfacial energy $\gamma = \frac{2}{3}\sqrt{2KA^3/B^2}$ are controlled by three parameters A, B, and K (Kendon *et al.* 2001). Desired wetting of the solid surface is obtained by introducing another energy functional for the fluid-solid interface $H\psi_s$ where ψ_s is the value of order parameter at the wall (Desplat *et al.* 2001; Briant *et al.* 2002). By tuning the parameter H which is redefined as $h = H\sqrt{2/KB}$ we can modify the properties of the surface.

We use the hybrid algorithm combining lattice Boltzmann technique for hydrodynamics and a method of lines for diffuse interface model to simulate this binary fluid system. The details of the algorithm are given in Chapters 4 and 5.

6.5 Results and Discussion

We have done simulations in a two dimensional domain with wall boundary conditions on two sides and Neumann boundary conditions on the other two sides. This is because we simulate only one half of the drop. Since lattice Boltzmann (LB) technique is used to solve the hydrodynamics, viscosity is related to the relaxation time as $\eta = \tau/3$. Also, all dimensional quantities are in LB units where the discretization of space and time are chosen with $\Delta x = 1$ and $\Delta t = 1$ so that the sound speed is $1/\sqrt{3}$.

6.5.1 Energy balance associated with CHE and verification of scaling estimates from simulation data

Before verifying the scalings derived in the previous sections, it is necessary to check the energy balance in the simulations. This is because,

1. It is well known that spurious velocities may be present in the interface region and in the contact line region (Pooley *et al.* 2008) in this diffuse interface model. They may cause additional dissipation of energy in the system and if they are large enough it may change the scalings derived.

2. The contact line movement is through the diffusion of the order parameter across the interface near the solid surface. If the time scale for the equilibriation of the order parameter is larger than the flow time scale, then gradients of order parameter may generate Marangoni effects near the contact line, altering the predicted growth laws.

Order parameter dynamics is governed by CHE and can be rearranged as

$$\begin{aligned} \nabla \cdot (\mathbf{u}\psi) &= M\nabla^2\mu - \frac{\partial \psi}{\partial t}, \\ \nabla \cdot (\mathbf{u}\psi\mu) - \psi\mathbf{u} \cdot \nabla\mu &= \mu(M\nabla^2\mu - \frac{\partial \psi}{\partial t}), \\ \nabla \cdot (\mathbf{u}\psi\mu) - M\mu\nabla^2\mu + \mu\frac{\partial \psi}{\partial t} &= \psi\mathbf{u} \cdot \nabla\mu. \end{aligned} \tag{6.27}$$

This $\psi\mathbf{u} \cdot \nabla\mu$ can be inserted into the energy equation derived from NSE to obtain a complete energy balance (Bird *et al.* 2006),

$$\partial_t \frac{u^2}{2} + \mu\partial_t\psi = \nabla \cdot \left(\mathbf{u}\frac{u^2}{2}\right) - \nabla \cdot (P\mathbf{u}) + P(\nabla \cdot \mathbf{u}) + \nabla \cdot (\mathbf{u} \cdot \tau_v) - \tau_\mathbf{v} : \nabla\mathbf{u} - \nabla \cdot (\mathbf{u}\psi\mu) + \mu M\nabla^2\mu \tag{6.28}$$

where τ_v is the viscous stress. Here the terms inside the divergence operator, $\nabla \cdot ()$, vanish in an integral sense in a periodic or bounded domain. They just serve to convect energy from one place to another within the domain, and do not act as a source or sink of energy. Just like $\tau_\mathbf{v} : \nabla\mathbf{u}$ gives rise to an irreversible dissipation, a part of $\mu M\nabla^2\mu$, i.e, $M|\nabla\mu|^2$ is always positive, hence is monotonic and is associated with the total change in the free energy due to order parameter dynamics.

It is easy to deal with energy balances associated with CHE and NSE separately. The energy associated with different terms of CHE as in Eq. 6.27 is verified in Fig. 6.1a which is performed as a consistency check. Now, in order to check the scaling estimates of the previous section, relevant terms are plotted in Fig. 6.1b. Here the total viscous dissipation $2\eta\Sigma\mathbf{e} : \mathbf{e}$, the corresponding scaling estimate $\eta U^2 R/h$, the driving force written as $\psi\nabla\mu \cdot \mathbf{u}$ and the corresponding scaling estimate $\sigma(1 - \cos\theta)U$ are plotted. It may be noted that the scaling estimates correctly capture the original behavior of viscous dissipation terms and and surface energy terms and differ only by a numerical factor. This is an indication that effects like Marangoni flow are negligible in the simulations. Numerical dissipation and dissipation due to spurious velocities are also negligible.

6.5.2 Equilibrium contact angle and complete wetting in diffuse interface models

As discussed earlier in section 6.4, desired wetting of the wall is achieved by introducing another energy functional at the solid-fluid interface. This is also explained in Chapter 5 in detail. Thus tuning the parameter h, which fixes the relative surface energies at the wall on either side of the interface, desired wetting may be obtained. In contrast to the simulations in Chapter 5 where we dealt with intermediate equilibrium contact angles, here we explore the entire range of contact angles. There are two points to be mentioned in this context.

Firstly it was observed that there was a small difference between the contact angle that

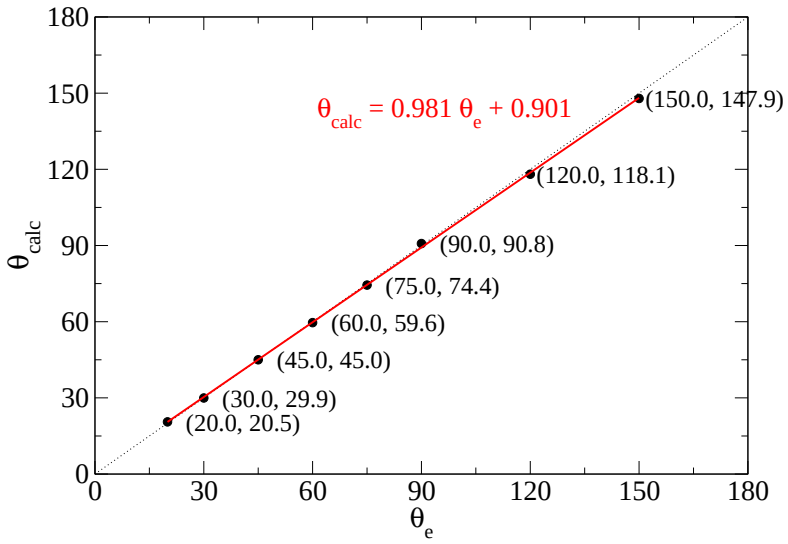

Figure 6.2: Final contact angle, θ_{calc} obtained from simulations is plotted against the equilibrium angle (θ_e) based on Eq. 5.7. These simulations have been done for $\eta_r = 1$ and $M = 0.1$ or $M = 1.0$. It may be seen that $\theta_{calc} = 0.9815\theta_e + 0.9012$ where both θ_{calc} and θ_e are expressed in degrees.

a drop attained and the prescribed equilibrium contact angle as illustrated in Fig. 6.2. This difference in angles is arising out of numerics. Note that there is a gradient of order parameter at the wall on either side of the interface and all the interfaces are diffuse. We call the final angle obtained from simulations as θ_{calc} which will be used in the calculations in later sections. Note that $\theta_{calc} = 0.9815\theta_e + 0.9012$ which is obtained by a linear fit of the data points shown in Fig. 6.2.

Since the interface is diffuse, the definition of the interface is not an unambiguous quantity in this model. As illustrated in Fig. 6.3 the general definition $\psi = 0$ may not really represent the interface, especially in highly wetting situations. For example, in Fig. 6.3a, $\psi = 0.5$ will give a precursor film in front of the contact line while $\psi = 0$ will give a finite contact angle. More importantly changing h to obtain partially wetting drops to completely wetting drops is a smooth transition in terms of order parameter field and no jump is seen at $h_{cr} = 0.6812$ which corresponds to $\theta_e = 0$ according to Eq. 5.7. In the following sections we consider $\psi = 0$ as the definition of interface and contact angle is based on this definition. Despite these ambiguities, it is worth mentioning that the results we obtain match very well with the theoretical predictions.

6.5.3 Partially and completely wetting drops

In order to verify the scaling estimates derived in the previous section 6.3, drop spreading simulations have been performed on wetting surfaces. In our frame work it is easy to achieve different wetting properties of the solid by tuning the parameter h which determines the solid-fluid interfacial energy. Both positive and negative spreading parameter can be obtained. The simulations are initialized with a drop shape as part of a circle with $\theta = 45°$ which is then allowed to relax. The two fluids are distinguished by order parameter values of $\psi = -1$ and $\psi = 1$ separated by a sharp interface. The diffusion of the order parameter results in an artificial dip in the contact radius in the beginning of the simulation before the spreading sets in. The

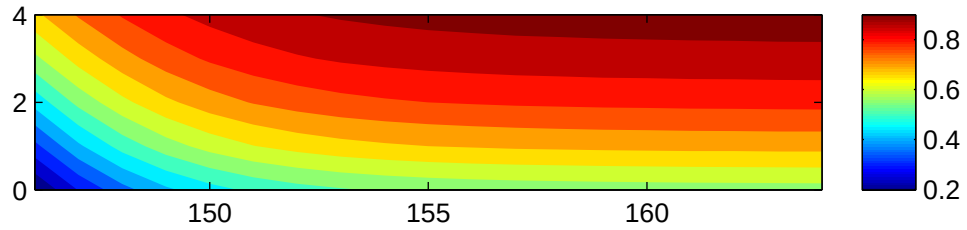

(a) $h = 0.5864, \theta_e = 30$

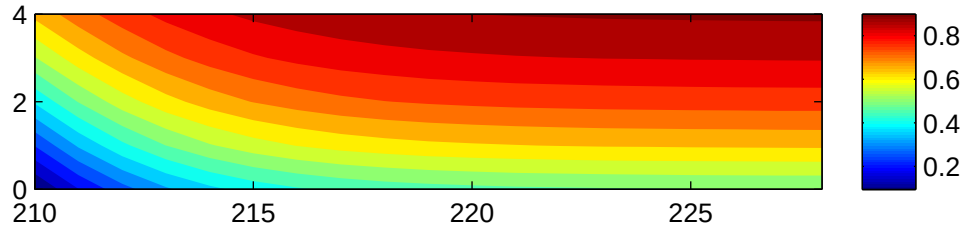

(b) $h = 0.6704, \theta_e = 10$

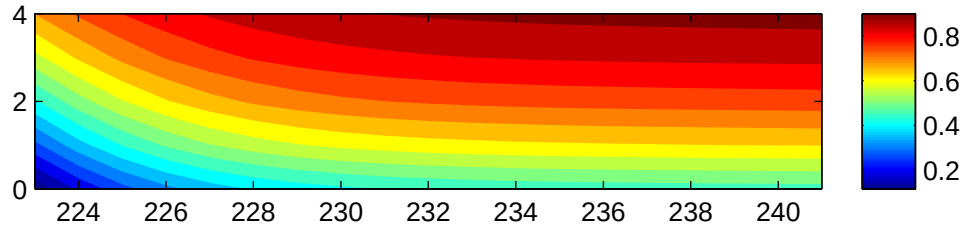

(c) $h = 0.725$

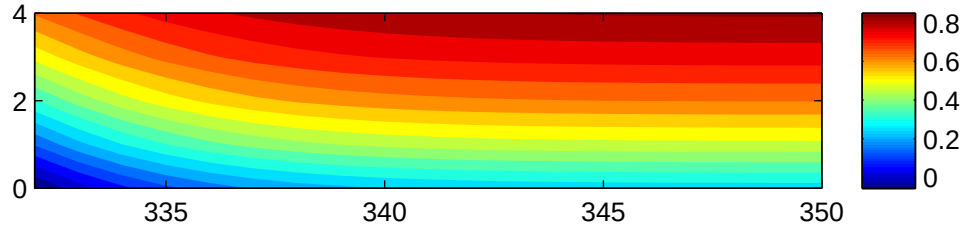

(d) $h = 0.9$

Figure 6.3: Order parameter field of the external fluid immediately outside the contact line. Left bottom point (origin) corresponds to the contact line. Note that a variation in h changes the order parameter field near the wall smoothly. There is no jump at $h = 0.6812$ and the transition from partially wetting to "super-wetting" is rather smooth.

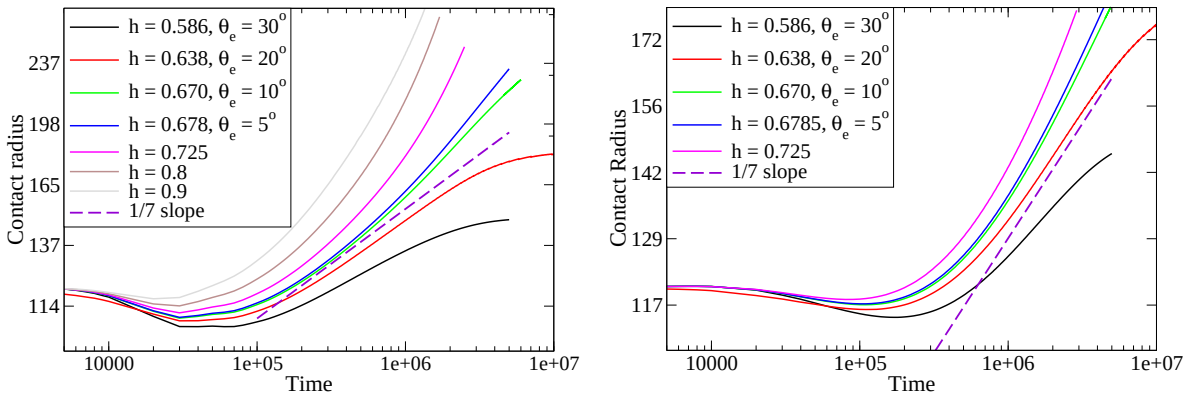

(a) $\eta = 0.015, \eta_r = 1, M = 0.1, \sigma = 9.4 \times 10^{-4}$. (b) $\eta = 0.15, \eta_r = 1, M = 0.1, \sigma = 9.4 \times 10^{-4}$.

Figure 6.4: Contact radius vs time for drops with positive and negative spreading parameter. Algebraic growth is observed for drops with small contact angle before they start to relax to the equilibrium state. Note that for $h > 0.6812$, spreading parameter is positive, representing highly wetting surface and no corresponding θ_e can be defined.

contact radius is measured as a function of time and is plotted in Fig. 6.4 in a log-log plot. Being consistent with the quasi-static assumption, the drop may be taken to be part of a circle at every instant of time, and a circle may be fitted to the interface. The contact radius is obtained from this fit. In Fig. 6.4, results obtained from two sets of simulations with different viscosities are plotted to show that our observations are general. Results of a detailed parametric study are discussed later.

Three different regimes may be observed in Fig. 6.4. The first is the well-known algebraic growth of contact radius according to Tanner's law. A curve with slope of 1/7 is shown in the figures with dashed lines. When the equilibrium contact angle is small, say as in the case of $\theta_e = 20°$, the contact radius indeed follows this algebraic growth for a decade in time, consistent with theory and observations in the literature. At later times, this algebraic growth ceases and the drop reaches the terminal stages of spreading. Here the driving force determined by the difference in the instantaneous and equilibrium contact angles is so small that the spreading is exponentially slow as predicted in the previous sections. This slowing down after the algebraic growth may be clearly seen, again in the case of $\theta_e = 20°$. For even larger equilibrium contact angles the algebraic growth is less clear and the exponent, if estimated, is different from 1/7. The exponential relaxation sets in sooner in this case. We deal with the case of spreading drops with finite equilibrium contact angles in the next section.

When h exceeds a critical value $h_{cr} = 0.6812$, the spreading parameter is positive. This corresponds to a first order wetting transition from a -ve to +ve spreading parameter (de Gennes 1985). A layer of liquid is formed at the solid surface and the wetting process corresponds to wetting on a prewetted film whose thickness may be larger than the interfacial thickness itself (Papatzacos 2002). Therefore the spreading process is faster as observed for several cases in Fig. 6.4 and we call this accelerated spreading regime as the growth is faster than that predicted by Tanner's law. The case of $\theta_e = 5°$ lies somewhere in between. In all these cases Tanner's law is observed for a small period of time, the duration becomes smaller as the spreading parameter becomes more positive.

Essentially we can identify three different kinds of growth. For contact angles that are

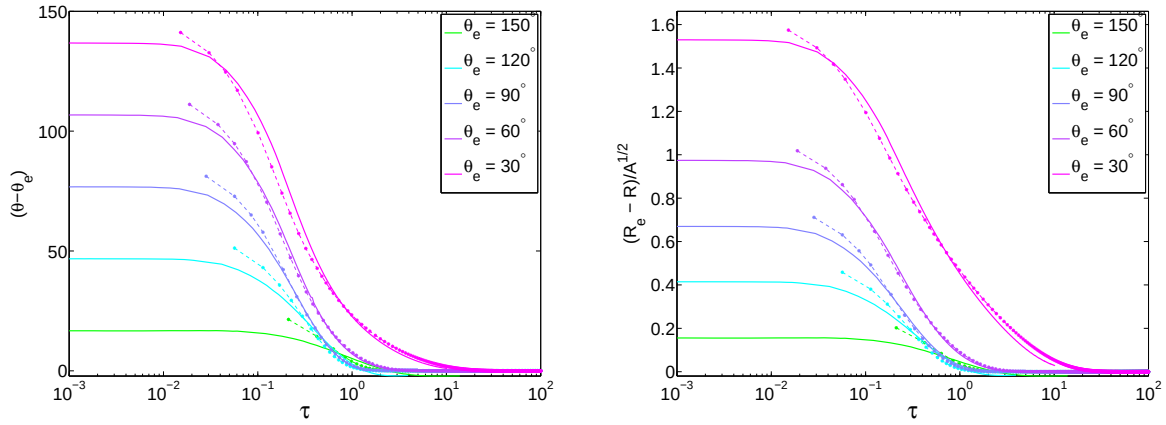

(a) Contact angle

(b) Contact radius

Figure 6.5: Evolution of contact angle and of radius as functions of nondimensional time τ. Continuous lines are obtained by integration Eq. 6.10 while symbols are obtained from the simulation. Since l which depends upon the cutoff length scale at the contact line is unknown it has been used as a fitting parameter. Values of l obtained for the best fit are $3.8, 11.2, 15.6, 16.6, 15.2$ for $\theta_e = 150°, 120°, 90°, 60°, 30°$ respectively. In these simulations $\eta = 0.15, \eta_r = 1, M = 1, \sigma = 9.4 \times 10^{-4}$.

small but finite, we have two regimes (i) Tanner's law, (ii) exponential relaxation that have already been discussed. For extremely small or effectively negative contact angles, we observe a different behavior, with faster spreading than Tanner's law predicts, which we may categorize as accelerated spreading. The appearance and duration of each of these regimes depend on both instantaneous and equilibrium contact angles as explained in section 6.3. These observations are important because depending upon the solid-fluid properties any of these regimes individually or combined may be observed in experiments and simulations. This may probably the reason (i) for the small duration of algebraic growth seen in simulations and experiments and (ii) of various exponents during this growth regime especially from simulations as discussed in the introduction (Milchev & Binder 2002; Milchev *et al.* 2002; He & Hadjiconstantinou 2003; Yaneva *et al.* 2003; Iwahara *et al.* 2003; Ding & Spelt 2007; Wolf *et al.* 2009).

6.5.4 Evolution of drop shape on partially wetting surfaces

Simulations have been performed for drops on partially wetting surfaces including hydrophilic and hydrophobic surfaces, i.e, θ_e is varied from 30° to 150°. Simulations have been started with a circular drop and then allowed to relax to its equilibrium shape. The results are plotted in Fig. 6.5 and compared with theoretical estimates as explained below.

In section 6.3 we have found that Eq. 6.10 describes the evolution of instantaneous contact angle. It is possible to numerically integrate this expression and compare with our simulation data. This is done in Fig. 6.5 where the continuous line is obtained from the numerical integration and the symbols are from the simulations. Both instantaneous contact angle and contact radius, as a difference from the corresponding equilibrium values, are plotted against the nondimensional time τ. This non-dimensionalisation of time involved an unknown quantity

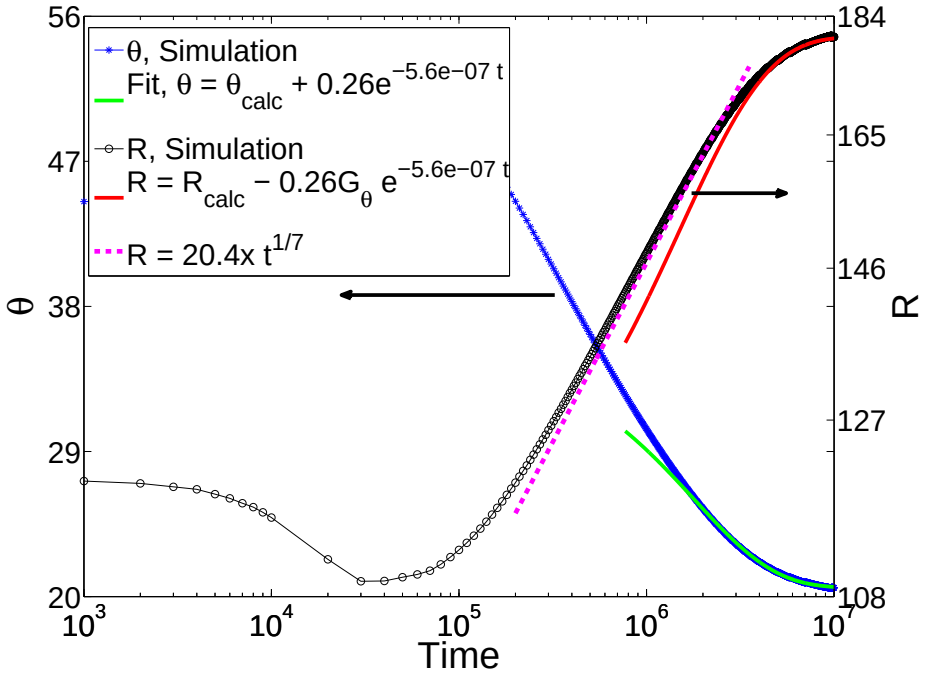

Figure 6.6: Here $\theta_e = 20°$ and $\theta_{calc} = 20.5°$. Other parameters are $\eta = 0.015, \eta_r = 1, M = 0.1, \sigma = 9.4 \times 10^{-4}$. Contact angle (on the left side) and contact radius (on the right side) are plotted against time. Symbols are from simulations. Constants describing evolution of θ are obtained from the best fit while these constants are used to generate the expression for evolution of R. Algebraic growth is clearly visible before the exponential relaxation. Clubbing the terms in the prefactor of exponential function in Eq. 6.15, $G_\theta = \sqrt{A}\theta_{calc} \sin\theta_{calc}/\alpha$ is defined.

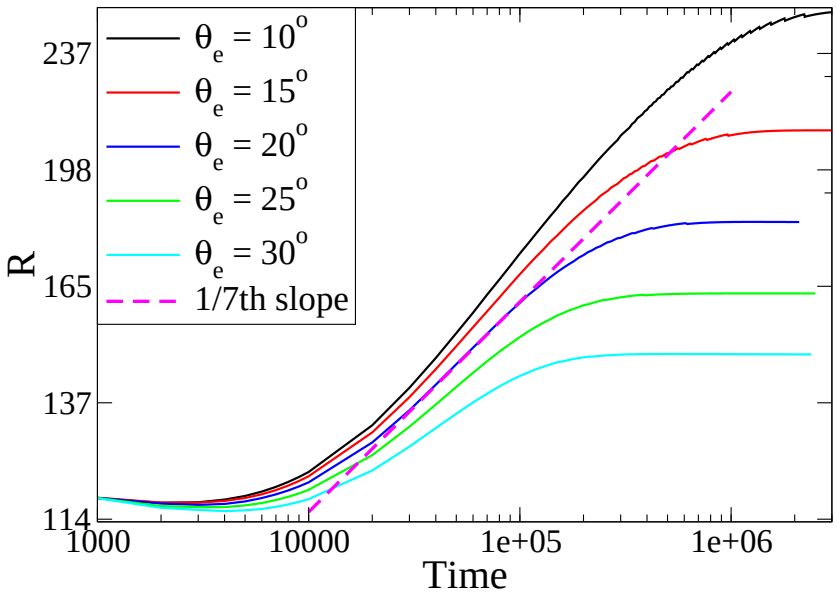

Figure 6.7: Two limits of Eq. 6.10 as explained in Eq. 6.17 and 6.18 may be clearly seen in case of small equilibrium contact angles. Duration of the algebraic growth goes down rapidly as the equilibrium contact angle increases. In these simulations $\eta = 0.15, \eta_r = 1, M = 0.1, \sigma = 4.7 \times 10^{-2}$.

l. Therefore the simulation data is fitted to the theoretical curve to yield the best value of l. Value of l obtained for the best fit are $3.8, 11.2, 15.6, 16.6, 15.2$ for $\theta_e = 150°, 120°, 90°, 60°, 30°$ respectively. It is interesting to note that l, in accordance with the predictions of de Gennes *et al.* (2004), is independent of the equilibrium contact angle in the range of 30° to 90°, and its numerical value is in the expected range (de Gennes *et al.* 2004). Two interesting facts come out of this calculation. The first is that Eq. 6.10 describes well the behavior over several decades of time, i.e for most of the spreading process and not just the terminal stage. Secondly, rather surprisingly, though derived under lubrication approximation, this equation describes the spreading process for large contact angles also.

We have already seen that Eq. 6.10 has two familiar limits, i.e, the algebraic growth and the exponential relaxation as described by Eq. 6.17 and 6.18. These two regimes can be identified clearly in case of small contact angle cases as illustrated in Fig. 6.6 and 6.7. In Fig. 6.6 results obtained from a simulation with $\theta_e = 20°$ are shown. Both contact angle and contact radius are plotted as a function of time and are denoted by symbols. Before reaching the terminal stages of spreading an algebraic growth spanning over a decade of time with a slope of 1/7 can be identified as shown by the dashed line. This is ensued by the exponential relaxation regime as illustrated by the continuous lines. In order to generate this exponential curve data points when $\delta << \theta_e$ were used. A two parameter fit in Eq. 6.14 was found to be necessary in this case unlike in Fig. 6.5. This is because of the two unknowns l, needed for the nondimensionalisation of time and C, the integration constant in Eq. 6.14. As mentioned earlier small difference were found between θ_{calc} and θ_e calculated from h. We have used θ_{calc} in fitting the plots. For example θ_{calc} is measured as 20.5° from the simulations whereas $\theta_e = 20°$ in the particular case in Fig. 6.6. Once the evolution of θ was fitted to obtain l and C, the same were used in the expression 6.15 to make an evolution equation of R with no further fitting parameters. This is plotted as the continuous line in Fig. 6.6 which matches very well with the simulation data. Note that R_{calc} is calculated from Eq. 6.8 using θ_{calc}. In short, the two regimes described by Eq. 6.17 and 6.18 can be clearly identified in the case of small θ_e spreading cases.

As discussed earlier, the durations of each of these regimes depend upon the instantaneous and equilibrium contact angles. This dependence is illustrated in Fig. 6.7 where equilibrium contact angle is varied from 5° to 30°. The smaller the equilibrium contact angle, the longer the duration of the algebraic growth regime. Above 20° it is very hard to observe this regime since exponential regime sets in rapidly and the algebraic regime disappears very early.

From Fig. 6.5 it was seen that Eq. 6.10 fairly describes the drop spreading process even for large contact angles. The algebraic growth regime will completely be absent in these cases, and exponential regime prevails as shown in Fig. 6.8. In these cases simulations were started with a circular drop and allowed to relax. The equilibrium contact angles are chosen as 150°, 120°, 90° and 60°. As mentioned earlier a two parameter fit of Eq. 6.14 is done to calculate l and C. The final value of contact angle obtained from the simulation, θ_calc is used for θ_e. These values are used in Eq. 6.15 to generate the evolution equation for R which matches very well with the simulation data. Therefore, one may infer that the exponential relaxation remains valid for the spreading of drops with large equilibrium contact angles including that on hydrophobic surfaces. It may be interesting to note that the simulation data matches with Eq. 6.15 slightly

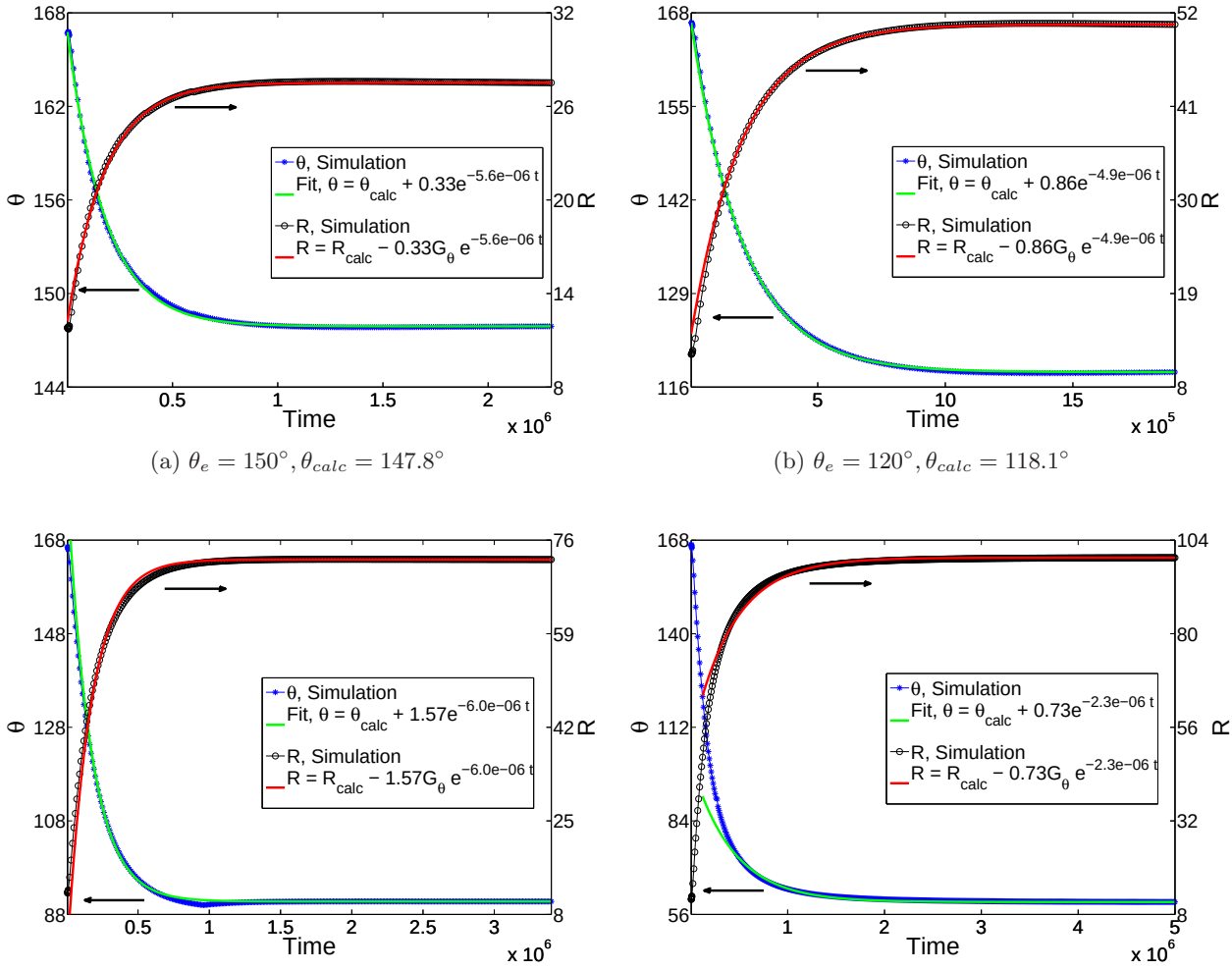

(a) $\theta_e = 150°, \theta_{calc} = 147.8°$

(b) $\theta_e = 120°, \theta_{calc} = 118.1°$

(c) $\theta_e = 90°, \theta_{calc} = 90.8°$

(d) $\theta_e = 60°, \theta_{calc} = 59.7°$

Figure 6.8: Examples showing the prevalence of exponential regime during the spreading process for drops with large contact angles including hydrophobic surfaces. Note that $G_\theta = \sqrt{A}\theta_{calc} \sin\theta_{calc}/\alpha$ is defined. In these simulations $\eta = 0.15, \eta_r = 1, M = 1, \sigma = 9.4 \times 10^{-4}$.

well in case of large contact angles (eg. 150°) than small contact angles (eg. 60°), which may be because $\delta << \theta_e$ always in the former case.

6.5.5 Dewetting

Simulations have been performed to study the dewetting dynamics of drops. It may be noted that the scaling estimates done in section 6.3 are independent of whether the drop is relaxing to its equilibrium state by spreading or dewetting. Hence the expressions derived remain valid for dewetting cases also as illustrated in Fig. 6.9. Here the simulations have been started for a drop which has a contact angle of 30°. The equilibrium contact angles are chosen as 45° and 150°. As shown in the figure, the drop relaxes to its equilibrium values and this process can be explained using the exponential relaxation mechanism that we have already discussed.

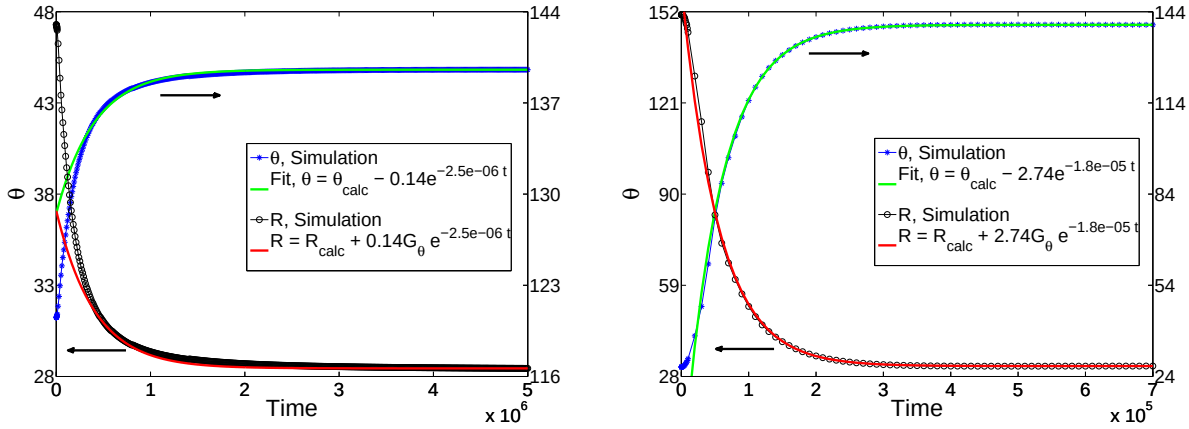

(a) $\theta_e = 45°, , \theta_{calc} = 44.8°$ (b) $\theta_e = 150°, \theta_{calc} = 147.5°$

Figure 6.9: Both contact angle and radius are plotted as a function of time in dewetting of drops. Simulations were started with a drop of $\theta = 30°$ and are allowed to relax to a large equilibrium contact angle. It may be seen that exponential relaxation describes this process well. $G_\theta = \sqrt{A}\theta_{calc} \sin\theta_{calc}/\alpha$ is defined. In these simulations $\eta = 0.015, \eta_r = 1, M = 0.1, \sigma = 9.4 \times 10^{-4}$.

6.5.6 Checks on simulation results

Here we will investigate the effect of initial conditions, domain size and various definitions on the simulations results before proceeding to a parametric analysis.

Simulations in Fig. 6.8 were started with a circular drop while those in Fig. 6.6 were started with a drop shape that is part of a circle with $\theta = 45°$. Under the quasi-static assumption, these different initial conditions should not matter, but it is necessary to verify this assumption from the simulations themselves. Therefore tests were done with three different initial conditions (i) part of a circle with $\theta = 45°$, (ii) a semicircular drop with $\theta = 90°$ and (iii) a full circle with $\theta = 180°$. Results of these simulations are shown in Fig. 6.10. It may be seen that after the initial transients the drop spreads analogously in all the cases implying that the initial conditions are not important in studying the long term spreading behavior that we deal with here. Similarly two other definitions are to be checked. The first is the definition of the interface. Since we have a diffuse interface model with a thick interface, one may define the interface in various ways. It is possible to describe the interface as an isodensity line at $\psi = -0.9$, $\psi = 0.0$ and $\psi = 0.9$. As illustrated in Fig. 6.11a, these definitions do not matter and the drop mass spreads according to the theory described earlier. Secondly it is possible to define a length scale characterizing the growth in different ways. Results so far discussed have all been using contact radius which is measured by fitting part of a circle on the interface and measuring the base radius from it. We can also measure the base radius as the distance to the contact line from the center of the drop. This may differ from the former definition due to (i) deviations from a circular shape and (ii) the bend near the contact line. One may also use area/height as another relevant length scale which comes from the approximation of the drop shape as a wedge. It may be noted from Fig. 6.11b that the growth laws we have discussed so far are independent of any of these definitions.

We have wall boundary conditions on the top and bottom and Neumann boundary conditions on other two sides. Since the model that we use involve an external fluid it is possible that the domain boundaries may affect the drop dynamics through the external fluid flow. Therefore it

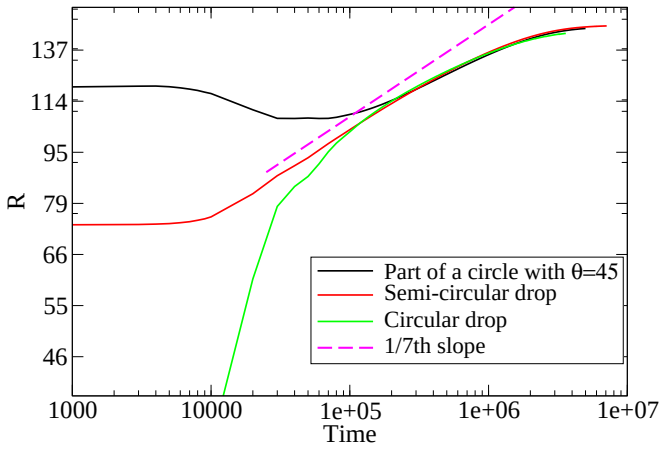

Figure 6.10: Effect of initial conditions on the asymptotic behavior of the drop spreading. Here $\theta_e = 30$. Algebraic growth followed by exponential relaxation may be observed in all cases. In these simulations $\eta = 0.15, \eta_r = 1, M = 0.1, \sigma = 9.4 \times 10^{-4}$

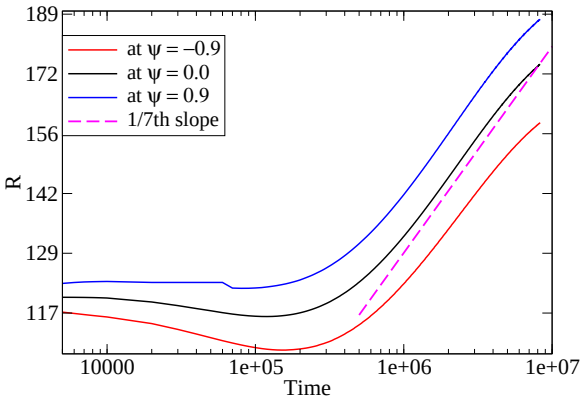

(a) Since we have a diffuse interface model, the interface is defined as $\psi = -0.9$, $\psi = 0.0$ and $\psi = 0.9$. All definitions are consistent.

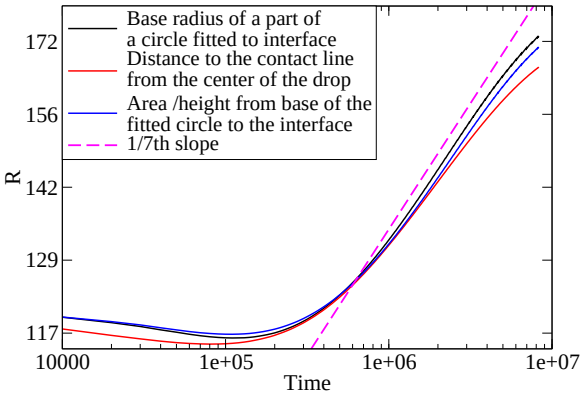

(b) Different measures for the length scale to check the growth laws.

Figure 6.11: Various definition of interfaces and contact radius are possible in this diffuse interface model. However the results are independent of these definitions. These plots are for the simulation with $\theta_e = 20°$ same as used in Fig. 6.4.

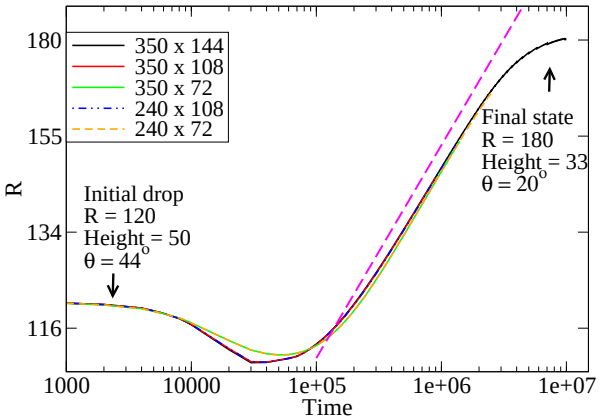

(a) $\theta_e = 20°$

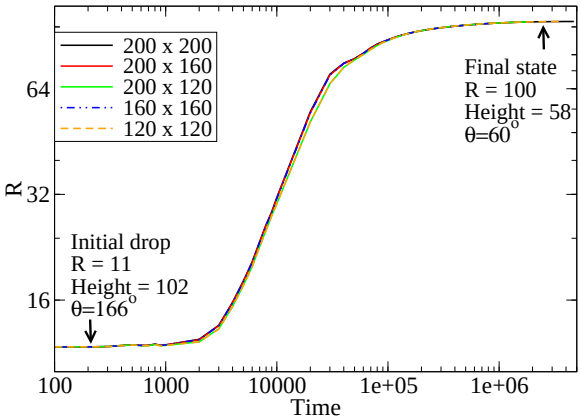

(b) $\theta_e = 60°$

Figure 6.12: Domain boundaries do not affect the spreading dynamics, even when they are very close to the drop. In these simulations $\eta = 0.015, \eta_r = 1, M = 0.1, \sigma = 9.4 \times 10^{-4}$

is important to test whether the domain boundaries affect the results that we obtain and this is done in Fig. 6.12. Here the viscosity of the drop and the external fluid are kept the same. As illustrated such effects are negligible even when the boundaries are very close to the drop.

Drop shapes

In order to understand whether the drop shapes are considerably affected by different growth laws as seen in Fig. 6.4 we plot them in Fig. 6.13. Shapes corresponding to simulations with different θ_e at the same time are plotted in 6.13a, 6.13b and 6.13c. Original drop shapes are plotted in Fig. 6.13a. In order to compare these shapes, the axes have been rescaled with the height of the drop in Fig. 6.13b. All the drops have the same height now, and the highly wetting drop is very flat compared to drops with -ve spreading parameter. Next, we scale the abscissa with drop radius so that all drops have same height and radius as shown in Fig. 6.13c. If all drop shapes are part of circles, then all the shapes will collapse to a single curve. Though this is not the case, very little difference may be observed between various shapes indicating that geometry may not be a decisive parameter in the problem. Deviations are seen to be larger for highly wetting surfaces and are magnified in Fig. 6.13c. Thus assumption of part of a circle is always good to represent these spreading fluid masses. An approximation to circle is just a convenient way of representing mass conservation. For example, in deriving Tanner's law, approximation of the contact line region to a wedge is sufficient to estimate the scaling laws. Also plotted are the shapes at different times but with same contact radius (i) at $R = 130$ and (ii) at $R = 180$ in Fig. 6.13d and 6.13e respectively. Again, no noticeable difference in the shapes can be seen.

It may also be noted that a bend of the interface may always be seen at the contact line, especially in case of small contact angles. The length scale associated with this bend is of the order of interfacial thickness and therefore the presence of this bend is neglected. However it may be noted that the order parameter field around the contact line may lead to ambiguous definitions of interface and contact angle as mentioned in section 6.5.2.

Drop size

In order to see whether there is an explicit dependence of drop size on the duration of these regimes, drop size was halved and another simulation conducted for the case of $\theta_e = 20^\circ$ of Fig. 6.4. The contact radius is plotted as a function of time in Fig. 6.14, but it is scaled so that the contact radii match in both cases. One may see from the plots that the duration of the algebraic regime decreases as the drop size reduces, though it lasts for almost a decade in both cases.

6.5.7 Effect of various parameters on the spreading process

Four different parameters, namely (i) surface tension, (ii) viscosity, (iii) viscosity contrast between the fluids and (iv) mobility are varied to study the effect of these individual quantities on spreading process. The results are illustrated in Fig. 6.15, 6.16, 6.17 and 6.18. In each case, two different contact angles, $\theta_e = 20^\circ$ and $\theta_e = 60^\circ$ are chosen. As illustrated in Fig. 6.15, increase in surface tension increases the driving force and hence faster spreading can be observed. Similarly decreasing viscosity (of both drop and surrounding fluid) reduces the dissipation losses and faster spreading may be seen as illustrated in Fig. 6.16 for both contact angles. When viscosity is considerably small, inertial effects may become important. Due to this, non monotonic or

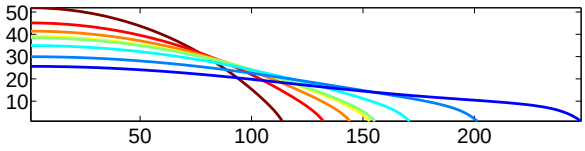

(a) Drop shapes at the same time which constituted Fig. 6.4. Color coding is explained in 6.13c. The drop with largest positive spreading parameter has spread the maximum in a given time.

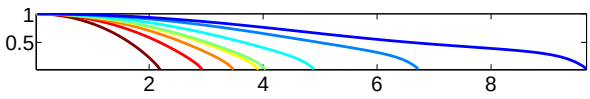

(b) Both abscissa and ordinate in 6.13a are scaled with the respective drop heights.

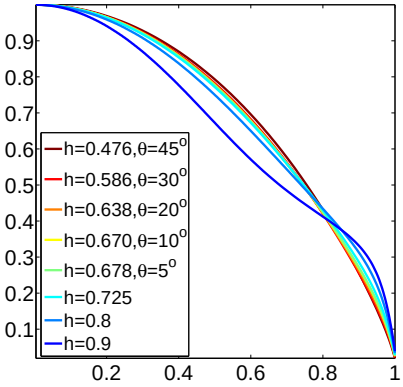

(c) Abscissa of 6.13a is scaled with respective drop radius and the ordinate with drop height. The largest deviations from a circle is observed for drops on highly wetting surfaces and these deviations are magnified here due to the scalings of the axis.

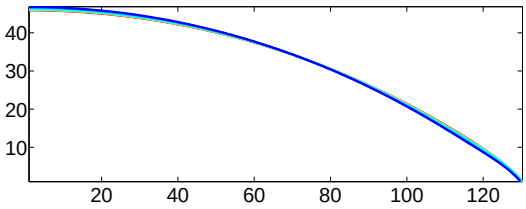

(d) Shapes at different times, but having the same contact radius of 130

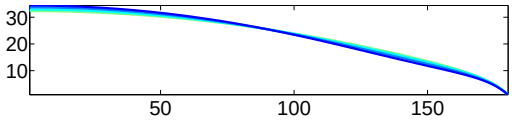

(e) Shapes at different times, but having the same contact radius of 180

Figure 6.13: Shapes of drops described in Fig. 6.4 are shown here. Subplots 6.13a, 6.13b and 6.13c are at time 10^6, and are respectively unscaled, scaled with height, and scaled with height and radius to see that very little difference among them. In 6.13d and 6.13e, shapes at different times but with same contact radius are shown, again to see only small differences among the shapes.

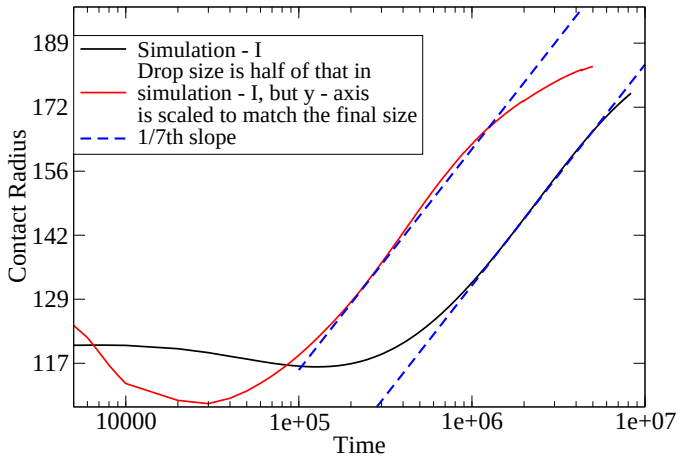

Figure 6.14: The duration of algebraic growth is smaller for the smaller drop though the regime lasts for almost a decade in both cases. Also for the smaller drop, the algebraic growth regime is not as neat as for the large drop, probably because of the inaccuracies arising from the numerics. Here $\eta = 0.15, \eta_r = 1, M = 0.1, \sigma = 9.4 \times 10^{-4}$.

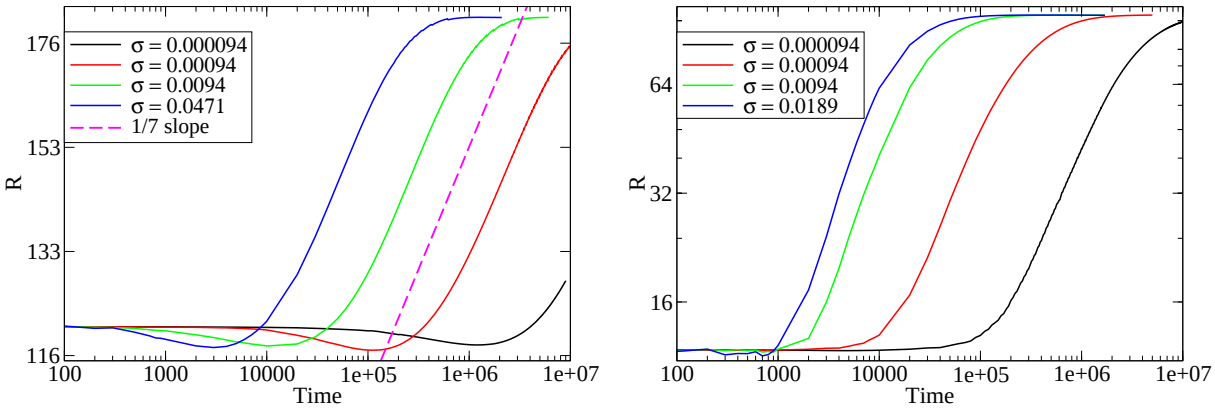

(a) $\theta_e = 20°$ (b) $\theta_e = 60°$

Figure 6.15: As surface tension increases,the driving force increases and the spreading is faster. Other parameters used are $\eta = 0.15, \eta_r = 1, M = 0.1$.

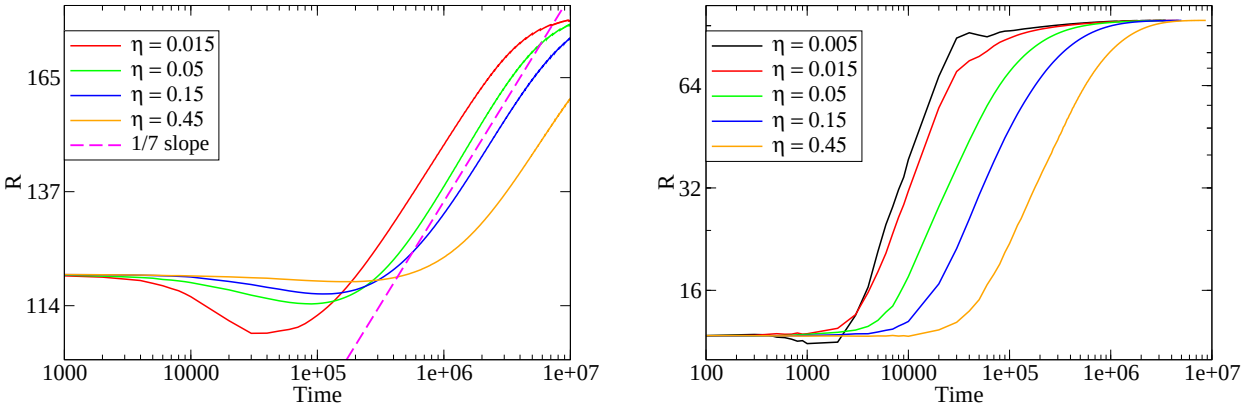

(a) $\theta_e = 20°$ (b) $\theta_e = 60°$

Figure 6.16: As viscosity increases, spreading is slower, as expected. Other parameters used are $\eta_r = 1, M = 0.1, \sigma = 9.4 \times 10^{-4}$.

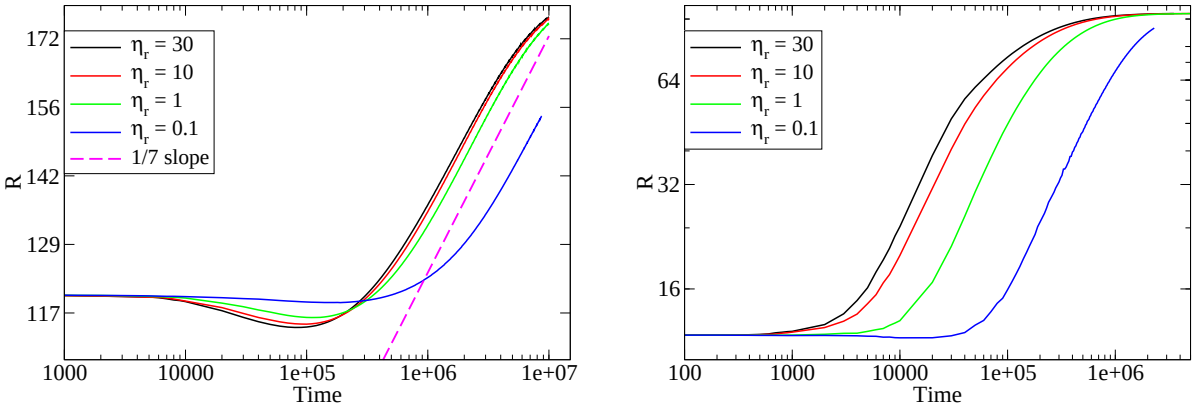

(a) $\theta_e = 20°$ (b) $\theta_e = 60°$

Figure 6.17: As viscosity ratio increases, spreading becomes faster. Other parameters used are $\eta = 0.15, M = 0.1, \sigma = 9.4 \times 10^{-4}$.

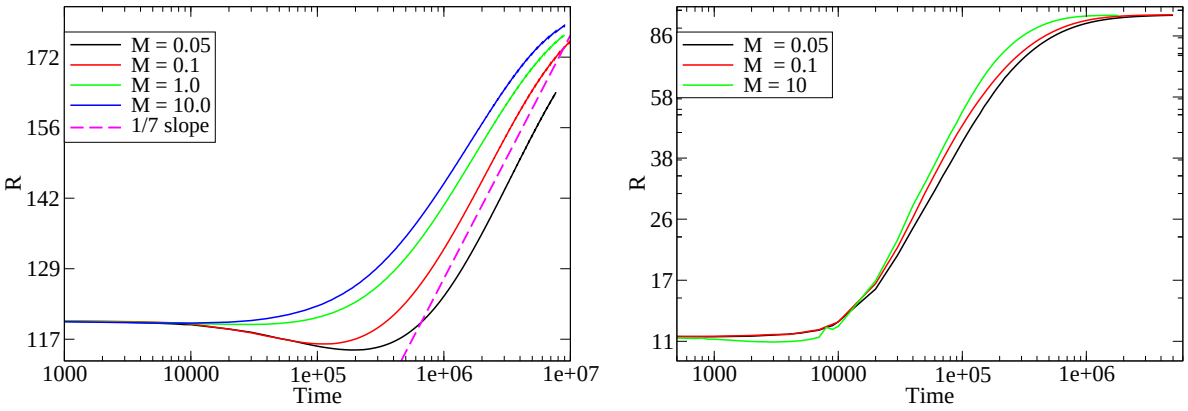

(a) $\theta_e = 20°$ (b) $\theta_e = 60°$

Figure 6.18: Spreading is faster when mobility is increased. Other parameters used are $\eta = 0.15, \eta_r = 1, \sigma = 9.4 \times 10^{-4}$.

even oscillatory spreading rates have been reported (Ding & Spelt 2007). We look at the effect of external fluid in Fig. 6.17, again for two different equilibrium contact angles. Here viscosity ratio, η_r, is defined as the ratio of viscosity of the drop to that of the external fluid. In Fig. 6.17 viscosity of the drop is kept as a constant and the viscosity ratio is changed. As viscosity ratio increases, i.e the viscosity of the external fluid reduces, spreading becomes faster but not very significantly. But when the viscosity of the external fluid is larger than the drop itself spreading is considerably slower. Faster spreading may be observed when mobility, M, is increased. Since mobility plays a direct role in the slip at the contact line in diffuse interface models (Yue *et al.* 2010) this faster spreading may be due to the contact line slip.

6.6 Conclusions

Capillary spreading of drops on solid surfaces is studied using a hybrid algorithm of lattice Boltzmann method and diffuse interface model. Different regimes during the spreading process are identified from simulations. Scaling estimates by balancing capillary and viscous forces provide evolution equations for instantaneous contact angle and contact radius as a function of time. It may be seen that the equations have two familiar limits (i) an algebraic growth which is commonly known as Tanner's law and (ii) an exponential relaxation regime. This establishes the connection between the two laws observed, respectively, for completely wetting and partially wetting drops. For sufficiently small contact angles, these two regimes are identified in simulations. The duration of each of these regimes depends on the instantaneous and equilibrium contact angles. It turns out that the evolution equation derived under the lubrication approximation can describe the spreading process even for large contact angles. More specifically the exponential regime can describe most part of both wetting and dewetting process of all contact angles. For highly wetting surfaces, an accelerated regime of spreading is observed.

This detailed study spanning the entire range of contact angles provides a comprehensive picture about the dynamics of spreading of drops on solid surfaces. Not only this explains why Tanner's law is reported only over small durations of time, it also suggests why various exponents are reported during the algebraic growth regime. Since drop spreading is a common process used

to study the contact line movement, we hope that our systematic analysis on wetting/dewetting constituting the entire range of equilibrium contact angles will deepen the understanding of the problem and will help to design better experiments. Also this analysis provides the basis to study various other effects such as inertia, gravity, precursor films and thermal fluctuations on perfectly wetting, hydrophilic and hydrophobic surfaces.

Chapter 7

Conclusions and Future Work

This thesis concentrates on the study of statics and dynamics of drops on solid surfaces. Detailed conclusions are provided at the end of each chapter. However an overview is provided here followed by a list of future studies that needs to be taken up.

Our energy minimization procedure in Chapter 2 to determine pendant drop shapes with free boundaries yielded single boundary condition representing both pinned and unpinned drops. A novel method of obtaining static shapes through numerical energy minimization also yielded the microscopic force balance as the boundary condition. Not only is the connection between the microscopic and macroscopic force balance thus established, this analysis also delineated stable and unphysical drops shapes. Infinitely long but with finite volume, Kelvin drops are found, which are statically stable. Minimum contact area solutions emerging from the numerics are found to be spurious. We hope our analysis will inspire experimentalists to generate some of these fascinating shapes and theorists to perform a dynamic stability analysis to explain the non-existence of the multi-lobed shapes. A similar energy minimization study applied to drops on inclined surfaces in Chapter 3 showed that the unpinned end always achieves Young's equilibrium contact angle and this helped us to derive simple expressions relating the drop volume and contact angles. Unlike pendant drops, a choice of ground state for potential energy arises here. Two realistic bases, the front pinned and the back pinned drops are chosen. Similarly a detailed force balance reveals the importance of reaction forces at the solid surface and shows that there is a maximum volume can be held on an inclined surface. These detailed studies show guidelines to manipulate solid-fluid properties to support required static drop volumes and also highlights the caps of these designs.

Our detailed hybrid algorithm using lattice Boltzmann method and diffuse interface model in Chapter 4 incorporating several features is a multi-purpose algorithm capable of investigating several multiphase fluid flow problems. Viscosity contrast between the fluids, desired wetting boundary conditions, gravity and thermal fluctuations obeying fluctuation dissipation theorem at the discrete space for binary fluids extend the scope of this algorithm to many macro-scale and mesoscale problems. Two different methods based on finite difference and finite volume to spatially discretize Cahn Hilliard equation are introduced and several bench marking studies are done. Applying this algorithm to dynamics of drops on inclined surfaces in Chapter 5, we distinguish the roll vs slide motion inside these drops. A rather uncommon method of triple decomposition of the velocity gradient tensor helps us to perform this analysis. Several intuitions are verified and quantitative relations are obtained. Prominent among them is the universal relation obtained between the amount of rolling motion and a shape factor for a fixed contact line slip length and viscosity contrast but independent of capillary and gravitational forces. It is expected that our analysis will provide guidelines in several applications which include novel design of material surfaces where rolling motion may or may not be desirable. Capillary

driven spreading of drops on horizontal surfaces is also studied using the hybrid algorithm over a range of contact angles in Chapter 6. This detailed study provides a comprehensive picture of drop dynamics during spreading and de-wetting processes. A general expression obtained from lubrication approximation for the evolution of contact angle is found to be valid for a range of contact angles. Different limits of this expression correspond to known regimes of spreading and these are also identified in the simulations. This systematic analysis explains the discrepancies in the literature connecting different regimes of spreading, provides a deeper understanding of the spreading process and will help in design of better experiments in the study of contact line dynamics.

The present work has opened up a plethora of questions which require further investigations and some of them are mentioned below.

1. A dynamic stability analysis of axisymmetric, multi-lobed Kelvin drops which are statically stable is required to understand their existence/non-existence. If proven dynamically stable, then it will require the sophisticated skills of experimentalists to demonstrate these shapes. Also presently lacking in the literature is a dynamic stability analysis of pendant drops with unpinned contact line. This study will really help us estimate the maximum volume of static pendant drops and see the importance of static stability analysis. Also a comparison with stability analysis of pinned drops from the literature will throw light on the importance of pinning in making these static shapes. It will be interesting to study these shapes and their stability if it were hanging from an axisymmetric object like a cone instead of a flat surface which is generally seen in several geological structures.

2. Finding of minimum contact area shapes as spurious minimum energy solutions in the numerical energy minimization to calculate pendant drop shapes represents a larger problem in the numerical optimization procedures in reduced probing space. In our case, it was possible to establish the spuriousness from the corresponding analytical energy minimization procedure and from the knowledge of boundary conditions. However such physical insights may not be available, which may be the very reason for performing numerical procedures to determine the solutions and hence these spurious solutions may appear. An investigation into such examples from mechanics and a better mathematical framework to capture these spurious solutions in the optimization problems are thus needed.

3. In order to study the three dimensional minimum energy shapes of drops supported on inclined surfaces it may be necessary to perform a two dimensional optimization problem. It will also be interesting to compare the drop shapes with different choices of ground states for potential energy, compare with real shapes and predict the location of pinning depending upon surface properties. So will be the analysis of contact angle variation along the contact line and the shape of the contact line itself. Similarly a detailed force balance including normal reaction forces on a general three dimensional drop will be cumbersome, but numerical evaluations may surely be done to understand the distribution and role of reaction forces in these cases.

4. The development of lattice Boltzmann-Langevin simulations of binary mixtures opens up different directions to take up. Replacing the scalar order parameter with a tensor

order parameter to study the dynamics of soft matter mixtures will be a direct extension. Role of thermal fluctuations in several mesoscale problems such as (i) nucleation and spinodal decomposition in binary mixtures, (ii) fluctuations enhanced droplets spreading and dewetting and jet break ups (iii) Brownian dynamics of droplets and rheology of Brownian emulsions etc. are to yet to be unfolded in the literature in detail and some of the ongoing efforts are in these directions. An example of enhanced spreading of drops due to thermal fluctuations is shown in Fig. 7.1.

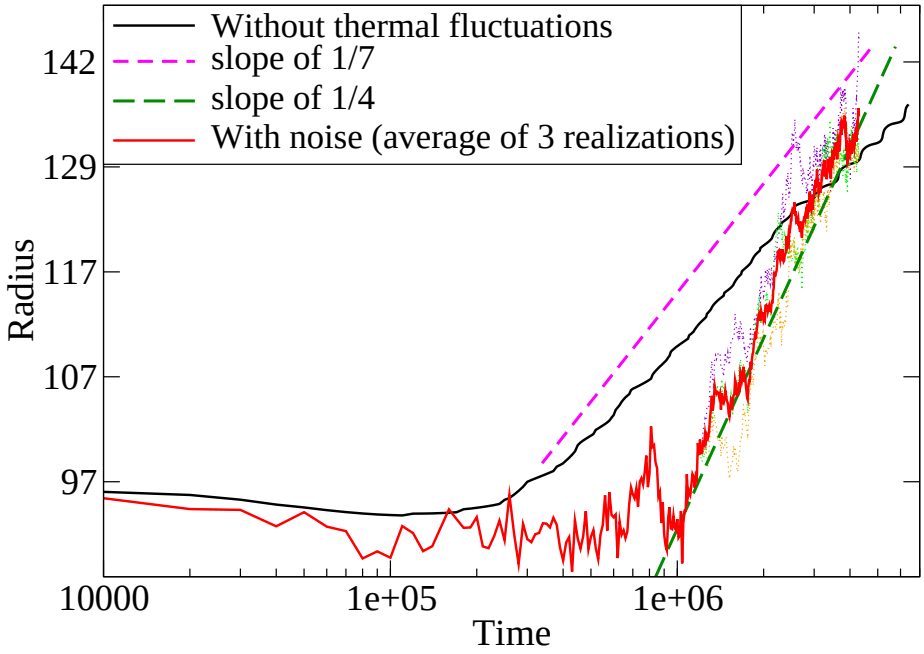

Figure 7.1: Illustration of the effect of thermal fluctuations on drop spreading on wetting surfaces. Thermal fluctuations enhance the rate of spreading.

5. Drop dynamics on inclined surfaces was restricted two dimensions in this thesis. An obvious extension to three dimensions requires modification of procedure of triple decomposition of velocity gradient tensor. This analysis will help us to verify the qualitative predictions made in this thesis and compare with experiments. But even without that, the roll vs slide motion inside the drops in a cross sectional plane of the drop is doable from PIV measurements in experiments. Another important parameter is drop inertia which turned out to be not important in our studies. It is necessary to clarify this question in a more fundamental level. Also it is a good idea to compare the results with simulations using a different technique especially the role of contact line mechanism and slip length.

6. Similarly, extension of drop spreading studies to three dimensions is imperative to ensure that the regimes that are identified in this thesis remain valid and the durations of different regimes. A comprehensive study may be then taken up from the results available in the literature and identify their regimes to show the consistency with our model. These calculations are to be then repeated in a macroscopic level in presence of inertial effects and gravity and at a mesoscopic level in presence of fluctuations.

7. An interesting question then arises from the competition of gravity and capillary forces.

This may be easily addressed by studying the droplet spreading on an inclined surface. It will be easy to analyze this problem in two dimensions where the advancing and receding line will behave differently. Effect of this capillary vs gravity competition on various regimes that are identified in the spreading problem and the roll vs slide motion used in drops on inclined surfaces will be interesting and will help to understand the fundamentals of drop dynamics.

8. It is very easy to simulate drop dynamics on solid surfaces with surface tension gradients in three dimensions. The translational velocity and the instantaneous shapes that the drop achieve can be then calculated. This understanding will have implications in nano and microfluidics applications. Thermal fluctuations in these Marangoni driven flows may turn out to be crucial as these fluctuations serve to explore various configurations and may have non-trivial effects. Such studies have never been done so far.

9. A necessary improvement to be incorporated in the algorithm is to simulate drops with large density differences. This requires modification of lattice Boltzmann algorithm. This will also help to study the inertial effects in the drop dynamics more clearly.

10. Contact line movement in a diffuse interface model is due to the diffusion of order parameter. In certain situations this mechanism is found to be important in drop dynamics. For example the effect of slip length in deciding the amount of rolling motion. Such effects are to be compared with theory or experiments to understand the implications of the mechanism that removes contact line singularity in the diffuse interface model.

11. Since it is possible to adjust the contact angle locally in the hybrid algorithm, it will be easy to implement non-ideality of the solid surfaces through the introduction of chemical heterogeneities and efforts are going on this direction. This will help us to simulate static drops on inclined surfaces in our algorithm and hence it will be possible to study the transient motion of drops as they start to move. This is important because the drop motion initiated by an incremental tilt of the plate may be easy to study from a linear analysis.

12. Lubrication equations describe the drop dynamics very well in the case of small equilibrium contact angles. While the other limit of almost circular shapes are studied less, with studies so far restricted only to scaling analysis. Deviations from the circular shape due to the drop deformation or a contact angle $< 180^\circ$ and its effect on dynamics may be taken up through a perturbation analysis. A combination of these two limits should describe the drop motion for any arbitrary contact angles. For example, the roll vs slide distinction made for drops on inclined surfaces may be interpreted as a consequence of the two limits providing theorteical explanations for the observations in simulations.

13. We have seen the important difference between static drop shapes on surfaces inclined at α and $180^\circ - \alpha$ angles. Both incipient motion and steady state motion of drops at these inclinations and their comparison can be very rewarding in terms of understanding the physics of droplet motion and study the competition between capillary and gravitational forces.

Appendix A

Comparison of discrete Laplacian operators

In order to ensure the isotropy of the discrete form of the Laplacian operator, we have compared four available expressions of the operator existing in the literature. Controlling the degree of isotropy of the diffusive term of the order parameter governing equation (Eq. 4.8), i.e, $\nabla^2\mu$ is crucial to avoid spurious interface pinning. Note that the evaluation of chemical potential (μ) itself contains Laplacian of order parameter. We give the details of the comparisons here.

Consider a 3d cubic lattice as shown in Fig. A.1: it has 6 nearest neighbors, denoted as N_1, 12 next nearest neighbors, denoted as N_2 and 8 next next nearest neighbors, denoted as N_3. Correspondingly the set of lattice vectors with one, two and three non zero components form the set $\mathbf{c}_i^{N_1}$, $\mathbf{c}_i^{N_2}$ and $\mathbf{c}_i^{N_3}$ respectively where $[\mathbf{c}_i^{N_1}, \mathbf{c}_i^{N_2}, \mathbf{c}_i^{N_3}] \in \mathbf{c}_i$. Then

$$[\nabla^2\psi(\mathbf{r})]_{CD} = \sum_{i=1}^{6} \psi(\mathbf{r} + \mathbf{c}_i^{N_1}) - 6\psi(\mathbf{r}) \tag{A.1}$$

$$[\nabla^2\psi(\mathbf{r})]_{PK} = \frac{14}{30}\sum_{i=1}^{6} \psi(\mathbf{r} + \mathbf{c}_i^{N_1}) + \frac{3}{30}\sum_{i=1}^{12} \psi(\mathbf{r} + \mathbf{c}_i^{N_2}) + \frac{1}{30}\sum_{i=1}^{8} \psi(\mathbf{r} + \mathbf{c}_i^{N_3}) - \frac{128}{30}\psi(\mathbf{r}) \tag{A.2}$$

$$[\nabla^2\psi(\mathbf{r})]_{SO} = \frac{6}{22}\sum_{i=1}^{6} \psi(\mathbf{r} + \mathbf{c}_i^{N_1}) + \frac{3}{22}\sum_{i=1}^{12} \psi(\mathbf{r} + \mathbf{c}_i^{N_2}) + \frac{1}{22}\sum_{i=1}^{8} \psi(\mathbf{r} + \mathbf{c}_i^{N_3}) - \frac{80}{22}\psi(\mathbf{r}) \tag{A.3}$$

$$[\nabla^2\psi(\mathbf{r})]_{LB} = \frac{1}{9}\left[\sum_{i=1}^{26} \psi(\mathbf{r} + \mathbf{c}_i) - 26\psi(\mathbf{r})\right] \tag{A.4}$$

where $\psi(\mathbf{r}) = \psi(x, y, z)$. The suffixes CD, PK, SO and LB stand for central difference, Patra-Kartunnen, Shinozaki-Oono and lattice Boltzmann, respectively. Eq. A.1 is the standard central finite difference expression. Eq. A.2 has been systematically derived by imposing conditions of rotational invariance and isotropy of the operator (Patra & Karttunen 2005). Eq. A.3 is popular in the cell-dynamics and phase separation studies (Shinozaki & Oono 1993). Eq. A.4 is a simple expression used in lattice Boltzmann simulations (Desplat *et al.* 2001). The corresponding Fourier transforms are

$$[L(\mathbf{q})]_{CD} = 2\left\{[c_x + c_y + c_z] - 3\right\} \tag{A.5}$$

$$[L(\mathbf{q})]_{PK} = \frac{1}{30}\left\{28\left[c_x + c_y + c_z\right] + 12\left[c_xc_y + c_xc_z + c_yc_z\right] + 8\left[c_xc_yc_z\right] - 128\right\} \tag{A.6}$$

$$[L(\mathbf{q})]_{SO} = \frac{1}{22}\left\{12\left[c_x + c_y + c_z\right] + 12\left[c_xc_y + c_xc_z + c_yc_z\right] + 8\left[c_xc_yc_z\right] - 80\right\} \tag{A.7}$$

$$[L(\mathbf{q})]_{LB} = \frac{1}{9}\left\{2\left[c_x + c_y + c_z\right] + 4\left[c_xc_y + c_xc_z + c_yc_z\right] + 8\left[c_xc_yc_z\right] - 26\right\} \tag{A.8}$$

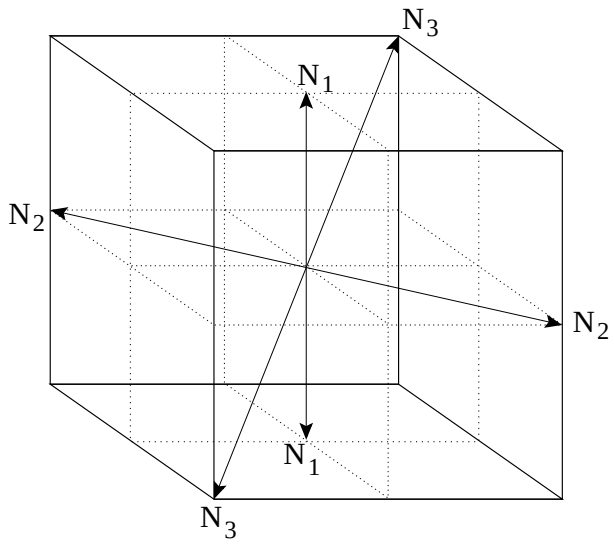

Figure A.1: Stencil used for Laplacian calculation for various schemes illustrated in this appendix. Here N_1 is for the nearest neighbors, N_2 is for next nearest neighbors and N_3 is for next next nearest neighbors. For clarity only one pair of each of them is marked.

where $c_x = \cos q_x, c_y = \cos q_y, c_z = \cos q_z$.

Clearly all the Laplacian operators are negative definite (except at $q = 0$). Fig. A.2 shows the magnitude of the different expressions of the Laplacian operator in wave vector planes with constant q_z. These plots clearly display the four fold symmetry of the lattice. Nonetheless, the effect is less pronounced for the expression suggested by Shinozaki and Oono (A.2c) and so we have used Eq. A.3 for the calculations in section 4.6 - 4.7 and in Chapters 5 - 6.

In the finite volume approach to solve the order parameter evolution, fluxes are calculated (Eq. 4.45) on the links connecting the lattice nodes. Ensuring FDT leads to an equivalent Laplacian operator whose Fourier transform reads

$$[L(\mathbf{q})]_{FV} = -\frac{1}{9}\left\{[2s_x + s_x c_y c_z]^2 + [2s_y + s_y c_x c_z]^2 + [2s_z + s_z c_x c_y]^2\right\} \tag{A.9}$$

where $s_x = \sin q_x, s_y = \sin q_y, s_z = \sin q_z$. This is also plotted in Fig. A.2 for comparison purpose.

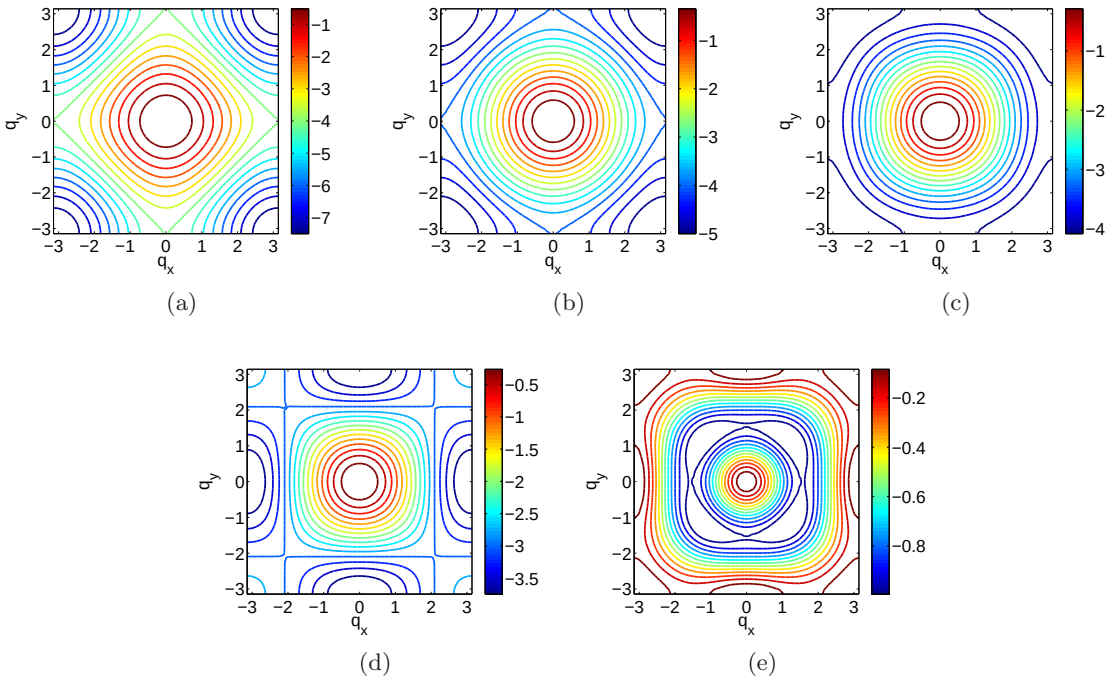

Figure A.2: (Color Online) Fourier transform of Laplacian operators in q_z = constant plane (a) finite difference operator, Eq. A.6 (b) Patra and Kartunnen Eq. A.7 (Patra & Karttunen 2005), (c) Shinozaki and Oono Eq. A.8 (Shinozaki & Oono 1993), (d) lattice based schemes Eq. A.8 (Desplat *et al.* 2001), (e) calculating divergence of flux defined on links in the finite volume approach (Eq. A.9 in 4.6.2)

Appendix B

Improvement in application of wetting boundary conditions

As seen in 5.2, application of wetting boundary conditions were not good at very small and very large contact angles when measured by fitting part of a circle to the interface. In order to check this boundary condition a different geometry was adopted. Two fluids confined between the walls which have equilibrium contact angles as θ_e and $180 - \theta_e$. Therefore the equilibrium configuration is a straight line and it is easy to measure the angles. However the straight interface seems to take a bend near the walls as illustrated in Fig. B.1.

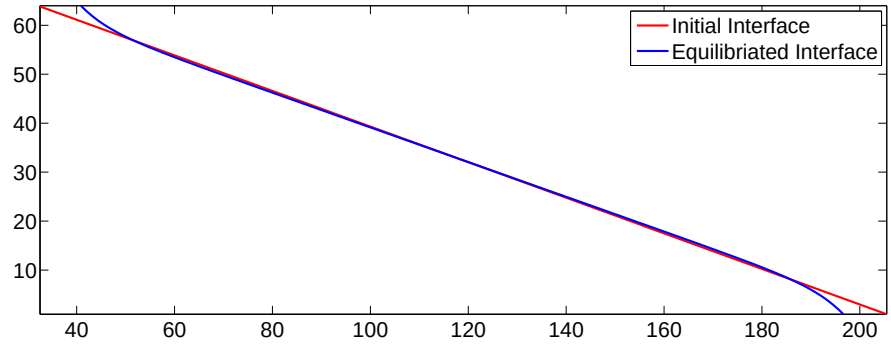

Figure B.1: Two fluids confined between two walls with complementary contact angles have a flat interface. Simulations was started with a flat interface. This takes a bend very near the wall when contact angles are large or small. In this picture wall are chosen with equilibrium contact angles as 20° and 160°.

In order to check whether this bending is due to the numerical approximation of gradients, a higher order method was implemented. Since wall is located at mid grid in the bounce back scheme implemented in the lattice Boltzmann algorithm, a Lagrange's interpolation method was used to calculate the normal component of gradient of order parameter at the wall. When $C = 0$, which is the case we have dealt with here, in Eq. 5.6, application of Lagrange's interpolation method using 4 points gives

$$\frac{H}{K} = \frac{-23\psi_0}{24} + \frac{7\psi_1}{8} + \frac{\psi_2}{8} - \frac{\psi_3}{24} \tag{B.1}$$

where ψ_i represents the value of order parameter at the i^{th} grid point. Hence the value of order parameter at the ghost grid may be calculated as

$$\psi_0 = \frac{K(21\psi_1 + 3\psi_2 - \psi_3) - 24H}{23K} \tag{B.2}$$

The results are shown in Fig. B.2. It may be seen that a higher order method to calculate

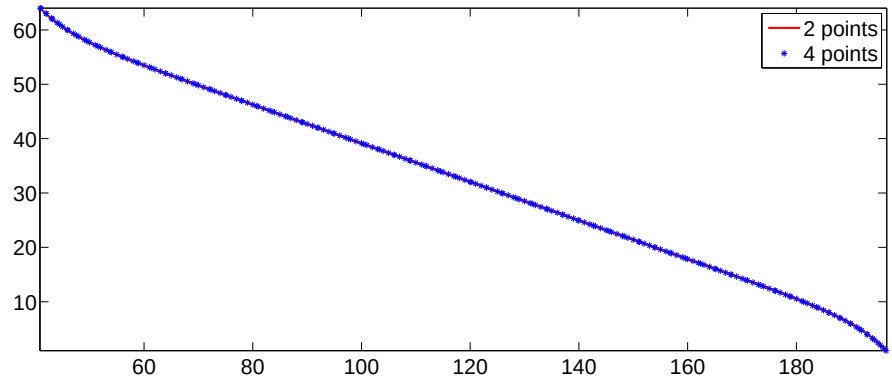

Figure B.2: No improvement is obtained even when a higher order method is implemented to calculate the derivative of order parameter at the wall as part of applying wetting boundary condition as illustrated here.

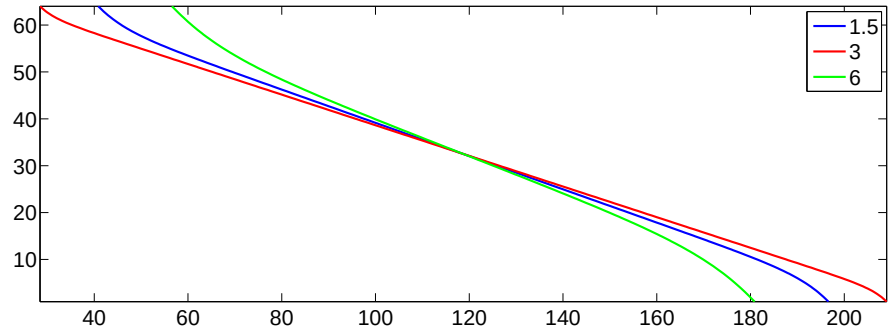

Figure B.3: Interface, defined as $\psi = 0$, as a function of interfacial thickness.

derivative does not help in removing the artificial bend seen near the wall.

In order to check the effect of diffuse interface, interfacial thickness was varied as illustrated in Fig. B.3. As seen, interfacial thickness of 3 grid points seems optimum in these calculations.

References

Abramowitz, M. & Stegun, I. A. 1965 *Handbook of mathematical functions with formulas, graphs and mathematical tables*. Dover, Newyork.

Adhikari, R. 1995 Fluctuating hydrodynamics of binary fluids using a hybrid lattice boltzmann method. http://www.ka.sara.nl/home/willem/www.sara.nl/projects/projects_04_01_185/185_report.pdf.

Adhikari, R., Stratford, K., Cates, M. E. & Wagner, A. J. 2005 Fluctuating lattice boltzmann. *Europhys. Lett.* **71** (3), 473.

Aidun, C. K. & Clausen, J. R. 2010 Lattice-Boltzmann Method for Complex Flows. *Annu. Rev. Fluid Mech.* **42** (1), 439–472.

Anderson, D., McFadden, G. & Wheeler, A. 1998 Diffuse-interface methods in fluid mechanics. *Annu. Rev. Fluid Mech.* **30**, 139–165.

Asinari, P. 2005 Viscous coupling based lattice boltzmann model for binary mixtures. *Phys. Fluids* **17**, 067102.

Atzberger, P. J. 2010 Spatially adaptive stochastic numerical methods for intrinsic fluctuations in reaction-diffusion systems. *J.Comput. Phys.* **229** (9), 3474 – 3501.

Atzberger, P. J., Kramer, P. R. & Peskin, C. S. 2007 A stochastic immersed boundary method for fluid-structure dynamics at microscopic length scales. *J. Comput. Phys.* **224**, 1255.

Aussillous, P. & Quéré, D. 2004 Shapes of rolling liquid drops. *J. Fluid Mech.* **512**, 133–151.

Bashforth, F. & Adams, J. C. 1883 *An Attempt to Test the Theories of Capillary Action by Comparing the Theoretical and Measured Forms of Drops of Fluid*. Cambridge: University Press.

Batchelor, G. K. 1967 *An Introduction to Fluid Dynamics*. Cambridge University Press.

Berejnov, V. & Thorne, R. E. 2007 Effect of transient pinning on stability of drops sitting on an inclined plane. *Phys. Rev. E* **75**, 066308.

Bhattacharjee, A. K., Menon, G. I. & Adhikari, R. 2008 Numerical method of lines for the relaxational dynamics of nematic liquid crystals. *Phys. Rev. E* **78**, 026707.

Biance, A.-L., Clanet, C. & Quéré, D. 2004 First steps in the spreading of a liquid droplet. *Phys. Rev. E* **69**, 016301.

Bikerman, J. J. 1950 Sliding of drops from surfaces of different roughnesses. *J. Colloid. Sci.* **5**, 349.

Bird, J. C., Mandre, S. & Stone, H. A. 2008 Short-time dynamics of partial wetting. *Phys. Rev. Lett.* **100**, 234501.

Bird, R. B., Stewart, W. E. & Lightfoot, E. N. 2006 *Transport Phenomena*. John Wiley & Sons, Inc.; 2nd edition (December 11, 2006).

Blake, T. & Shikhmurzaev, Y. 2002 Dynamic wetting by liquids of different viscosity. *Journal of Colloid and Interface Science* **253** (1), 196 – 202.

Blokhuis, E. M. 2009 On the spectrum of fluctuations of a liquid surface: From the molecular scale to the macroscopic scale. *J. Chem. Phys.* **130**, 014706.

Bonn, D., Eggers, J., Indekeu, J., Meunier, J. & Rolley, E. 2009 Wetting and spreading. *Rev. Mod. Phys.* **81** (2), 739–805.

Boucher, E. A. & Evans, M. J. B. 1975 Pendent drop profiles and related capillary phenomena. *Proc. R. Soc. Lon. Ser-A.* **346** (1646), 349–374.

Boucher, E. A., Evans, M. J. B. & Kent, H. J. 1976 Capillary phenomena. ii. equilibrium and stability of rotationally symmetric fluid bodies. *Proc. R. Soc. Lon. Ser-A.* **349** (1656), 81–100.

Briant, A. J., Papatzacos, P. & Yeomans, J. M. 2002 Lattice boltzmann simulations of contact line motion in a liquid-gas system. *Phil. Trans. R. Soc. Lond. A* **360**, 485–495.

Briscoe, B. J. & Galvin, K. P. 1991 The sliding of sessile and pendent droplets; the critical condition. *Colloid. Surface.* **52**, 219.

Brown, R. A., Jr, F. M. O. & Scriven, L. E. 1980 Static drop on an inclined plate: Analysis by the finite element method. *J. Colloid. Interf. Sci.* **73**, 76.

Brunt, B. 2004 *The Calculus of Variations*. NewYourk, Berlin, Heidelberg: Springer-Verlag.

Buick, J. M. & Greated, C. A. 2000 Gravity in a lattice boltzmann model. *Phys. Rev. E* **61** (5), 5307–5320.

Capuani, F., Pagonabarraga, I. & Frenkel, D. 2004 Discrete solution of the electrokinetic equations. *J. Chem. Phys.* **121**, 973.

Castner, D. G. & Ratner, B. D. 2002 Biomedical surface science: Foundations to frontiers. *Surf. Sci.* **500** (1-3), 28 – 60.

Chaikin, P. M. & Lubensky, T. C. 1995 *Principles of Condensed Matter Physics*. Cambridge.

Chen, J.-D. 1988 Experiments on a spreading drop and its contact angle on a solid. *Journal of Colloid and Interface Science* **122** (1), 60 – 72.

Chen, Q., Rame, E. & Garoff, S. 1996 The velocity field near moving contact lines. *J. Fluid Mech.* **337**, 49–66.

Chesters, A. K. 1977 An analytical solution for the profile and volume of a small drop or bubble symmetrical about a vertical axis. *J. Fluid. Mech.* **81** (4), 609–624.

Chibbaro, S., Biferale, L., Diotallevi, F., Succi, S., Binder, K., Dimitrov, D., Milchev, A., Girardo, S. & Pisignano, D. 2008 Evidence of thinfilm precursors formation in hydrokinetic and atomistic simulations of nanochannel capillary filling. *Europhys. Lett.* **84** (4), 44003.

Clarke, A. 1995 The application of particle tracking velocimetry and flow visualisation to curtain coating. *Chem. Eng. Sci* **50**, 2397–3407.

Concus, P. & Finn, R. 1979 The shape of a pendent liquid drop. *Proc. R. Soc. Lon. Ser-A.* **292** (1391), 307–340.

Daniel, S., Chaudhury, M. K. & Chen, J. C. 2001 Fast drop movements resulting from the phase change on a gradient surface. *Science* **291** (5504), 633–636.

Das, A. K. & Das, P. K. 2009 Simulation of drop movement over an inclined surface using smoothed particle hydrodynamics. *Langmuir* **25**, 11459.

Davidovitch, B., Moro, E. & Stone, H. A. 2005 Spreading of viscous fluid drops on a solid substrate assisted by thermal fluctuations. *Phys. Rev. Lett* **95**, 244505.

Desplat, J. C., Pagonabarraga, I. & Bladon, P. 2001 Ludwig: A parallel lattice-boltzmann code for complex fluids. *Comput. Phys. Commun.* **134**, 2001.

Ding, H. & Spelt, P. D. M. 2007 Inertial effects in droplet spreading: a comparison between diffuse-interface and level-set simulations. *J. Fluid Mech.* **576**, 287–296.

Donev, A., Vanden-Eijnden, E., Garcia, A. & Bell, J. 2010 On the accuracy of finite-volume schemes for fluctuating hydrodynamics. *Comm. App. Math. And Comp. Sci* **5**, 149.

Dunweg, B., Schiller, U. D. & Ladd, A. J. C. 2007 Statistical mechanics of the fluctuating lattice boltzmann equation. *Phys. Rev. E* **76**, 036704.

Dussan, E. B. 1979 On the spreading of liquids on solid surfaces: static and dynamic contact lines. *Annu. Rev. Fluid. Mech* **11**, 371–400.

Dussan, E. B. 1985 On the ability of drops or bubbles to stick to non-horizontal surfaces of solids. part 2. small drops or bubbles having contact angles or arbitrary size. *J. Fluid Mech.* **151**, 1.

Dussan, E. B. & Chow, R. T. 1983 On the ability of drops or bubbles to stick to non-horizontal surfaces of solids. *J. Fluid Mech.* **137**, 1.

Dussan, E. B. & Davis, S. H. 1974 On the motion of a fluid-fluid interface along a solid surface. *J. Fluid Mech.* **65** (1), 71–95.

Dzyaloshinskii, I. E. & Volovick, G. E. 1980 Poisson brackets in condensed matter physics. *Ann. Phys.* **125**, 67.

Eggers, J. 2002 Dynamics of liquid nanojets. *Phys. Rev. Lett* **89**, 084502.

Eggers, J. & Evans, R. 2004 Comment on "dynamic wetting by liquids of different viscosity, by t.d. blake and y.d. shikhmurzaev". *Journal of Colloid and Interface Science* **280** (2), 537 – 538.

ElSherbini, A. I. & Jacobi, A. M. 2004*a* Liquid drops on vertical and inclined surfaces i. a method for approximating drop shapes. *J. Colloid. Interf. Sci.* **273**, 566.

ElSherbini, A. I. & Jacobi, A. M. 2004*b* Liquid drops on vertical and inclined surfaces i. an experimental study of geometry. *J. Colloid. Interf. Sci.* **273**, 556.

ElSherbini, A. I. & Jacobi, A. M. 2006 Retention forces and contact angles for critical liquid drops on non-horizontal surfaces. *J. Colloid. Interf. Sci.* **299**, 841.

Extrand, C. W. & Kumagai, Y. 1995 Liquid drops on an inclined plane: The relation between contact angles, drop shape and retentive force. *J. Colloid. Interf. Sci.* **170**, 515.

Feuillebois, F., Bazant, M. Z. & Vinogradova, O. I. 2009 Effective slip over superhydrophobic surfaces in thin channels. *Phys. Rev. Lett* **102**, 026001.

Finn, R. 1999 Capillary surface interfaces. *Not. Am. Math. Soc.* **46** (7), 770–781.

Finn, R. 2006 The contact angle in capillarity. *Physics of Fluids* **18** (4), 047102.

Finn, R. 2008*a* Comments related to my paper "the contact angle in capillarity". *Physics of Fluids* **20** (10), 107104.

Finn, R. 2008*b* Erratum: "the contact angle in capillarity" [phys. fluids [bold 18], 047102 (2006)]. *Physics of Fluids* **20** (10), 109901.

Finn, R., McCuan, J. & Wente, H. 2011 Thomas youngs surface tension diagram Its history, legacy, and irreconcilabilities. *Journal of Mathematical Fluid Mechanics* pp. 1–9, 10.1007/s00021-011-0079-5.

Finn, R. & Shinbrot, M. 1988 The capillary contact angle, ii: The inclined plane. *Math. Method. Appl. Sci.* **10**, 165.

Flekkoy, E. G. & Rothman, D. H. 1995 Fluctuating fluid interfaces. *Phys. Rev. Lett* **75**, 260.

Flekkoy, E. G. & Rothman, D. H. 1996 Fluctuating hydrodynamic interfaces: Theory and simulation. *Phys. Rev. E* **53**, 1622.

Frenkel, Y. 1948 On the behavior of liquid drops on a solid surface 1. the sliding of drops on an inclined surface. *J. Exptl. Theoret. Phys (USSR)* **18**, 659.

de Gennes, P. G. 1985 Wetting: statics and dynamics. *Rev. Mod. Phys.* **57**, 827–863.

de Gennes, P. G., Brochard-Wyart, F. & Quere, D. 2004 *Capillarity And Wetting Phenomena: Drops, Bubbles, Pearls, Waves*. Spring Street, New York, USA: Springer.

Gompper, G., Schick, M. & Domb, C. 1994 *Phase Transitions and Critical Phenomena: Self-assembling Amphiphilic Systems*. Academic Press.

Gonnella, G., Orlandini, E. & Yeomans, J. M. 1999 Phase separation in two-dimensional fluids: The role of noise. *Phys. Rev. E* **59**, 4741.

Grand, N. L., Daerr, A. & Limat, L. 2005 Shape and motion of drops sliding down an inclined plane. *J. Fluid Mech.* **541**, 293–515.

Grant, M. & Desai, R. C. 1983 Fluctuating hydrodynamics and capillary waves. *Phys. Rev. A* **27**, 2577.

Gross, M., Adhikari, R., Cates, M. E. & Varnik, F. 2010 Thermal fluctuations in the lattice boltzmann method for nonideal fluids. *Phys. Rev. E* **82**, 056714.

Gross, M., Cates, M. E., Varnik, F. & Adhikari, R. 2011 Langevin theory of fluctuations in the discrete boltzmann equation. *J. Stat. Mech: Theory Exp.* **2011** (03), P03030.

Grunau, D., Chen, S. & Eggert, K. 1993 A lattice boltzmann model for multi-phase fluid flows. *Phys. Fluids A* **5** (10), 2557.

He, G. & Hadjiconstantinou, N. G. 2003 A molecular view of tanner's law: molecular dynamics simulations of droplet spreading. *J. Fluid Mech.* **497**, 123–132.

He, X., Chen, S. & Zhang, R. 1999 A lattice boltzmann scheme for incompressible multiphase flow and its application in simulation of rayleigh-taylor instability. *J. Comput. Phys.* **152**, 642–663.

Heslot, F., Cazabat, A. M., Levinson, P. & Fraysse, N. 1990 Experiments on wetting on the scale of nanometers: Influence of the surface energy. *Phys. Rev. Lett.* **65**, 599–602.

Hocking, L. M. 1994 The spreading of drops with intermolecular forces. *Phys. Fluids* **6**, 3224.

Hocking, L. M. & Davis, S. H. 2002 Inertial effects in time-dependent motion of thin films and drops. *J. Fluid Mech.* **467**, 1 – 17.

Hocking, L. M. & Rivers, A. D. 1982 The spreading of a drop by capillary action. *J. Fluid Mech.* **121**, 425 – 442.

Hohenberg, P. C. & Halperin, B. I. 1977 Theory of dynamic critical phenomena. *Rev. Mod. Phys.* **49**, 435.

Huppert, H. E. 1982 The propagation of two-dimensional and axisymmetric viscous gravity currents over a rigid horizontal surface. *J. Fluid Mech.* **121**, 43–58.

Ibanes, M., Ojalvo, J. G., Toral, R. & Sancho, J. M. 2000 Dynamics and scaling of noise-induced domain growth. *Eur. Phys. J. B* **18**, 663.

Iliev, S. D. 1995 Iterative method for the shape of static drops. *Comput. Methods Appl. Mech. Engrg.* **126**, 251.

Iliev, S. D. 1997 Static drops on an inclined plane: Equilibrium modeling and numerical analysis. *J. Colloid. Interf. Sci.* **194**, 287.

Iwahara, D., Shinto, H., Miyahara, M. & Higashitani, K. 2003 Liquid drops on homogeneous and chemically heterogeneous surfaces A two-dimensional lattice boltzmann study. *Langmuir* **19** (21), 9086–9093.

J. Wu, H. Ma, M. Z. 2006 *Vorticity and Vortex Dynamics*. NewYourk, Berlin, Heidelberg: Springer.

Jacqmin, D. 2000 Contact-line dynamics of a diffuse fluid interface. *J. Fluid Mech.* **402**, 57–88.

Jeong, J. & Hussain, F. 1995 On the identification of a vortex. *J. Fluid Mech.* **285**, 69–94.

Jerison, E. R., Xu, Y., Wilen, L. A. & Dufresne, E. R. 2011 Deformation of an elastic substrate by a three-phase contact line. *Phys. Rev. Lett.* **106**, 186103.

Joanny, J. F. & de Gennes, P. G. 1984 A model for contact angle hysteresis. *J. Chem. Phys* **81**, 552.

Jr, H. M. & Son, S. 1987 Further considerations of two-dimensional condensation drop profiles and departure sizes. *Warme Stoffubertrag* **21**, 163.

Kawasaki, K. 1960 Study of wettability of polymers by sliding water drop. *J. Colloid. Sci.* **15**, 402.

Kendon, V. M., Cates, M. E., Pagonabarraga, I., Desplat, J. C. & Bladon, P. 2001 Inertial effects in three-dimensional spinodal decomposition of a symmetric binary fluid mixture: a lattice boltzmann study. *J. Fluid. Mech.* **440**, 147.

Khatavkar, V. V., Anderson, P. D. & Meijer, H. E. H. 2007 Capillary spreading of a droplet in the partially wetting regime using a diffuse-interface model. *J. Fluid Mech.* **572**, 367–387.

Kim, H., Lee, H. & Kang, B. H. 2001 Sliding of liquid drops down an inclined solid surface. *J. Colloid. Interf. Sci.* **247**, 372–380.

Koch, K. & Barthlott, W. 2009 Superhydrophobic and superhydrophilic plant surfaces: an inspiration for biomimetic materials. *Philos. Trans. R. Soc. London, Ser. A* **367** (1893), 1487–1509.

Kolar, V. 2007 Vortex identification: New requirements and limitations. *Int. J. Heat and Fluid Flow* **28**, 638–652.

Krasovitski, B. & Marmur, A. 2005 Drops down the hill: Theoretical study of limiting contact angles and the hysteresis range on a tilted plate. *Langmuir* **21**, 3881–3885.

Ladd, A. J. C. 1994 Numerical simulations of particulate suspensions via a discretized boltzmann equation. part 1. theoretical foundation. *J. Fluid Mech.* **271**, 285.

Landau, L. D. & Lifshitz, E. M. 1959 *Fluid Mechanics*. Pergamon Press.

Langaas, K. & Yeomans, J. M. 2000 Lattice boltzmann simulation of a binary fluid with different phase viscosities and its application to fingering in two dimensions. *Eur. Phys. J. B* **15**, 133–141.

Larkin, B. K. 1965 Numerical solution of the equation of capillarity. *J. Colloid. Interf. Sci.* **23**, 305.

Lavi, B. & Marmur, A. 2004 The exponential power law: partial wetting kinetics and dynamic contact angles. *Colloids and Surfaces A Physicochemical and Engineering Aspects* **250** (1-3), 409–414.

Lawal, A. & Brown, R. A. 1982 The stability of inclined sessile drops. *J. Colloid. Interf. Sci.* **89**, 346.

Leal, L. G. 2007 *Advanced Transport Pheonmena: Fluid Mechanics and Convective Transport Processes*. Cambridge University Press.

LeVeque, R. J. 2002 *Finite Volume Methods for Hyperbolic Problems*. Cambridge.

Liskovets, O. A. 1965 The method of lines. *J. Differ. Equations.* **1**, 1308.

Lopez, J., Miller, C. A. & Ruckenstein, E. 1976 Spreading kinetics of liquid drops on solids. *J. Colloid. Interf. Sci.* **56** (3), 460 – 468.

Lunati, I. 2007 Young's law and the effects of interfacial energy on the pressure at the solid-fluid interface. *Physics of Fluids* **19** (11), 118105.

Luo, L. & Girimaji, S. S. 2003 Theory of the lattice boltzmann method: Two-fluid model for binary mixtures. *Phys. Rev. E* **67**, 036302.

Macdougall, G. & Ockrent, C. 1942 Surface energy relations in liquid/solid systems i. the adhesion of liquids to solids and a new method of determining the surface tension of liquids. *Proc. R. Soc. Lon. Ser-A.* **180** (981), 151–173.

Mahadevan, L. & Pomeau, Y. 1999 Rolling droplets. *Phys. Fluids* **11**, 2449.

Majumdar, S. R. & Michael, D. H. 1976 The equilibrium and stability of two dimensional pendent drops. *Proc. R. Soc. Lon. Ser-A.* **351** (1664), 89–115.

Marchand, A., Weijs, J. H., Snoeijer, J. H. & Andreotti, B. 2011 Why is surface tension a force parallel to the interface? *American Journal of Physics* **79** (10), 999–1008.

Merabia, S. & Pagonabarraga, I. 2006 A mesoscopic model for (de)wetting. *The European Physical Journal E: Soft Matter and Biological Physics* **20** (2), 209–214.

Michael, D. H. 1981 Meniscus stability. *Annu. Rev. Fluid. Mech* **13**, 189–215.

Michael, D. H. & Willaims, P. G. 1976 The equilibrium and stability of axisymmetric pendent drops. *Proc. R. Soc. Lon. Ser-A.* **351**, 117–127.

Milchev, A. & Binder, K. 2002 Droplet spreading: A monte carlo test of tanner's law. *J. Chem. Phys.* **116** (17), 7691–7694.

Milchev, A., Milchev, A. & Binder, K. 2002 Nanodroplets on a solid plane: wetting and spreading in a monte carlo simulation. *Computer Physics Communications* **146** (1), 38 – 53.

Milinazzo, F. & Shinbrot, M. 1987 A numerical study of a drop on a vertical wall. *J. Colloid. Interf. Sci.* **121**, 254.

Mitragotri, S. & Lahann, J. 2009 Physical approaches to biomaterial design. *Nat. Mat.* **8**, 15–23.

Mognetti, B. M., Kusumaatmaja, H. & Yeomans, J. M. 2010 Drop dynamics on hydrophobic and superhydrophobic surfaces. *Faraday Discuss.* **146**, 153–165.

Moradi, N., Varnik, F. & Steinbach, I. 2011 Contact angle dependence of the velocity of sliding cylindrical drop on a flat substrate. *Europhys. Lett.* **95** (4), 44003p1–p6.

Nash, R. W., Adhikari, R. & Cates, M. E. 2008 Singular forces and pointlike colloids in lattice boltzmann hydrodynamics. *Phys. Rev. E* **77**, 026709.

O'Brien, S. B. G. 1991 On the shape of small sessile and pendant drops by singular perturbation techniques. *J. Fluid. Mech.* **233**, 519–537.

O'Brien, S. B. G. 2002 Asymptotics of a sequence of pendant drops. *SIAM. J. Appl. Math* **62** (5), 1569–1580.

Orlandini, E., Marenduzzo, D. & Yeomans, J. M. 2005 Shear dynamics in cholesterics. *Comput. Phys. Commun.* **169**, 122.

Oron, A., Davis, S. H. & Bankoff, S. G. 1997 Long-scale evolution of thin liquid films. *Rev. Mod. Phys.* **69**, 931–980.

Padday, J. F. 1971 The profiles of axially symmetric menisci. *Philos. T. R. Soc. Lond.* **269** (1197), 265–293.

Padday, J. F. & Pitt, A. R. 1973 The stability of axisymmetric menisci. *Philos. T. R. Soc. Lond.* **275** (1253), 489–528.

Pagonabarraga, I., Wagner, A. J. & Cates, M. E. 2002 Binary fluid demixing: The crossover region. *J. Stat. Phys.* **107**, 39.

Papatzacos, P. 2002 Macroscopic two-phase flow in porous media assuming the diffuse-interface model at pore level. *Transp. in Porous Media* **49**, 139–174, 10.1023/A:1016091821189.

Patra, M. & Karttunen, M. 2005 Stencils with isotropic discretization error for differential operators. *Numer. Meth. Part. Diff. Eq.* **22**, 936.

Petschek, R. & Metiu, H. 1983 A computer simulation of the time dependent ginzburg landau model for spinodal decomposition. *J. Chem. Phys* **79**, 3443.

Pitts, E. 1973 The stability of pendent liquid drops. part 1. drops formed in a narrow gap. *J. Fluid. Mech.* **59**, 753–767.

Pitts, E. 1974 The stability of pendent liquid drops. part 2. axial symmetry. *J. Fluid. Mech.* **63** (3), 487–508.

Plateau 1873 *Statique Experimentale et theorique des liquides soumis aux seules forces molÃ©culaires*. Paris: Gauthier-Villars.

Pooley, C. M., Kusumaatmaja, H. & Yeomans, J. M. 2008 Contact line dynamics in binary lattice boltzmann simulations. *Phys. Rev. E* **78**, 056709.

Prasianakis, N. I., Karlin, I. V., Mantzaras, J. & Boulouchos, K. B. 2009 Lattice boltzmann method with restored galilean invariance. *Phys. Rev. E* **79**, 066702.

Pujado, P. R., Huh, C. & Scriven, L. E. 1972 On the attribution of an equation of capillarity to young and laplace. *J. Colloid. Interf. Sci.* **38** (3), 662–663.

Qian, T., Wang, X.-P. & Sheng, P. 2003 Molecular scale contact line hydrodynamics of immiscible flows. *Phys. Rev. E* **68**, 016306.

Quere, D. 2005 Non-sticking drops. *Rep. Prog. Phys.* **68**, 2495.

Quere, D., Azzopardi, M. J. & Delattre, L. 1998 Drops at rest on a tilted plane. *Langmuir* **14**, 2213.

Rauscher, M. & Dietrich, S. 2008 Wetting phenomena in nanofluidics. *Annu. Rev. Mater. Sci.* **38**, 143–172.

Richard, D. & Quere, D. 1999 Viscous drops rolling on a tilted non-wettable solid. *Europhys. Lett.* **48** (3), 286.

Rioboo, R., Marengo, M. & Tropea, C. 2002 Time evolution of liquid drop impact onto solid dry surfaces. *Exp. Fluids* **33** (1), 112–124.

Rogers, T. M., Elder, K. R. & Desai, R. C. 1988 Numerical study of the late stages of spinodal decomposition. *Phys. Rev. B* **37**, 9638.

Rotenberg, B., Pagonabarraga, I. & Frenkel, D. 2008 Dispersion of charged tracers in charged porous media. *Europhys. Lett.* **83**, 34004.

Rotenberg, B., Pagonabarraga, I. & Frenkel, D. 2010 Coarse-grained simulations of charge, current and flow in heterogeneous media. *Faraday Discuss.* **144**, 223.

Rotenberg, Y., Boruvka, L. & Neumann, A. W. 1984 The shape of non-axisymmetric drops on inclined planar surfaces. *J. Colloid. Interf. Sci.* **102**, 424.

Rothstein, J. P. 2010 Slip on superhydrophobic surfaces. *Annu. Rev. Fluid Mech.* **42**, 89–109.

Roura, P. & Fort, J. 2001 Equilibrium of drops on inclined hydrophilic surfaces. *Phys. Rev. E* **64**, 011601.

Rowlinson, J. S. & Widom, B. 1982 *Molecular Theory of Capillarity*. Dover Publications.

de Ruijter, M. J., Charlot, M., VouÃ©, M. & De Coninck, J. 2000 Experimental evidence of several time scales in drop spreading. *Langmuir* **16** (5), 2363–2368.

de Ruijter, M. J., De Coninck, J. & Oshanin, G. 1999 Droplet spreading partial wetting regime revisited. *Langmuir* **15** (6), 2209–2216.

Sakai, M., Song, J., Yoshida, N., Suzuki, S., Kameshima, Y. & Nakajima, A. 2006 Direct observation of internal fluidity in a water droplet during sliding on hydrophobic surfaces. *Langmuir* **22**, 4906–4909.

Scardovelli, R. & Zaleski, S. 1998 Direct numerical simulation of free-surface and interfacial flow. *Annu. Rev. Fluid Mech.* **31**, 567–603.

Servantie, J. & Muller, M. 2008 Statics and dynamics of a cylindrical droplet under an external body force. *J. Chem. Phys* **128**, 014709.

Shikhmurzaev, Y. D. 1997 Spreading of drops on solid surfaces in a quasi-static regime. *Phys. Fluids* **9**, 266.

Shikhmurzaev, Y. D. 2008*a* *Capillary Flows with Forming Interfaces*. Chapman & Hall/CRC.

Shikhmurzaev, Y. D. 2008*b* On young's (1805) equation and finn's (2006) 'counterexample'. *Physics Letters A* **372** (5), 704 – 707.

Shikhmurzaev, Y. D. & Blake, T. D. 2004 Response to the comment on "j. colloid interface sci. 253 (2002) 196 by j. eggers and r. evans". *Journal of Colloid and Interface Science* **280** (2), 539 – 541.

Shinozaki, A. & Oono, Y. 1993 Spinodal decomposition in 3-space. *Phys. Rev. E.* **48**, 2622.

Sikalo, S., Wilhem, H. D., Roisman, I. V., Jakirlic, S. & Tropea, C. 2005 Dynamic contact angle of spreading droplets Experiments and simulations. *Phys. Fluids* **17**, 062103.

Snoeijer, J. H. & Andreotti, B. 2008 A microscopic view on contact angle selection. *Phys. Fluids* **20**, 057101.

Snoeijer, J. H., Rio, E., Grand, N. L. & Limat, L. 2005 Self-similar flow and contact line geometry at the rear of cornered drops. *Phys. Fluids* **17**, 072101–1–12.

Squires, T. M. & Quake, S. R. 2005 Microfluidics: Fluid physics at the nanoliter scale. *Rev. Mod. Phys.* **77**, 977–1026.

Starov, V., Kalinin, V. & Chen, J.-D. 1994 Spreading of liquid drops over dry surfaces. *Advances in Colloid and Interface Science* **50** (0), 187 – 221.

Style, R. W. & Dufresne, E. R. 2012 Wetting on deformable substrates, from liquids to stiff solids. *arXiv:1203.1654v1 [cond-mat.soft]* .

Succi, S. 2001 *The Lattice Boltzmann Equation for Fluid Dynamics and Beyond*. Oxford University Press.

Suzuki, S., Nakajima, A., Sakai, M., Sakurada, Y., Yoshida, N., Hashimoto, A., Kameshima, Y. & Okada, K. 2008 Slipping and rolling ratio of sliding acceleration for a water droplet sliding on fluroalkylsilane coatings of different roughness. *Chem. Lett.* **37** (1), 58–59.

Swain, P. S. & Lipowsky, R. 1998 Contact angles on heterogeneous surfaces: a new look at cassie's and wenzel's laws. *Langmuir* **14**, 6772–6780.

Tadmor, R., Chaurasia, K., Yadav, P. S., Leh, A., Bahadur, P., Dang, L. & Hoffer, W. R. 2008 Drop retention force as a function of resting time. *Langmuir* **24**, 9370.

Tanner, L. H. 1979 The spreading of silicone oil drops on horizontal surfaces. *Journal of Physics D: Applied Physics* **12** (9), 1473.

Thampi, S. P. & Govindarajan, R. 2011 Minimum energy shapes of one-side-pinned static drops on inclined surfaces. *Phys. Rev. E* **84**, 046304.

Thomson, W. 1886 Capillary attraction. *Nature* **34**, 290–294.

Tretheway, D. C. & Meinhart, C. D. 2002 Apparent fluid slip at hydrophobic microchannel walls. *Phys. Fluids* **14**, L9–12.

Tsai, P., Peters, A. M., Pirat, C., Wessling, M., Lammertink, R. G. H. & Lohse, D. 2009 Quantifying effective slip length over micropatterned hydrophobic surfaces. *Phys. Fluids* **21**, 112002.

Wente, H. C. 1980 The symmetry of sessile and pendent drops. *Pac. J. Math* **88** (2), 421–470.

Wilkie, J. 2004 Numerical methods for stochastic differential equations. *Phys. Rev. E* **70**, 017701.

Willis, A. M. & Freund, F. B. 2009 Enhanced droplet spreading due to thermal fluctuations. *J. Phys.: Condens. Matter* **46**.

Wilson, K. G. & Kogut, J. 1974 The renormalization group and the [epsilon] expansion. *Phys. Rep. C* **12**, 75.

Wolansky, G. & Marmur, A. 1999 Apparent contact angles on rough surfaces: the wenzel equation revisited. *Colloid. Surface. A* **156**, 381–388.

Wolf, F. G., dos Santos, L. O. E. & Philippi, P. C. 2009 Modeling and simulation of the fluidsolid interaction in wetting. *J. Stat. Mech: Theory Exp.* **2009** (06), P06008.

Xu, A., Gonnella, G., Lamura, A., Amati, G. & Massaioli, F. 2005 Scaling and hydrodynamic effects in lamellar ordering. *Europhys. Lett.* **71**, 651.

Yadav, P. S., Bahadur, P., Tadmor, R., Chaurasia, K. & Leh, A. 2008 Drop retention force as a function of drop size. *Langmuir* **24**, 3181.

Yaneva, J., Milchev, A. & Binder, K. 2003 Dynamics of a spreading nanodroplet: A molecular dynamic simulation. *Macromol. Theory Simul.* **12** (8), 573–581.

Yarin, A. L. 2006 Drop impact dynamics: Splashing, spreading, receding, bouncing... *Annu. Rev. Fluid Mech.* **38**, 159–192.

Yonemoto, Y. & Kunugi, T. 2009 Discussion on a mechanical equilibrium condition of a sessile drop on a smooth solid surface. *J. Chem. Phys* **130**, 144106.

Yue, P., Zhou, C. & Feng, J. J. 2010 Sharp interface limit of the cahn hilliard model for moving contact lines. *J. Fluid Mech.* **645**, 279–294.

Zarate, J. M. O. & Sengers, J. V. 2006 *Hydrodynamic Fluctuations in Fluids and Fluid Mixtures*. Elsevier.